DEFORMED STRUCTURES IN NEUTRON-RICH $A \approx 100$ NUCLEI STUDIED BY ISOMER AND β-DELAYED γ-RAY SPECTROSCOPY

FRANK BROWNE

A thesis submitted in partial fulfilment of the requirements of the University of Brighton for the degree of Doctor of Philosophy

June, 2016

Deformed structures in neutron-rich $A \approx 110$ nuclei studied by isomer and β-delayed γ-ray spectroscopy

Author:

Frank Browne

Supervisor:

Prof. Alison M. Bruce

University of Brighton

Science & Technology Facilities Council

RIKEN NiSHiNA CENTER

A thesis submitted in partial fulfilment of the requirements of the University of Brighton for the degree of Doctor of Philosophy

June, 2016

Abstract

Neutron-rich A∼110 nuclei have been the subject of intensive discussion since the discovery of a rapid onset of ground-state static quadrupole deformation in the A>100 Zr nuclei over 60 years ago. The results presented in this thesis further the experimental knowledge of such deformations towards more exotic isotopes in this region.

An experiment was carried out at the Radioactive Isotope Beam Factory, RIKEN, Wako-shi, Japan. Nuclei of interest were produced through the in-flight abrasion fission of a 345 MeV/nucleon ^{238}U beam by a 555 mg/cm^2 ^{9}Be target and selected by the BigRIPS spectrometer according to their mass-to-charge ratio and atomic charge. They were implanted into the WAS3ABi silicon stack and γ rays emitted following β-decay, or decay of isomeric states were detected in an array of 12 cluster HPGe (EURICA) and 18 $LaBr_3$(Ce) detectors.

A newly implemented fast β-γ timing configuration provided access to the lifetimes of excited states in the nanosecond regime. In particular, the lifetime of the 2_1^+ state of ^{106}Zr is reported for the first time, as well as a more precise measurement for ^{104}Zr, compared to the adopted value. These measurements, combined with the energy of the ground-state transition, have been used to deduce the reduced transition probability and from this a model-dependent value for the ground-state deformation. New isomeric states have also been observed in ^{102}Zr, ^{113}Nb and ^{115}Mo.

The reduced transition probability of the $2_1^+ \rightarrow 0_{g.s}^+$ transition in ^{106}Zr shows a marked decrease from that of ^{104}Zr. This reflects the energy systematics, and further confirms the deformed sub-shell closure at N=64. Comparisons of the systematics of the observed reduced transition probabilities to those calculated in the IBM-1 model show poor agreement. However, calculations based on the nuclear-shell model in a deformed basis state, show good agreement with observation, demonstrating the reliability of the employed ground-state wavefunction. The isomeric state in ^{102}Zr is ascribed to a change in the K quantum number, and the isomeric states in ^{113}Nb and ^{115}Mo are proposed to be due to shape stabilisation of excited states.

Contents

List of Tables

List of Figures

Acknowledgements

On one of my darker days, I Googled what it was to be a "good scientist", my favourite answer went along the lines of, "A good scientist should welcome every problem as though it were a dear friend". During my career, I have met few who embody this philosophy as much as my supervisor, Prof. Alison M. Bruce, to whom I offer my deepest gratitude for allowing me the opportunity to undertake a PhD under her esteemed tutelage. My thanks also extend to Prof. Zsolt Podolyák for his capacity as my second supervisor. To Sumikama-san I thank for being the spokesperson for the experiment detailed in this thesis, but I am most indebted for his imbuing onto me the sense and skills of robust data analysis, in the pursuit of obtaining the best results possible.

My return to Brighton (same city, different university) was graced by a supportive and friendly research group, these characteristics have not changed as a function of group member. In the beginning there was Oli and Camino. Oli has my thanks for fond memories in the office, mostly involving our races to complete the Guardian quick crossword. Camino, whose "unique" perspectives on the IBM have given me insight into what constitutes a good nuclear model, has evolved from a colleague to a cherished friend. After Camino, was Chantal, who I would like to thank for always knowing what teaching I should be doing, and I hope one day she learns to duplex. For all too short a time, there was Cristina, I thank her for her constant willingness to help, and our adventures around Brighton. Last, and probably least, there is Eugenio, who is far from lazy, or stupid, and I would like to thank for being an excellent Halo coach.

Whilst at RIKEN, I had the privilege of working with some of the most outstanding scientists I have had the pleasure of encountering, in some way, or another they have all had their influence on me. P-A for taking me under his wing from my first time in Japan when I was a scared visitor who didn't like sushi. I would like to thank

Shunji for his infallible good humour, which made the decay spectroscopy team such a pleasure to work in. The way I live my life has been somewhat disorderly, this changed, mostly, when I became friends with Pieter, whose organisational prowess has inspired me to at least keep my inbox empty. Also, I would like to thank Shunji and Pieter for their roles in my becoming an IPA student. The hard work of Xu on the sorting codes and generally knowing everything has been invaluable throughout my PhD. I also acknowledge Giuseppe for his viewpoints on the field, and our cultural exchanges. I would like to thank my fellow IPA students for the journey we shared, the first tranche being, Jan, Guillaume and Zsolt, and the second Laura, Zena, Simon and Daniel. My good friend Wu outlasted all other IPA students, with whom I can always rely on for a profound discussion, I wish Wu every success.

Here, I provide special mention some outstanding people whom I have met during conferences, workshops and experiments. To be begin with, Liliana, whose support has been invaluable, especially as I write this, and has taught me not to cry too much on my way to heaven. We CAN do it!! I would like to thank Gary Simpson for his patience in describing the facets of numerous nuclear models, and for his thoughtful considerations of ideas that I present to him. Volker for his particular interest in correcting the drafts of work I have sent to him. Watanabe-san for his work on the LaBr array at RIKEN.

Closer to home, I have had the support of a sublime group of friends. My undergraduate colleagues for all their help in the early days, James Piggles, Manatee and the Worsdale, and for pints and their associated prizes. Special mention to Sam and Tonia for their delicious meals which have kept me alive. Dr. Jessi for our evenings of pints and discussions of PhD life. Daftpunk for his excellent computing advice, that has saved me from disaster on multiple occasions. I'd like to thank the Andy and Dan for their roles as the other two amigos. Also, for Leo for making the MSc year such a great one, full of LaTeXcompetitiveness.

The above is far from a complete list, and if there are glaring omissions you have maaaany apologies from me.

Finally, I would like to thank my family, in particular Dad 'n' Joni for their generous support and always being one phone call away. Without them I would not have been able to make it this far.

Declaration of authorship

I declare that the research contained in this thesis, unless otherwise formally indicated within the text, is the original work of the author. The thesis has not been previously submitted to this or any other university for a degree, and does not incorporate any material already submitted for a degree.

Signed:

Dated:

Chapter 1

Introduction

The atomic nucleus, which comprises two types of fermions, protons and neutrons, presents a perplexing quantum mechanical problem due to its many-body nature and the strong interaction of its constituents. One of the most intriguing and fundamental emergent properties of the nucleus is the shape that these *nucleons* are distributed across. When the number of both protons and neutrons equal the "magic numbers" (2, 8, 20, 28, 50, 82...) of Mayer and Jensen [1, 2], the nucleonic distribution is spherical. However, when the nucleon numbers are mid-way between the magic numbers, the nuclear distribution can take on a stabilised non-spherical configuration. The quadrupole deformations constitute the simplest form of stable deviations from spherical shapes. The two types of this deformation are labelled as prolate (rugby ball) and oblate (discus). Quantifying the magnitude of these distortions in isotopic chains which exhibit rapid shape changes as a function of nucleon number are of particular theoretical and experimental interest. Such regions highlight a remarkable sensitivity of the deformation, which is a collective phenomenon, to single-particle effects. As such, they provide a stringent test of nuclear models as well as an essential input for the development of modern theoretical frameworks [3].

1.1 Structures in the neutron-rich zirconium region

The zirconium isotopic chain ($Z = 40$) and its neighbours are located centrally with respect to the $1f_{7/2}$ ($Z = 28$) and $1g_{9/2}$ ($Z = 50$) major proton shell closures, making them an exemplary case study of mid-shell nuclei. Close to the $N = 50$ shell closure

the pf proton shell closure at $Z = 40$ is reinforced, with the consequence semi-magic ^{90}Zr (semi-magic) exhibits doubly-magic behaviour [4, 5]. For $N = 52$ and $N = 54$ weak proton-neutron coupling is responsible for shape co-existing structures in ^{94}Zr [6], as well as mixed symmetry states in ^{92,94}Zr [7]. The 2_1^+ energy of ^{96}Zr exhibits doubly-magic behaviour, after which there is a brief shape-phase transitional region [8, 9, 10, 11] up until $N = 60$, where a large degree of collectivity and static ground-state quadrupole deformation is manifest [11, 12]. The starkness of the onset of this collectivity is best demonstrated by the reciprocal energies of the 2_1^+ states, which are known to relate directly to the ground-state deformation of a nucleus. These are shown in Fig. 1.1, which highlights the evolution of nuclear structure described above.

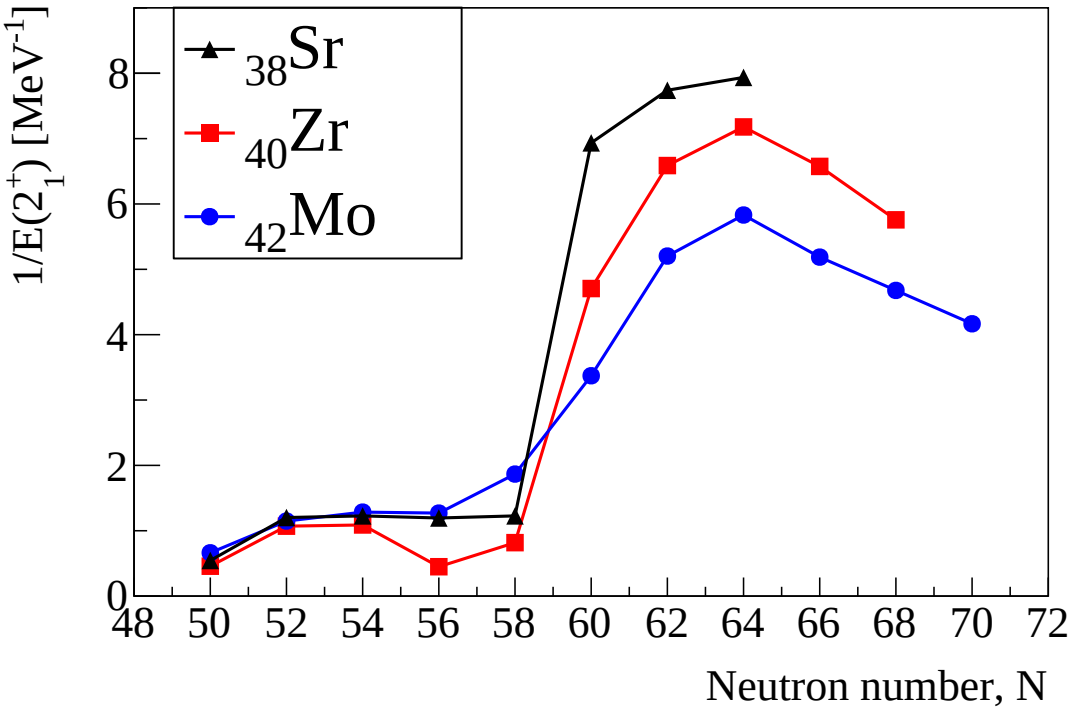

Figure 1.1: Reciprocal of the known 2_1^+ energies of Sr, Zr and Mo isotopes between $N = 50$ and $N = 70$ as a function of neutron number. Note the very high 2_1^+ energies of ^{90}Zr and ^{96}Zr and the very large decrease in the energy at $N = 60$. Data from Ref. [13].

The onset of deformation at $N = 60$ was first attributed to proton-neutron interactions between the $\pi g_{9/2}$ and $\nu g_{7/2}$ orbitals [14, 15], an effect which is even more pronounced in $N \geq 60$ nuclei due to the greater occupation of the deformation-driving high-j low-Ω $\nu h_{11/2}$ orbitals [16, 17, 18, 19]. The classification of the ground-state de-

formations was found to be prolate through laser spectroscopy measurements of ^{101}Zr [20].

The development of axially symmetric ground-state configurations of the $N \geq 60$ Zr isotopes is in contrast to its higher-Z neighbours, which favour triaxial shapes [21, 22, 23, 24], demonstrated for the Mo ($Z = 42$) isotopes in Fig. 1.1 by their larger 2_1^+ energies when compared to the Zr isotopic chain. Conversely, the lower-Z Sr isotopes exhibit a more severe transition to strongly deformed ground-state deformations [25], shown as lower 2_1^+ energies for the $N \geq 60$ isotopes in Fig. 1.1 as compared to the Zr isotopes. The axially symmetric nature of the deformation of the $N \geq 60$ isotopes provides an excellent reference case for a more universal understanding of the structure of nuclei located centrally with respect to the $50 < N < 82$, $28 < Z < 50$ shells.

1.2 Research objectives

The primary research objective of this work is to extend the knowledge of the deformations of the neutron-rich Zr isotopes, whilst being vigilant to identify any *new* isomeric states which may result from shape stabilisation in excited states. These goals shall be achieved through measurements made using a high-efficiency high-purity germanium (HPGe) array augmented with novel scintillation detectors, deployed in a next-generation radioactive-isotope beam facility.

1.3 Research methods

Precision deformation values of the neutron-rich ^{104,106}Zr isotopes shall be derived from the measurement the lifetimes of their 2_1^+ states. This will account for the second measurement of the lifetime of the 2_1^+ state in ^{104}Zr [26] and the first for the same state in ^{106}Zr. In order to make these measurements an experiment was conducted at the Radioactive Isotope Beam Factory (RIBF), at the RIKEN Nishina Center (RNC), Wakō-shi, Japan, where the decay of stopped radioactive isotope (RI) beams were examined using a multi-faceted cutting-edge detector configuration.

This work presents the first application of β-delayed γ-ray fast-timing measurements of RI beams produced through the in-flight fission mechanism. The excellent timing properties of the cerium-doped lanthanum tri-bromide ($LaBr_3(Ce)$) detector array used

in this investigation, coupled with the uniquely-high intensities of RI beam production capable at the RIBF, enable this cutting-edge method to be used.

1.4 Chapter plan

The contents of this thesis are laid out as follows:

- **Chapter 2:** Overview of relevant nuclear phenomenology, followed by presentation of predictions of ground-state shapes and $2_1^+ \rightarrow 0_{g.s}^+$ transition probabilities from contemporary nuclear model calculations,
- **Chapter 3:** Description of the experimental apparatus used in the investigation,
- **Chapter 4:** Detailed explanation of the analysis of data and extraction of results,
- **Chapter 5:** Presentation of the results, including the lifetimes of the 2_1^+ states of ^{104,106}Zr, and presentation of the decay of newly observed isomeric states,
- **Chapter 6:** The interpretation of results, focussing on the deduction of the transition probabilities from the 2_1^+ state to the ground-state and deformations of ^{104,106}Zr, discussed within the context of the model predictions presented in Chap. 2. As well as a brief discussion of the newly observed isomeric states,
- **Chapter 7:** A summary of the work, citing the major research outcomes and the outlook of complementary work.

Chapter 2

Theoretical Background

There exist a plethora of nuclear models, each with its own advantages and disadvantages when attempting to explain the many facets of nuclear structure. For example, the shell model [2] provides an intuitive and robust explanation of how nuclear structure evolves close to the *magic numbers* [1] of protons and neutrons, where single-particle effects are dominant. However, its elegance soon vanishes towards the mid-shell regions, where the coherence of many particles' wavefunctions gives rise to *collectivity*. Explored in this chapter are the models whose results pertain to the deformation and collective structure of the neutron-rich Zr region. Discussed shall be the shape-predicting finite-range droplet model (FRDM) [27] and results from a recent Hartree-Fock-Bogolyubov (HFB) [28] calculation [29], which predicts an abrupt shape change between ^{104}Zr and ^{106}Zr. The dependence of the projected shell model (PSM) [30] on deformation shall be discussed, as well as the importance of the various parameters of the interacting boson model (IBM) [31] Hamiltonian with respect to the generation of nuclear collectivity.

2.1 Basic nuclear properties

Since the models which will be discussed later in this chapter are derived from both the microscopic and macroscopic properties of the nucleus, it is first instructive to define some of the basic concepts which have, in most cases, formed the foundation of the modern understanding of nuclear structure. We discuss here two of the key aspects of nuclear structure which underpin our current understanding: the bulk properties of

the nuclear fluid and the shell structure of protons and neutrons.

2.2 Liquid drop model

Amongst the first successful nuclear models was that of the *liquid drop*, introduced in 1935 by Weizsäcker [32], which described the nucleus as a droplet of Fermi fluid. The shell model is to the single-particle understanding of the nucleus, as the liquid drop model (LDM) is to its macroscopic understanding.

Perhaps the most elucidative aspect of the LDM, and the one in which the Fermi liquid approximation has the largest impact, is its capability to describe the so-called *mass defect*, where the mass of a group of bound nucleons is less than that of the group's individual constituents. The mass defect is usually called the *binding energy* and given by the Bethe-Weizsäcker formula, which can be written [33],

$$B.E.(A,Z) \;=\; a_{\mathrm{v}}A - a_{\mathrm{s}}A^{2/3} - a_{\mathrm{C}}Z(Z-1)A^{-1/3} - a_{\mathrm{A}}(A-2Z)^2A^{-1} + \delta_{\mathrm{p}}, \qquad (2.1)$$

where

$a_{\mathrm{v}}A$ is the volume term, which describes the gain in binding energy from each bound nucleon,

$a_{\mathrm{s}}A^{2/3}$ is the surface term, it reduces the binding energy since the nuclear force is unsaturated on the nuclear surface,

$a_{\mathrm{C}}Z(Z-1)A^{-1/3}$ is the Coulomb term, which also reduces the binding energy due to the Coulomb repulsion of the protons,

$a_{\mathrm{A}}(A-2Z)^2A^{-1}$ is the asymmetry term, in which the unequal shell filling of the neutrons and protons leads to a decrease in binding energy,

δ_{p} represents the increase of binding energy for a "fully paired" nucleus (even-even), relative to a system with an unpaired proton, or neutron (even-odd, or odd-even),

and a decrease in binding for an unpaired neutron and proton (odd-odd). It takes on many values, one set of which is [34],

$$\delta_{\mathrm{p}} = \begin{cases} +a_{\mathrm{p}}A^{-1/2} & \text{if even-even,} \\ 0 & \text{if even-odd, or odd-even,} \\ -a_{\mathrm{p}}A^{-1/2} & \text{if odd-odd.} \end{cases} \tag{2.2}$$

Equation 2.1, is also known as the *semi-empirical mass formula*, since the parameters a_{v}, a_{s}, a_{C}, a_{A} and a_{p} are determined through a fit to known masses of nuclides. The nuclear mass excess is then given as,

$$M(Z,A) = ZM_H + (A-Z)M_n - [B.E.(Z,A) + ZM_e]\,, \tag{2.3}$$

where M_H is the mass of a hydrogen atom (the mass of the proton *and* an electron, M_e) and M_n is the mass of a neutron. Figure 2.1 shows the binding energy per nucleon, i.e. Eq. 2.1 divided by A, as a function of proton and neutron number for $1 \leq Z \leq 200$ and $1 \leq N \leq 200$, using the parameter values of Ref. [35]. It gives the first indication of the so-called *drip-lines*, which form the border of bound, $BE(Z,A) > 0$, and unbound, $BE(Z,A) \leq 0$, nuclear systems, with the most strongly bound systems in the medium-mass region with $N \approx Z$. The effect of the Coulomb term is obvious in the heavier mass regions, where a greater number of neutrons are required to increase the binding to overcome the Coulomb repulsion of the increased number of protons.

Whilst intuitive and capable of explaining some features of the nuclear landscape, the LDM lacks treatment of shell structure and is primitive in its characterisation of the strong nuclear force.

2.3 Shell structure

The nuclear shell model was the first model to reproduce the magic numbers of nuclei observed from experiment [1, 2]. In the shell model, the nucleons are treated as though they are particles trapped in a potential, V, and have motions independent of each other.

To describe the "particle in a box" problem, the Hamiltonian employed should

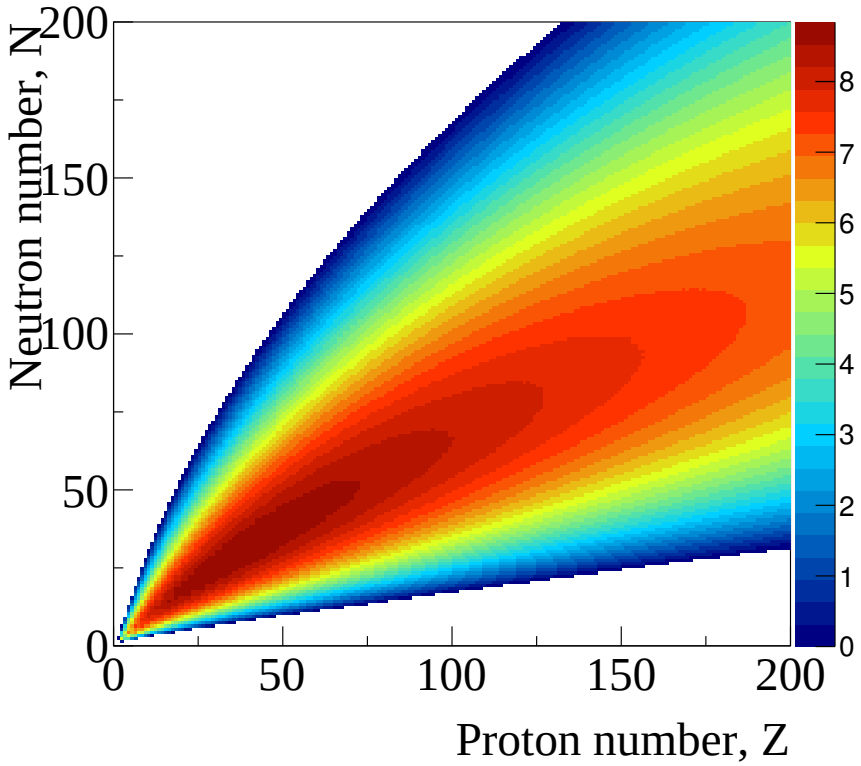

Figure 2.1: The binding energy (given by Eq. 2.1) per nucleon plotted as a function of proton and neutron number. The z axis is in MeV/A. See text for details.

contain the kinetic energy of the particle and the potential, V, within which it is trapped. In analogy to the classic kinetic energy, $p^2/2m$, the kinetic energy operator of quantum mechanics is,

$$\hat{T} = -\frac{\hbar^2}{2m}\nabla, \tag{2.4}$$

where m is the reduced mass of the particle, $\hbar$ is the reduced Planck's constant and ∇ is the vector differential operator. The one-particle Hamiltonian, which describes the total energy of a system, for an arbitrary potential is then given by,

$$H = -\frac{\hbar^2}{2m}\nabla + V(\vec{r}_i), \tag{2.5}$$

where $\vec{r}_i$ is the distance of the particle from the centre of the potential V. The potential, V, can take on a variety of shapes and the consequence of its functional form to the ordering of the energy level shall be discussed subsequently.

The operation of Eq. 2.5 on the wavefunction, ψ, of a particle gives the Schrödinger

Equation,

$$\left[-\frac{\hbar^2}{2m}\nabla^2 + V(\vec{r})\right]\psi(\vec{r}) \;=\; E_a\psi(\vec{r}), \tag{2.6}$$

where E_a is an allowed energy of the particle. The eigenvalues of Eq. 2.6 give the allowed energy levels of the nucleons in the potential $V(\vec{r})$, therefore, the shell structure shall be strongly dependent on its functional form. A potential which provides simple and illuminating solutions to Eq. 2.6 is the one-dimensional simple harmonic oscillator (SHO),

$$V(r) \;=\; \frac{1}{2}kr^2, \tag{2.7}$$

which gives eigenenergies of Eq. 2.6 as [36],

$$E_n \;=\; \hbar\omega_0\left(n + \frac{3}{2}\right), \tag{2.8}$$

where ω_0 is the angular frequency of the oscillation of the particle in the lowest energy state, and n is the principal quantum number. These energies are shown on the left side of Fig. 2.2 and are labelled according to n. The occupancy of each of the harmonic oscillator states in three-dimensions is related to the principal quantum number by $(n+1)(n+2)$ [36].

The simple shell structure of the SHO soon evolves into a more complex one when the potential is changed. The infinite square well potential is given by,

$$V(r) \;=\; \begin{cases} 0, & 0 < r < a, \\ \infty, & \text{otherwise}, \end{cases}, \tag{2.9}$$

where the "walls" of the potential are at 0 and a. The solution of Eq. 2.6 with the potential of Eq. 2.9 causes the degenerate energy levels of the SHO to split into the levels shown in the second column of Fig. 2.2. The splitting of these levels from their principal quantum states of the SHO comes as a result of the *angular momentum* quantum number, l, which takes on values of, 0, 1, 2, 3... given in spectroscopic notation by the letters s, p, d, f.... The numbers to the left of the these labels in Fig. 2.2 represent a counter of how many states have the same l value, for example, the $3s$ state is the third state to have $l = s$. If the potential described in Eq. 2.9 was given a finite value of V_0 at 0 and a, the effect would be to lower all of the energy states, as shown in the

third column of Fig. 2.2. The occupancy of states generated by the infinite and finite square wells are related to the angular momentum by $2(2l+1)$ [36].

A more realistic nuclear potential is given by the Woods-Saxon potential[37],

$$V(r) \;=\; \frac{-V_0}{1+\exp\left(\frac{r-R}{a}\right)}, \tag{2.10}$$

where R gives the mean radius of the nucleonic distribution and a its "skin depth". In this modification the mean radius reflects the fact that the surface of the nucleus is somewhat diffuse, and the skin depth accounts for the short, but finite, range of the strong nuclear force. The solution of Eq. 2.6 with the potential of Eq. 2.10 gives rise to the level structure of the fourth column of Fig. 2.2, note that, already, the magic numbers of 2, 8 and 20 are reproduced.

The observed magic numbers did not match the predicted magic numbers until 1949, when Mayer, Haxel and Jensen [1, 2] introduced a strong spin-orbit interaction term, $\vec{l}\cdot\vec{s}$, to the nuclear Hamiltonian, to account for the self-interaction of the intrinsic spin of an individual nucleon, $s=\pm 1/2$, with its angular momentum, l, as well as a weaker self-interaction of the orbital angular moment, $\vec{l}^2$. The modified Schrödinger equation is given by,

$$\left[-\frac{\hbar^2}{2m}\nabla^2 + V(r) + C\vec{l}\cdot\vec{s} + D\vec{l}^2\right]\psi(\vec{r}) \;=\; E_a\psi(\vec{r}), \tag{2.11}$$

where the potential $V(r)$ is that of Eq. 2.10 and C is the strength of the spin-orbit interaction and D is the strength of the angular momentum self-interaction. The last two columns of Fig. 2.2 show the numerically computed solutions to Eq. 2.11, note the reproduction of the observed magic numbers. Note the different shell structure of protons compared to neutrons for nucleon number >82, this is due to an extra, but weak, Coulomb term that can be included in Eq. 2.11 to account for the Coulomb interaction. The subscripts of the two right-most columns refer to the $j=l+s$ value of the orbital, in which the degeneracy is given by, $2j+1$ [36].

In this section, a brief and schematic outline of the origin of the magic numbers has been presented. In particular, we have seen the drastic effects that the functional form of the nuclear potential can have on the single-particle shell structure. This provides a conducive starting point for the discussion of the effects of deformed potentials.

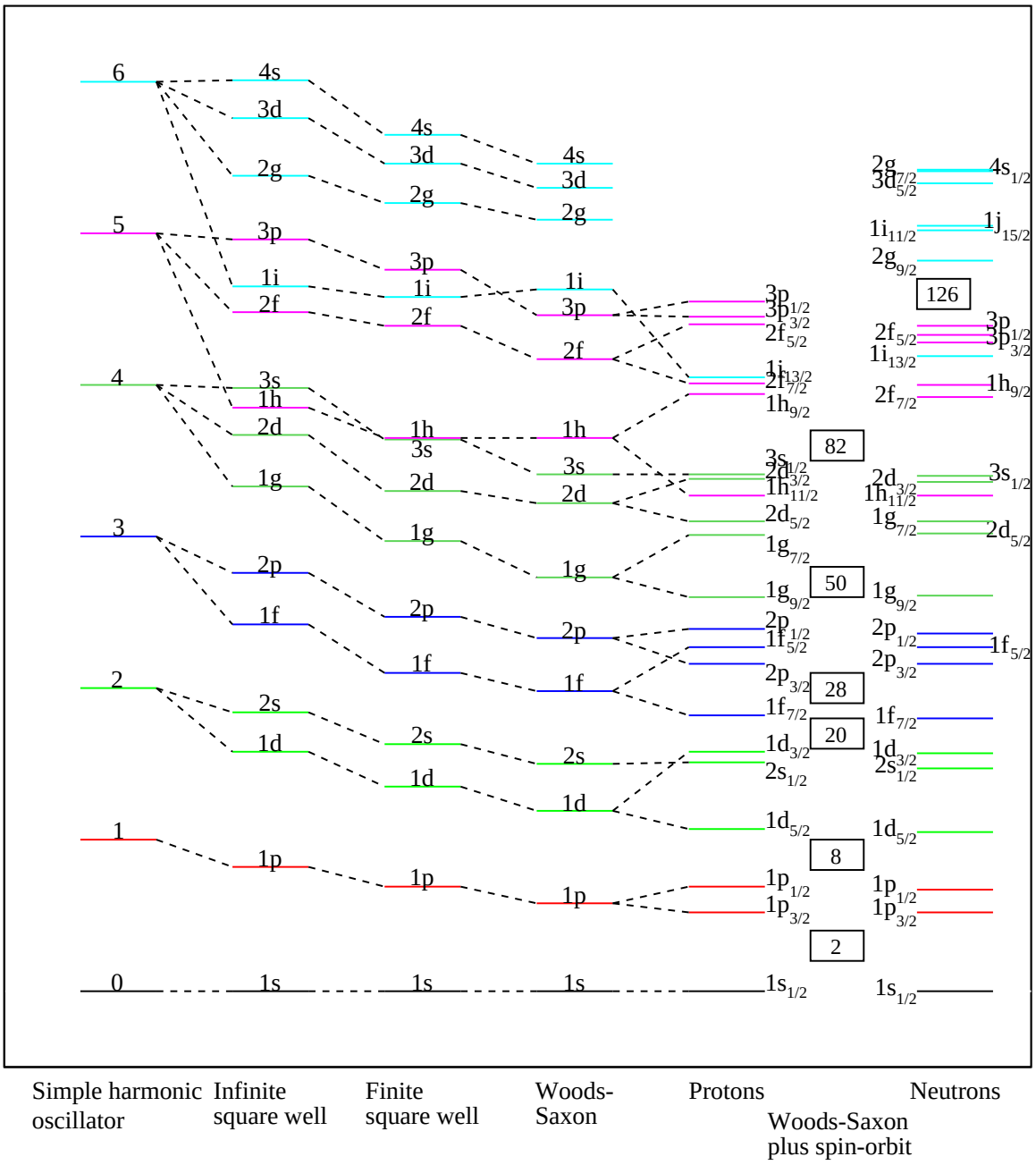

Figure 2.2: Schematic view of the effects that different potential wells, labelled along the bottom, have on shell structure. The levels are coloured according to their principal quantum level of the SHO. The boxed numbers between the fifth and sixth columns indicate the classic magic numbers for neutrons and protons. Figure adapted from Ref. [38].

2.4 Deformation

A common feature of mid-shell nuclei is the non-spherical distribution of nucleons and this has profound consequences for the single-particle and macroscopic properties of the nucleus. Only the wavefunction of the s orbital assume a spherical shape. The

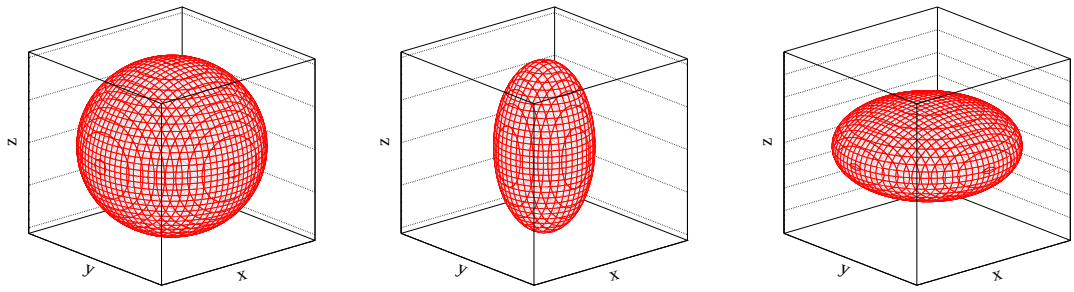

(a) $\beta_2 = 0$ (Spherical) (b) $\beta_2 > 0$ (Prolate) (c) $\beta_2 < 0$ (Oblate)

Figure 2.3: Comparison between common nuclear shapes.

other orbitals exhibit a preference to direction with respect to a symmetry axis. The partial filling of the orbital with asymmetric wavefunctions, which have a high density in the mid-shell, as shown in Fig. 2.2, drives the nucleonic distribution towards an axially symmetric shape. Depicted in Fig. 2.3, alongside a reference sphere, are the prolate and oblate shapes, which constitute the most common statically deformed shapes.

The stable deformations of Figs. 2.3b and 2.3c are defined in terms of their surface, assuming a quadrupoloid, as mapped by the radius parameter, R [39],

$$R(\theta, \phi) \;=\; R_0 \left(1 + \alpha_{00} Y_{00} + \alpha_{20} Y_{20}\right), \tag{2.12}$$

where $R_0 = 1.25 \cdot A^{1/3}$ fm, α_{00} is the amplitude of the spherical harmonic Y_{00} (a sphere) and Y_{20} is the spherical harmonic describing a quadrupole shape, with α_{20} being its amplitude, usually called β_2. In the absence of the spherical term in Eq. 2.12, α_{20} is usually denoted, β, which relates the difference of the semi-major, b, and semi-minor, a, axes of the nucleus, ΔR, by [40],

$$\beta \;=\; \frac{4}{3}\sqrt{\frac{\pi}{5}}\frac{b-a}{R_0}, \tag{2.13}$$

meaning a positive value of β would give a prolate shape and a negative value an oblate shape, as depicted in Figs. 2.3b and 2.3c, respectively.

A consequence of the deformed nucleonic distribution is the existence of a non-zero electric quadrupole moment, Q, in the ground-state configuration. The value of Q can be extracted from a uniformly charged ellipsoid described by the wavefunction ψ

through the operation [41],

$$Q = \int \psi^*(\vec{r}) \left(3z^2 - r^2\right) \psi(\vec{r}) \mathrm{d}\vec{r}, \tag{2.14}$$

where z is refers to the coordinate from the centre of along its symmetry axis, and the integral is over the nucleonic distribution. If ψ describes a uniformly charged nucleonic distribution, and we transfer to the cylindrical coordinates, the integration of Eq. 2.14 yields,

$$Q = \frac{2}{5} Z \left(b^2 - a^2\right), \tag{2.15}$$

where a and b are the semi-minor and -major axes, respectively. From Eq. 2.15 it can be seen that in the spherical case $Q = 0$, in the prolate $(b > a)$ $Q > 0$ and for oblate $(b < a)$ $Q < 0$.

2.4.1 Deformed shell structure

In this section, the origin of deformed shell structure shall be addressed. The single-particle Hamiltonians defined here provide the basis of the single-particle description for the PSM and HFB models discussed later. The labels of single-particle orbits in a deformed nucleus arise naturally from the discussion, and shall be used later on in the thesis when discussing the configurations of excited states of interest.

The Hamiltonian for an axially deformed harmonic oscillator was introduced by Nilsson as [42, 43],

$$H = -\frac{\hbar^2}{2m}\nabla + \frac{1}{2}m \left[\omega_x \left(x^2 + y^2\right) + \omega_z^2 z^2\right] + C\vec{l} \cdot s + D\vec{l}^2, \tag{2.16}$$

where the oscillator frequencies are the same in the x and y directions, $\omega_x = \omega_y$ and different along the symmetry axis, ω_z. It is possible to reformulate Eq. 2.16 such that it relates directly to the deformation of the nucleus. This is achieved through the introduction of the parameter, δ, which relates to the β_2 of Eq. 2.13 by,

$$\delta \approx \frac{3}{4}\sqrt{\frac{5}{\pi}}\beta_2. \tag{2.17}$$

The deformation parameter of Eq. 2.17 is obtained through the oscillation frequencies,

$$\omega_x = \omega_y = \omega_0(\delta)\sqrt{1+\frac{2}{3}\delta}, \tag{2.18}$$

$$\omega_z = \omega_0(\delta)\sqrt{1-\frac{4}{3}\delta}, \tag{2.19}$$

where ω_0 is the oscillator frequency of the corresponding spherical nucleus, where an assumption of volume conservation is made [44]. If the deformation were to become prolate, according to Eqs. 2.18 and 2.19, the oscillation frequencies in the $x-y$ plane would become larger, and that in the z-direction would decrease. This is reasonable considering that in this case the quanta traversing the z-direction would have to travel further. The situation is reversed when the oblate deformation is considered.

By expressing Eq. 2.16 in spherical coordinates, and using the definitions of ω_0 and δ, an alternate and equivalent Nilsson Hamiltonian is obtained [43],

$$H = -\frac{\hbar^2}{2m}\nabla + \frac{1}{2}m\omega_0^2\vec{r}^2 - m\omega_0^2\vec{r}^2\beta_2 Y_{20}(\theta,\phi) + C\vec{l}\cdot\vec{s} + D\vec{l}^2, \tag{2.20}$$

where the second term accounts for the harmonic oscillator potential, the third term, expressed here in terms of β_2 from Eq. 2.17.

This formulation reduces to the spherical Hamiltonian of Eq. 2.11 for $\beta_2 = 0$ and, for small deformations, the spherical quantum numbers remain valid, meaning that the deformation term is included as a perturbation to the usual solutions. However, in the limit of a large nuclear deformation the spin-orbit and orbit-orbit terms become negligible and Eq. 2.20 reduces to the Hamiltonian of an anisotropic harmonic oscillator. Moreover, in this limit, the spherical quantum numbers are no longer valid, and should be replaced with the cylindrical quantum numbers [44],

n_z, the number of oscillation quanta along the symmetry axis,

n_ρ, the number of oscillation quanta perpendicular to the symmetry axis,

m_l, the projection of the orbital angular momentum onto the symmetry axis.

Then the principal quantum number is given by,

$$N = n_z + 2n_\rho + m_l, \tag{2.21}$$

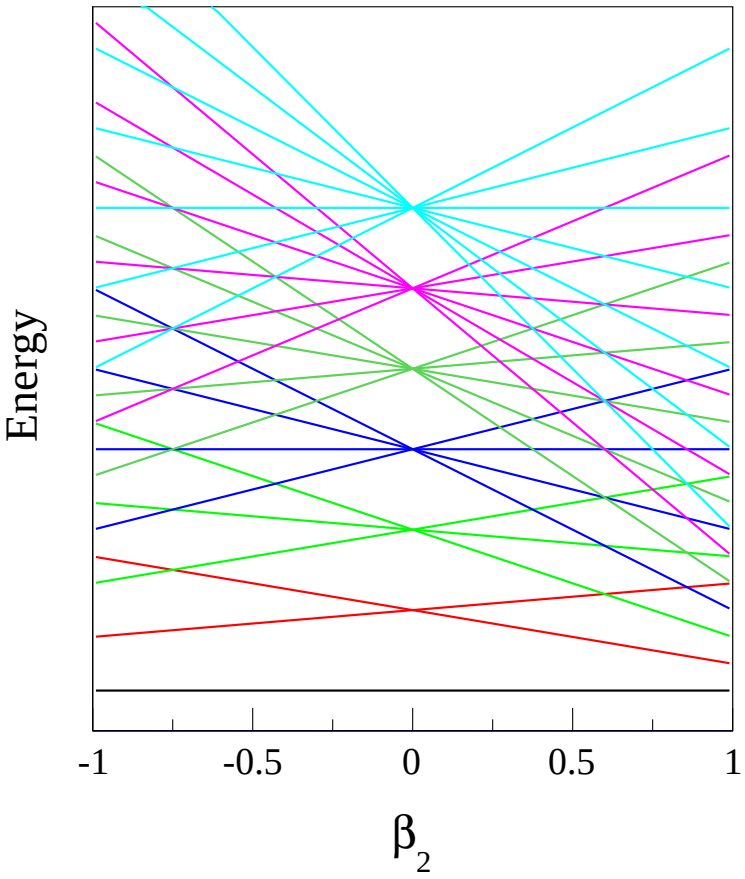

Figure 2.4: Diagram showing the evolution of shell structure for a SHO as a function of the deformed potential according to Eq. 2.22. The colours are coded to correspond with the SHO levels shown in Fig. 2.2.

where n_ρ is doubled due to the symmetry of the x-y plane. So, the eigenstates of Eq. 2.20 for a strongly deformed nucleus are given by,

$$E = \hbar\omega_0 \left[\left(N + \frac{3}{2} \right) + \frac{3}{4}\sqrt{\frac{5}{\pi}}\beta_2 \left(\frac{N}{3} - n_z \right) \right], \tag{2.22}$$

and since, according to Eq. 2.21, $0 \leq n_z \leq N$, there will be a breaking of degenerate states. The magnitude of separation shall be dependent on β_2, as shown in Fig. 2.4. In the same way that axial symmetry causes the *projection* of the orbital angular momentum onto the symmetry axis to become a good quantum number, so the projection of the spin-component, m_s, of the *total* angular momentum is also a good quantum number. Therefore, in the deformed basis the analogue of total angular momentum is

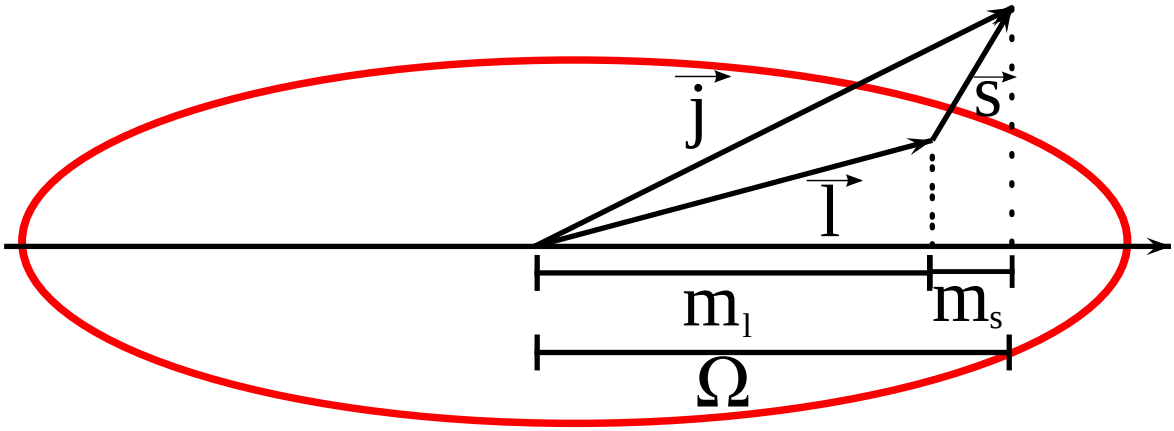

Figure 2.5: Diagram of an axially symmetric (prolate deformed) nucleus. The projection onto the symmetry axis of the $\vec{j} = \vec{l} + \vec{s}$ is Ω with the individual projections of the angular momentum, $\vec{l}$, and intrinsic nucleon spin, $\vec{s}$, given as m_l and m_s, respectively.

given by,

$$\Omega \;=\; m_l + m_s \;=\; m_l \pm \frac{1}{2}, \tag{2.23}$$

which is depicted on Fig. 2.5. It is conventional to refer to the orbits of deformed nuclei by their "Nilsson labels" [45],

$$\Omega^{\pi}\left[Nn_z m_l\right], \tag{2.24}$$

where π is the parity of the state given by $(-1)^N$. This classification shall be used later on in the thesis to define configurations of excited states of interest.

2.5 Signatures of deformation

This section outlines some of the patterns of low-lying energy levels associated with different types of collective behaviour. These shall be used to justify the treatment of some nuclei as rigidly deformed to deduce the magnitude of their ground-state deformations. Additionally, they shall be discussed as features that the global parameters of a Hamiltonian must be able to reproduce.

If nuclei are axially symmetric and exhibit rotational behaviour, the excitation energies are expected to follow a well defined relation,

$$E_{\mathrm{rot}}(J^+) \;=\; \frac{\hbar^2}{2I} J(J+1), \tag{2.25}$$

where I is the moment of inertia and only even J are allowed in the ground-state band

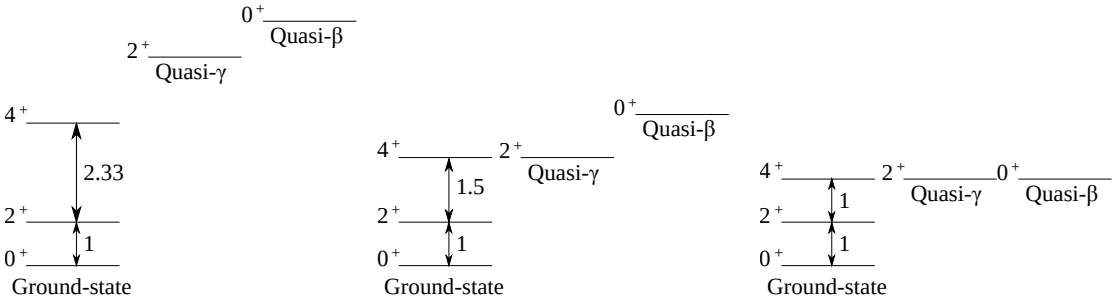

(a) Static β_2 deformed. (b) γ-soft. (c) Vibrational.

Figure 2.6: Comparison between the characteristic spectra of the major categories of nuclear collectivity. The energy gaps between 4_1^+ and 2_1^+ states are normalised to the $2_1^+ - 0^+$ energy gap.

J^π	$E\ [\hbar^2/(2I)]$
2^+	6
4^+	20
6^+	42

Table 2.1: The spin-parities of the first 3 levels of a rotational nucleus and their corresponding energies according to Eq. 2.25. The energies are expressed in units of $\hbar^2/(2I)$.

[43], giving rise to the rotational ground-state band, with $J^\pi = 2^+, 4^+, 6^+ \ldots$. The moment of inertia is expected to remain constant within the low-spin regime. The resultant energies of the $J^\pi = 2^+, 4^+, 6^+ \ldots$ states, in units of $\hbar/(2I)$, are given in Tab. 2.1 and the ratios of the energy levels alone should then provide evidence of a deformed ground-state. It is conventional to use the ratio, $R_{4/2} = E(4^+)/E(2^+)$, since this relates to the two lowest, and often only known, energy levels of the ground-state rotational band. From Tab. 2.1, $R_{4/2} \approx 3.33$ corresponds to a well deformed rigid rotor, whereas $R_{4/2} \approx 2.5$ signifies a nucleus which is soft to β and γ vibrations. Nuclei whose excitations are predominantly single-particle have $R_{4/2} \lesssim 1.5$ [46]. At higher spins the lack of rigidity of the nucleus is manifest in the centrifugal stretching of the nucleonic distribution, which changes I [47].

In addition to the rotational ground-state band, the band-heads of vibrational bands, of both β and γ types, also act as signs of deformation. For nuclei whose ground-state have a stable deformed configuration, the band-heads of the β and γ bands will be high with respect to the 4_1^+ state, as shown in Fig 2.6a. If the ground-state is soft towards the γ degree of freedom, then only the γ-band shall be lowered and in the limit of a purely triaxial nucleus the 2^+ band-head is at the same energy as the

4_1^+ level, as shown in Fig. 2.6b. For nuclei which exhibit vibrational structure about a spherical basis, both the γ and β band-heads are reduced, again, in the limit that the ground-state is spherical and the excitation is purely vibrational they are equal in excitation energy to the 4_1^+ level of the ground-state band [43].

2.6 Models

In the previous sections of this chapter, the discussion focussed on a few fundamental concepts of nuclear structure. In particular, the nucleus' behaviour as a drop of Fermi liquid and its inherent shell structure. Contemporary nuclear models have developed and synergised these approaches to provide accurate predictions and elegant explanations of nuclear phenomena.

The *macroscopic-microscopic* approach is an example of a methodology which considers both bulk and shell properties of the nucleus. One such approach is the finite-range droplet model (FRDM) which extends Eq. 2.1 to include effects induced by a deformed nucleonic distribution, a finite-range nuclear force and shell effects. Another approach is that of the variation of the nuclear mean-field which subsequently affects the generated wavefunctions. The aim of the variation is to generate wavefunctions which will themselves generate the input potential, this form of self-consistent theory is known as the Hartree-Fock-Bogolyubov (HFB) method. Both the FRDM and HFB methods provide theoretical predictions for ground-state deformations. An observable related to the magnitude of the ground-state deformation is the transition probability between the 2_1^+ and $0_{\text{g.s.}}^+$ states of even-even nuclei. The values used in this work are provided by the projected shell model (PSM) and the interacting boson model (IBM). The former uses as an input the deformations from either experiment, or predicted from theories such as the FRDM. The IBM uses algebraic generator techniques deduced from a Hamiltonian which has a global set of parameters fitted to a range of nuclei.

Discussed here are the principles and key results of the models which shall be used later as comparison to the experimental results presented in this thesis.

A note on deformation parameters

So far, we have defined the deformation parameters, β_2 in Eq. 2.13 and δ in Eq. 2.17. However, some nuclear models use the Nilsson deformation parameters denoted by $\epsilon_{2,4}$. To relate the two, further deformation parameters are introduced, $\lambda_{2,4}$, which are the coefficients of the Legendre Polynomials, $P_{2,4}(\cos\theta)$, which generate the angular dependent aspects of the nuclear surface, or potential [48]. These are related to the Nilsson parameters by [49],

$$\lambda_2 = \frac{-\frac{4}{3}\epsilon_2 + \frac{2}{9}\epsilon_2^2 - \frac{4}{3}\epsilon_2\epsilon_4}{1 + \frac{2}{9}\epsilon^2}, \tag{2.26}$$

$$\lambda_4 = \frac{2\epsilon_4 - 0.606\epsilon_2\epsilon_4}{1 + \frac{2}{9}\epsilon^2}, \tag{2.27}$$

which in turn give,

$$\beta_2 = \frac{-0.5\lambda_2 + 0.106\lambda_2^2 + 0.214\lambda_2\lambda_4 + 0.055\lambda_4^2 - 0.134\lambda_2^3}{(1 + 0.075\lambda_2^2 + 0.0416\lambda_4^2 - 0.018\lambda_2^3)\sqrt{5/4\pi}}. \tag{2.28}$$

The difference between ϵ_2 and the value of β_2 calculated by Eq. 2.28 vary from between 3-8% and represent the same mode of deformation. In the following discussion, for the sake of simplicity, we refer to the parameters as used by the models.

2.7 Finite-range droplet model

The FRDM builds on the success of the liquid drop model (LDM), described in Sec. 2.2, by extending and refining Eq. 2.1 through the use of a realistic nuclear potential and including the effects of deformation on the pairing energy terms. A Yukawa-plus-exponential potential is used to describe the nuclear force, which is folded over a general shape, as opposed to a sphere. The Coulomb force is considered in terms of an average charge distribution of general shape. Additionally, the separability of the proton and neutron distributions is introduced, as well as the compressibility of the nuclear liquid [27]. This constitutes the macroscopic part of the binding energy to which shell corrections are added to give the total potential energy:

$$E_B = E_{\text{macro}} + E_{\text{micro}}. \tag{2.29}$$

Here the E_{macro} term of Eq. 2.29 is reproduced as it is given in Ref. [27],

$$
\begin{aligned}
& E_{macro}(Z,N,\text{shape}) \; = \\
& M_H Z + M_n N && \bullet \text{ mass excess of } Z \text{ hydrogen atoms and } N \text{ neutrons} \\
& + \left(-a_1 + J\bar{\delta}^2 - \frac{1}{2}K\bar{\epsilon}^2\right) A && \bullet \text{ volume energy} \\
& + \left(a_2 B_1 + \frac{9}{4}\frac{J^2}{Q}\bar{\delta}^2 \frac{B_s^2}{B_1}\right) A^{2/3} && \bullet \text{ surface energy} \\
& + a_3 A^{1/3} B_k && \bullet \text{ curvature energy} \\
& + a_0 A^0 && \bullet \text{ Finite range force and diffuseness correction} \\
& + c_1 \frac{Z^2}{A^{1/3}} B_3 && \bullet \text{ Coulomb energy} \\
& - c_2 Z^2 A^{1/3} B_r && \bullet \text{ redistribution energy} \\
& - c_4 \frac{Z^2}{A^{1/3}} && \bullet \text{ Coulomb exchange correction} \\
& - c_5 Z^2 \frac{B_w B_s}{B_1} && \bullet \text{ surface redistribution energy} \\
& + f_0 \frac{Z^2}{A} && \bullet \text{ proton form factor correction to the Coulomb energy} \\
& - c_a (N-Z) && \bullet \text{ charge-asymmetry energy} \\
& + W \left(|I| + \begin{cases} 1/A, & Z \text{ and } N \text{ odd and equal} \\ 0, & \text{otherwise} \end{cases} \right) && \bullet \text{ Wigner energy} \\
& + \begin{cases} \bar{\Delta}_p + \bar{\Delta}_n - \delta_{np}, & Z \text{ and } N \text{ odd} \\ \bar{\Delta}_p, & Z \text{ odd and } N \text{ even} \\ \bar{\Delta}_n, & Z \text{ even and } N \text{ odd} \\ 0, & Z \text{ and } N \text{ even} \end{cases} && \bullet \text{ average pairing energy} \\
& - a_{\text{el}} Z^{2.39} && \bullet \text{ energy of bound electrons} \quad (2.30)
\end{aligned}
$$

where, a_1, $a_2 B_1$, J are the same as a_{v}, a_{s} and a_{A} of Eq. 2.1, respectively, and the terms in red are those which are dependent on shape.

Due to their particular sensitivity to the nuclear shape, the volume, surface and Coulomb terms of Eq. 2.30 shall be discussed here, after defining the newly introduced

factors:

- $\bar{\delta}$, the average asymmetry of the proton and neutron densities. This factor allows for the spatial separation of neutron and proton distributions, enabling neutron-skin formation,

- $\bar{\epsilon}$, average compressibility term, which dictates the compression of the nuclear liquid as a result of surface tension,

- K, nuclear compressibility constant,

- Q, surface stiffness constant.

The B_X terms of Eq. 2.30 represent shape-dependent integrals, of which $\bar{\delta}$ and $\bar{\epsilon}$ depend on B_V, B_S, B_1, and B_1, B_3, respectively. The most important and elucidative of these within the context of deformed nucleonic distributions are B_1, B_S and B_3, where:

- B_1 gives the energy from the range-limited, to $a = 0.68$ fm, Yukawa-plus-exponential potential over a generalised nuclear surface,

$$B_1 = \frac{A^{-2/3}}{8\pi^2 r_0^2 a^4} \int\int_V \left(2 - \frac{|\vec{r} - \vec{r}'|}{a}\right) \times \frac{e^{-|\vec{r}-\vec{r}'|/a}}{|\vec{r} - \vec{r}'|/a} \mathrm{d}^3 r \mathrm{d}r', \tag{2.31}$$

- B_S is the surface energy that is defined in the liquid drop model,

$$B_S = \frac{A^{-2/3}}{4\pi r_0^2} \int_S \mathrm{d}S, \tag{2.32}$$

- B_3 gives the Coulomb energy for a generalised shape, with a diffuseness defined by the range, $a_{\mathrm{den}} = 0.70$ fm,

$$B_3 = \frac{15A^{-5/3}}{32\pi^2 r_0^5} \int\int_V \frac{\mathrm{d}^3 r \mathrm{d}^3 r'}{|\vec{r} - \vec{r}'|} \times \left[1 - \left(1 + \frac{1}{2}\frac{|\vec{r} - \vec{r}'|}{a_{\mathrm{den}}}\right) e^{-|\vec{r}-\vec{r}'|/a_{\mathrm{den}}}\right]. \tag{2.33}$$

The volume term of Eq. 2.30 allows for the compression of the nuclear volume with the $K\bar{\epsilon}^2$ term, which shall decrease with A due to its origin from the surface tension. Another key feature of the volume term is the inclusion of a *bulk surface* asymmetry term, $J\bar{\delta}^2$, which allows differing proton and neutron densities, only at the surface. In the surface energy term, the surface energy constant, a_2, is scaled by the value of

the B_1 integral to account for a generalised nuclear shape. The effects of the differing surface densities of the proton and neutron surfaces are also included here, with their spherical surface energies, given by B_S, normalised to the value of B_1 to account for their distributions taking on a general shape. The Coulomb term takes on a similar form as in Eq. 2.1, but here a homogeneous charge distribution is calculated for a generalised shape, through the B_3 integral.

The microscopic part of Eq. 2.29 takes into account the shell and pairing effects. The single-particle model utilises a potential comprising the sum of the shape-dependent Yukawa and Coulomb potentials, as well as the spin-orbit potential. The average energy of the calculated single-particle states are corrected with Strutinsky's shell-correction method (SCM) [50], which subtracts the average energy of the single-particle states from their total. The pairing calculations are performed using the Lipkin-Nogami (LN) approach to the Bardeen-Cooper-Schrieffer (BCS) method [51, 52], which takes into consideration variations of particle-numbers at the Fermi surface. Corrections to the pairing calculations are performed in a similar fashion to the SCM, i.e the average of the pairing correction energies is subtracted from the sum of the pairing energies. These computations give the binding energy contributions from shell and pairing effects.

The FRDM computes the deformation of nuclei by minimising the energy of Eq. 2.30 with respect to the quadrupole and hexadecapole deformations achieved through a grid search of the deformation defining parameters, ϵ_2 and ϵ_4, where the ϵ_4 parameters are typically very small. After the values of ϵ_2 and ϵ_4 which give the lowest total energy are found, a minimisation is also computed with respect to the ϵ_6 parameter. The results of these procedures are displayed in Fig. 2.7 where it is evident that the model reproduces well the expected spherical distributions along the magic numbers and highlights the deformed regions between them. It also highlights the suddenness of the onset of the deformation for the neutron-rich nuclei with $Z \approx 40$. The inset of Fig. 2.7 shows the deformations predicted for the Zr isotopic chain, which shall be compared to the experimentally determined values in Chap. 6.

For completeness, the binding energy per nucleon predicted by the FRDM is also presented here. These include the shell corrections, which don't influence the shape predictions, but will increase, or decrease the total mass. Figure 2.8 shows the binding energy per nucleon as a function of proton and neutron number as predicted by the

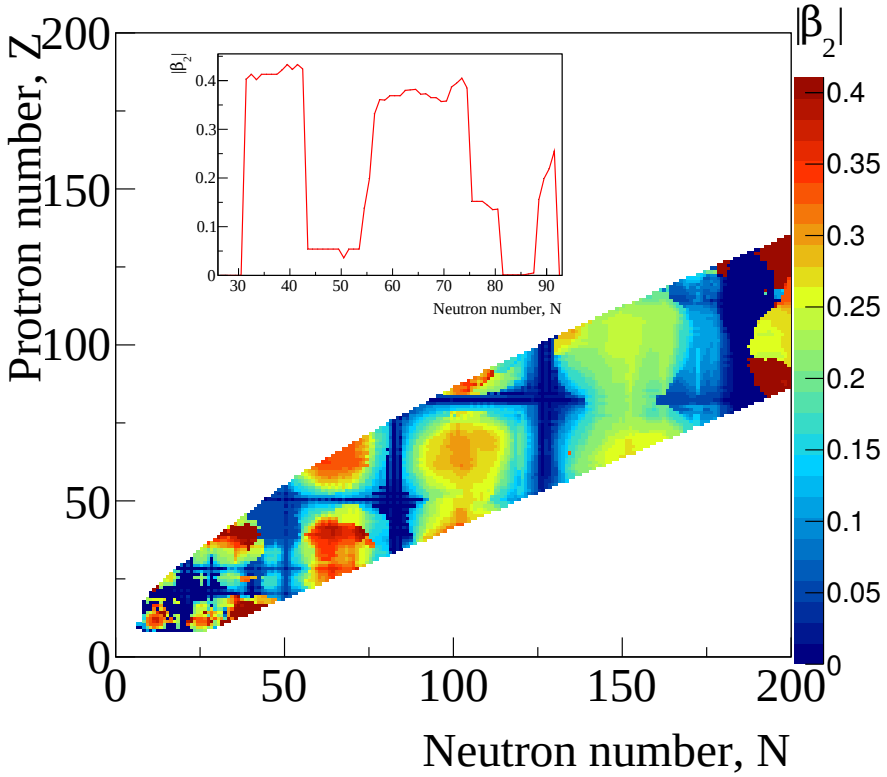

Figure 2.7: Predicted values of $|\beta_2|$ as a function of neutron and proton number. Notice the small deviations from sphericity close to the magic numbers, and the region of large deformation in the $28 < Z < 50$ and $50 < N < 82$ region. The inset shows the predicted deformations of the Zr isotopic chain. Data taken from Ref. [27]

FRDM.

2.8 Hartree-Fock-Bogoliubov shape calculations

The HFB method is an approach whereby a set of wavefunctions are derived from an estimated potential and the potential generated from these wavefunctions is then checked against the estimated potential. If the potentials match, the solution is reached, if not, the estimated potential is adjusted. The first step of this method is to construct a Hamiltonian which reflects the mean-field generated by the contribution of nucleons acting individually [41],

$$H_{\mathrm{HFB}} = \sum_{i=1}^{A} h(i), \tag{2.34}$$

where, $h(i)$ is the Hamiltonian from a nucleon, i. A given nucleon will then interact with this potential in a 1-body manner. The solution to this Hamiltonian will then give

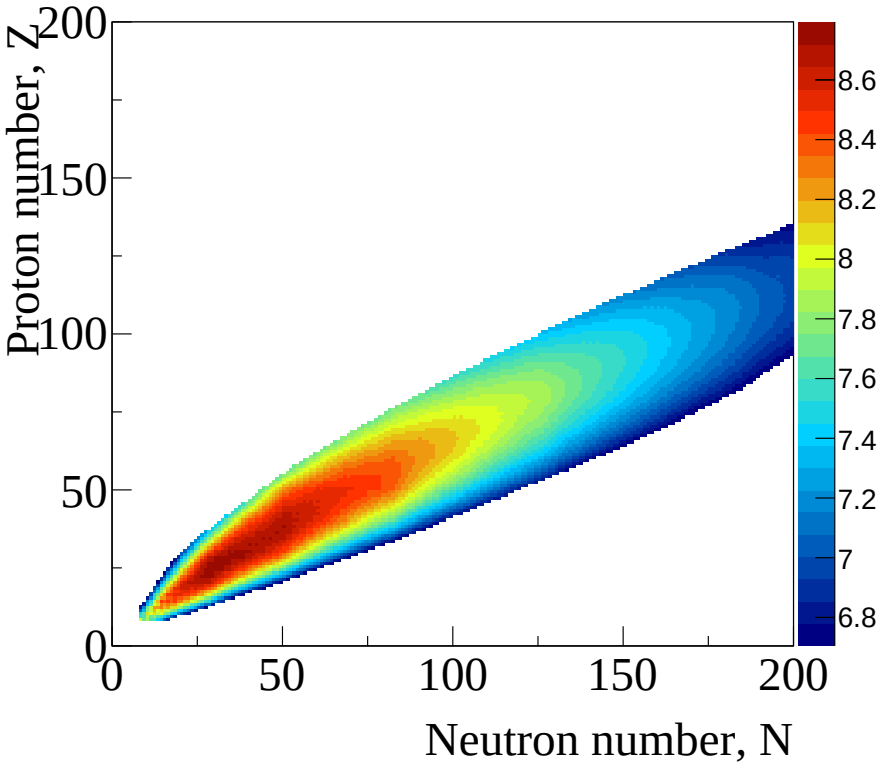

Figure 2.8: Predicted values of the binding energy per nucleon as a function of neutron and proton number. Notice how the drip lines are much more limiting than in Fig. 2.1, and the abruptness of the boundary between bound and unbound nuclei (the z scale has been expanded to accentuate the mass differences). Data taken from Ref. [27]

rise to a set of HFB wavefunctions, Ψ_{HFB}. Within the context of this work, ground-state configurations are of interest, for which the HFB method is particularly pertinent since it can be shown that the energy expectation value computed for any set of HFB wavefunctions will be less than, or equal to the *exact* intrinsic ground-state energy of the system [53],

$$\frac{\langle\Psi|\hat{H}|\Psi\rangle}{\langle\Psi|\Psi\rangle} \geq E_{\mathrm{g.s.}}. \tag{2.35}$$

Therefore, for any selection of wavefunction, one should always choose the one which provides the lowest energy expectation value.

Once the HFB wavefunctions successfully generate the input potential, the quadrupole moment can be extracted by using the quadrupole operator on the final wavefunction,

$$Q_{20} = \frac{1}{2}\langle\Phi_{HFB}|\,2z^2 - x^2 - y^2\,|\Phi_{HFB}\rangle\,, \tag{2.36}$$

as in Eq. 2.14.

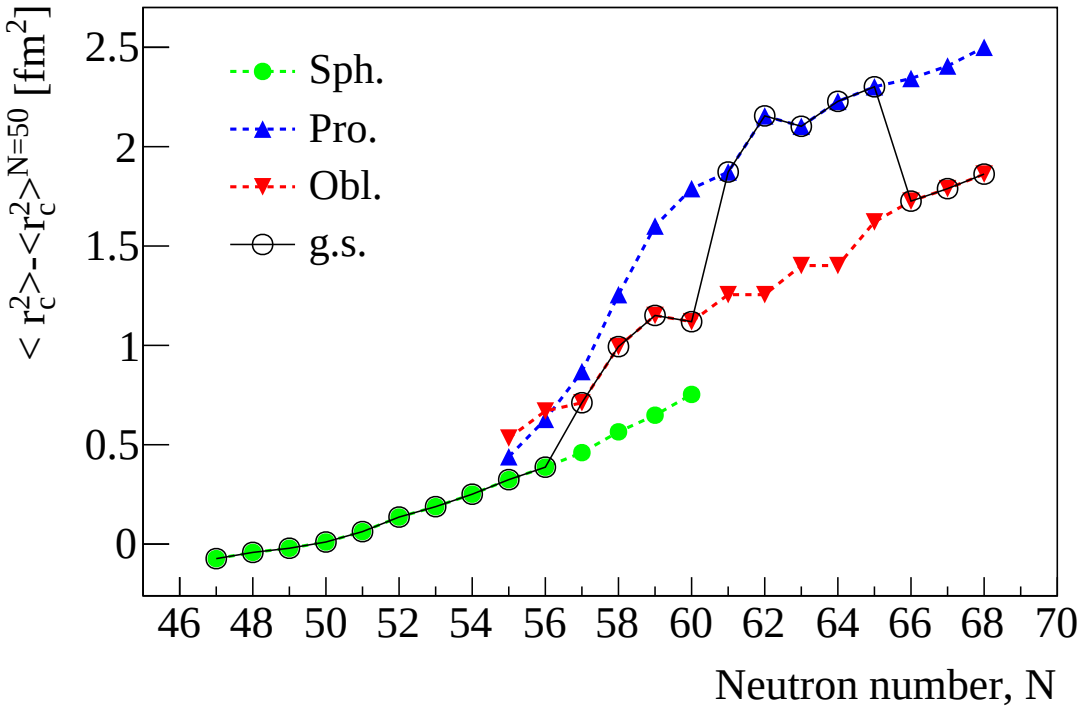

Figure 2.9: Calculated mean-square charge radii of Zr isotopes with $47 \leq N \leq 68$ with respect to that of ^{90}Zr. The enclosed symbols represent those solutions which are predicted to be the ground-state. Figure adapted from Ref. [29].

It is then possible to observe, as a function of deformation, the overall energy of the system given in Eq. 2.35, and therefore observe at which shape the minimum lies. The mean-square charge radii of Ref. [29], whose calculations employ the Gogny interaction [54], with a D1S parametrisation [55], for the Zr isotopes are presented in Fig. 2.9. The mean square charge radii of the energy minima of spherical, prolate and oblate shapes are given, and the ground-state shape of each nucleus indicated. An intriguing feature of the calculations of Ref. [29] is the small energy difference between the prolate and oblate shapes for the Zr nuclei with an energy difference of ~ 0.5 MeV. This small energy gap indicates that the HFB's prediction is that of a linear superposition of these states, and that the predicted ground-state shape is very sensitive to the details of the calculations. Therefore, it will be of great interest to determine whether the predicted prolate-oblate transition between ^{104}Zr and ^{106}Zr, shown in Fig. 2.9, occurs.

2.9 Projected shell model

For nuclei far from the shell closures shown in the far-right of Fig. 2.2, the configuration space required for shell model calculations to describe even the most simple ground- and excited-states become vast, and the physical interpretation is lost in the minutiae of the results. It is then convenient to use a model which truncates the active number of valence nucleons effectively and reflects the underlying physics of the situation. To this end the PSM was developed [56, 57], as a natural extension to the axial symmetry group, SU(3), truncation scheme developed by Elliott *et al.* [58], to represent the shell structure of the nucleus in a deformed basis. The characterisation of the deformed mean-field of the nucleus in question is an essential input to this model since, it not only provides the projections basis, but also fixes the strength of the quadrupole-quadrupole interaction in a self-consistent manner [59].

The Hamiltonian employed by the PSM is that of the harmonic oscillator, Eq. 2.16, with the addition of residual interactions to account for pairing and quadrupole forces,

$$\hat{H} = \hat{H}_0 - \frac{\chi}{2}\sum_{\mu}\hat{Q}^{\dagger}_{\mu}\hat{Q}_{\mu} - G_M\hat{P}^{\dagger}\hat{P} - G_Q\sum_{\mu}\hat{P}^{\dagger}_{\mu}\hat{P}_{\mu}, \tag{2.37}$$

where the operators are defined as,

$$\hat{Q}_{\mu} = \sum_{\alpha\beta} c^{\dagger}_{\beta} Q_{\mu\alpha\beta} c_{\beta}, \qquad \text{Quadrupole operator} \tag{2.38}$$

$$\hat{P}^{\dagger} = \frac{1}{2}\sum_{\alpha} c^{\dagger}_{\alpha} c^{\dagger}_{\bar{\alpha}}, \qquad \text{Pairing operator} \tag{2.39}$$

$$\hat{P}^{\dagger}_{\mu} = \frac{1}{2}\sum_{\alpha\beta} c^{\dagger}_{\alpha} Q_{\mu\alpha\beta} c^{\dagger}_{\bar{\beta}}, \qquad \text{Monopole-quadrupole operator} \tag{2.40}$$

and χ, G_M and G_Q are their respective strengths, and $Q_{\mu\alpha\alpha}$ is the quadrupole generator of the SU(3) group and given by,

$$Q_{\mu\alpha\alpha'} = \sqrt{\frac{4\pi}{5}}\delta_{NN'}\left\langle Njm \left| \left(\frac{r}{b}\right)^2 Y_{2\mu} \right| N'j'm' \right\rangle, \tag{2.41}$$

where the subscripts α and β, denote a set of spherical harmonic oscillator numbers, N, j, m, and their time-reversed counterparts denoted with $\bar{\alpha}$ and $\bar{\beta}$.

The single-particle HFB Hamiltonian of Eq. 2.37 is required to evaluate the quadrupole

moment contributions of each nucleon,

$$\hat{H}_{\mathrm{HFB}} = \hat{H}_0 - \chi \sum_{\mu} \left\langle \hat{Q}_\mu \right\rangle \hat{Q}_\mu - G_M \left\langle \hat{P} \right\rangle \left(\hat{P} + \hat{P}^\dagger \right) - G_Q \sum_{\mu} \left\langle \hat{P}_\mu \right\rangle \left(\hat{P}_\mu + \hat{P}_\mu^\dagger \right), \quad (2.42)$$

where the terms enclosed in $\langle \dots \rangle$ are the expectation values measured with respect to the HFB ground-state [30]. The first two terms of Eq. 2.42 can be equated to the *stretched* Nilsson potential [59],

$$H^\tau_{\mathrm{N}ilsson} = H^\tau_0 - \frac{2}{3} \epsilon_\tau \hbar\omega_\tau \hat{Q}_0, \quad (2.43)$$

where τ denotes either proton, or neutron, and, H^τ_0 is the same as in Eq. 2.37. The neutron and proton oscillator frequencies are given as,

$$\omega_\tau = \omega_0 \left(1 \pm \frac{N-Z}{A} \right)^{\frac{1}{3}}, \quad (2.44)$$

in which the sign is positive for a neutron, and negative for a proton. By diagonalising Eq. 2.43 onto the defined deformed basis and applying the BCS method [60], the single-particle structure of the basis state is found. The sum of the expectation values of the quadrupole moments of the valence neutrons and protons, $\left\langle \hat{Q}_0 \right\rangle_{n,p}$, in the Nilsson orbits is then calculated. To ensure that the $\left\langle \hat{Q}_0 \right\rangle_{n,p}$ values generate the specified deformed mean-field, a HFB minimisation condition [61] is imposed in the form of,

$$\chi_{\tau\tau'} = \frac{\frac{2}{3}\epsilon \hbar\omega_\tau \hbar\omega_{\tau'}}{\hbar\omega_n \left\langle \hat{Q}_0 \right\rangle_n + \hbar\omega_p \left\langle \hat{Q}_0 \right\rangle_p} \quad (2.45)$$

where, since the relation is isoscalar, the subscript τ denotes either proton, or neutron. This value of χ is then fixed in Eq. 2.37.

Within the context of this work, the most important variable which the PSM is to predict is the ground-state transition probability from the 2^+_1 state, $B(E2; 2^+_1 \to 0^+_{g.s.})$. The transition probability is related to the quadrupole operator by [62],

$$B(E2; I_i \to I_f) = \frac{e^2}{2I_i + 1} \left| \left\langle \psi_{I_f} \left\| \hat{Q}_L \right\| \psi_{I_i} \right\rangle \right|^2, \quad (2.46)$$

in much the same way as it is defined in the usual shell model. The reduced matrix

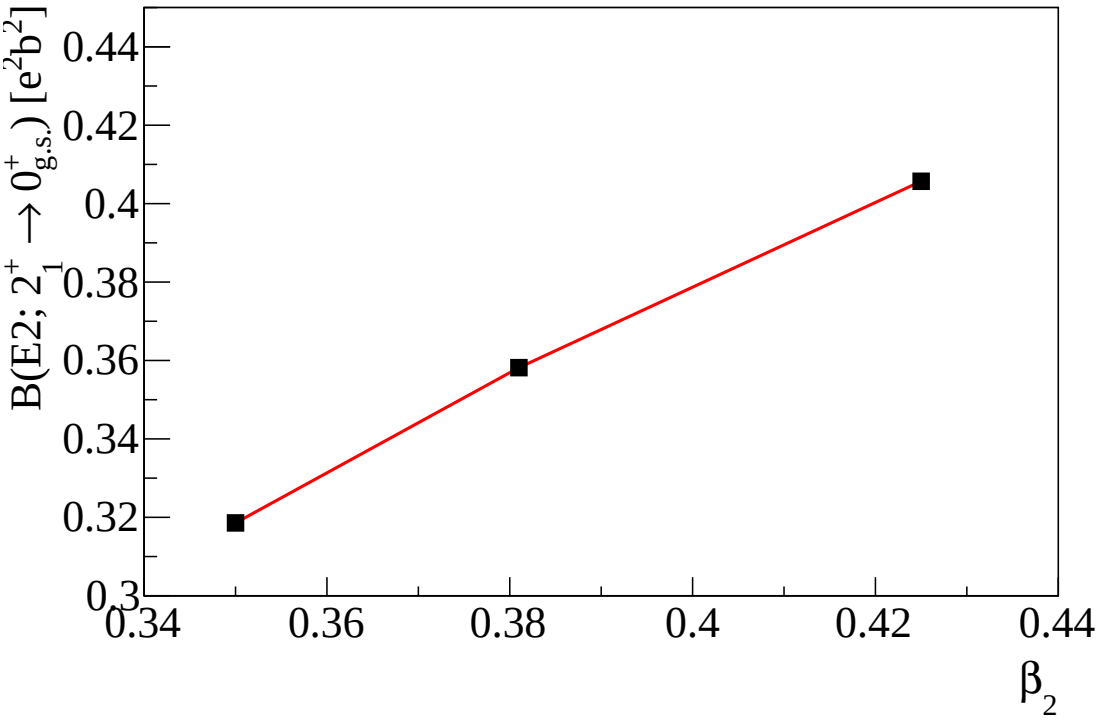

Figure 2.10: The evolution of the reduced transition probability as a function of deformation parameter, β_2, for ^{104}Zr. Results taken from Ref. [63].

element of Eq. 2.46 is related to the operator in Eq. 2.41, as well as the terms relating to the projections of the angular momenta of the initial and final wavefunctions onto a deformed basis [62]. The effect on the $2_1^+ \rightarrow 0_{g.s}^+$ transition probability by the input deformation parameter is demonstrated for ^{104}Zr in Fig. 2.10. Figure 2.11 shows the input deformations and related $B(E2; 2_1^+ \rightarrow 0_{g.s.}^+)$ values for ^{102,104,106}Zr, where the lowest β_2 value of Fig. 2.10 is used.

It is evident from the influence of Eq. 2.45 on Eq. 2.37, and therefore the single-particle wavefunctions of the basis state, as well as the diagonalisation of Eq. 2.43, that the input deformation is a valuable constraint to impose on the PSM. Moreover, due to its sensitivity to deformation, as well as the single-particle structure of the initial and final wavefunctions, the experimental determination of $B(E2; 2_1^+ \rightarrow 0_{g.s.}^+)$ values in the neutron-rich Zr region will provide a greater insight into the efficacy of the PSM for the description of well-deformed nuclei. To work towards this, the calculations of Ref. [63], presented in Fig. 2.11, shall be compared with experimental values.

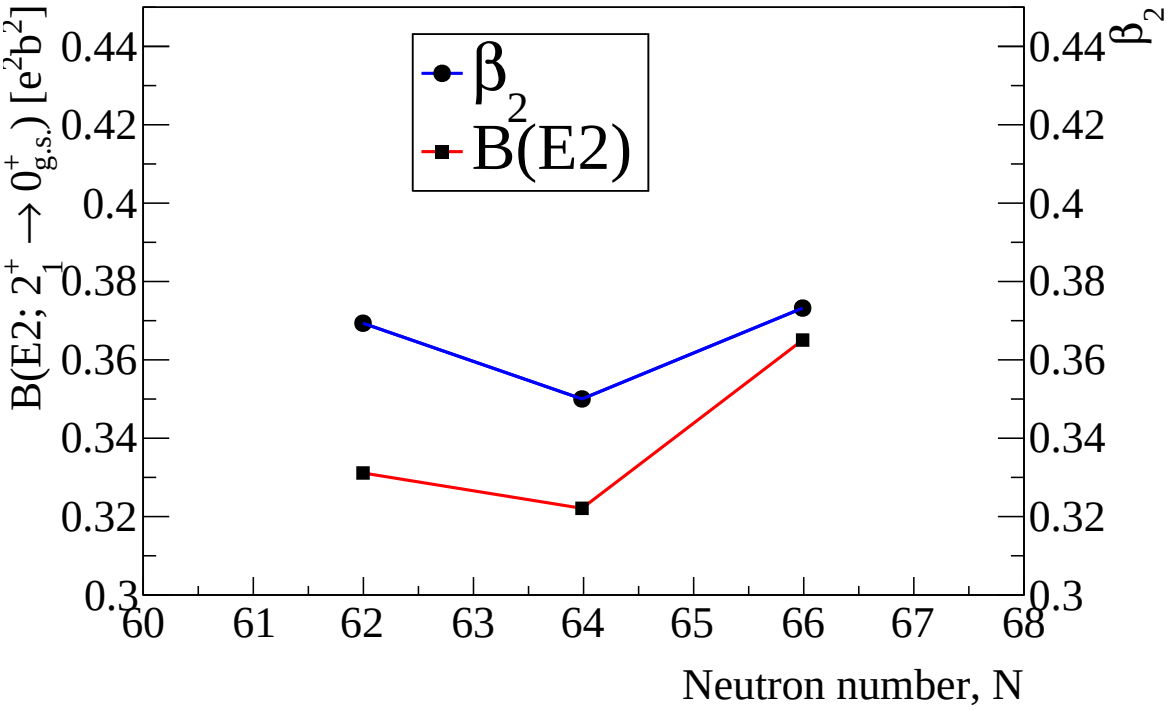

Figure 2.11: The predicted $2_1^+ \rightarrow 0_{g.s}^+$ $B(E2)$ values for ^{102,104,106}Zr with their respective deformation parameters. Data points taken from Ref. [63].

2.10 The interacting boson model: the algebraic approach

The IBM [31] is a somewhat abstract philosophy in the field of nuclear structure physics, since it relies on the concepts of group theory and the treatment of paired nucleons as bosons. Discussed here is the first incarnation of the theory, labelled as IBM-1, in which no distinction is made between protons and neutrons. In the IBM-1 framework, the nucleons are considered to couple into bosons with a spin of either 0, or 2, classified as s and d bosons, respectively.

In the language of group-theory, the major collective motions of the nucleus are described using the sets, U(5) (anharmonic vibrator), SU(3) (symmetric rotor) and O(6) (γ-soft rotor). In the extreme cases of these limits, the Hamiltonian takes the

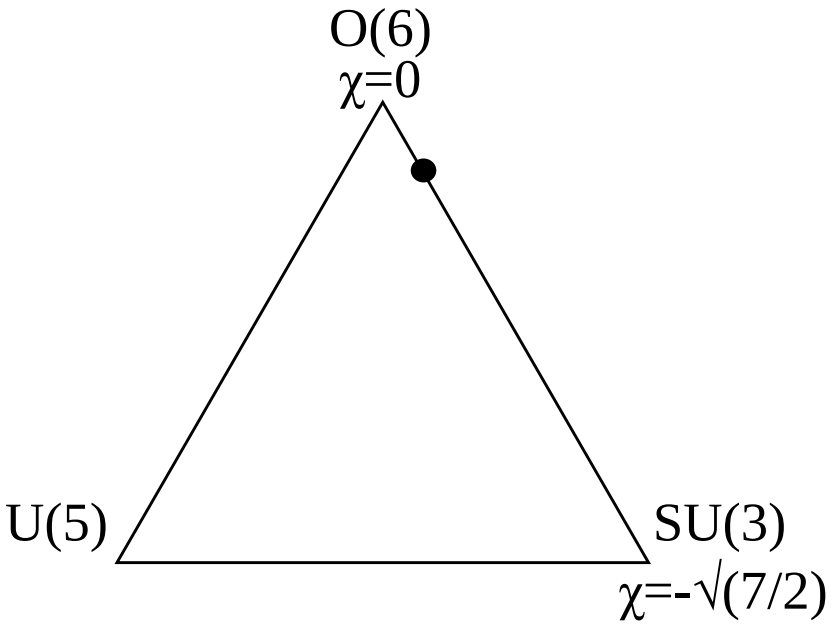

Figure 2.12: The parameters of Eq. 2.55 (minus the τ-compression term) represented by the *Casten triangle*. The vertices represent the three symmetries of the IBM. The black dot shows the location of $\chi = -0.2$.

form,

$$\mathrm{U}(5) : H = \epsilon \hat{n}_d + \kappa' \hat{L} \cdot \hat{L}, \tag{2.47}$$

$$\mathrm{SU}(3) : H = \kappa \hat{Q} \cdot \hat{Q} + \kappa' \hat{L} \cdot \hat{L}, \tag{2.48}$$

$$\mathrm{O}(6) : H = \kappa' \hat{L} \cdot \hat{L} + \kappa'' \hat{P}_+ \cdot \hat{P}_- + c_3 \hat{T}_3 \cdot \hat{T}_3. \tag{2.49}$$

where ϵ, κ, κ', κ'' and c_3 are free parameters. The operators of Eqs. 2.47, 2.48 and 2.49 are defined as,

$$\hat{n}_d = d^\dagger \cdot d, \quad \text{The number of } d\text{-bosons,} \tag{2.50}$$

$$\hat{L}_\mu = \sqrt{10} \left[d^\dagger \times \tilde{d} \right]^{(1)}_\mu, \quad \text{The angular momentum operator,} \tag{2.51}$$

$$\hat{Q}_\mu = \left[d^\dagger \times \tilde{s} + s^\dagger \times \tilde{d} \right]^{(2)}_\mu + \chi \left[d^\dagger \times \tilde{d} \right]^{(2)}_\mu, \quad \text{The quadrupole operator,} \tag{2.52}$$

$$\hat{P}_+ = \left[s^\dagger \times s^\dagger + \sqrt{5} d^\dagger \times d^\dagger \right]^{(0)}_0, \quad \hat{P}_- = \left(\hat{P}_+ \right)^\dagger, \quad \text{Pairing operator,} \tag{2.53}$$

$$\hat{T}_{3,\mu} = \left[d^\dagger \times d \right]^{(3)}_\mu, \quad \text{The octupole boson operator.} \tag{2.54}$$

At their extremes, the Hamiltonian of the U(5), SU(3) and O(6) groups generate

spectra similar to those depicted in Figs. 2.6c, 2.6a and 2.6b, respectively. However, since most nuclei, particularly the transitional nuclei, are not well represented by *only* one of these symmetric groups a Hamiltonian which includes all the relevant terms from Eqs. 2.47, 2.48 and 2.49 is required. For this work, the theoretical predictions, which shall be presented later and compared to experimental values, were calculated with the following Hamiltonian [64],

$$\hat{H} = \epsilon \hat{n}_d + \kappa \hat{Q} \cdot \hat{Q} + \kappa' \hat{L} \cdot \hat{L} + \kappa'' \hat{P}_+ \cdot \hat{P}_- + \lambda \hat{n}_d^2. \tag{2.55}$$

In this parametrisation, there is no octupole term, but the inclusion of the last term, $\lambda \hat{n}_d^2$, acts to increase the moment of inertia of the nucleus as a function of the angular momentum, an effect known as the τ-compression [65].

Within the framework of the consistent-Q formalism (CQF) [66], the Hamiltonian for nuclei which are transitioning between the SU(3) and O(6) symmetries becomes [43],

$$H = \kappa \hat{Q} \cdot \hat{Q} + \kappa' \hat{L} \cdot \hat{L}. \tag{2.56}$$

for a nucleus which exhibits a pure SU(3) symmetry, $\chi = -\sqrt{7/2}$ and nuclei that are purely O(6) in nature have $\chi = 0$, in this case Eq. 2.56 generates only O(6) wavefunctions. Therefore, in a manner similar, but not analogous, to the case of the PSM the strength of the quadrupole force is related to the value of χ. The critical values of χ are displayed on the so-called *Casten's triangle* in Fig. 2.12. The value of χ used in the calculations of Ref. [64] is shown on Fig. 2.12 as a black dot.

Of particular interest within the context of this thesis is the quadrupole operator, $\hat{Q}$. In the framework of the IBM, the $E2$ transition operator is defined by,

$$\hat{T}(E2) = e_B \hat{Q}, \tag{2.57}$$

where e_B is the effective boson charge, in analogy to the familiar effective charge of fermions. It should be noted that the due to the use of the CQF, the $\hat{Q}$ in Eq. 2.57 is identical to that in Eq. 2.55, defined by Eq. 2.52, implying a dependence of $E2$ transition probability on χ.

In Ref. [64] the parameters of Eq. 2.55, given in Tab. 2.2, are obtained through a fit of the ground-state, quasi-γ and quasi-β bands of the $^{100\text{-}104}$Zr, $^{94\text{-}110}$Mo, $^{98\text{-}114}$Ru and

ϵ	κ_{00}	κ_{10}	κ_{01}	κ'_{00}	κ'_{10}	κ'_{01}	κ''	λ_{00}	λ_{10}	λ_{01}
695	-35.8	-72.4	47.9	18.3	12.8	-15.8	1.4	-115.9	-166.1	161.2

Table 2.2: Parameters used in Eq. 2.55 in units of keV. Reproduced from Ref. [64].

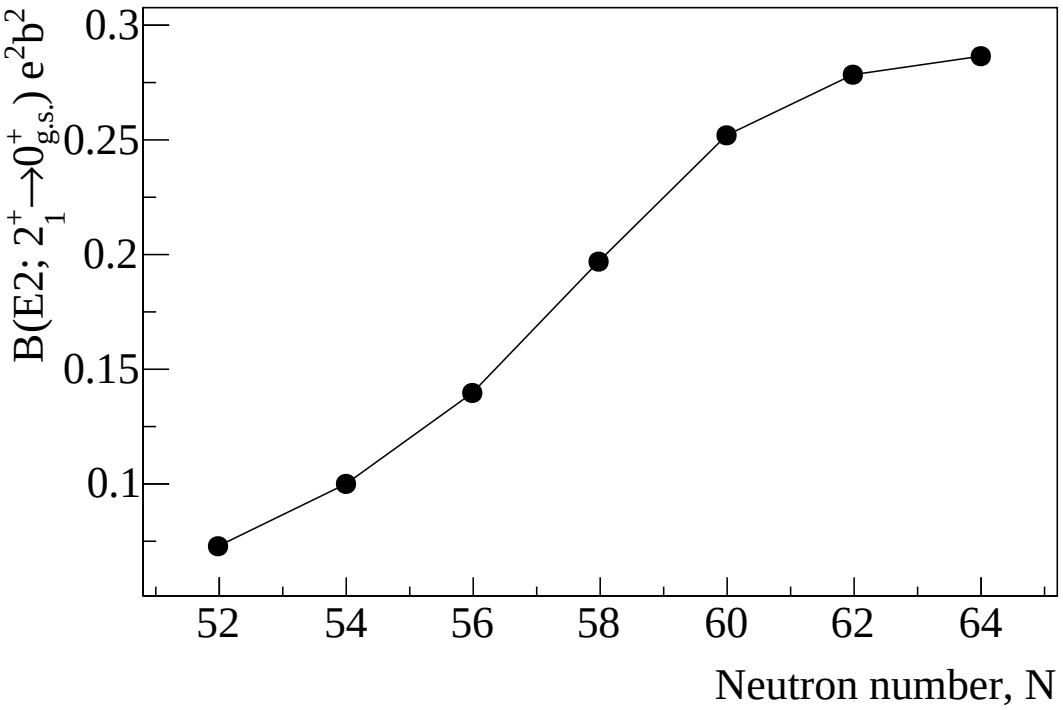

Figure 2.13: Predictions of the $2_1^+ \rightarrow 0_{g.s}^+$ transition probabilities for even-even Zr nuclei as predicted from the IBM with the Hamiltonian of Eq. 2.55 with the parameter values give in Tab. 2.2. [64].

$^{102\text{-}120}$Pd nuclei. Additionally, the χ parameter was determined to be -0.2, which was used to predict the $2_1^+ \rightarrow 0_{g.s}^+$ ground-state transition probabilities of even-even nuclei, plotted in Fig. 2.13. These will be compared against experimental values in Chap. 6.

2.11 Concluding remarks

In this chapter, contemporary calculations regarding ground-state shapes and $2_1^+ \rightarrow 0_{g.s}^+$ reduced transition probabilities have been presented. In particular, differing ground-state shapes are predicted by the FRDM and HFB calculations, the latter suggesting a dramatic shape change, from prolate to oblate. The importance of having correctly defined ground-state deformations has been addressed for the PSM Hamiltonian to give an accurate quadrupole-quadrupole interaction strength. Predictions from contempo-

rary IBM calculations of the $2_1^+ \rightarrow 0_{g.s}^+$ transition probability have been presented, which are derived from a Hamiltonian whose parameters are obtained from a global fit.

The experimental objectives are then clear, to obtain reduced transition probabilities and ground-state deformations from lifetime measurements of the first excited states of the neutron-rich, even-even Zr nuclei. This will provide a test of the ground-state deformations of the FRDM and HFB predictions, it will also provide a constraint for future PSM calculations. The experimental values of $2_1^+ \rightarrow 0_{g.s}^+$ transition probabilities will also provide evidence as to the validity of the parameters employed in the IBM Hamiltonian, as well as those predicted by the PSM.

Chapter 3

Experimental Details

The investigation into the neutron-rich zirconium region was carried out at the Radioactive Isotope Beam Factory (RIBF), which is jointly operated by the RIKEN Nishina Center (RNC) and the University of Tokyo's Center of Nuclear Study (CNS). The RIBF provides a variety of high-intensity primary beams which, in the case of the ^{238}U beam used the current work, are accelerated using a 5-stage acceleration scheme. The low-Z production target used to induce the abrasion-fission reaction was relatively thick in order to exploit the high-intensity of the primary beam. Such a thick target leads to a large angular and momentum spread in the fission fragments. To compensate for these straggling effects the Big RIKEN Projectile Fragment Separator (BigRIPS) is designed for unparalleled acceptance with respect to both the angular and momentum spread of the incoming secondary ions. Identification of the fragments was carried out using mass-to-charge determination in the second-stage of BigRIPS and atomic charge determination in the ZeroDegree Spectrometer (ZDS). An active stopper of 5 double-sided silicon-strip detectors (DSSSDs) provided the means to measure the subsequent β-decays of implanted fragments. Gamma rays emitted from states following β-decay, or from isomeric states, were measured using a combined array of high-purity germanium (HPGe) and cerium-doped lanthanum tri-bromide ($LaBr_3$(Ce)) detectors.

3.1 Primary beam production and acceleration

Uranium ions were ejected from a metallic uranium rod by the sputtering method and provided with an initial acceleration by a 28 GHz microwave guide [67]. The

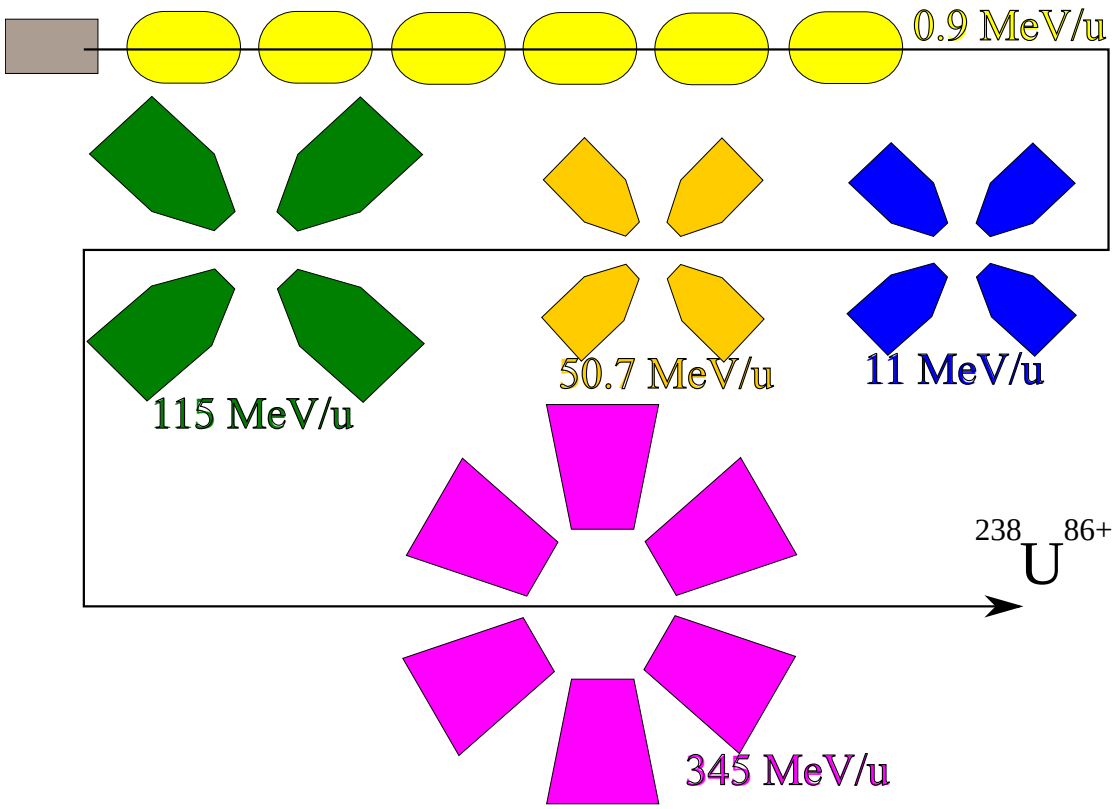

Figure 3.1: Schematic overview of the acceleration scheme used for the acceleration of ^{238}U to 345 MeV/u. The grey box represents the U source and microwave guide, the yellow, blue, orange, green and fuchsia shapes represent the RILAC, RRC, fRC, IRC and SRC, respectively. The final energy after each acceleration stage is given in the same colour as the accelerator the beam is exiting.

ejected ions were further accelerated by the RIKEN Linear Accelerator (RILAC), and then by four cyclotrons, the RIKEN Ring Cyclotron (RRC), the fixed-frequency Ring Cyclotron (fRC), the Intermediate Ring Cyclotron (IRC) and, finally, the Superconducting Ring Cyclotron (SRC) [68]. The RRC, fRC, and IRC are each powered by four sector magnets and two radio-frequency (RF) acceleration cavities, whereas the SRC comprises 6 superconducting sector magnets and 4 RF accelerating cavities. Figure 3.1 shows the sequence of accelerators used and the beam energy upon exiting each accelerator. The final primary beam energy was 345 MeV/nucleon, equivalent to 70% of the speed of light.

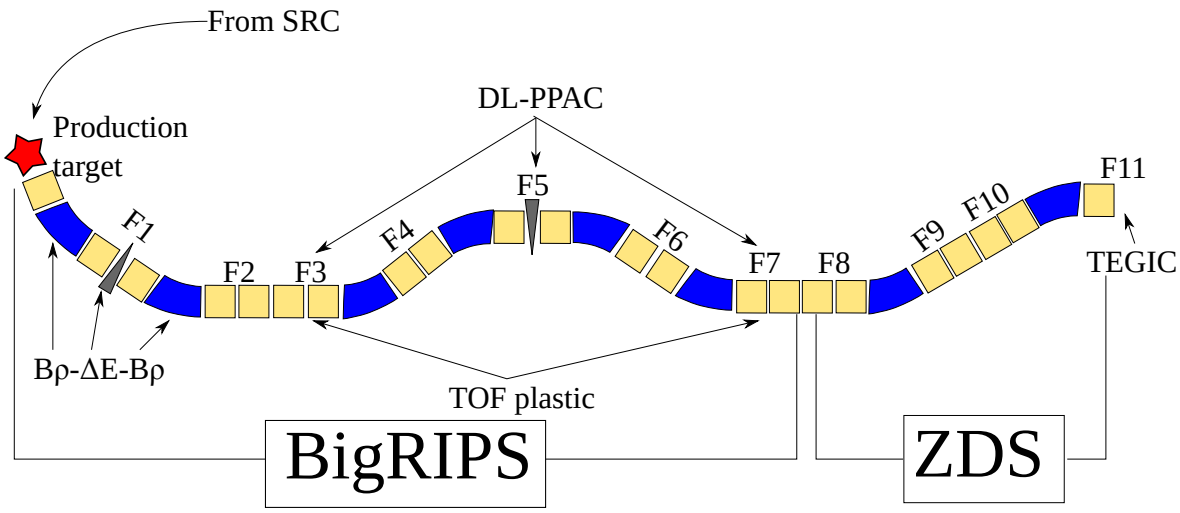

Figure 3.2: A schematic of the BigRIPS and ZDS spectrometers. The blue shapes represent the dipole magnets, the yellow squares are the superconducting quadrupole triplets (STQs) and the grey triangles are the Al wedge degraders. Labelled with FX are the focal planes, which always lie in between two STQs. The $B\rho$-ΔE-$B\rho$ separation stage is labelled, as well as the positions of the beam-line detectors, see text for details.

3.2 Secondary beam production and separation

A 555 mg/cm^2 ^{9}Be production target located at the entrance of BigRIPS, see Fig. 3.2, was bombarded by the primary beam to induce in-flight abrasion-fission, depicted in Fig. 3.3. The advantage of this mechanism is the preferential production of very neutron-rich $Z \approx 40$ isotopes [69].

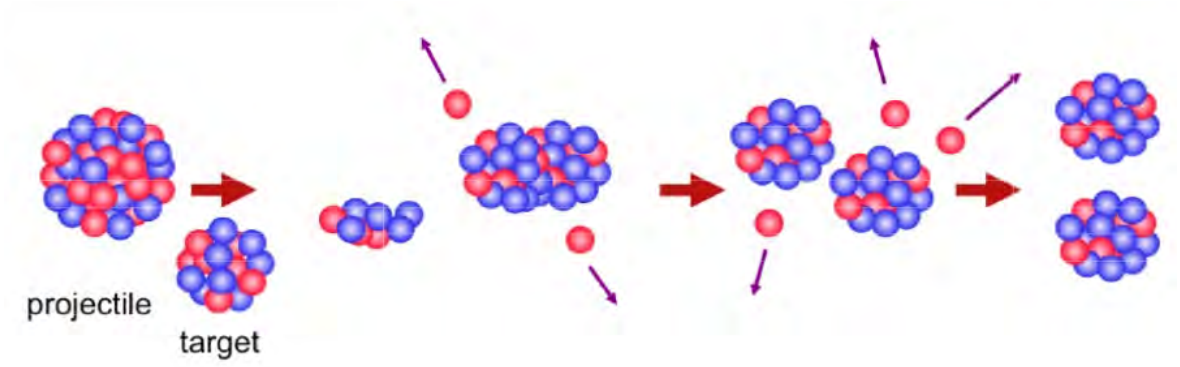

Figure 3.3: Diagram showing the mechanism of abrasion-fission. In the case of this experiment, the projectile is ^{238}U and the target is ^{9}Be, see text for details. Figure is taken from Ref. [69]

The implication of the relatively low primary beam energy and thick production target is the increased straggling of the secondary ions. This results in a large angular and momentum spread of the secondary beam, $\Delta p/p \sim 10\%$ and 100 msr, respectively.

BigRIPS compensates for this by having a wide-aperture entrance window and employing STQs. The former provides an angular acceptance of 80 msr and the latter a momentum acceptance of 6%. [70].

Spatial separation of the various species of the secondary beam according to their mass-to-charge ratio and ionic charge is achieved in the first stage of BigRIPS, between the production target and the F2 focal plane in Fig. 3.2. The differing radii of curvature of ions through the dipole magnets provides separation depending to their mass-to-charge ratio. An aluminium wedge degrader of central thickness 8 mm was placed at the F1 focal plane and another of 4.5-mm thickness at the F5 focal plane, labelled on Fig. 3.2 as grey triangles, these provided separation of ions depending on their energy loss, and, therefore, their atomic number [71]. Since the separation happens in the order of bending in the first dipole, then the energy loss in the degrader and then bending in a second dipole, this method of separation is known as the $B\rho$-ΔE-$B\rho$ technique.

3.3 Beam-line detectors

Complete particle identification (PID) of fission fragments requires measurement of their mass-to-charge ratio, as well as their atomic number. These are measured in the second stage of BigRIPS and ZDS, respectively.

The properties of the in-flight ion that are necessary for the determination of the mass-to-charge ratio can be obtained by equating the force it feels from its motion in a uniform magnetic field and the centripetal force it experiences. In a non-relativistic frame this is given by,

$$\frac{mv^2}{\rho} = Q\left(\vec{E} + \vec{v} \times \vec{B}\right), \tag{3.1}$$

where m is the mass of the ion, ρ is its radius of curvature, v is its velocity, Q is its charge, $\vec{E}$ and $\vec{B}$ are the electric and magnetic fields through which the ion is travelling, respectively. In the relativistic frame, in atomic mass units, u, the ion mass becomes, γAu, where γ is the Lorentz factor, $1/\sqrt{1-\beta^2}$, and A is the atomic mass. If the velocity is then expressed in terms of c, the speed of light, and Eq. 3.1 is rearranged to give the mass-to-charge ratio,

$$\frac{A}{Q} = \frac{B\rho}{\beta\gamma uc}. \tag{3.2}$$

According to Eq. 3.2, the observables of interest are the ions' velocity and their radii of curvature in the dipole magnets, which have a known B-field applied.

The measurement of the atomic charge of ions is related to their energy deposition according to the Bethe-Bloche equation [72],

$$-\frac{dE}{dx} = \frac{4\pi e^4 Q^2}{m_e v^2} n Z_a \left[\ln \frac{2 m_e v^2}{I} - \ln\left(1-\beta^2\right) - \beta^2 \right], \tag{3.3}$$

where

e is the electronic charge,

m_e is the rest mass of the electron,

n is the number density of the absorber,

Z_a is the atomic number of the absorber,

I is the excitation and ionisation potential of the absorber.

Therefore, with the measurement of dE/dx, along with the velocity of the ion, its charge (atomic number), Q, can be determined through the use of Eq. 3.3.

Time-of-flight detectors

The velocity measurement required for Eqs. 3.2 and 3.3 is taken as the ratio of the time taken for the ion to travel between the F3 and F7 focal planes, their TOF, and the distance between them, d. The time difference between signals from two plastic scintillators at each focal plane provide the TOF of a fragment passing between them. Each scintillation detector has a photo-multiplier tube (PMT) on the left and right side, so that the average of the PMT signals makes the timing signal independent of the position of interaction in the detector. Therefore, the TOF is given by,

$$\text{TOF} = \frac{(T_{F7L} + T_{F7R}) - (T_{F3L} + T_{F3R})}{2}, \tag{3.4}$$

where T_{F3L}, T_{F3R}, T_{F7L}, and T_{F7R} are the time-differences of the respective PMT measured with respect to the left-side PMT of the F11 scintillator. Then the velocity

of the fragment can be determined by,

$$v = \frac{d}{\mathrm{TOF}}, \tag{3.5}$$

where d is the distance between the two scintillators as followed by the central trajectory of an ion, 46.976 m[1].

Beam position detectors

The position measurements required for Eq. 3.2 are performed using position-sensitive dual-layer delay-line parallel plate avalanche chambers (DL-PPACs) located at the F3, F5 and F7 focal planes. The operational principle of these is the same as for ordinary PPACs, however, a delay-line is introduced to compensate for the high-intensity particle beams achieved at the RIBF [73]. Figure 3.4 shows a schematic of single-layer of a DL-PPAC. The interaction position along the x and y wires, P_x (mm)

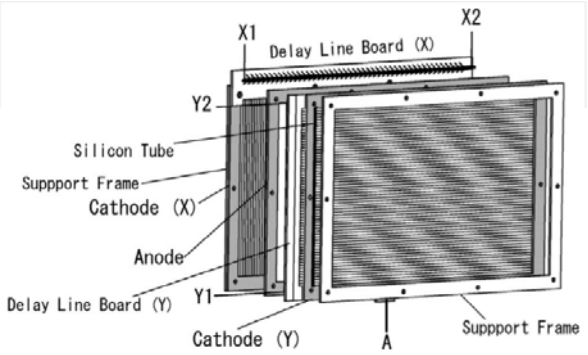

Figure 3.4: An exploded view of a DL-PPAC. Figure taken from Ref. [73].

and P_y (mm), is obtained from the time-difference between the ends of the delay-line, $Y1$, $Y2$, $X1$ and $X2$ of Fig. 3.4, where the reference time is the signal from the anode. The relations applied to get the interaction position are [73],

$$P_x = \frac{k_x\,(T_{x1} - T_{x2})}{2} + X_{\mathrm{off}}, \tag{3.6}$$

$$P_y = \frac{k_y\,(T_{y1} - T_{y2})}{2} + Y_{\mathrm{off}}, \tag{3.7}$$

where T_{x1} (ns), T_{x2} (ns), T_{y1} (ns), and T_{y2} (ns) are the times taken for the signals to reach either end of the detection wires from the interaction point, k_x (mm/ns) and

[1]For off-central trajectories, corrections based on position measurements of the ions are made.

k_y (mm/ns) are factors which convert from the time difference to position and are obtained from calibrations using a "masked" α source, where the mask has a series of regularly spaced slits at known distances [73]. For reference, the dimensions, positions and types of DL-PPACs used for the experiment are given in Tab. 3.1.

Position	Type	Dimensions	Number
F3	Double	240x150 mm	1
		150x150 mm	1
F5	Double	240x150 mm	2
F7	Double	240x150 mm	1
		150x150 mm	1

Table 3.1: The physical dimensions of the DL-PPACs used in this experiment at each focal plane, adapted from [74]

Gas ionisation chamber for energy-loss measurements

A gas ionisation chamber (IC) situated at the final focal plane (F11) of the ZDS is used to measure the energy-loss of ions, so that the atomic number can be extracted from Eq. 3.3. The tilted-electrode gas ionisation chamber (TEGIC), which is a development of the familiar multi-sampling ionisation chamber (MUSIC), was employed since the tilted-electrodes, shown in Fig. 3.5, compensate for effects that occur in a high-intensity beam environment, as well as reducing recombination in the fill gas [75].

As in all MUSICs, the electrons liberated from the gas molecules from their interaction with the fission fragment flow to the anode, whilst the ionised gas molecules drift towards the cathode. Since the electrons' velocity is so much faster than the gas molecules, the charge collection of the anodes is completed much faster than that of the cathodes. Therefore, in order negate potential signal pile-up from a high particle rate, only the anodes provide signal to the readout electronics, whilst the cathodes are grounded, as shown in Fig. 3.5. The geometric mean of the signals from the anodes are taken for the energy-loss of the ion across the TEGIC,

$$\Delta E_{\mathrm{Raw}} = \sqrt[6]{\prod_{i=0}^{6} \mathrm{d}E_i}, \tag{3.8}$$

where $\mathrm{d}E_i$ is the signal collected from each anode. This method naturally excludes events in which not all anodes provide a signal, which may relate to an ion being

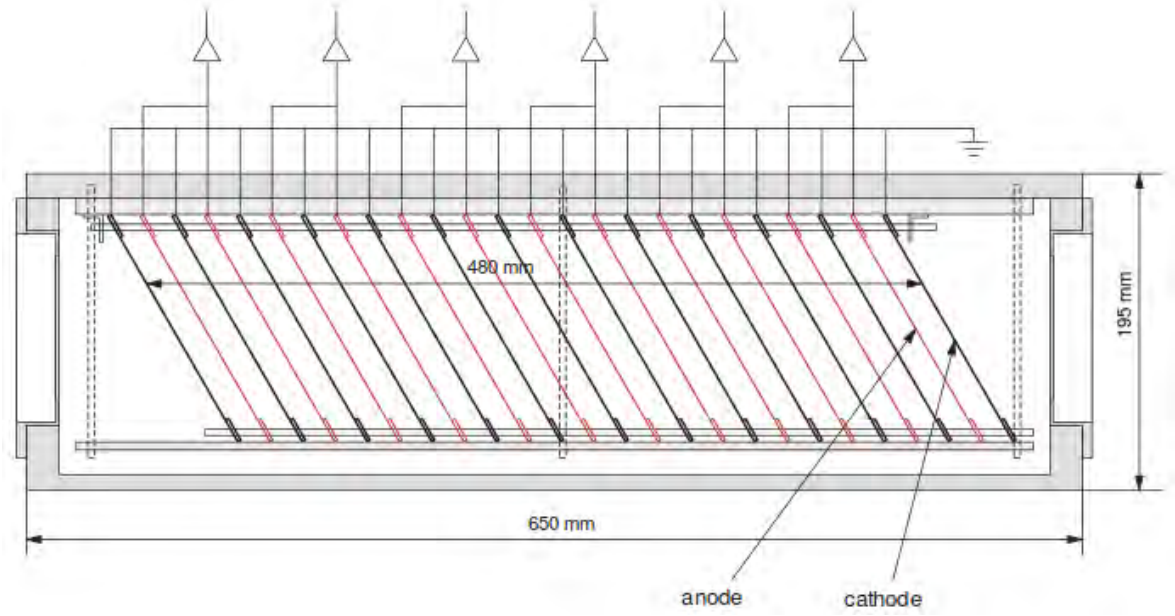

Figure 3.5: A cross-sectional view of the TEGIC. Note the only the anodes are connected to the amplifiers, whereas the cathodes are grounded. The dashed lines represent support structures. Figure taken from [75].

stopped, e.g. by reacting with a detector component, in the chamber.

3.4 Detectors for measuring radiative decays

After exiting the F11 focal plane, the transported ions traverse ∼2 m of free air before being stopped in an array of 5 highly-segmented double-sided silicon-strip detectors (DSSSDs) which constitute the Wide-range Active Silicon Strip Stopper Array for β and Ion detection (WAS3ABi). The array is sensitive to the position of both ion implantations and their subsequent β-decay. Surrounding WAS3ABi is a mixed array of 84 HPGe detectors, which comprise the EUROBALL-RIKEN Cluster Array (EURICA), and an array of 18 cerium-doped lanthanum tri-bromide ($LaBr_3(Ce)$) detectors. The configuration is shown in Fig. 3.18a. Additionally, two plastic scintillator detectors (β-plastics) are positioned upstream, and downstream of WAS3ABi, in order to precisely measure the time of β-decay. They are used in conjunction with the $LaBr_3(Ce)$ array to measure the lifetimes in the nanosecond regime of states populated through β-decay.

3.4.1 WAS3ABi silicon array

In this experiment, WAS3ABi comprised five DSSSDs, each with 60 strips along the x-axis, and 40 along the y-axis. Each strip has a square cross-sectional area of 1×1 mm^2, giving a total active area of 60×40 mm^2. The granularity of WAS3ABi alleviates some of the problems of correlating ions with β-decays in a high particle rate environment, however, the device still provides the limiting factor for overall beam intensity, with it being limited to 100 implantations/second. Figure 3.6a shows WAS3ABi and the β-plastics on the test-bench, and Fig. 3.6b shows them in the EURICA frame.

WAS3ABi energy calibration

The energy calibration of WAS3ABi was non-trivial, since its multi-layered nature ruled out the use of a "bare" electron source, therefore, γ rays correlated with EURICA were used. A ^{60}Co source was placed in close proximity to WAS3ABi and the acquisition was set such that the trigger was provided by coincidences between WAS3ABi and EURICA. This allowed the measurement of the sum of the energy deposited by Compton scattered γ rays in WAS3ABi, E_{Si}, and their subsequent absorption in EURICA, E_{Ge}. The sum of their energies should equal the energy of the emitted γ-ray, i.e. 1.17, or 1.33 MeV. The energy-energy matrix depicted in Fig. 3.7, shows clearly the two lines relating to the γ rays of the ^{60}Co source. A 2-dimensional cut was taken around each of these correlation lines and a simple linear regression was applied to the events inside each of the cuts to calibrate each strip. An example of a fitted line is shown as the red-dashed line in Fig. 3.7.

A correction to the initial calibration was applied using matrices of the summed energies measured in WAS3ABi and EURICA, E_{sum}, versus that of just WAS3ABi, as shown in Fig. 3.8. In this case, the two correlation lines should follow the two red lines, which depict the 1.17 and 1.33 MeV γ rays. The correction was applied by conducting an iterative scan of gains applied to E_{Si} and measuring the resultant gradients of the E_{sum} vs. E_{Si} correlation distributions of Fig. 3.8. The gain of E_{Si} which yielded a zero gradient was selected. The results of the gain scan are shown in Fig. 3.9, an improved version of Fig. 3.8 is shown in Fig. 3.10, note that the correlated lines are still offset from the actual values, shown by the red lines, but an offset is added to rectify this.

(a) Inside the WAS3ABi chamber. The central structures with ribbon cables attached are the 5 DSSSDs and the plastic scintillators are the black sheets at either side of the DSSSD.

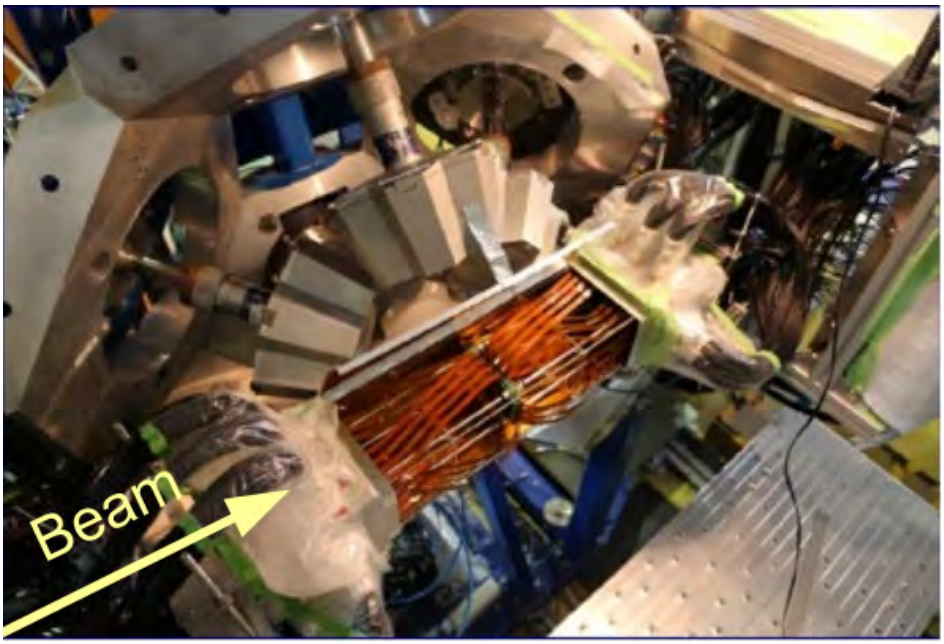

(b) The WAS3ABi chamber in its place within the EURICA array.

Figure 3.6: Images of the WAS3ABi array alone and within the EURICA frame.

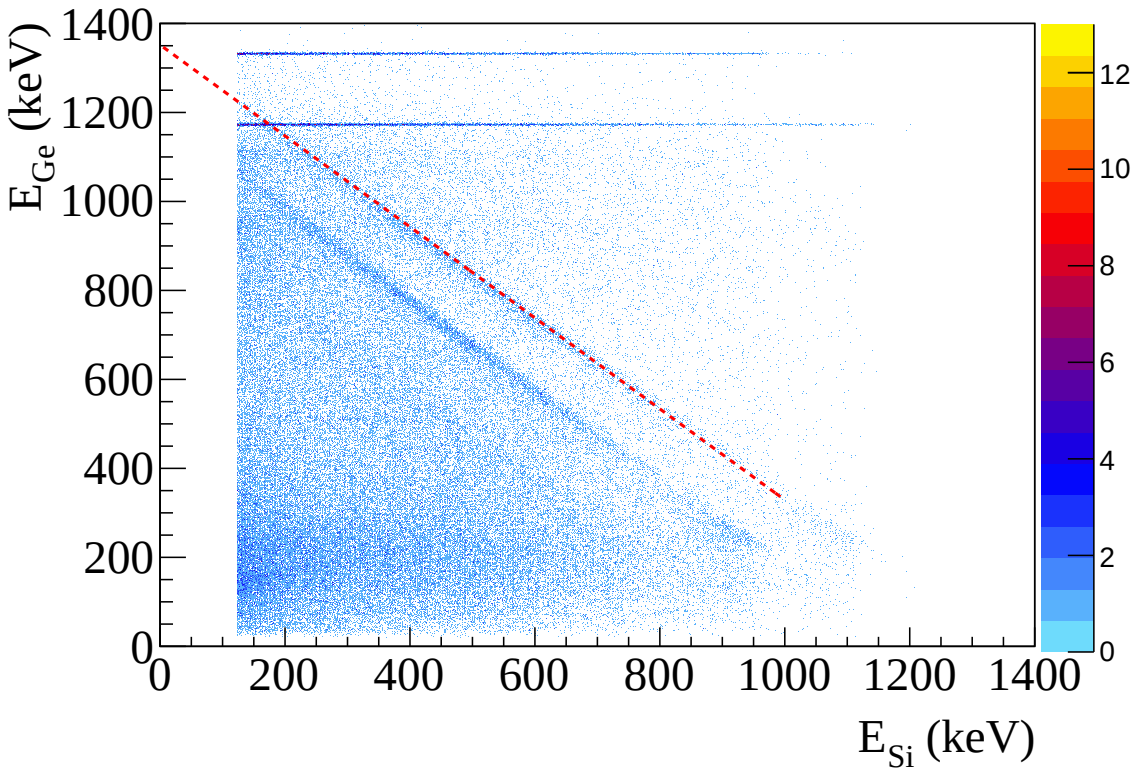

Figure 3.7: Energy measured in EURICA plotted against energy measured in WAS3ABi. The two diagonal correlation lines are used for the energy calibration of the strips. The red line shows an example linear fit.

3.4.2 EURICA HPGe array

High-resolution γ-ray spectroscopy is provided by 12 of the Cluster detectors which previously comprised the RISING array [76]. Each cluster comprises 7 tapered coaxial HPGe crystals in a close-packed configuration, as shown in Fig. 3.11a [77]. These clusters were mounted into a support structure which holds them in a 4π configuration surrounding the WAS3ABi chamber, Fig. 3.11b highlights the close-packed configuration, Fig. 3.11c shows the 4π placement of the detectors, and Fig. 3.11d shows the support frames and liquid nitrogen dewars. The angles with respect to the beam-line, distances from the central point of WAS3ABi and applied voltages of the crystals are given in Tab. 3.2.

Energy calibration

The energy calibration of EURICA was performed with a ^{152}Eu source. For each crystal the 121-, 244-, 344-, 778-, 964- and 1408-keV peaks were fitted in the raw

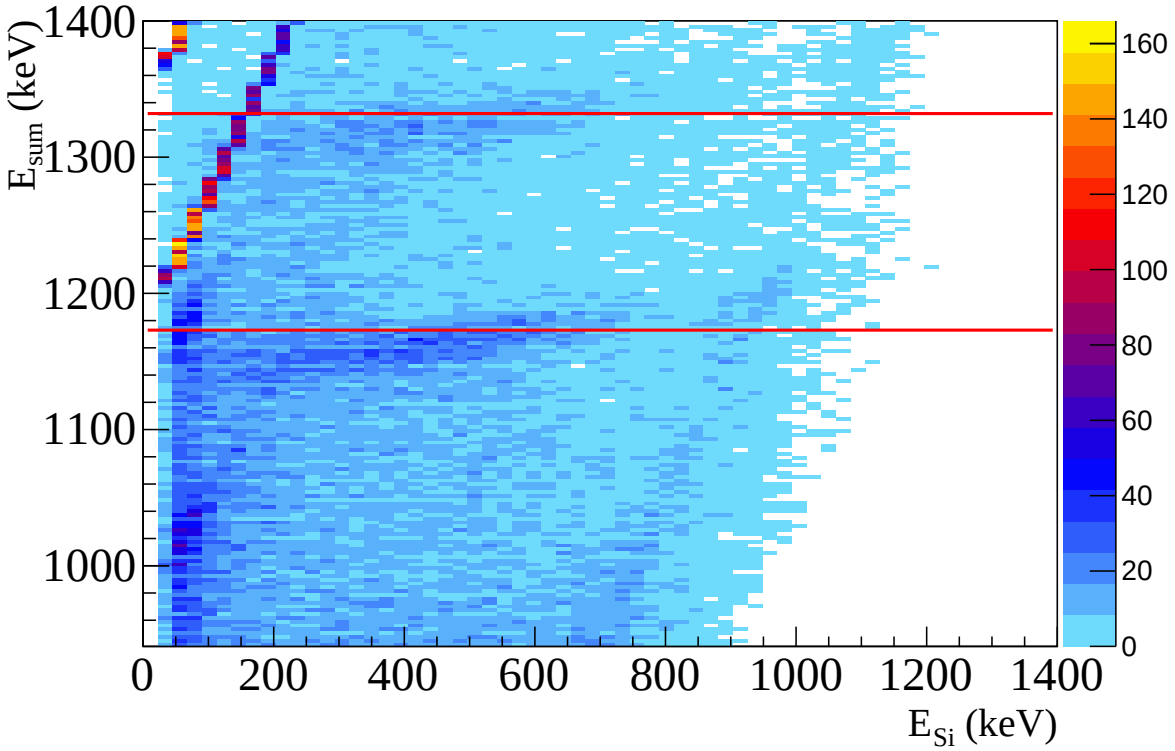

Figure 3.8: Summed energy of both EURICA and WAS3ABi plotted against just WAS3ABi energy. The two red lines show the expected position of the 1.17 and 1.33-MeV transitions.

spectrum, and a linear regression made for converting from channel to energy. The calibrated ^{152}Eu spectrum taken with the entire array is shown in Fig. 3.12.

Full-Width at Half Maximum characterisation

For the purposes of characterisation and to better notice γ-ray energy peaks which may not be completely resolved, it is of use to know the expected full width at half-maximum (FWHM) of the array as a function of energy. Fits were performed to several peaks of the ^{152}Eu spectrum shown in Fig 3.12 to extract the FWHM. The results of the fits are shown in Fig 3.13, along with a fit to a polynomial formula, displayed in Fig. 3.13, as suggested by the RadWare package [79], where x is the γ-ray energy, and a, b and c are empirically fitted parameters.

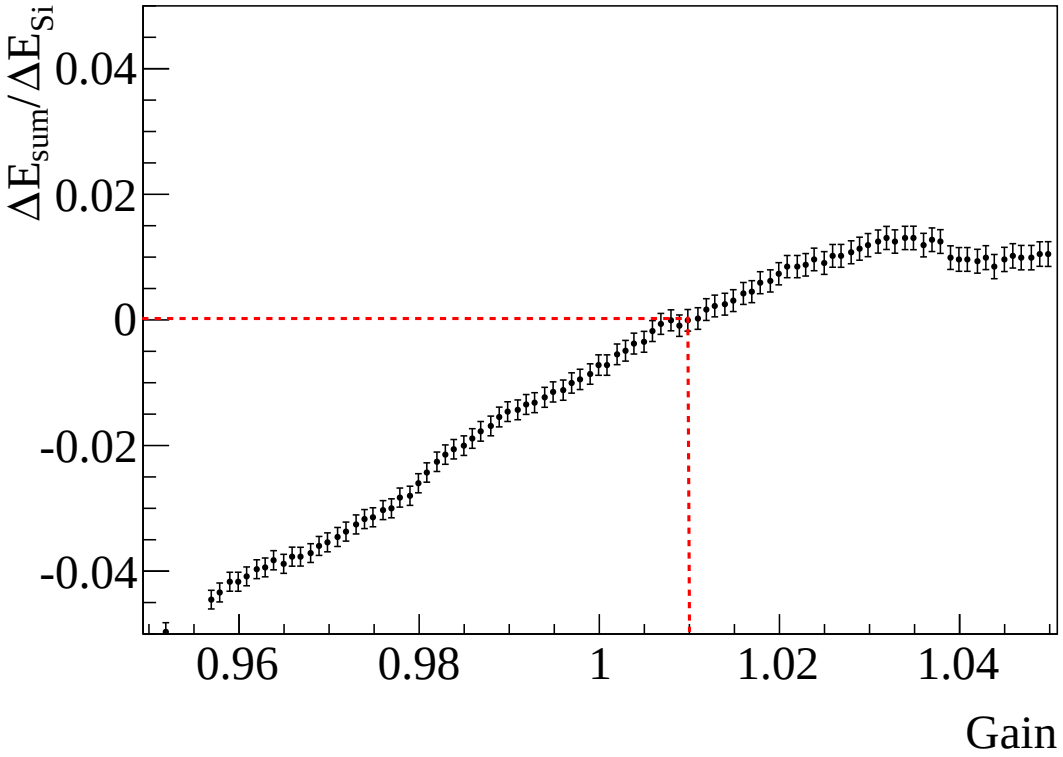

Figure 3.9: The gradient of the correlation lines of Fig. 3.8 as a function of the gain applied to the energy measured in a silicon strip. The dashed red-line shows the gain value which satisfies the optimal result, i.e. a zero gradient.

Add-back

The close-packed configuration of the Cluster detectors allows for implementation of an add-back algorithm, whereby the full energy of a γ ray that Compton scatters between crystals is reconstructed. The algorithm is initiated if two crystals detect a γ ray within a 105 ns time window and the sum of the deposited energies is above a threshold of 120 keV. The possible hit patterns of a Cluster and decision results of the algorithm are shown in Fig. 3.14. The procedure decreases Compton background and increases detection efficiency, as shown in Figs. 3.17 and 3.15, respectively.

Efficiency characterisation

The characterisation of EURICA's efficiency plays an essential role in the production of nuclear level schemes. To ensure that the knowledge of efficiency extends over the energy range of interest, a combination of ^{152}Eu and ^{133}Ba sources was employed in the measurements. The sources were chosen for their low-activity, 10.6 and 13.4 kBq,

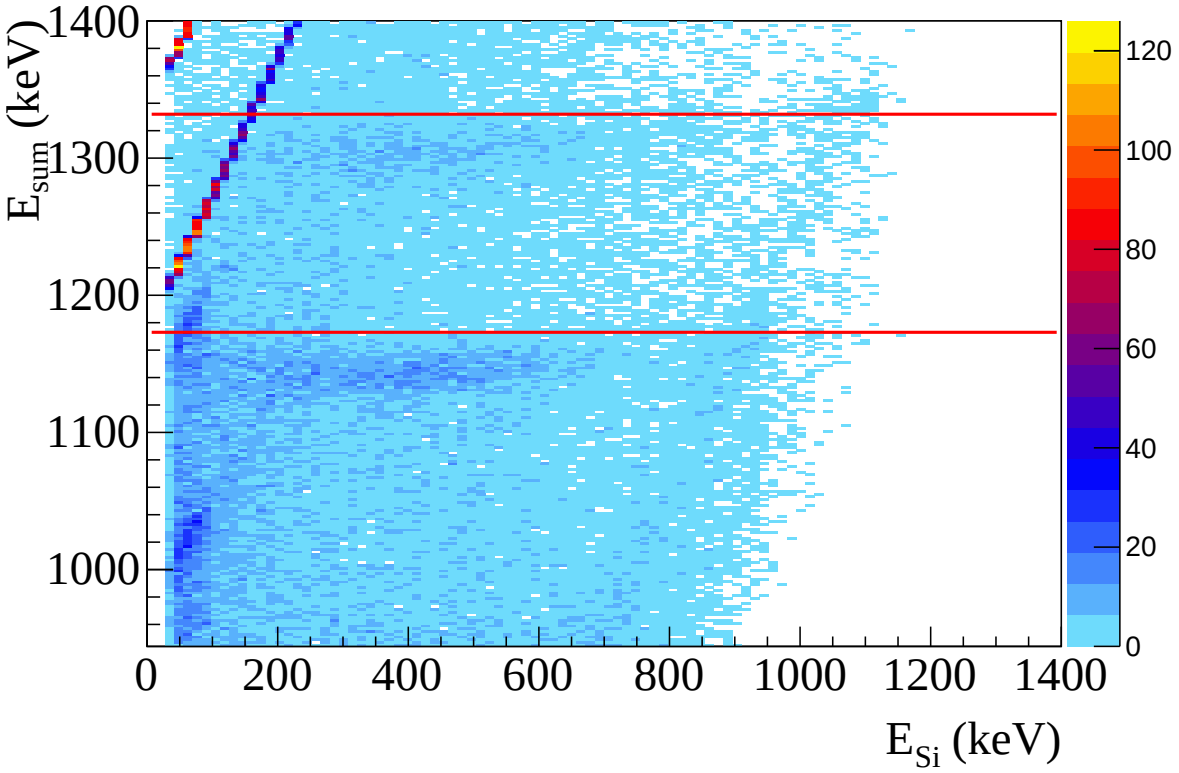

Figure 3.10: The same as Fig. 3.8, except with the gain calibration deduced from Fig 3.9. Note that the offset to align the correlated lines to their expected positions is not applied.

respectively, decreasing the chance of pile-up signals.

The sources were placed in a central position within the WAS3ABi chamber, as shown in Fig. 3.16. In one measurement, the ^{152}Eu source was placed upstream, illustrated by the red rectangle in Fig. 3.16b, and the ^{133}Ba downstream, the black rectangle in Fig. 3.16b. A second measurement was carried out with the positions reversed. The difference in the efficiencies measured at each of these positions was sufficiently small to allow both measurements to be combined.

For the efficiency measurement, the data acquisition was triggered once every millisecond by a pulse generator. This time interval was chosen as it is much longer than the deadtime of the EURICA electronics, which was measured to be of 300 μs. Each acquisition gate was 100 μs in length, and an additional software condition of 75 μs was imposed starting 12.5 μs after the initial trigger. This condition negates any spurious effects at the edges of the hardware gate.

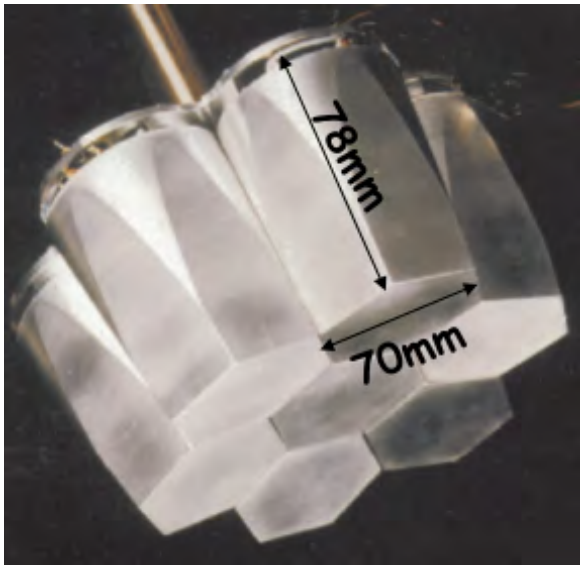

(a) An un-encapsulated Cluster detector. The dimensions of the crystal are shown. Note the close-packed configuration.

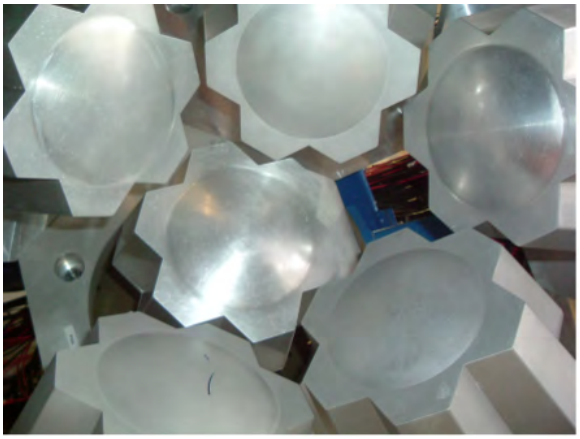

(b) Image of an hemisphere of the array showing how six encapsulated detectors are arranged in the array. Image from [78].

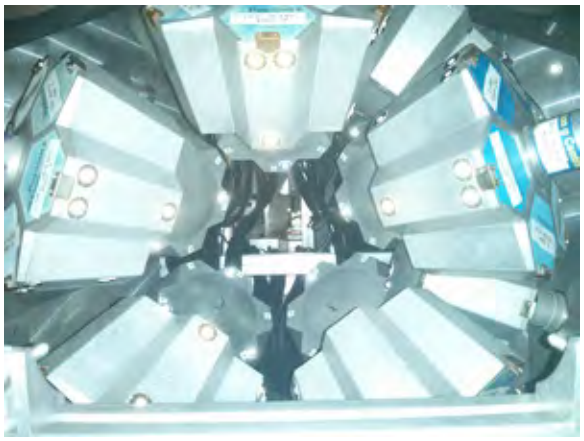

(c) Upstream view of the configuration of the Cluster detectors when the hemispheres are closed. The WAS3ABi chamber is absent.

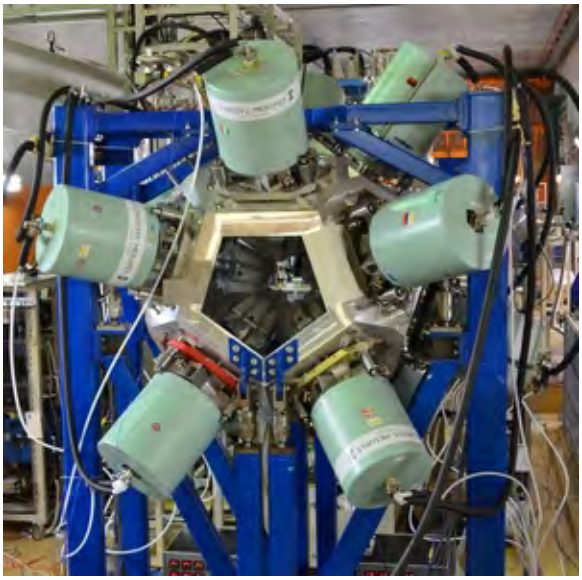

(d) The entire EURICA array with support structure and the cryostats for liquid nitrogen storage.

Figure 3.11: Various images showing the physical attributes of the EURICA array.

Cluster	θ (°)	ϕ (°)	Distance (cm)	Crystal Applied High-voltage (V)						
				A	B	C	D	E	F	G
1	51	234	229	4000	4000	4000	4000	3500	4000	3500
2	51	162	217	4000	4000	3500	4000	4000	4000	4000
3	51	90	230	4000	3000	4000	4000	3000	4000	3000
4	129	234	232	4000	4000	4500	4000	4500	4000	3500
5	129	162	219	3500	4000	4000	4000	4000	4000	4000
6	129	90	221	4000	4000	4000	4000	4500	4000	4000
7	90	54	210	4000	3500	4000	3500	4000	4500	3500
8	90	342	248	3500	3500	3000	3000	3500	3500	3000
9	51	306	233	4000	3500	4000	4000	4000	4000	3000
10	51	18	234	4000	4000	4500	4000	4000	4000	4000
11	129	306	227	4000	4500	4500	4000	4000	4000	4000
12	129	18	233	3500	4000	3500	3000	4000	3500	3500

Table 3.2: Summary of the operational characteristics of the Cluster detectors. "Distance" refers to the distance of the face of the detectors to the central point of WAS3ABi.

The absolute efficiency of each data point was computed by,

$$\varepsilon \;=\; \frac{A_\gamma}{N_{\text{acq.}} \cdot T_{\text{acq}} \cdot \mathcal{A} \cdot I_\gamma}, \tag{3.9}$$

where:

A_γ is the area of the peak of the transition in question.

$N_{\text{acq.}}$ is the total number of acquisition triggers during the reading (42433096),

T_{acq} is the length of each acquisition (75 μs),

$\mathcal{A}$ is the activity of the source (Bq),

I_γ is the absolute intensity of the transition in question,

The results from the efficiency calibration for both single crystal hits and the add-back procedure are shown in Fig. 3.17 with a fit performed to [79],

$$\varepsilon \;=\; \exp\left\{\left[\left(A + Bx + Cx^2\right)^{-G} + \left(D + Ey + Fy^2\right)^{-G}\right]^{-1/G}\right\}. \tag{3.10}$$

Here $x = \ln(E_\gamma/100\ keV)$ and $y = \ln(E_\gamma/1000keV)$. A, B and C describe the efficiency at low energies, D, E and F at high energies, and G is an interaction parameter between the two regions defining the sharpness of the turnover region. Since the photo-peak

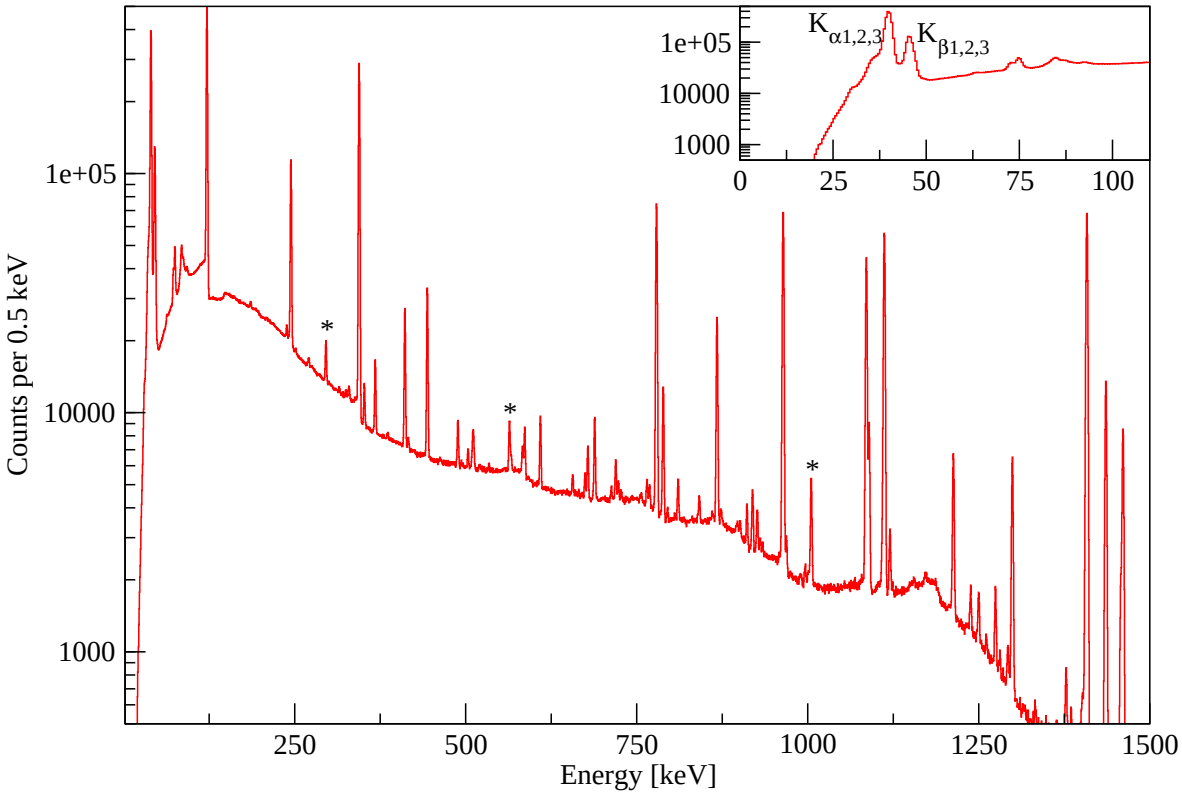

Figure 3.12: The γ-ray energy spectrum of ^{152}Eu measured in EURICA. The asterisks represent background peaks from the environment. .

reconstruction of the add-back procedure enhances the efficiency, this shall be used in the data analysis presented later.

3.4.3 Fast-timing configuration

The capability to measure lifetimes of excited states in the nanosecond regime gives access to detailed nuclear structure information. In this experiment such capability was provided by the use of a $LaBr_3(Ce)$ array used in conjunction with plastic scintillators. The BC-148 plastic scintillators, (hereafter referred to as "β-plastics") previously mentioned in Sec. 3.4.1, provide a more precise timing measurement of β-electron detection than WAS3ABi ($\sigma \approx 300$ ns). Similarly, the $LaBr_3(Ce)$ array provides a better time resolution than that of EURICA, at the expense of energy resolution.

β-plastics

The β-plastics are positioned 1 mm upstream and downstream of the first and last DSSSD of the WAS3ABi array and have dimensions 45$\times$ 65$\times$ 2 mm^3, see Figs. 3.16 and 3.6a. Each β-plastic is optically coupled to two PMTs, designated "left" and "right"

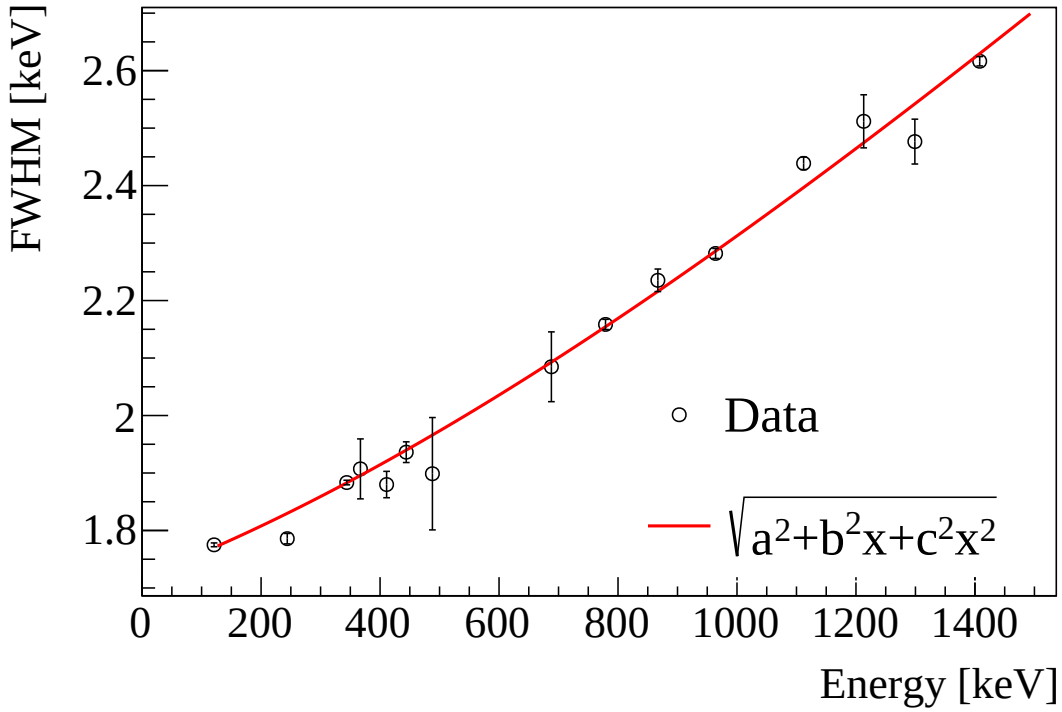

Figure 3.13: Values of FWHM as a function of energy where the data is taken from the spectrum in Fig. 3.12 and the red line represents a fit function, given as an inset, to the data points.

when looking in the downstream direction. The positions of the β-plastics with respect to the $LaBr_3$(Ce) array and WAS3ABi are shown in Fig. 3.18b.

To enable better differentiation between an ion and β-electron detection, the PMTs were connected to high- and low-gain analogue-to-digital converter (ADC). As with the F3 and F7 TOF detectors, to negate position dependent timing effects, the average of the timing signals of the β-plastics are used to measure the electron detection time,

$$T_\beta = \frac{T_{\beta L} + T_{\beta R}}{2}, \tag{3.11}$$

where $T_{\beta L,R}$ are the times measured in the left and right PMTs with respect to the trigger signal.

The different distances of the WAS3ABi DSSSD layers with respect to the β-plastics implies that the electron detection efficiency by the β-plastics shall depend onto which layer the ion implants. To properly characterise this, comparison is made between the number of detected β-decay events in a WAS3ABi layer alone, and the number of

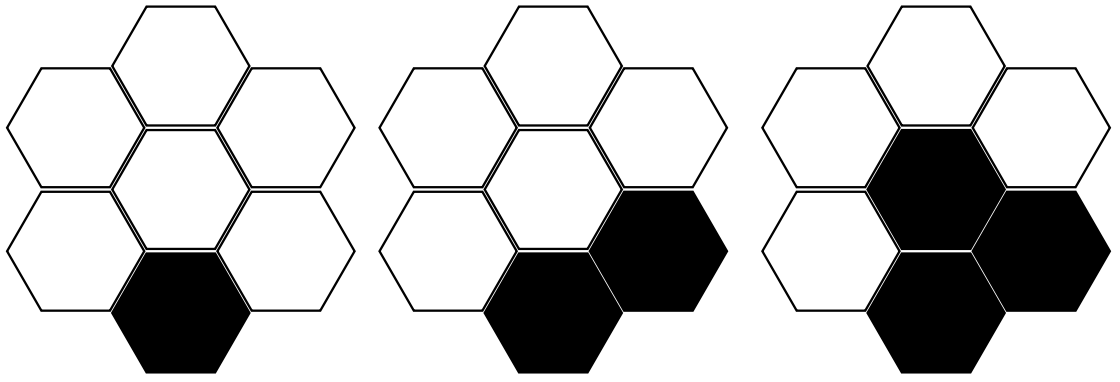

(a) **Single accepted.** (b) **Both summed.** (c) **All summed.**

(d) **All summed.** (e) **Two single events recorded** (f) **Adjacent hits summed and a single event**

Figure 3.14: The possible coincident hit-patterns within the Clusters and actions taken when they arise.

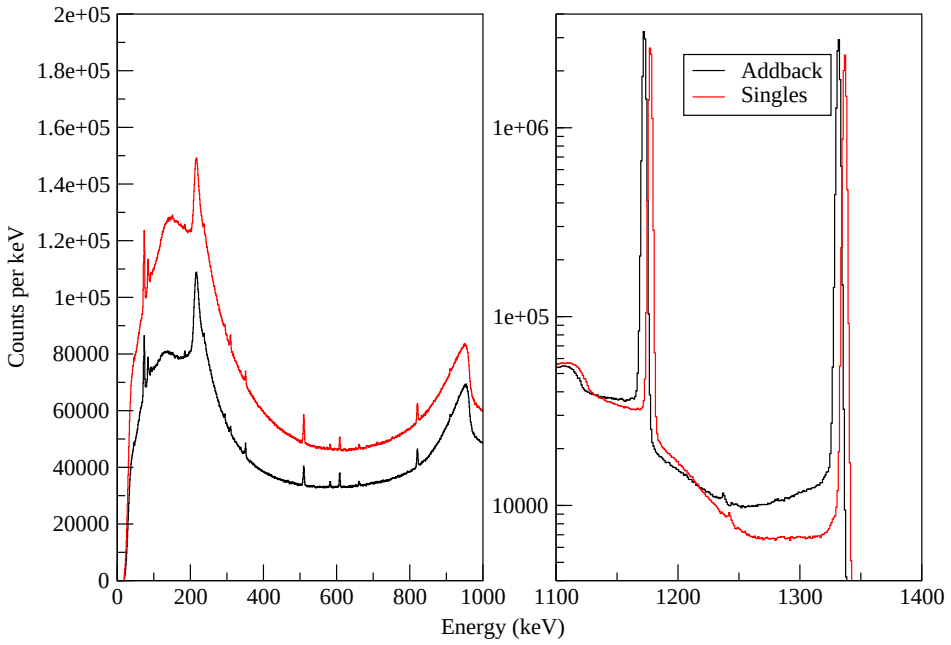

Figure 3.15: The left panel shows the Compton background resulting from the 1173- and 1332-keV transitions, note the significant suppression in background when the addback is applied. The right panel shows the 1173- and 1332-keV transitions, the background reduction caused by the addback algorithm is apparent. The singles spectrum of the right figure is offset by +5 keV in order for a better comparison to be made.

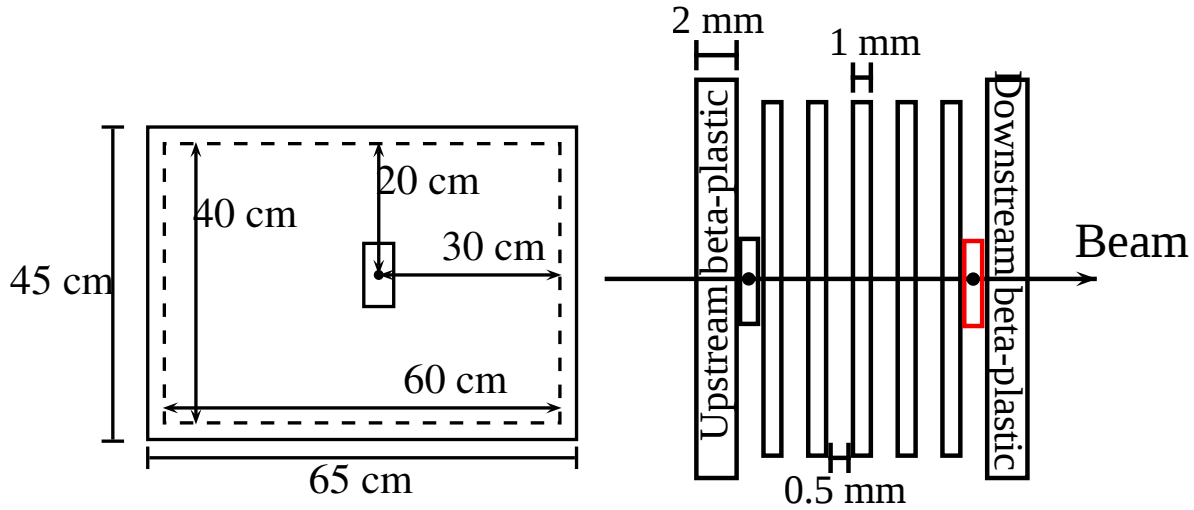

(a) The stopper array as viewed from downstream. The dashed lines represent WAS3ABi behind the upstream β-plastic, which is shown by the solid line. The beam axis and source position are denoted by the central black dot.

(b) Profile view of the stopper array, where the beam axis is labelled. The source capsule positions are represented by a black and red rectangle, with the dot inside representing the position of the source pellet.

Figure 3.16: Diagrams showing the positions of the calibration sources used for the efficiency calibration of EURICA, see text for details.

events in coincidence with an electron detection in the β-plastic also. In order to fully qualify as a β-electron detection in the β-plastics, there must be a good signal in the

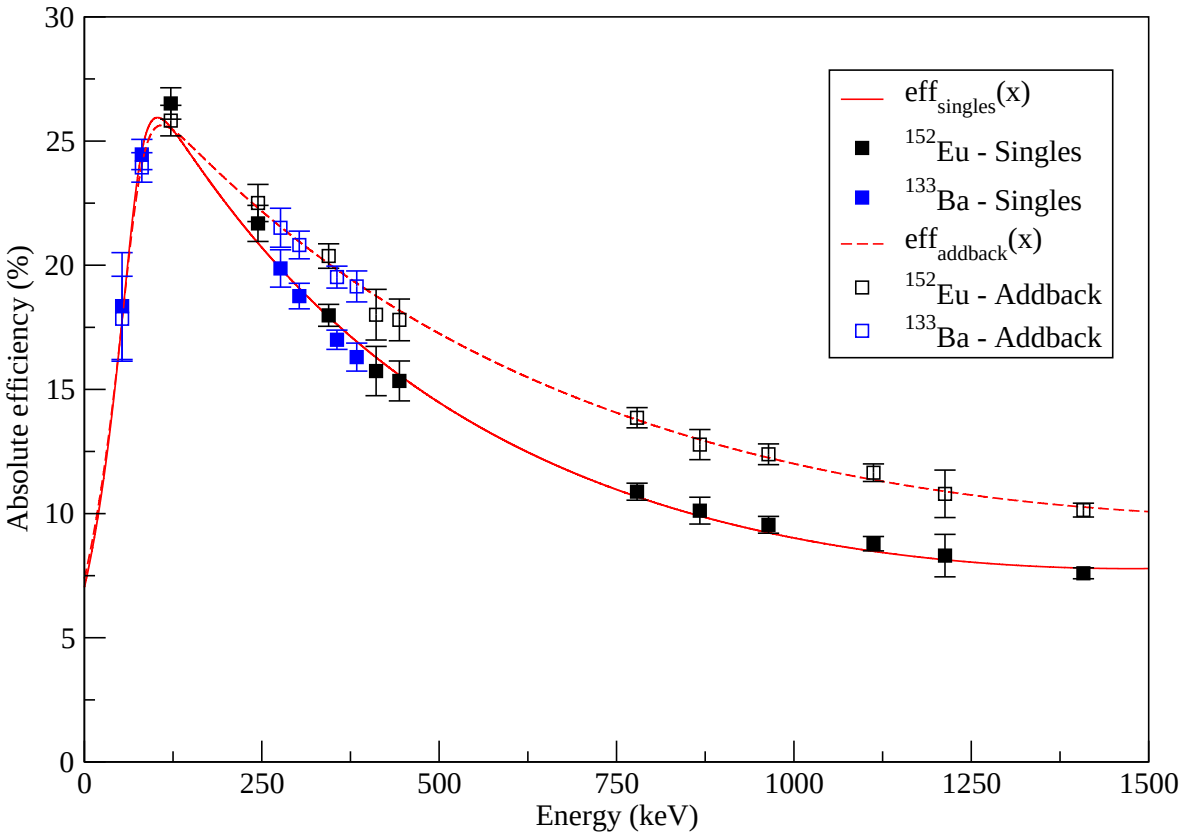

Figure 3.17: The absolute efficiency curve of the EURICA Cluster detectors for singles (solid line) and add-back (dashed). The gain in efficiency of add-back is demonstrated. The curves are fitted to Eq. 3.10.

ADC and TDC of both left and right PMT. The results of the efficiency measurement are shown in Fig.3.19, note that since the last DSSSD layer was operated in a low-gain mode, it was not included.

Lanthanum bromide array

The $LaBr_3(Ce)$ array comprised 18 38.1⌀× 50.8 mm crystals of which 17 were functioning during the experiment. Each crystal was surrounded by a 5 mm thick cylindrical lead shield, to act as a passive anti-Compton shield for scattered γ rays, these are clearly shown in Fig. 3.18c. The detectors were arranged into three arrays of six. The arrays were orientated perpendicular to the beam axis and at azimuthal angles of 126°, 198° and 270°, where the direction to the left of the beam direction in the horizontal plane represents 0^0. Their distances with respect to the centre of WAS3ABi, the angles of their support frames with respect to the beam axis and operational voltages of their respective PMTs can be found in Tab. 3.3.

The energy calibration of the $LaBr_3(Ce)$ array were carried out using ^{152}Eu and ^{60}Co

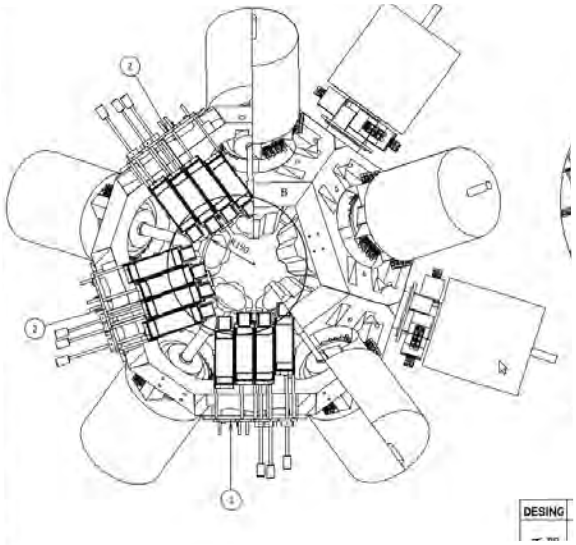

(a) A schematic of the array from Ref. [80], with the beam direction out of the paper. Those assemblies labelled with a 2 are the $LaBr_3$ (Ce) arrays, whilst the other positions are filled with the Cluster detectors

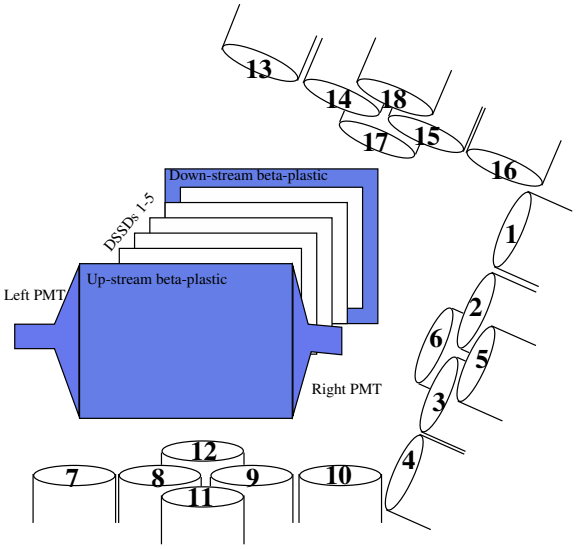

(b) A representation of the fast-timing configuration with the $LaBr_3$(Ce) detectors indexed. The beam-direction goes into the page.

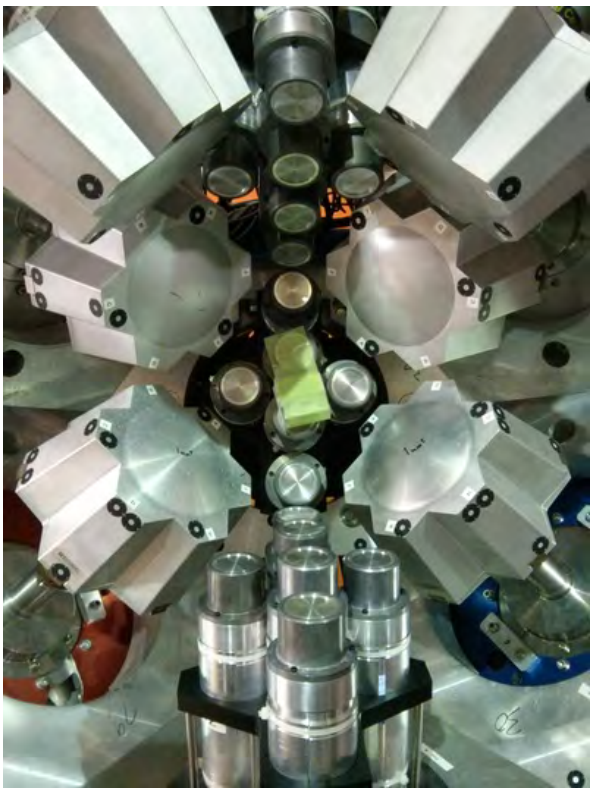

(c) A view of the right hemisphere of EURICA, when looking downstream, showing the arrangement of the $LaBr_3$ (Ce) detectors with respect to the Cluster detectors. The beam direction goes from right to left.

Figure 3.18: Various representations of the $LaBr_3$(Ce) array. See text for details.

Det. number	θ (°)	ϕ (°)	Distance (mm)	Applied High-voltage (V)
1	90	198	280	1300
2	90	198	240	1350
3	90	198	240	1300
4	90	198	280	1450
5	90	198	245	1400
6*	90	198	245	1300
7	90	126	280	1450
8	90	126	235	1300
9	90	126	235	1350
10	90	126	240	1350
11	90	126	240	1400
12	90	126	245	1450
13	90	270	280	1300
14	90	270	250	1350
15	90	270	255	1400
16	90	270	280	1350
17	90	270	280	1400
18	90	270	280	1400

Table 3.3: The angles, distances, and PMT operating voltages of the $LaBr_3$ (Ce) detectors used during the experiment. "Distance" refers to the distance from the face of the detector to the central point of the WAS3ABi detector. The angles, θ and ϕ, refer to the support structures of the arrays. The asterisk indicates the detector which was not operating correctly.

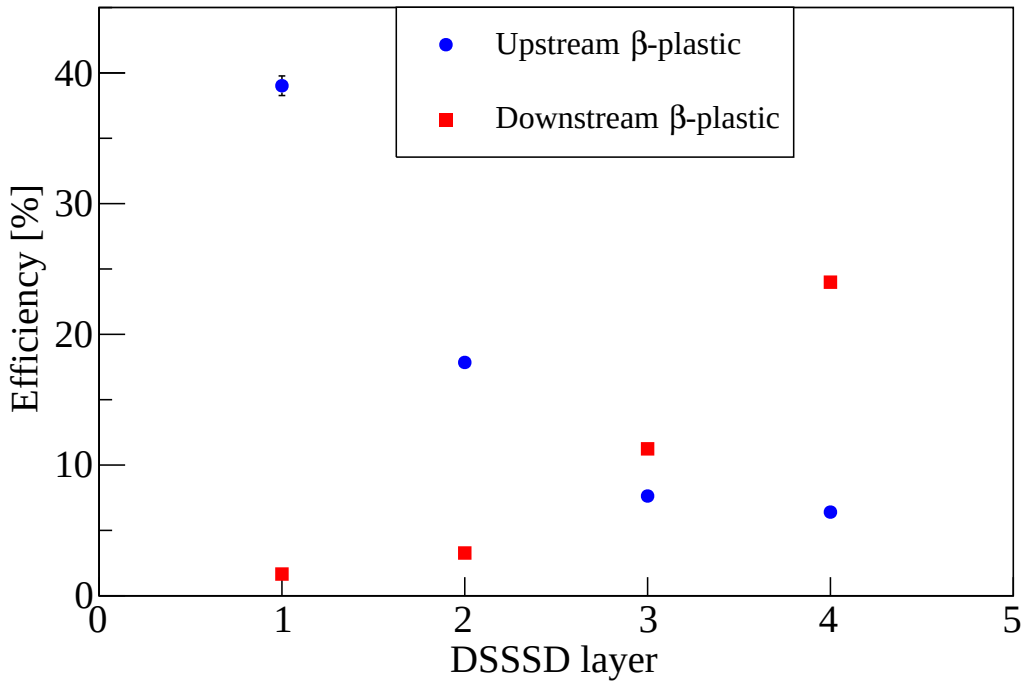

Figure 3.19: The β detection efficiency of the β-plastic detectors as a function of DSSSD layer. The layers are numbered starting with the most downstream.

sources placed at a central position with respect to WAS3ABi, shown in Fig. 3.16. The comparatively poor resolution of the $LaBr_3$(Ce) detectors means that only the 122-, 242- and 341-keV peaks could be resolved, this is demonstrated in Figs. 3.20, which also shows the backgrounds created by radioactive ^{138}La isotope. For higher energy characterisation, a ^{60}Co source was used, the spectrum for this is shown in Fig. 3.21.

Timing calibration of β-γ time spectra

The measurement of the lifetimes of states populated through the β-decay of nuclei implanted into WAS3ABi were taken between the β-plastics, positioned upstream and downstream of WAS3ABi, and the $LaBr_3$(Ce) detectors. The TDC of each $LaBr_3$(Ce) detector PMT was calibrated using pulses generated from a time calibrator where the pulses were 100 ps apart, as shown in Fig. 3.22a. The differences between the pulses, where the pulse at channel ~225 was considered $T = 0$, were plotted against the channel and a straight-line fit was performed, as shown in Fig. 3.22b, giving the channel-to-ns conversion coefficients.

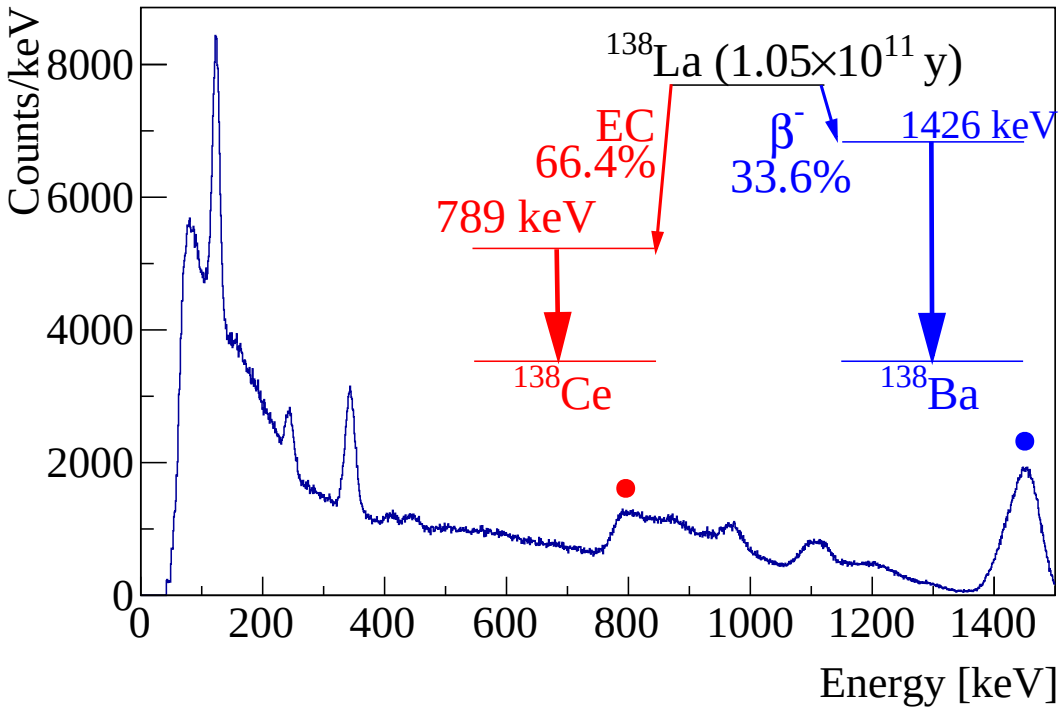

Figure 3.20: The γ-ray energy spectrum of ^{152}Eu measured in the $LaBr_3$(Ce) array. The red and blue circles represent the backgrounds generated by their respective colours shown in the inset decay scheme of ^{138}La.

3.5 Data acquisition

There are three separate data acquisition systems relating to BigRIPS, WAS3ABi and the γ-ray detection array readouts. Details of the WAS3ABi and γ-ray branch are described here, as is the trigger system. The description of the acquisition system of BigRIPS [81] is beyond the scope of this work.

3.5.1 Triggers

There are two types of event that initiate data taking, the first is a fragment's implantation, and the second its subsequent β-decay. The former is initiated by the F11 trigger, and the latter by a usable signal in WAS3ABi. There are some cases when it is not convenient to request an acquisition window, such as when the electronics are already acquiring, processing, or transferring data. In these cases the trigger is suppressed, giving rise to *requested* and *accepted* triggers. The accepted-rejected decision is made by the VMEbus Universal Logic Module, Virtex 4 (VULOM4) [82], which takes

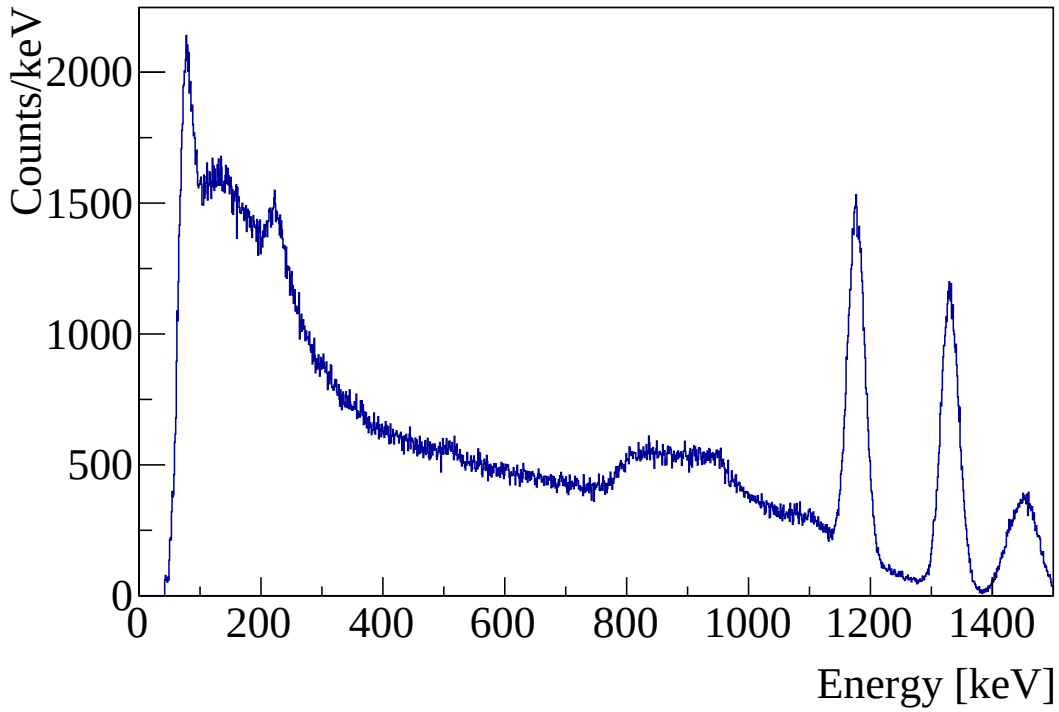

Figure 3.21: The γ-ray energy spectrum of ^{60}Co measured in the $LaBr_3$(Ce) array.

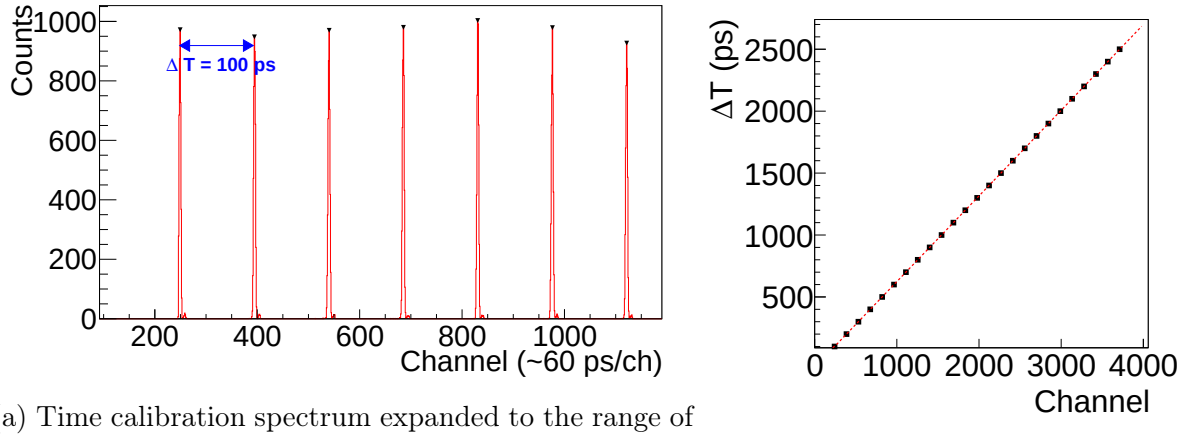

(a) Time calibration spectrum expanded to the range of 100<channel<2000.

(b) Result of linear fit.

Figure 3.22: Sample spectra of calibration from TDC channel to time.

inputs from the TRIVA7 (master) and TRIVA5 (slave) modules, to ascertain whether the on-rack read-out modules are busy. In addition, the TRIVA modules provide start suppression to the TDCs in case the read-out modules are busy [83]. The trigger system is shown schematically in Fig. 3.23.

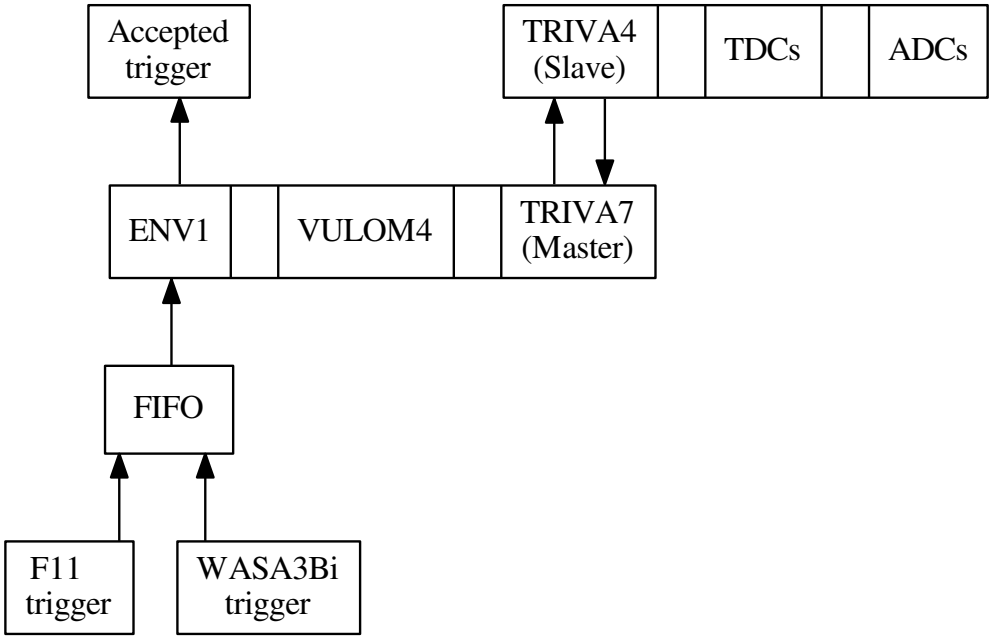

Figure 3.23: Schematic of the trigger scheme, see text for details.

3.5.2 WAS3ABi

The WAS3ABi detector is sensitive to two types of events, fragment implantation and their subsequent β-decay. The implantation case requires a coincidence between a signal from the F11 plastic scintillator and a signal in a WAS3ABi ADC channel from the x-strips exceeds a threshold value. The requirement of a β-decay-like event is that a signal in both the x- and y-strips are measured above a threshold [84]. The electronic readout scheme of WAS3ABi is shown in Fig. 3.24.

3.5.3 EURICA array

The EURICA acquisition consists of two separate branches, for the processing digital and analogue signals. The digital branch provides signals to the XIA Digital Gamma Finder (DGF) modules [85], which provide signal amplification, processing of energy and time signals, and readout functions. The analogue branch provides signals to a set of timing filter amplifiers (TFAs) which provide the input of digital constant fraction discriminators (CFDs), such a configuration provides a higher digital timing resolution

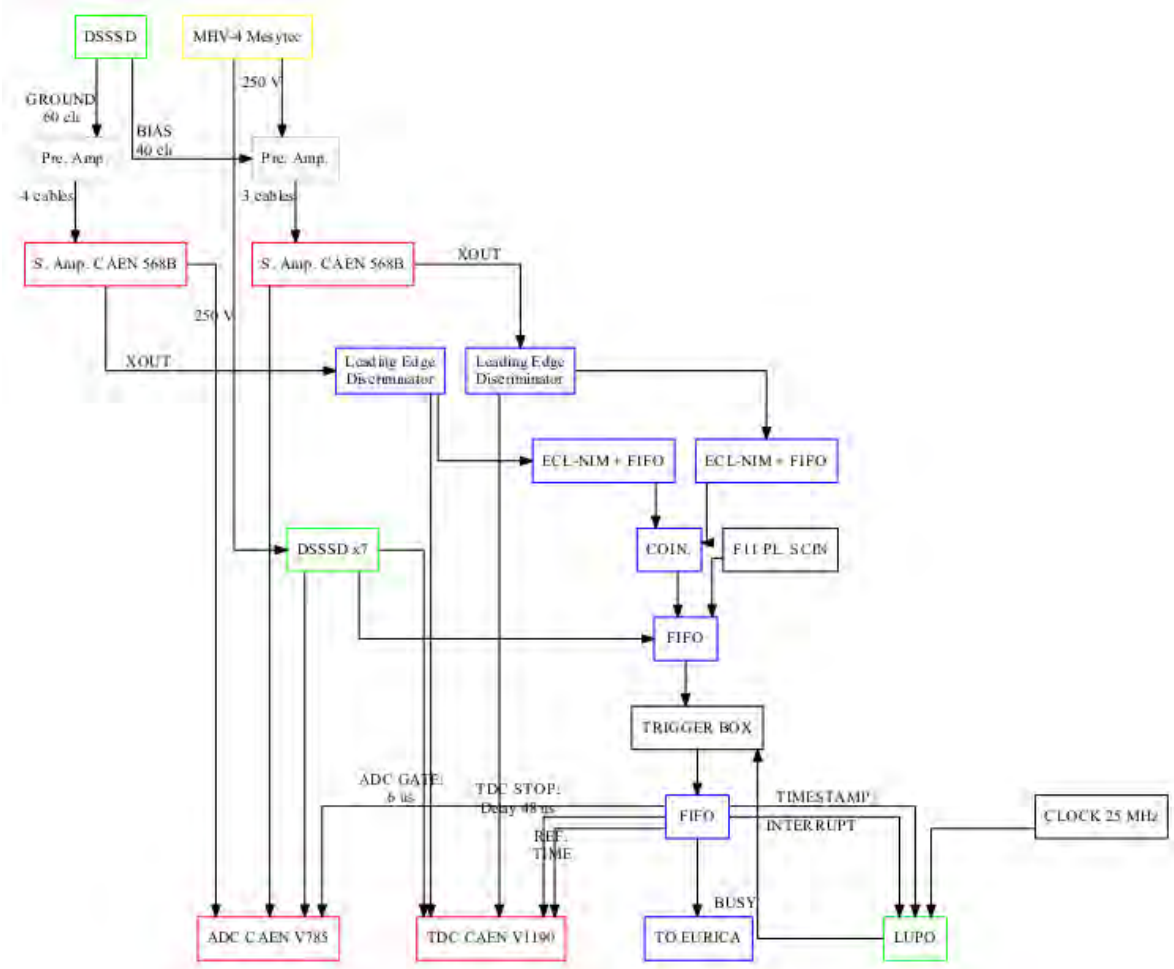

Figure 3.24: Electronic readout scheme for WAS3ABi. Taken from Ref. [84].

than is achievable with the DGF branch. The signal from the CFDs is sent to long- and short-range TDCs, with dynamic ranges of 800 μs at 0.73 ns/channel and 1.2 μs at 0.31 ns/channel, respectively. The timing of the DGF modules and the long-range TDCs are operated in a common start mode, where the trigger initiates the timing in all modules which is stopped by a γ-ray measurement. Whereas the short-range TDCs are operated in a common stop mode, where the time is started by the detection of a γ ray and is stopped by a delayed trigger signal. The electronic readout scheme for EURICA is shown in Fig. 3.25.

3.5.4 $LaBr_3$ (Ce) array

The electronic readout system of the $LaBr_3$(Ce) array has separate branches for time and energy. Unlike the EURICA branches, in which identical signals are sent to both branches, the branches for the $LaBr_3$(Ce) are distinct. The distinction arises from

the anode and dynode signals of the PMT being different, with the anode providing the timing signal and the dynode the energy signal. Due to the short-lived nature of the states that the $LaBr_3$(Ce) detectors are to observe, the acquisition window is 20 μs after the trigger, allowing for a finer digital resolution of the TDCs. The energy signals of the $LaBr_3$(Ce) are amplified by CAEN Mod. N568B spectroscopy amplifiers, which feed CAEN V785 ADCs. The signal provided by the anode is sufficiently strong to not require amplification, it is directly fed into an Ortec 935 CFD. The time signal is sent to short-range (CAEN V767) and long-range (CAEN V1190A) TDCs, with ranges of 250 ns at 16.4 ns/bin and 20 μs at 0.038 ns/bin, respectively. The start of the short-range TDC is provided by a γ-ray detection in the $LaBr_3$(Ce) detectors and stopped by a signal in the β plastics. The start of the long-range TDC is provided by an accepted trigger, and stopped by a γ-ray detection. The schematic of the electronics for the $LaBr_3$(Ce) array is shown in Fig. 3.26

3.6 Signal correlation

The synchronisation of the signals produced by the data-acquisition systems for BigRIPS, WAS3ABi and γ-ray detectors is achieved through the matching of timestamps, which are provided by a 25 MHz external clock. In order for an event measured in the three separate systems to be merged, the timestamp of each must be within $\approx$150 ns of each other.

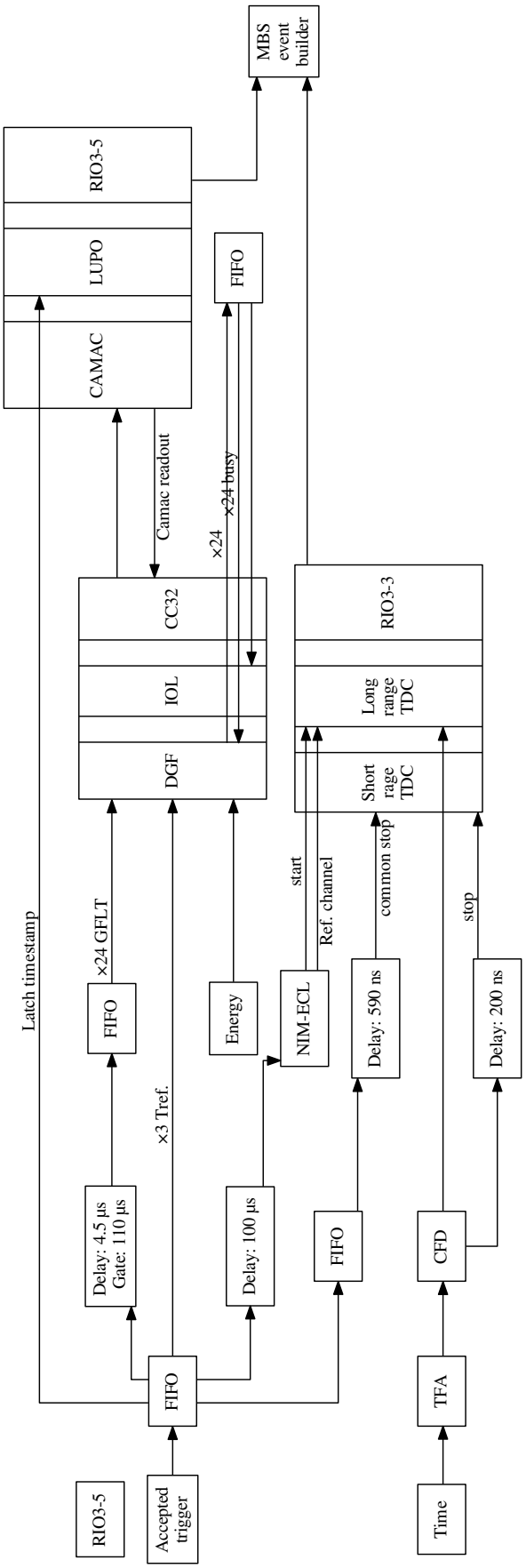

Figure 3.25: Electronic readout scheme for EURICA.

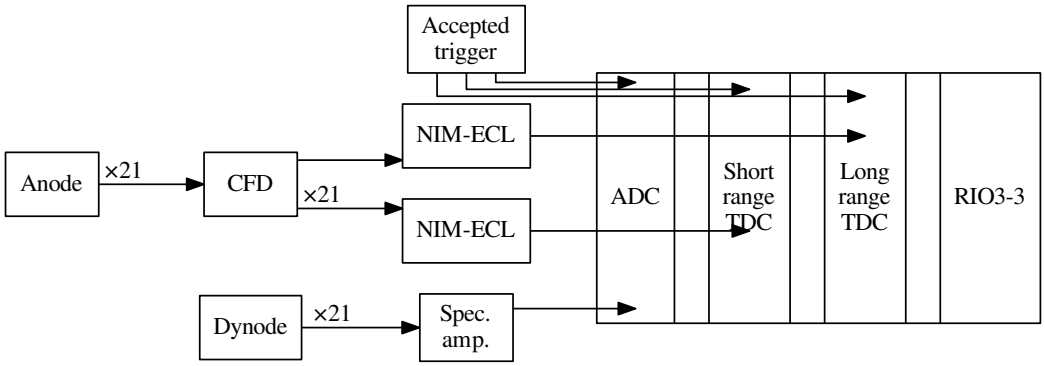

Figure 3.26: Electronic readout scheme for the $LaBr_3(Ce)$ array.

Chapter 4

Data analysis

The analysis of the data collected for the investigation can, broadly speaking, be sub-divided into the three major tasks: identification of ions in BigRIPS, detecting the ions' implantation and β-decay positions in WAS3ABi, and the detection of β-delayed and isomeric γ rays. The latter is further divided according to the analysis of γ rays detected in EURICA and those detected in the $LaBr_3(Ce)$ array. Detailed in this section are the procedures carried out on the data in order to produce high-quality spectra.

4.1 Particle identification

The detectors responsible for particle identification (PID) and their operational principles were introduced in Sec. 3.3. Detailed here are the analysis procedures carried out to obtain a preliminary PID, followed by the use of correlations between the various detectors to increase the resolution of the mass-to-charge ratio, as well as the removal of background events.

4.1.1 Determination of atomic number

Although the measurement of atomic number, Z, occurs at the final focal plane, F11, of BigRIPS it is convenient to determine this value first since it is necessary for the A/Q measurement. As stated in Sec. 3.3, the energy-loss, ΔE, of an ion passing through the TEGIC depends on its atomic number. By expressing the ion velocities in

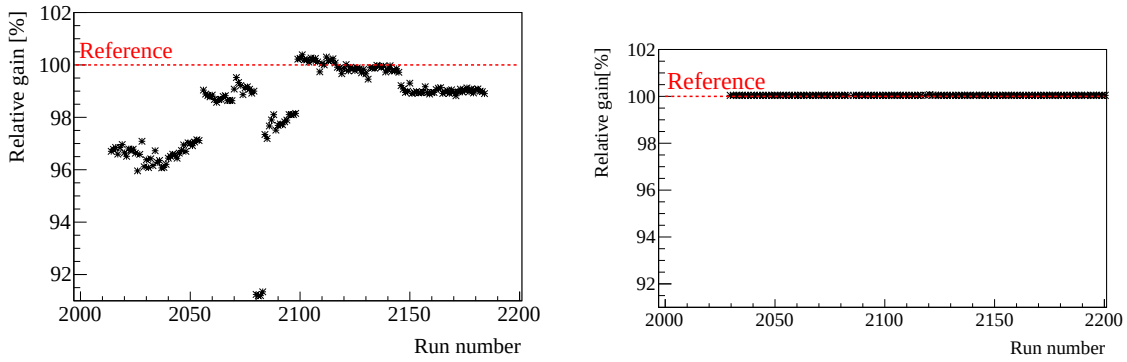

Figure 4.1: (Left) The gain-shift of the TEGIC as a function of run number, measured with respect to run #2111 (shown as the dashed red-line). (Right) The result of the gain-shift correction.

Eq. 3.3 in terms of $\beta(= v/c)$, letting $Q = Z$, and combining constants we get,

$$Z = a_1 \cdot \beta \sqrt{\frac{\Delta E}{\ln(b \cdot \beta^2) - \ln(1 - \beta^2) - \beta^2}} + a_2. \tag{4.1}$$

Since there is no material along the beam-line past F7, the β is measured between the F5 and F7 focal planes. The parameter b represents $(2m_e c^2)/I$, where I is provided as a design value of the TEGIC, $I = 4866\ m_e c^2$.

To improve the resolution of the energy-loss spectrum, a correction is applied to counteract the gain-drift effects due to the varying temperature of the fill gas of the ionisation chamber. This effect is shown as a function of run number in the left plot of Fig. 4.1, where the gains are measured with respect to that of run #2111 (red dashed line). The energy-loss spectra were then corrected against the TOF measurement through their correlation depicted in Fig. 4.2a and calibrated using calibration coefficients determined from the ATIMA code [86]. The projection of the energy-loss is then performed to produce a spectrum such as that shown in Fig. 4.2b.

To assign the $Z = 40$ value to the correct peak of the energy-loss spectrum of Fig. 4.2b, a gate was imposed on each peak and the resultant γ-ray spectrum measured in EURICA was checked for the characteristic isomer decay of ^{108}Zr [12]. All other Z values were assigned relative to the Zr peak. With knowledge of the Z values, the calibration of a_1 and a_2 was made by a linear fit between Z vs. ΔE. A resolution of $\sigma(Z) = 0.155$ for the Zr peak is attained following the above procedure.

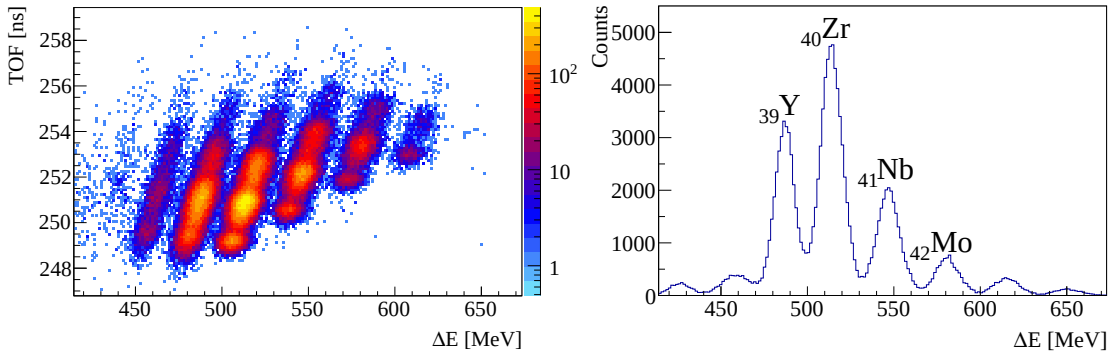

(a) (b)

Figure 4.2: (a) The correlation of energy loss measured in the TEGIC with the TOF of ions. Each slanting distribution relates to an element. (b) Spectrum of energy loss in the TEGIC for a single run (#2111). The peaks are labelled according to the elements they represent.

4.1.2 Determination of mass-to-charge ratio

The basic information required for mass-to-charge determination is given by Eq. 3.2. The measurements required from the beam-line detectors are the velocity of the particle and its bending radius in the dipole magnets. However, in order to properly define the ion's trajectory through the superconducting quadrupole triplets (STQs), consideration must be given to the ion-optics of the bending (dipoles) and focussing (STQs) magnets.

Trajectory reconstruction

The bending radius, ρ, is determined through the reconstruction of an ion's trajectory through the dipole magnets. Such reconstruction becomes non-trivial due to the focussing STQs located between the position sensitive parallel plate avalanche chamber (PPAC) detectors and the dipoles. The measurements taken from the PPACs ultimately give the entrance position of the ion to the STQs. From there the trajectory is reconstructed using transfer matrices which describe the magnetic fields inside the STQs.

The PPACs provide the entrance point to the STQs through means of a relatively simple tracking procedure. The angle a shown in Fig. 4.3 is computed and used to extrapolate the ion's trajectory, through a drift region (one where no magnetic field is

applied), into the entrance of the STQ. This angle is computed by,

$$a \;=\; \tan\left(\frac{x_1 - x_0}{\mathrm{d}z_1 - \mathrm{d}z_0}\right). \tag{4.2}$$

The distances between the focal plane (fpl, in Fig. 4.3) and the PPAC layers are given by design values, listed in Tab. 4.3, and the x- and y-positions[1] are given by Eqs. 3.6 and 3.7. It follows from Eq 4.2 and Fig. 4.3 that the position of the ion at the focal plane will be given by,

$$x_{\mathrm{fpl}} \;=\; \mathrm{d}z_0 \tan(a) + x_0. \tag{4.3}$$

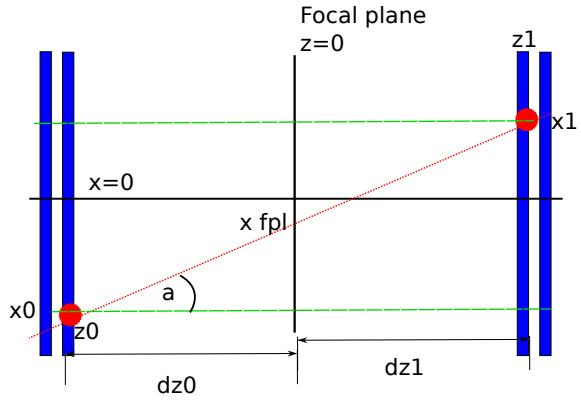

Figure 4.3: A view from above of the principle of PPAC position calculations. Each blue rectangle represents a PPAC. The interaction positions of the ions are given by $x_{0,1}$ and the distances from the interaction positions to the focal plane are given by $dz_{0,1}$. The ion path is exaggerated to elucidate the measurements of interest.

The total of the times for each end of the cathode wires to provide a signal, $T_{\mathrm{sum}} = T_{x1,y1} + T_{x2,y2}$ from Eqs. 3.6, should be a constant limited to the total length of the cathode electrodes and the delay-lines, this is shown as the peak at $T_{\mathrm{sum}} \approx 100$ in Fig. 4.4. The tail-component of the distribution would, therefore, indicate signals travelling at superluminal speeds, however, their origin is from multiple hits of cathode wires from δ rays and particles that fragment during transit through BigRIPS. The removal of such events was achieved by imposing the condition that the T_{sum} should be within the limits of the peak, shown in Fig. 4.4 as the red lines. If events from both layers of a PPAC are within the condition, then the average of the x and dz positions are used, if only one layer of each then PPAC are used, then the measured values are used directly.

[1]For the purposes of the identification carried out here only the x position is used.

Chamber	Index	Cathode	Length (mm)	dz_0
F3	4	X	240	-18.7
		Y	150	-10.1
	5	X	240	10.1
		Y	150	18.7
	6	X	150	871.3
		Y	150	879.9
	7	X	150	908.7
		Y	150	900.1
F5	10	X	240	-418.7
		Y	150	-410.1
	11	X	240	-381.3
		Y	150	-389.9
	12	X	240	231.3
		Y	150	239.9
	13	X	240	268.7
		Y	150	260.1
F7	14	X	240	-868.7
		Y	150	-860.1
	15	X	240	-831.3
		Y	150	-839.9
	16	X	150	76.3
		Y	150	84.3
	17	X	150	113.7
		Y	150	105.1

Table 4.1: Summary of PPAC properties with their index, length of the cathode wires and the design values used for their distance from their respective focal planes. Note that the F3 focal plane position appears to be between the first set of PPACs.

Upon determining the position-vectors of ions at the focal planes either side of a dipole from the PPACs, it is necessary to operate on them with a *transfer matrix*, since the ions' route through the STQs and dipoles is not direct. This matrix contains the solutions to a series of Taylor expansions which pertain to the magnetic field maps of the STQs and dipoles. A schematic of the quantities of the position vector is shown in Fig. 4.5, where the angles a and b are measured with respect to a particle following the central trajectory. Symbolically, the transfer matrix between focal planes F3 and F5 acting on the position vector of focal plane F3, to create the position vector at focal

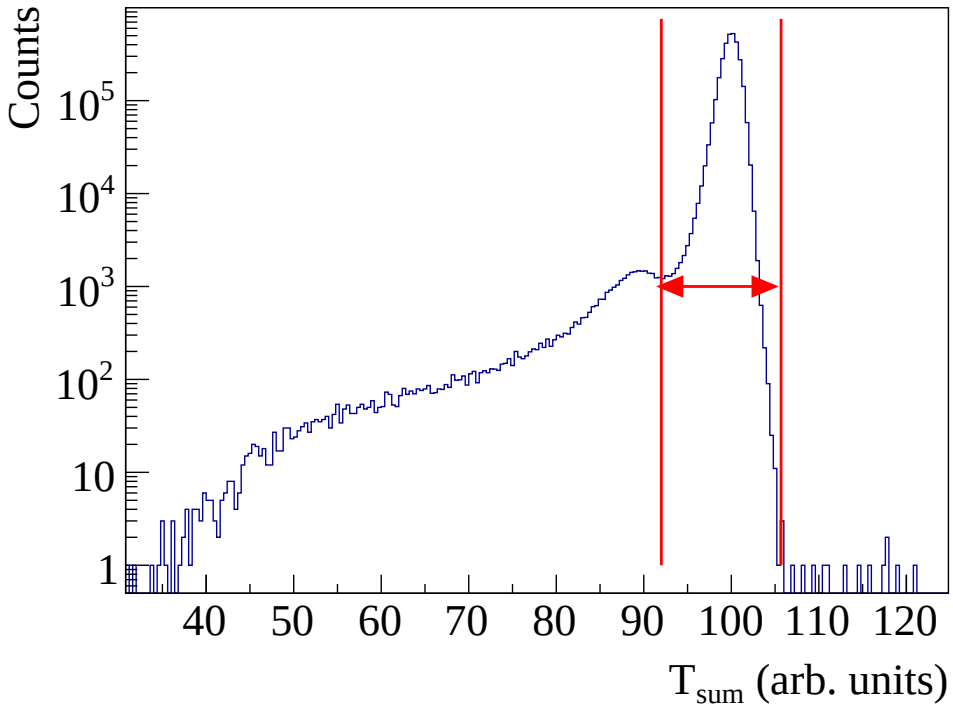

Figure 4.4: Spectrum of T_{sum} from an arbitrary PPAC. The solid red lines indicate the condition to use to reject background events.

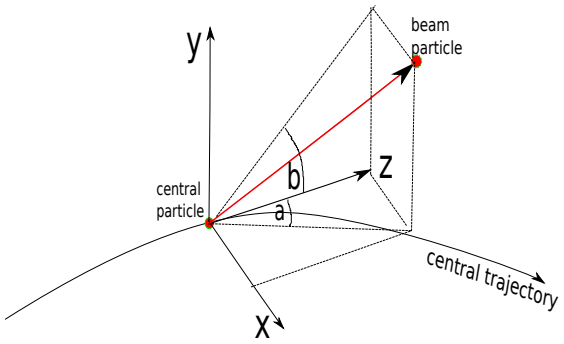

Figure 4.5: Schematic of the coordinate system used in the transport formalism.

plane F5 is given by,

$$\begin{pmatrix} x_5 \\ a_5 \\ y_5 \\ b_5 \\ l_5 \\ \delta \end{pmatrix} = \begin{pmatrix} (x|x) & (x|a) & (x|y)* & (x|b)* & (x|l)* & (x|\delta) \\ (a|x) & (a|a) & (a|y)* & (a|b)* & (a|l)* & (a|\delta) \\ (y|x)* & (y|a)* & (y|y) & (y|b) & (y|l)* & (y|\delta)* \\ (b|x)* & (b|a)* & (b|y) & (b|b) & (b|l)* & (b|\delta)* \\ (l|x)* & (l|a)* & (l|y)* & (l|b)* & (l|l) & (l|\delta) \\ (\delta|x)* & (\delta|a)* & (\delta|y)* & (\delta|b)* & (\delta|l)* & (\delta|\delta) \end{pmatrix} \begin{pmatrix} x_3 \\ a_3 \\ y_3 \\ b_3 \\ l_3 \\ \delta \end{pmatrix}, \tag{4.4}$$

where x, y, a, and b are depicted in Fig. 4.5 and are determined by the PPACs, l is the length difference between the central and beam particle trajectories and δ is the deviation of an ion's $B\rho$ value from that of the central value, $B\rho_0$ [87]. In the following paragraph it shall be made apparent that the value of δ is the term needed for correct A/Q determination. All terms marked with an asterisk are equal to zero assuming mid-plane symmetry, time-independence and no energy-loss.

For the horizontal plane, which is most important for mass-to-charge determination, it follows from Eq. 4.4 that,

$$x_5 \;=\; (x|x)x_3 + (x|a)a_3 + (x|\delta)\delta, \tag{4.5}$$

where

$(x|x)$ is the magnification between F3 and F5,

$(x|a)$ is the angular dependence of the trajectory, and should be zero if the focussing condition is realised

$(x|\delta)$, is the momentum dispersion,

and are calculated using the COSY INFINITY code [88].

The magnetic rigidity, $B\rho$, of an ion is calculated with respect to that of an ion travelling on the central trajectory, denoted as $B\rho_0$ [87]. The magnetic rigidity of all other ions are measured with respect to the central value with the momentum dispersion of Eq. 4.4,

$$B\rho \;=\; (1+\delta)\, B\rho_0, \tag{4.6}$$

which in combination with Eq. 4.5 gives,

$$B\rho \;=\; \left(1 + \frac{x_5 - (x|x)x_3 - (x|a)a_3}{(x|\delta)}\right) B\rho_0, \tag{4.7}$$

this is then substituted into Eq. 3.2 to give,

$$\frac{A}{Q} \;=\; \frac{1 + \left(\frac{x_5 - (x|x)x_3 - (x|a)a_3}{(x|\delta)}\right) B\rho_0}{\beta\gamma uc}, \tag{4.8}$$

for measurements between the F3 and F5 focal planes, the same procedure is carried out between the F5 and F7 focal planes. From the two results an average is taken of the mass-to-charge values.

4.1.3 Empirical enhancement of A/Q resolution

As an ion passes through BigRIPS, its mass-to-charge ratio will remain constant provided it undergoes no reaction with the beam-line components. After a reaction, the change of the mass-to-charge ratio will be discrete, consequently, any continuous changes in A/Q can be ascribed to the responses of the various beam-line detectors which provide its measurement.

According to Eq. 3.3 the energy deposited in a material by an ion of the same charge and velocity will be constant. As such, the energy deposited in the scintillators, ΔE, gives a rudimentary measurement of mass and charge. It is therefore useful to compare the energy signals of the plastic scintillators at F3 and F7 with the measured mass-to-charge ratio. The integrated charge signals measured in the left and right PMTs of the plastic scintillators are denoted by q_L and q_R, respectively, and their product gives the energy deposited in the scintillator by the ion in arbitrary units. For a given A/Q, $\Delta E^{1/2}$ measured in the scintillators, since ΔE is related to Z^2, should remain constant. Therefore, any deviation shall be attributed to slewing effects of the detectors responsible for the measurement of A/Q. The left plot of Fig. 4.6 shows $\Delta E^{1/2}$ measured in the F3 plastic scintillator versus the mass-to-charge ratio obtained from the method given in Sec. 4.1.2, the "slew" is evident and can be empirically corrected for. Since the A/Q ratio of Fig. 4.6 shows only a linear dependence on the energy deposited, a first order correction is applied by,

$$\frac{A}{Q} = \frac{A}{Q}_{raw} - 0.000105 \times \sqrt{q_{F3L} q_{F3R}}, \tag{4.9}$$

where the factor, -0.000105, was determined through an iterative scan to obtain the best A/Q resolution. The same procedure was applied to the F7 scintillator, however, as evident in the left plot of Fig. 4.7, the relation between $\sqrt{q_L q_R}$ and A/Q was of a higher order than in the case of the F3 scintillator. A second order term was sufficient to produce a constant A/Q for a given distribution, as shown in the right plot of

Fig. 4.7. The total correction term is then given by,

$$\frac{A}{Q} = \frac{A}{Q}_{raw} - 0.000105 \times \sqrt{q_{F3L} q_{F3R}} + 0.0012 \times \sqrt{q_{F7L} q_{F7R}} - 40 \times 10^{-7} \times q_{F7L} q_{F7R}, \quad (4.10)$$

where the factors 0.0012 and 40×10^{-7} were again found by an iterative search to give the best A/Q resolution.

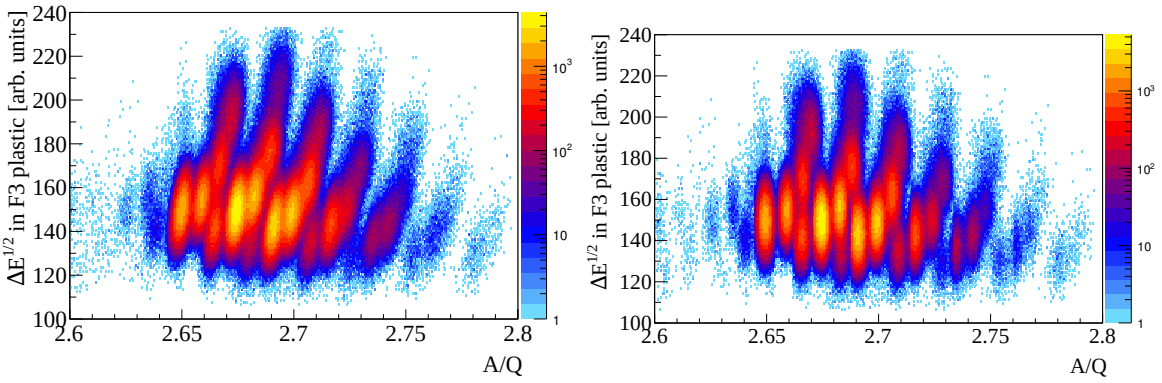

Figure 4.6: Figures depicting the relation of the geometric mean of the F3 plastic scintillator's integrated raw charge signals, against the uncorrected (left) and corrected (right) mass-to-charge ratios.

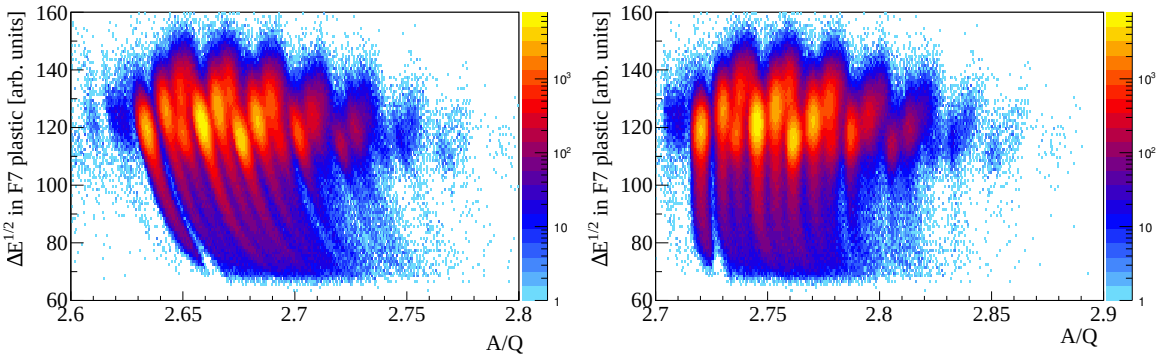

Figure 4.7: Relation of geometric mean of F7 plastic against the correction of A/Q with respect to F3 plastic only (left) and to both F3 and F7 plastics (right).

The improvement in quality of the mass-to-charge ratio is shown in Fig. 4.8 where the red line represents values obtained just from Eq. 4.8 and the blue line shows the values obtained with Eq. 4.10. The improvement is prominently displayed in the Z vs. A/Q plots shown in Figs. 4.12a (no corrections) and 4.12b (corrections applied). The original width of the mass-to-charge ratio for ^{108}Zr was $\sigma(A/Q) = 0.0021$ and the

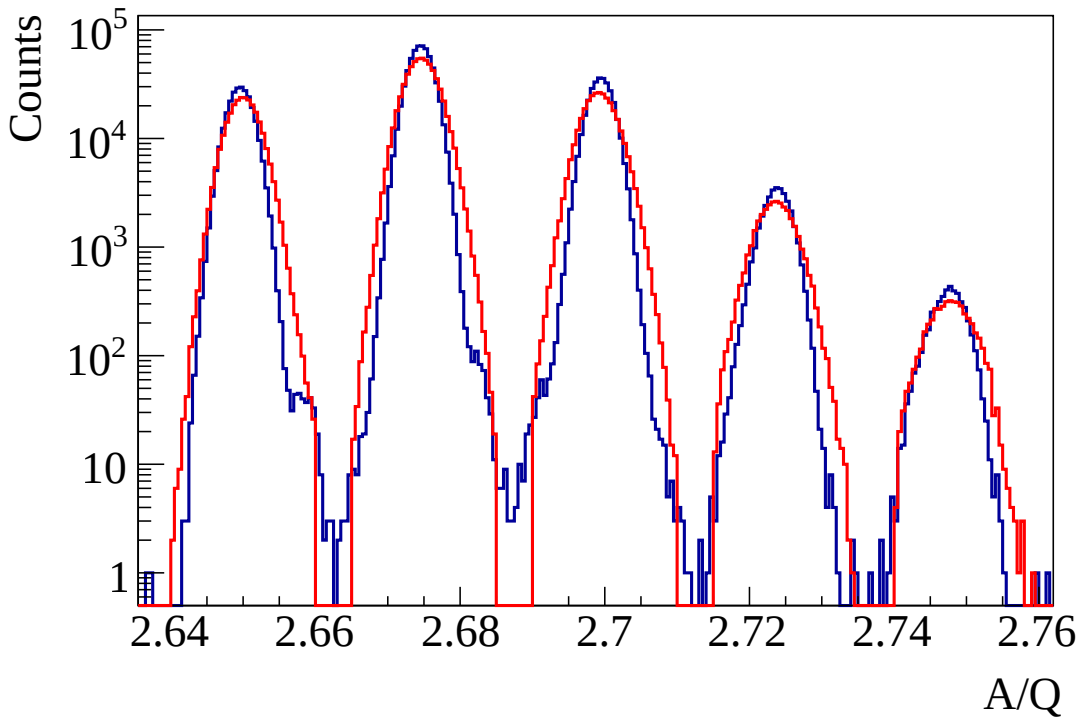

Figure 4.8: Mass-to-charge ratios of the zirconium isotopes. The red line shows the values obtained by only using Eq. 4.8, and the blue line shows the values corrected according to the measurements in the plastic scintillators at F3 and F7.

corrected value is $\sigma(A/Q) = 0.0016$.

4.1.4 Background removal

Whilst in transit through BigRIPS and ZDS, ions are liable to undergo nuclear reactions with the beam-line components, e.g. window entrances, or detector materials. The removal of such events can improve significantly the signal-to-background ratio observed in the PID plot. The correlations between beam-line detectors at different positions shall be used to include only the data which are consistent with ions that undergo no transmutation through BigRIPS.

In the first tranche of background removals, the concept of using the TOF detectors for energy measurements is revisited. It is expected that an ion, which has not undergone any form of reaction, or decay which changes its number of protons, would deposit the same amount of energy in a downstream detector as it would an upstream detector. Therefore, there should be a correlation between the magnitude of signals from energy-sensitive detectors through which the same ion passes. To observe these

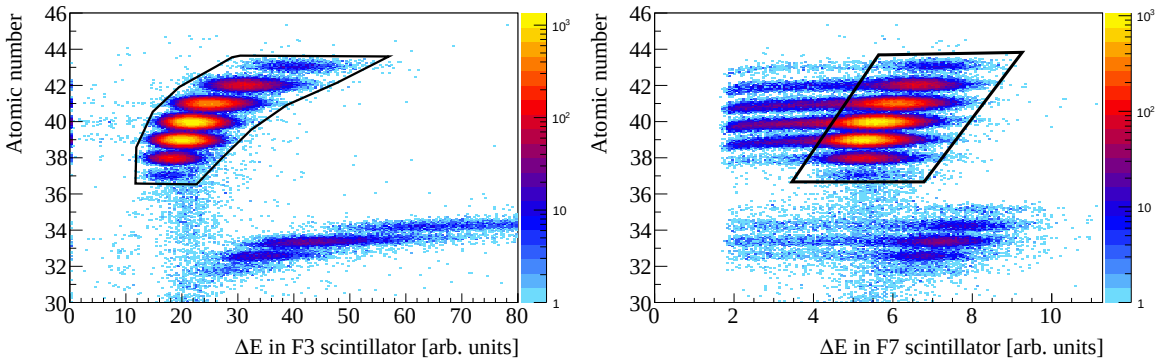

Figure 4.9: Plots show atomic number measured in the TEGIC versus the energy deposited in the F3 (left) and F7 (right) scintillators, the thick black lines show the cuts to reject inconsistent events.

correlations, a plot is made between the measured Z in the TEGIC and the energy deposited in each of the F3 and F7 scintillators, shown in the left (F3 plastic) and right (F7 plastic) of Fig. 4.9. The observed low-Z structures show inconsistent energy deposition between the scintillators and the TEGIC, as well as events relating to the incomplete charge collection in F7. Their rejection is achieved through applying the cuts depicted by the solid black lines in Fig. 4.9.

The beam profile, as measured by the angles at subsequent focal planes of BigRIPS, as defined in Fig. 4.3, provides another background rejection opportunity [87]. Figures 4.10a and 4.10b show the beam profile measured between F3 and F5, and F5 and F7, respectively. They show clear correlations for events which show a consistency of profile, as well as a few events which are not travelling the desired path through the spectrometer, meaning their identification will be erroneous. In order to reject the inconsistent events, the 2-dimensional plots of Figs. 4.10a and 4.10b are reduced to 1-dimensional spectra by the subtraction of the y-value from the x, as shown in Figs. 4.10c and 4.10d. The conditions shown by the red lines are then applied to reject those events not within the correct range of angle-difference distributions.

By the time the secondary beam has reached the F3 focal plane, its constituent nuclides have been sufficiently spatially separated to perform a rudimentary PID using only their x-position from the PPACs and the measured mass-to-charge ratio, this is shown in Fig. 4.11a. If a gate is applied to a known nuclide in this distribution, we can observe the corresponding distribution in the conventional PID plot (Z vs. A/Q).

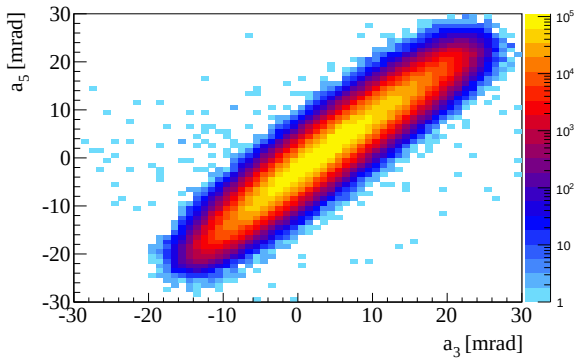

(a) Profile of beam between F3 and F5 measured with a_5 and a_3.

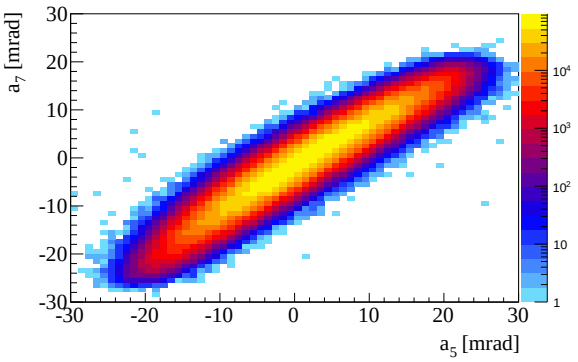

(b) Profile of beam between F5 and F7 measured with a_7 and a_5.

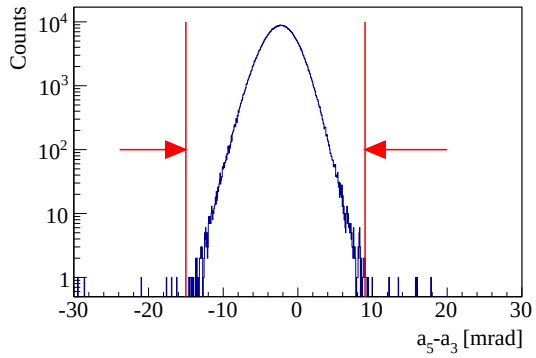

(c) One dimensional representation of Fig. 4.10a.

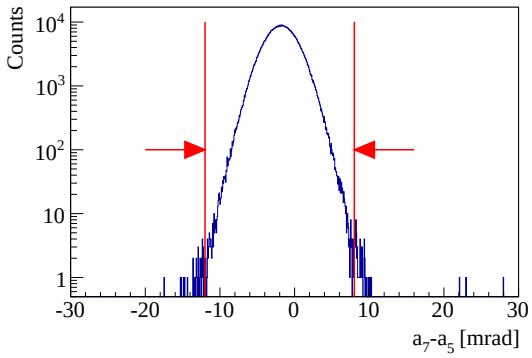

(d) One dimensional representation of Fig. 4.10b.

Figure 4.10: Beam profiles between F3 and F5 focal planes (left) and F5 and F7 focal planes (right). Cleaning conditions are shown by the red lines of the 1-dimensional representations.

This procedure is shown for ^{108}Zr[2] in Fig. 4.11, the resultant Z vs. A/Q PID shown in Fig. 4.11b from the gate shown in Fig. 4.11a shows a significant background for $Z < 40$ and $Z > 40$. The removal of these events is achieved by imposing a gate for each nuclide on the x_3 vs. A/Q PID, such as that depicted in Fig. 4.11a, a comparison is then made to the measured Z with the known Z of the nuclide. If the absolute difference between these two values is greater than 0.65, the event is rejected.

The combination of the enhanced A/Q resolution and the background removal provides considerable improvement to the quality of the PID plots, as shown in Fig. 4.12.

4.2 EURICA analysis

Of the two scenarios that EURICA is used to measure γ rays, from β-decay and isomer decay, it is the latter which is deserving of special attention. Such attention is required since γ rays emitted from isomeric states are measured in coincidence with the implantation of ions that they belong to. The process of this implantation creates a substantial background which must be considered, as well as the possibility that an ion, or light particle hits a crystal of EURICA. Additionally, since the lifetime, as well as energy, of the isomeric state is of interest, careful consideration should be given to the effects of timewalk, which is the perceived delay of the detection of low-energy γ rays arising from their electronic signals taking longer to reach the threshold level of a TDC.

4.2.1 Removal of overflow events

In the event of a very high-energy signal, larger than the ADC's dynamic range, in a crystal of EURICA, the timing signal can become spurious, not only for that crystal, but also its neighbours, this effect is shown in Fig. 4.13. Therefore, any event in which an overflow event is detected, is not included in the analysis. Since the dynamic ranges of the crystals are different, the threshold is set for each detector individually.

[2]An auspicious isotope to use due to its easy identification through its isomeric decay

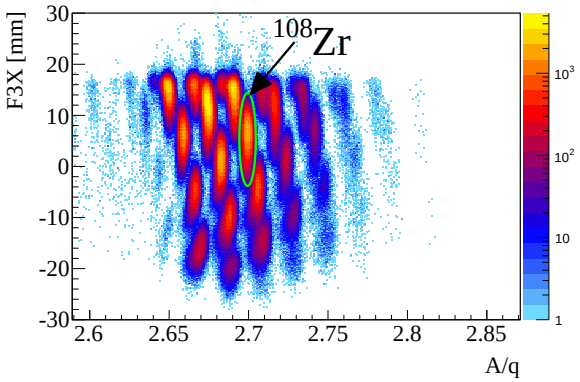

(a) Particle identification plot made from the corrected A/Q measurements and the x-position at the F3 focal plane.

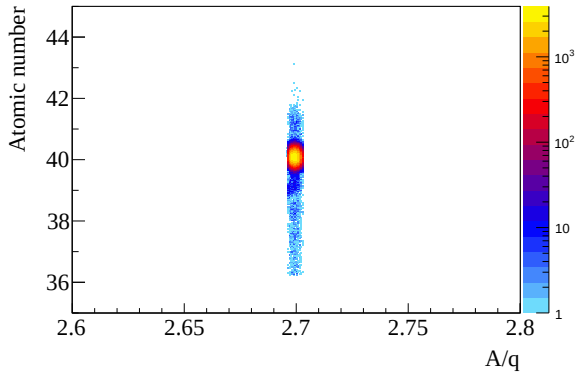

(b) Particle identifcation plot made from Z measurements in the TEGIC and corrected A/Q spectrum, gated on ^{108}Zr in the F3X vs. A/Q plot, see Fig. 4.11a.

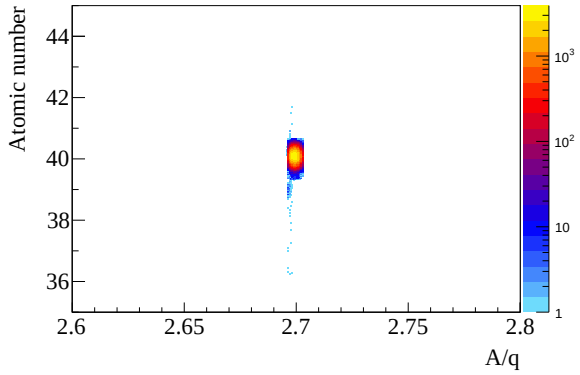

(c) The same as Fig. 4.11b, except with the cleaning condition imposed that the difference in the measured Z in the TEGIC and the the "real" atomic number is below a threshold.

Figure 4.11: Plots to illustrate the principle of removing reaction residues from the final PID, using measurements made at the F3 focal plane and F11.

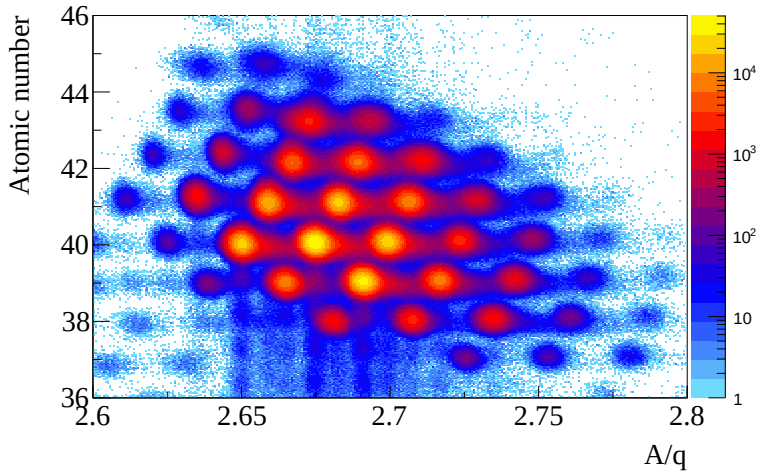

(a) PID plot with raw values of A/Q and no background rejection.

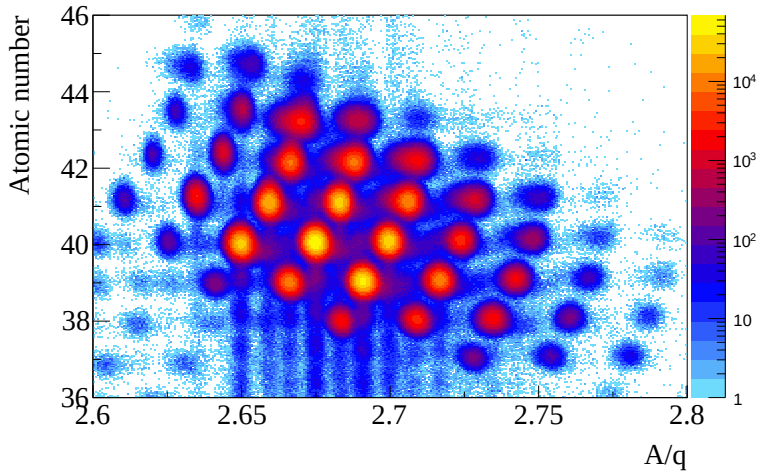

(b) PID plot with empirical corrections to A/Q give in Eqs. 4.9 and 4.10, and no background rejection.

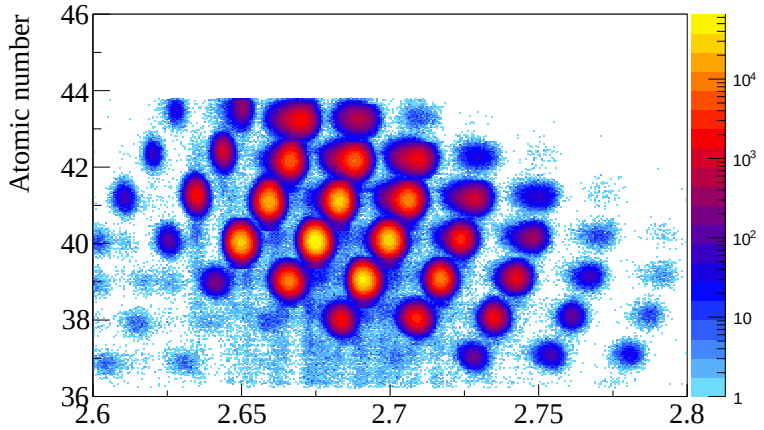

(c) PID plot with empirical corrections to A/Q of Eqs. 4.9 and 4.10, as well as background rejection being implemented.

Figure 4.12: Plots to show improvement of PID.

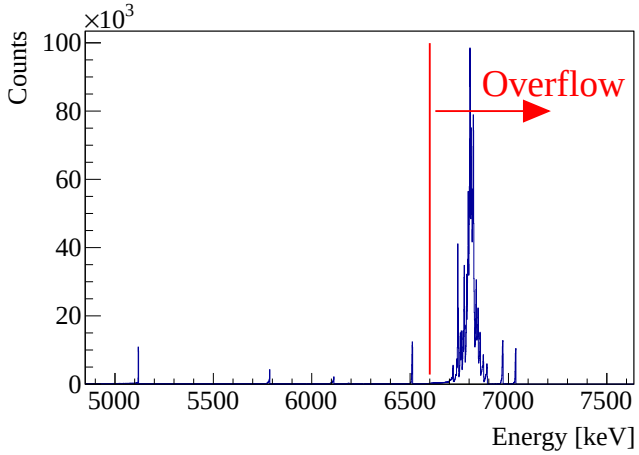

(a) Energy spectrum from EURICA showing the high-energy overflow events.

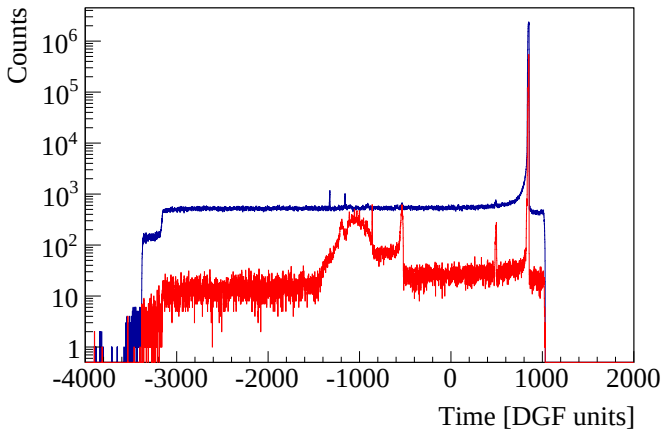

(b) The effect of overflow on the time spectrum of EURICA. The red-line is gated on the overflow signals of EURICA, and the blue line is gated on events below the overflow.

Figure 4.13: Demonstration of the effect that overflow events have on the EURICA time-spectrum.

4.2.2 Time-walk correction

The importance of the time-walk correction is two-fold for the case of EURICA; firstly, the time profiles of all crystals need to be uniform for the measurement of the lifetimes of isomeric states, and secondly, since the add-back and coincidence measurements rely on timing differences between the crystals, as such the crystal signals need to be aligned correctly.

The time-difference, ΔT, is defined, for isomer decays, as the difference between the ion implantation trigger (left side of the F11 PMT) and a γ-ray detection in EURICA. The Bremsstrahlung produced from the ion's implantation is commonly known as the "prompt-flash". As this name suggests, it occurs immediately with respect to the implantation. Therefore, this is a rather advantageous background for the case of the time-walk calibration since it extends across the entire energy range. However, it is important that the energy-time matrix used for the time-walk correction does not include decays from isomeric states. Therefore, ^{107}Zr was used for this purpose, its uncorrected energy-time matrix is shown in Fig. 4.14a. A polynomial of 4^{th} order was fitted to this distribution and then used as the correction to the energy-time matrix producing the matrix Fig. 4.14b. One of the key features of Fig. 4.14b is the $\sim$200 ns width of the time distribution, this provides the justification for the γ-γ and add-back coincidence time windows.

4.3 WAS3ABi

The strength of highly segmented silicon arrays such as WAS3ABi, described in Sec. 3.4.1, is their ability to precisely correlate an implanted ion with its subsequent β-decay. This is achieved through the position measurement of both the implantation and of any subsequent β-decay-like events, i.e. low energy deposition. A comparison is then made between these positions, and should they occur within a specified distance, the events are correlated. Further conditions imposed include the energy relation between the x- and y-strips, as well as the time in which the respective events occurred.

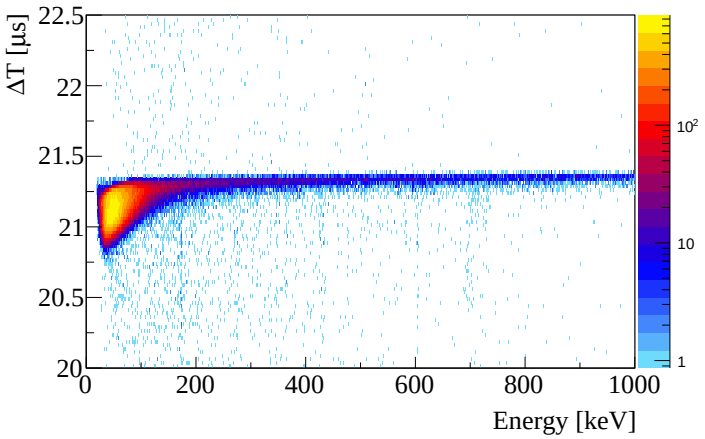

(a) An energy-time matrix constructed for all nuclei with no time-walk correction applied. The energy range is restricted to 1000 keV to accentuate the low-energy time-walk.

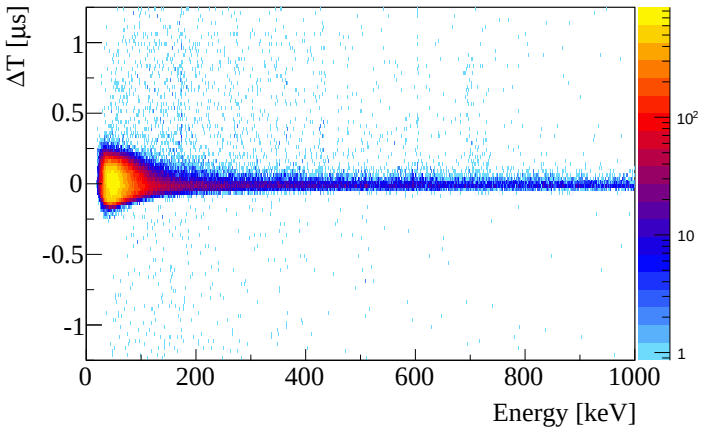

(b) The same as above, but corrected for time-walk. Note that the origin now lies at $\Delta T = 0$ and that the direction of ΔT has been reversed to better represent the decay of a state.

Figure 4.14: Energy-time matrices following an ion implantation into WAS3ABi. The prompt-flash demonstrates clearly the low-energy time-walk corrections, particularly evident at $E < 200$ keV.

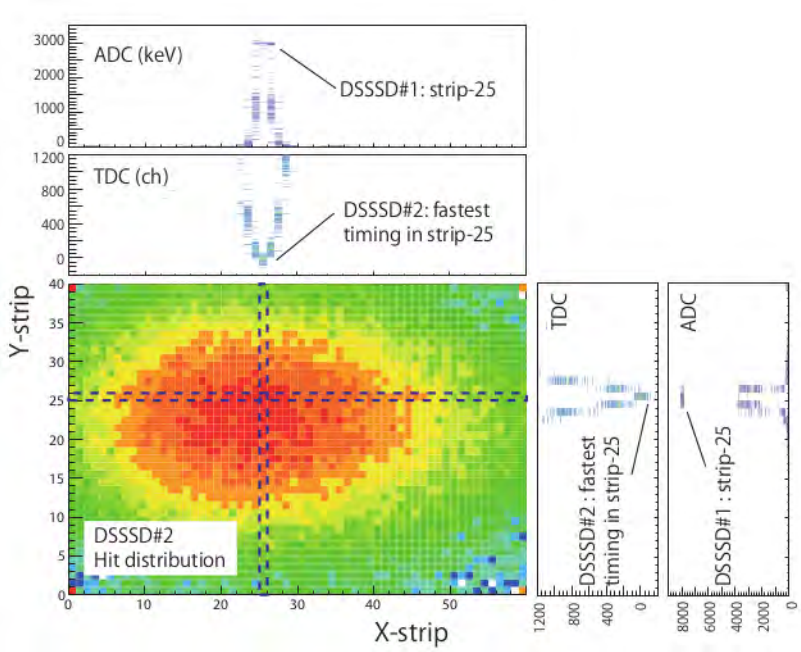

Figure 4.15: The DSSSD#2 Hit distribution plot shows the implantation positions for deduced from the strips that have the fastest signals in the TDC spectra. Note the correlation between energy deposition and timing spectra. See text for details. Figure taken from Ref. [89]

4.3.1 Ion implantation

The DSSSD layer into which an ion implants is determined by considering the energy spectra of each strip of each layer of WAS3ABi. Since the energy deposited into the DSSSDs is large (in the GeV range) for ions travelling through, or implanting, such events cause an overflow signal, as shown the ADC spectra in Fig. 4.15. This effect is used to determine the implantation layer by checking which DSSSD does not have an overflow signal in any of its strips and then selecting the layer immediately upstream as the implantation layer.

Ideally, the ADC signals of WAS3ABi would be delivered to a low- and high-gain branch, as this would give sensitivity to the energy ranges involved in ion implantations and β-decay events, respectively. In this case the pixel that measured the highest energy in the low-gain branch would be considered the implantation pixel. However, due to the limitation of available modules, and space to put them, this was not feasible in the experiment described here. The position determination of an ion implantation was, therefore, performed via timing measurements of the strips of WAS3ABi and the strip which had the fastest signal corresponded to the largest energy deposition. Figure 4.15

taken from Ref. [89], shows the clear relation between the energy measured in the strips through which an ion travels in DSSSD #1 and the timing signals measured in DSSSD #2. The fastest timing is observed in x-strip 25 and y-strip 25 in the second DSSSD, which also relate to the largest energy depositions in the same strips in the first DSSSD.

4.3.2 β detection

Due to the high granularity of WAS3ABi and relatively high Q_β-values of the β-electrons expected in this experiment ($\sim$6 MeV [13]), multiple strips are likely to fire per β-decay. As such, events where signals from contiguous strips are measured are considered as originating from a single event. The position from which the β-electron emanates from is given as the weighted mean of all the strips that fire,

$$X = \frac{\sum_{i=0}^{n} E(X_i)X_i}{\sum_{i=0}^{n} E(X_i)}, \tag{4.11}$$

where n denotes the number of strips that fire, $i = 0$ is the lowest indexed strip which fires, X_i is the i^{th} strip that fires and $E(X_i)$ is the energy measured in the i^{th} strip. The same formula applies for the y position. Those events that occur independently from neighbouring strips are considered as separate β-candidates.

It is anticipated that electrons emitted from β-decay would deposit the same energy in the x-strip as the y-strip [84]. As such, a correlation line of $E_x = E_y$ is expected on a plot of E_y vs. E_x, which is shown to be the case in Fig. 4.16a. Events inconsistent with the $E_x = E_y$ condition were rejected based on the difference of their energies, depicted in Fig. 4.16b. The acceptance condition was then based on a fit of a Gauss curve, the red line of Fig. 4.16b, events within $\pm 3\sigma$ of the curve were accepted, these limits shown as black lines on Fig. 4.16b.

4.4 Fast β-gamma timing

Here we discuss the considerations given to the analysis of data provided by the fast β-γ timing set up. Particular attention is drawn to the cleaning of the timing spectra, which is of paramount importance for precise timing measurements.

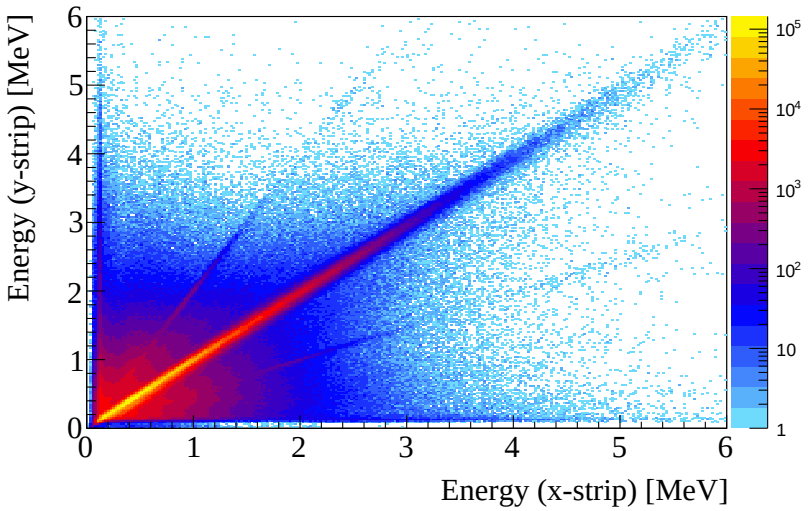

(a) An energy-energy matrix of the energy measured in the horizontal (x) and vertical (y) strips. There is a clear correlated component which relates to true β-decay events.

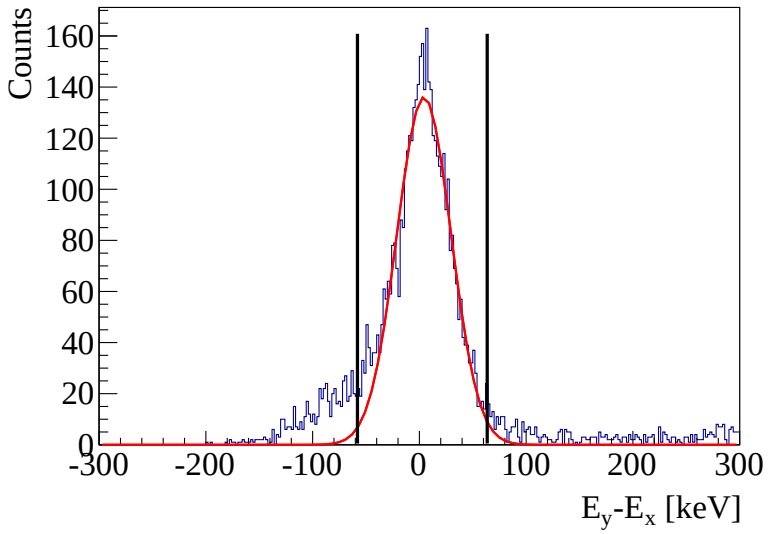

(b) The difference between the energies measured in the x and y strips of WAS3ABi. The red line represents a Gaussian fit to the data, and the black lines the cleaning gates imposed at $\pm 3\sigma$.

4.4.1 Cleaning conditions for β timing

Since the β-timing is taken from the average of the left and right PMTs attached to the β-plastics, it is necessary to ensure that good signals are observed in both. It was observed that in some cases a TDC signal occurred without a corresponding ADC signal, such events produced spurious timing signals. Figure 4.17a shows the ADC spectrum for the right-side, upstream PMT, the energy continuum is consistent with the β-decay energy spectrum. With no condition applied to the ADC spectrum, the TDC spectrum of Fig. 4.17c is produced. When the gate depicted as the red line in Fig. 4.17a was applied, the resultant TDC spectra shown in Fig. 4.17e is obtained. The removal of the delayed background at $3800 < \text{Time} < 4000$ is evident. At this point it is worth noting the small, sharp peak to the left of the main peak, this is produced from the rare occurrence that the right PMT becomes the event trigger in lieu of the right. It rather naturally brings us to the next cleaning condition, the requirement of the TDC event being within the peak which pertains to the β-decay events. As an example, the gate of the right-side, upstream PMT is shown in Fig. 4.17b, a similar condition is imposed on the left-side. Figure. 4.17d shows the un-gated time-difference of left and right PMT signals, it is evident that noise arises from those events outside the peak which has the β-decay timing information. The noise is drastically reduced when observing the TDC spectra with the gate imposed, shown in Fig. 4.17f.

4.4.2 Gain drift of $LaBr_3$(Ce) detectors

It is a well known issue that the signals produced by PMTs are susceptible to gain drift, due to a combination of unstable operating voltage, and temperature changes within the PMT casing. To monitor this, the prompt energy spectrum of the $LaBr_3$(Ce) detectors was observed upon an ion implantation. Since the time resolution of the $LaBr_3$(Ce) detectors is much better than that of EURICA, they are sensitive to energy peaks created from the reactions, or excitations, caused by ion implantation. Since the transitions of interest are all around $\sim$150 keV, it is fortuitous that there is a prompt peak at 147 keV, see Fig. 4.18a, with sufficient statistics to provide a run-by-run peak-position in each detector, Fig. 4.18b. There is no evident gain drift shown in Fig. 4.18b and all other detectors also demonstrate no appreciable gain shift. The reason for this stability could lie in the low count rates of this experiment, leading to no heating of

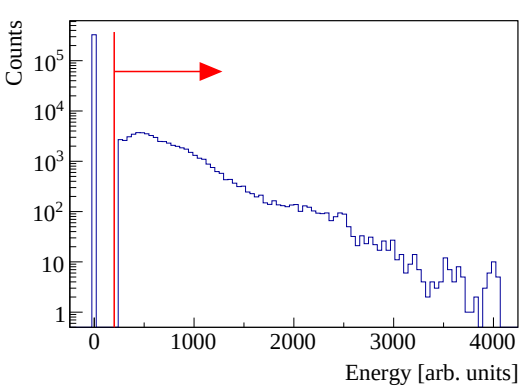

(a) ADC spectrum of the right-side, upstream PMT. The red line shows the gate applied.

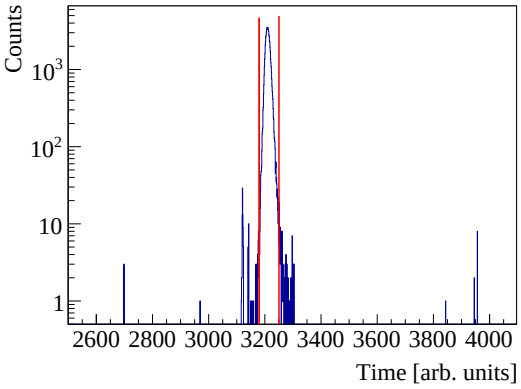

(b) TDC spectrum of the right-side, upstream PMT. The red lines show the gate applied.

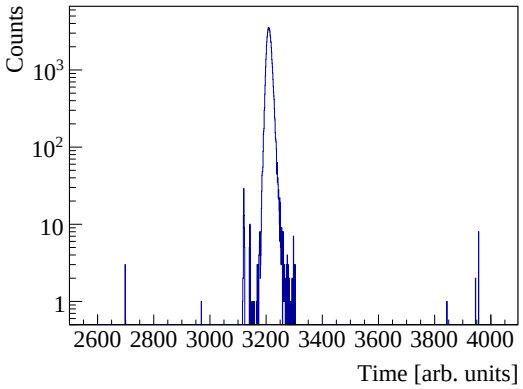

(c) TDC spectrum, ungated on the ADC, of right-side PMT.

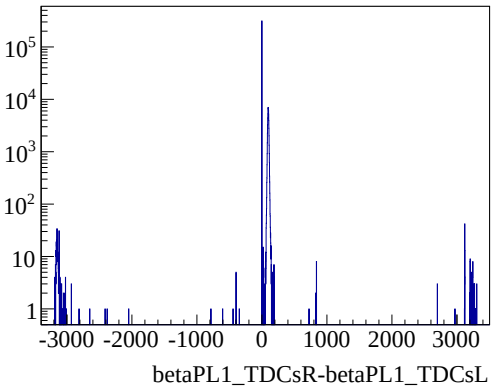

(d) Time-difference between the left and right PMT, ungated on the TDC above.

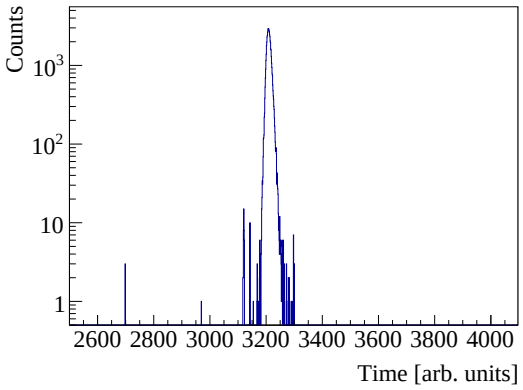

(e) TDC spectrum, using the gate on the ADC shown in Fig 4.17a.

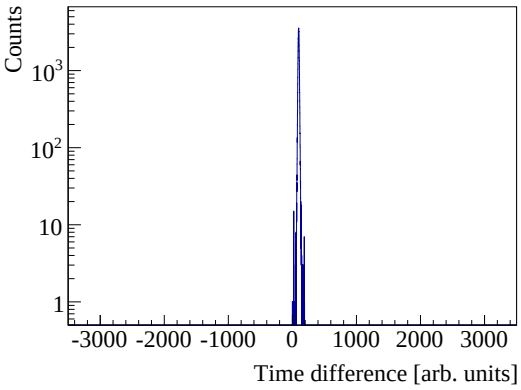

(f) Time-difference between the left and right PMT, gated on the TDC and ADC.

Figure 4.17: Series of plots showing the conditions applied to obtain clean time spectra for the detection of β electrons in the β-plastics.

PMTs thought to be the major cause of such effects [90].

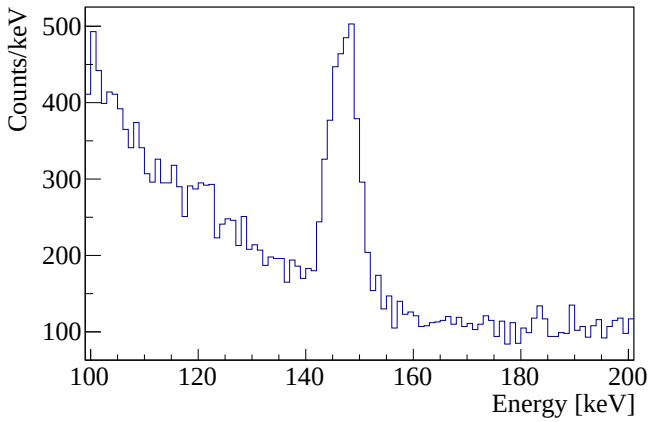

(a) Observed prompt energy peak at 147 keV in a single detector of the $LaBr_3(Ce)$ array from all runs.

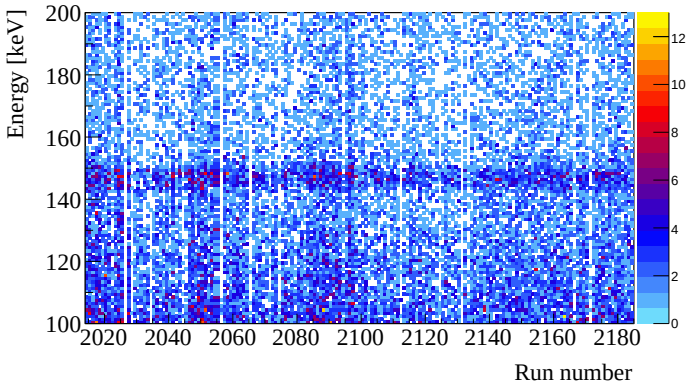

(b) Energy of peak in Fig. 4.18a as a function of run number. The 147 keV is clearly observed to be constant throughout the experimental run.

Figure 4.18

4.5 Time-walk correction of $LaBr_3(Ce)$

The time-walk calibration of the $LaBr_3(Ce)$ spectra is an important correction to make due to the effect it has on the timing resolution. The time is defined as the difference between the average timing signal of the β-plastics, and the time signal measured in a $LaBr_3(Ce)$ detector. The uncorrected energy-time matrix following β-decay is shown in Fig. 4.19b. Evident in this matrix is the region of delayed structures at $E \lesssim 300$ keV, a consequence of the mass region's relatively long-lived low-lying states. To prevent the delayed structures from influencing the polynomial fit, the structures which exist beyond the prompt distribution, ~ 0.5 ns, were excluded from the fit, as shown in Fig. 4.19b. The time-walk correction fit displayed as the dashed black line in Fig. 4.19b is then applied to give the corrected matrix in Fig. 4.19b.

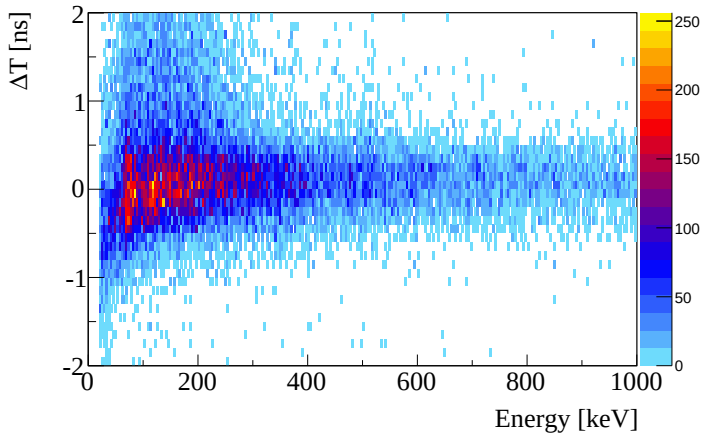

(a) Energy-time matrix without time-walk correction, measured in coincidence with correlated ion-β events. The long-lived, low-energy components are clearly visible at $E < 300\ keV$.

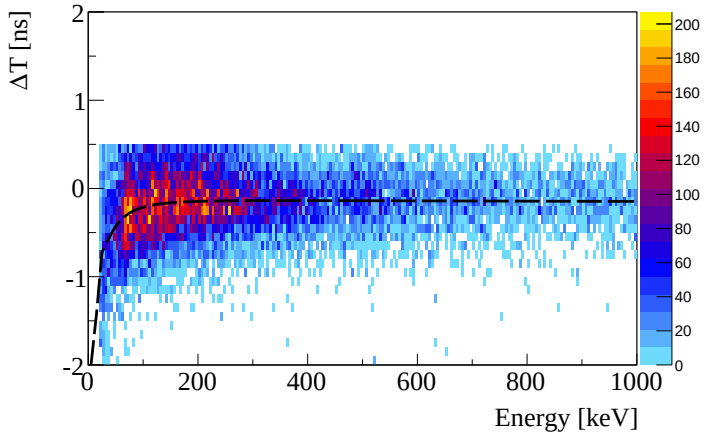

(b) The same as Fig. 4.19a except with the delayed, low-energy components rejected. The dashed black line shows the polynomial fit to the energy-dependent walk.

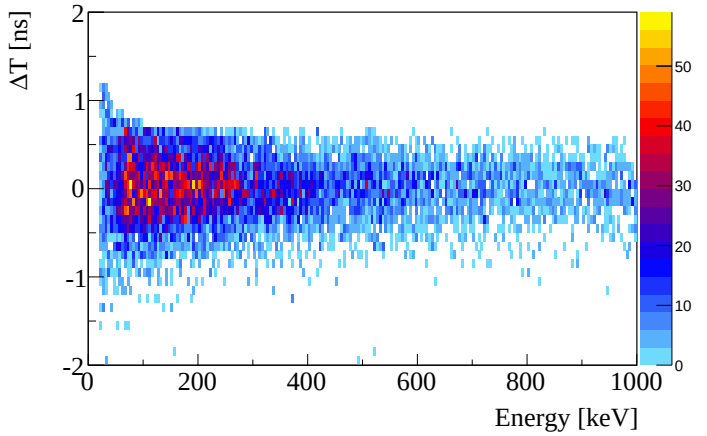

(c) The same as Fig. 4.19b, except with the correction shown by the dashed blank line applied. The improvement to the low-energy region of the timing is evident.[a]

[a]The reduced statistics are due to the correction applied to a different run with less statistics than Figs. 4.19a and 4.19b

Figure 4.19

Chapter 5

Results

In this chapter, the results are extracted from the data presented in Chap. 4. Isotopic selections are made with particle gates on the atomic number and mass-to-charge ratio. For the study of states populated through the β-decay of the selected ions, the ion-β correlations are made according to the relative position and time measurements of an ion implantation and the β-decay candidates associated with it. Energy-time matrices of the γ rays associated with the β-decay daughters of implanted ions are constructed from the energy measured in the $LaBr_3$(Ce) detectors and the timing signals in the β-plastic detectors. From these matrices, lifetimes are extracted for known levels in ^{102,104,106}Zr through the use of detailed fitting procedures, which are well suited to the low-yield, low-background nature of the measurements. As well as the measurement of states populated through β-decay of ^{102,104,106}Y, the lifetimes of isomeric states and the energy of the transitions which de-excite them are also reported for the first time in ^{113}Nb and ^{115}Mo.

5.1 Criteria for ion selection

The spectra of the mass-to-charge ratio and atomic number demonstrate Gaussian distributions, as shown in Figs. 4.8 and 4.12c, with resolutions of σ =0.155 and 0.0016, respectively (see Sec. 4.1). The particle identification (PID) plot shown in Fig. 5.1b is the same as that in Fig. 4.12c expanded about ^{106}Y. It shows that Z and A/Q can be treated as independent variables, therefore, the 2-dimensional Gaussian distribution which describes them has covariance terms equal to zero. Each distribution of nuclides

can then be described by the relation,

$$f(A/Q, Z) \;=\; h_0 \exp\left[-\left(\frac{(Z-Z_0)^2}{2\sigma_Z} + \frac{((A/Q)-(A/Q)_0)^2}{2\sigma_{A/Q}}\right)\right], \tag{5.1}$$

where h_0 is the height of the distribution, $\sigma_{Z,A/Q}$ are the resolutions of the atomic number and mass-to-charge ratio, and Z_0 and $(A/Q)_0$ are the centroid values, i.e. $Z_0 = 39$ and $(A/Q)_0 = 2.718$ for ^{106}Y. A 3-dimensional representation of Fig. 5.1b is shown in Fig. 5.1a, with Eq. 5.1 represented by the parallel red planes. A contour of Eq. 5.1 would then represent a particle gate, which can be expressed as an ellipse,

$$\left(\frac{Z-Z_0}{\sigma_Z}\right)^2 + \left(\frac{A/Q-(A/Q)_0}{\sigma_{A/Q}}\right)^2 \;=\; 4.605, \tag{5.2}$$

where 4.605 relates to a confidence level (C.L.) of 90% of a χ^2 distribution with two degrees of freedom [91]. Equation 5.2 is depicted by the red ellipse in Fig. 5.1b, which has the major and minor axes defined as, $2\sigma_Z\sqrt{4.605}$ and $2\sigma_{A/Q}\sqrt{4.605}$, respectively. It is evident from Fig. 5.1b that due to the background-removal and resolution enhancements detailed in Sec. 4.1, the 90% C.L. encapsulates the vast majority of events pertaining to the nuclide of interest, whilst remaining clear of the neighbouring distributions. This procedure provides a statistically rigorous isotope selection for the subsequent analysis of its β-decay and β-delayed γ rays.

5.2 ion-β correlation

The procedures outlined in Secs. 4.3.1 and 4.3.2 provide two data tables, one of ion implantation positions and another with positions of candidate β-decay events. Whilst the former is limited to the precision of the implantation pixel, the position of the β-electron is determined by the energy-weighted mean of each strip which fires (see Sec. 4.3.2), allowing for a better precision. In most cases, a non-discrete condition is imposed on the ion-β position, within which the β-decay candidates are validated. A β-candidate had to occur within distance of 1.5 mm from the edge of the implantation pixel to be validated, as shown in Fig. 5.2 [84].

Each β-decay is indexed with respect to the first β-decay. If the first β-decay of the implanted nuclide registered, the second β-decay would relate to the decay of

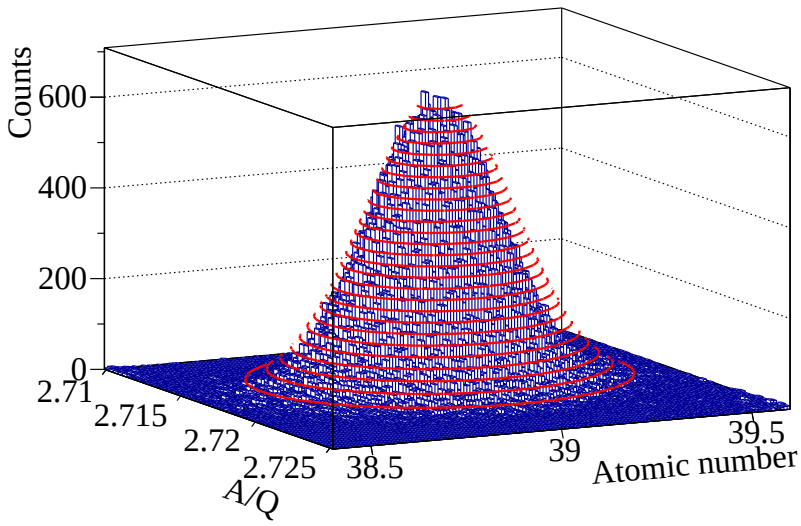

(a) A 3-dimensional depiction of the PID plot expanded about ^{106}Y. The blue boxes represent the experimentally observed counts, and the red lines indicate planes of constant height of Eq. 5.1 scaled to the experimentally observed distribution.

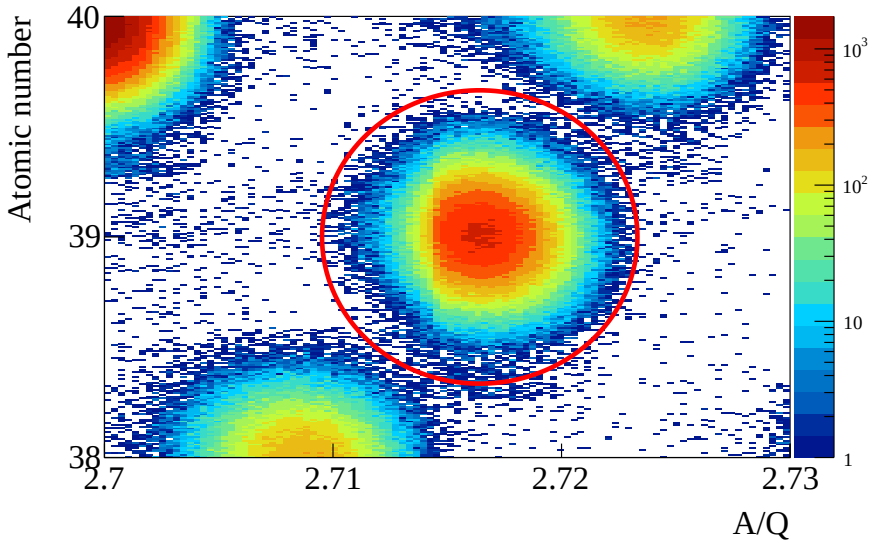

(b) The projection of (a). The red ellipse shows the 90% C.L. contour of Eq. 5.1, given by Eq. 5.2

Figure 5.1: An example particle gate on ^{106}Y.

its daughter nucleus. As such, only the first is selected for the subsequent analysis. Moreover, a time condition is imposed on the ion-β time such that only events occurring within approximately 5 β-decay half-lives of the parent nuclide are used.

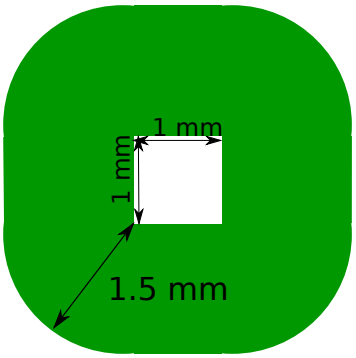

Figure 5.2: The white central square represents the implantation pixel of an ion. The surrounding green area is the area within which, inclusive of the implantation pixel, the β-decay must be measured in order to be correlated with the implanted ion.

5.3 Energy-time matrices for fast β-γ timing configuration

The construction of the energy-time matrices, from which the fast-timing measurements are made, require that the correlated β-decay electron is also measured in one of the β-plastic detectors (as well as adhering to the conditions described in Sec. 4.4). The efficiencies of the β-plastics are strongly dependent on implantation position, see Fig. 3.19. The implantation distributions for ^{102,104,106}Y are shown in Fig. 5.3. Since the implantations of ^{102,104}Y are primarily in the upstream DSSSD, the only significant β-electron detections happen in the upstream β-plastic, however, the implantations of ^{106}Y are predominantly in the central layer, meaning approximately equal detection of electrons in the upstream and downstream β-plastics. As such, the energy-time matrices for ^{102,104}Zr are constructed with the energy deposited in the $LaBr_3$(Ce) array and time difference, ΔT, measured between the average of the left and right PMTs signals of the upstream β-plastic. The energy-time matrix for ^{106}Zr is constructed using the events in both the upstream, and downstream β-plastics. The matrices for ^{102}Zr,^{104}Zr and ^{106}Zr are shown in Figs. 5.8, 5.14a and 5.15a, respectively.

5.4 Fit details

Before extracting lifetimes from the time-difference distributions, it is instructive to discuss the details of the fit functions and the fit method employed. The fit functions are constructed as normalised probability distribution functions (p.d.f.s) which describe

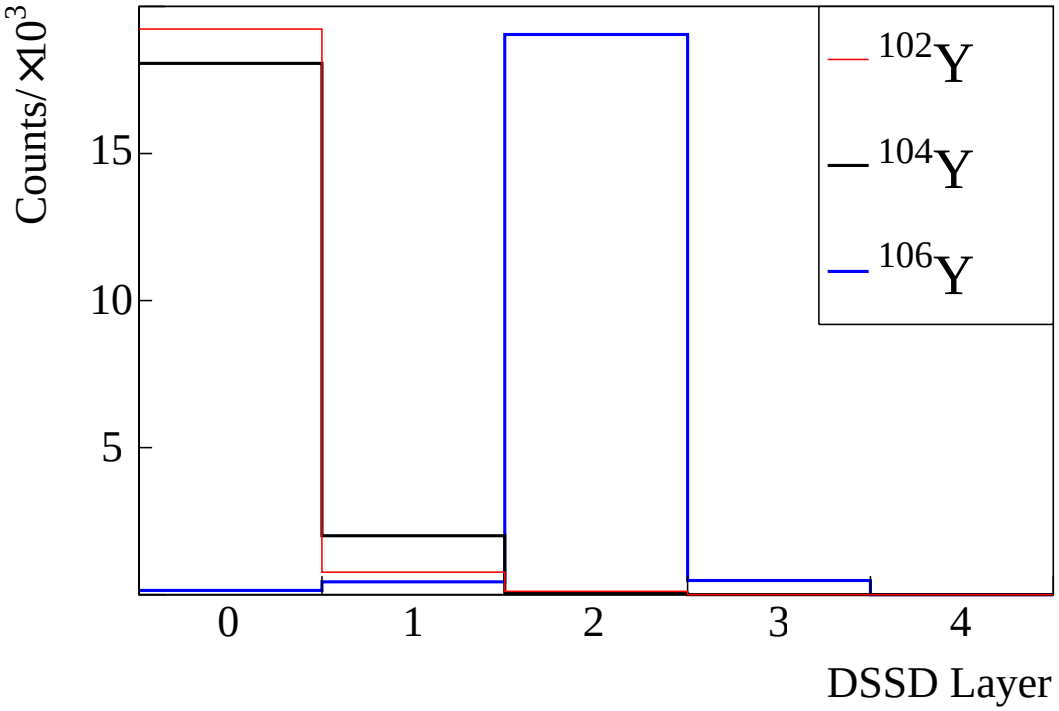

Figure 5.3: The distribution of implantations in the layers of WAS3ABi. The vast majority of ^{102,104}Y implant into the first layer, whereas the majority of ^{106}Y implant centrally.

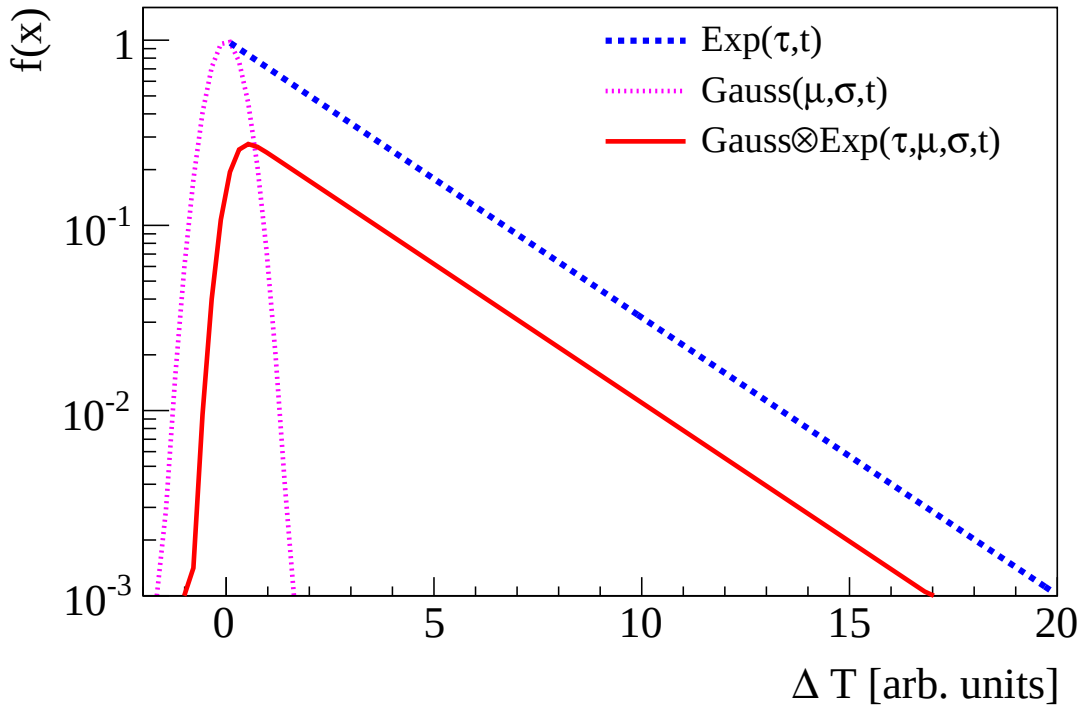

Figure 5.4: The probability distribution functions of an exponential decay (dashed blue line, Eq. 5.3), Gaussian distribution (dashed magenta, Eq. 5.4) and their convolution (solid red line, Eq. 5.7).

an exponential decay and, where appropriate, folded with the experimental resolution. The chosen fitting method was that of the maximum likelihood method (M.L.M.), due to the low-yield and low-background nature of the experiment. This technique is particularly appropriate as compared to the commonly used χ^2-minimisation since it does not assume a Gaussian distributed p.d.f. for each bin [92][1].

5.4.1 Probability distribution functions

The exponential decay function can be written in terms of the variable t and the mean lifetime of the decay, τ, as,

$$f(t,\tau) \;=\; \exp\left(-\frac{t}{\tau}\right), \tag{5.3}$$

which is plotted as the dashed blue curve in Fig. 5.4. Equation 5.3 can be modified to include the intrinsic resolution of the detector by performing a convolution with a

[1]This condition is fulfilled when $N_{\text{counts}} \geq 5$.

Gaussian function which describes the time resolution of the experimental configuration,

$$G(t,\mu,\sigma) \;=\; \exp\left[-\frac{(t-\mu)^2}{2\sigma}\right], \tag{5.4}$$

where the width, σ, is determined through a fit of the time spectrum of a prompt function. The mean, μ, is defined as zero because the data was corrected for time-walk to this channel, as described in Sec. 4.5. Equation 5.4 is depicted as the dotted magenta curve of Fig. 5.4. The convolution is given, schematically, as [93],

$$\begin{aligned} C(t) \;&=\; G(t,\mu,\sigma) \otimes f(t,\tau), && (5.5)\\ &=\; \exp\left[-\frac{(t-\mu)^2}{2\sigma}\right] \otimes \exp\left(-\frac{t}{\tau}\right), && (5.6)\\ &=\; \frac{1}{2\tau}\exp\left[\frac{1}{2\tau}\left(2\mu+\frac{\sigma^2}{\tau}-2t\right)\right]\operatorname{erfc}\left(\frac{\mu+\frac{\sigma^2}{\tau}-t}{\sqrt{2}\sigma}\right), && (5.7) \end{aligned}$$

where erfc(x) is the complimentary error function. Equation 5.7 is displayed as the solid red curve of Fig. 5.4.

5.4.2 Fit procedure

The M.L.M. is a powerful parameter determination technique which aims to maximise a probability density, $\mathscr{L}$, which is dependent on the parameters of the fit function, and of the distribution of data points. The maximum likelihood function itself is defined as the product sum over n data points [92],

$$\mathscr{L}\,(\tau) \;=\; \prod_{i=1}^{n} y_i\,(\mathbf{p};x_i)\,, \tag{5.8}$$

where y_i is a p.d.f., e.g. Eq. 5.7, which depends on a vector of parameters, $\mathbf{p}$ and a set of data points, x_i. The construction of Eq. 5.8 is such that, for a set of parameters which reflect well the distribution of the data points, the return value shall be large, and conversely for a set of $\mathbf{p}$ that does not represent the data well a small value is returned.

Since the employed fitting program, `MINUIT2` [94], is a minimisation routine, it is necessary to use the negative logarithm of $\mathscr{L}$, $-\ell$, as the function to optimise, so, for

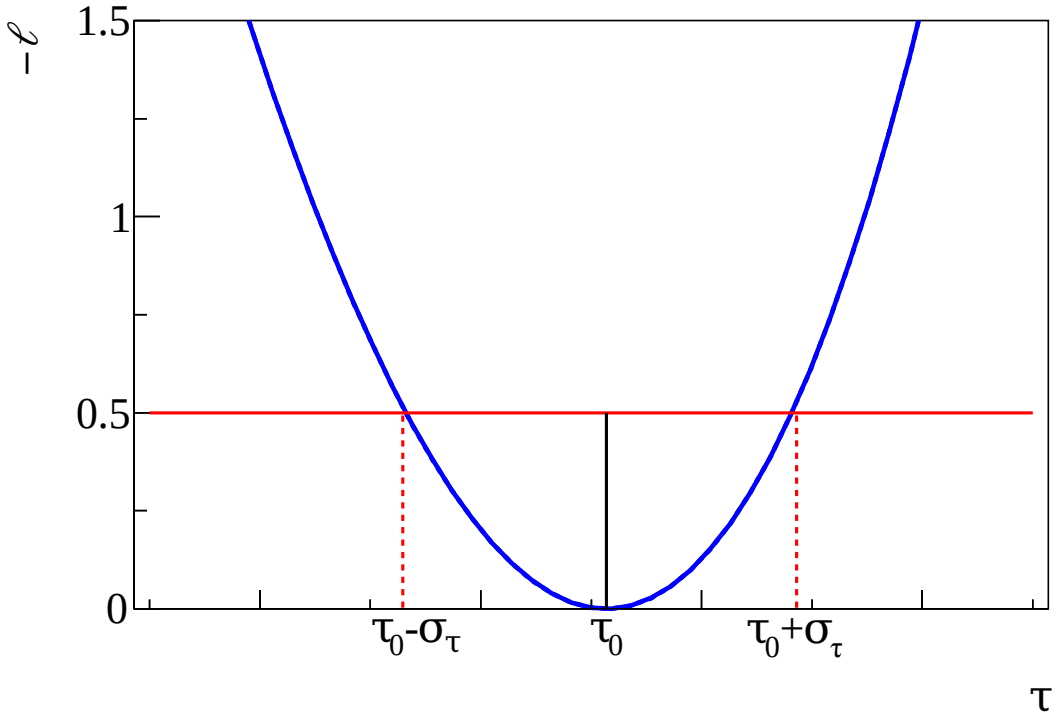

Figure 5.5: A schematic of a typical negative log-likelihood function (solid blue line) with a single lifetime as a parameter, Eq. 5.9. The most probable value of the parameter is given by the minimum value of $-\ell$ (solid black line), and its uncertainties the difference in τ required to increase $-\ell$ by 0.5 (dashed red lines, solid red line shows $-\ell + 0.5$ level).

Eqs. 5.3 and 5.7,

$$-\ell_E \;=\; -\sum_{i=1}^{n} \log\left[E_i(\tau; t_i)\right], \tag{5.9}$$

and,

$$-\ell_C \;=\; -\sum_{i=1}^{n} \log\left[C_i(\tau, \mu, \sigma; t_i)\right]. \tag{5.10}$$

Since the shape of $-\ell$ is Gaussian around its minimum value as a result of the Taylor expansion of ℓ, the uncertainty for the each parameter is given by the change in the parameter value needed to increase $-\ell$ by 0.5 from its minimum [92]. A typical negative log-likelihood function for Eq. 5.3 is shown in Fig. 5.5. It should be noted that, for clarity, the function is artificially shifted such that its minimum rests on the abscissa. In the current work, the centroid value of Eq. 5.7, μ is fixed to zero, therefore Eq. 5.10 becomes,

$$-\ell_C \;=\; -\sum_{i=1}^{n} \log\left[C_i(\tau, \sigma; t_i)\right], \tag{5.11}$$

which is dependent only on the lifetime being measured, and the width of the prompt distribution.

5.5 Prompt resolution of timing

The timing resolution, σ of Eqs. 5.4 and 5.7, is dependent on the timing response of both the β-plastic detectors and the $LaBr_3$(Ce) array. Therefore, a prompt transition from a level populated from the β-γ conditions outlined above should be used to characterise it. Since the time resolution of the $LaBr_3$(Ce) detectors is energy dependent, a transition close to the energy of the 2_1^+ states of ^{102}Zr (152 keV),^{104}Zr (139 keV)and ^{106}Zr (152 keV) should be used for this characterisation. The 160 keV $5^- \rightarrow 4^-$ transition in ^{102}Zr [95, 96], see Fig. 5.7, has been measured as prompt, with respect to the sensitivity of the current set-up. Due to the similarity of energies of this transition with that of the 2_1^+ (152 keV) in ^{102}Zr, it was necessary to impose an energy gate on the EURICA around the 152 keV transition in order to produce a clean transition in the $LaBr_3$(Ce) detectors. The resultant time-difference spectrum is shown in Fig. 5.6, where the Gaussian fit yielded a width of $\sigma = 311(20)$ ps.

5.6 Lifetimes of states in ^{102}Zr

The energy-time matrix of ^{102}Zr, shown in Fig. 5.8, shows a long-lived component for the 579-keV transition which de-excites the 4^- state, see Fig. 5.7, as well as the expected delayed component pertaining to the $2_1^+ \rightarrow 0_{g.s}^+$ transition. Whilst the existence of the isomeric 4^- state is intriguing, it makes the measurement of the 2_1^+ state more difficult. The 3^+ state which is fed from the 4^- state and feeds the 2_1^+ state was assumed to be prompt since the delayed structure of the 1090-keV transition, labelled in Fig. 5.8, does not extend further than that of the 579-keV transition. The lifetime of the 4^- state is first measured, and then by employing the Bateman equations [97], which take into account side-feeding from prompt and delayed transitions, a measurement is made of the 2_1^+ state.

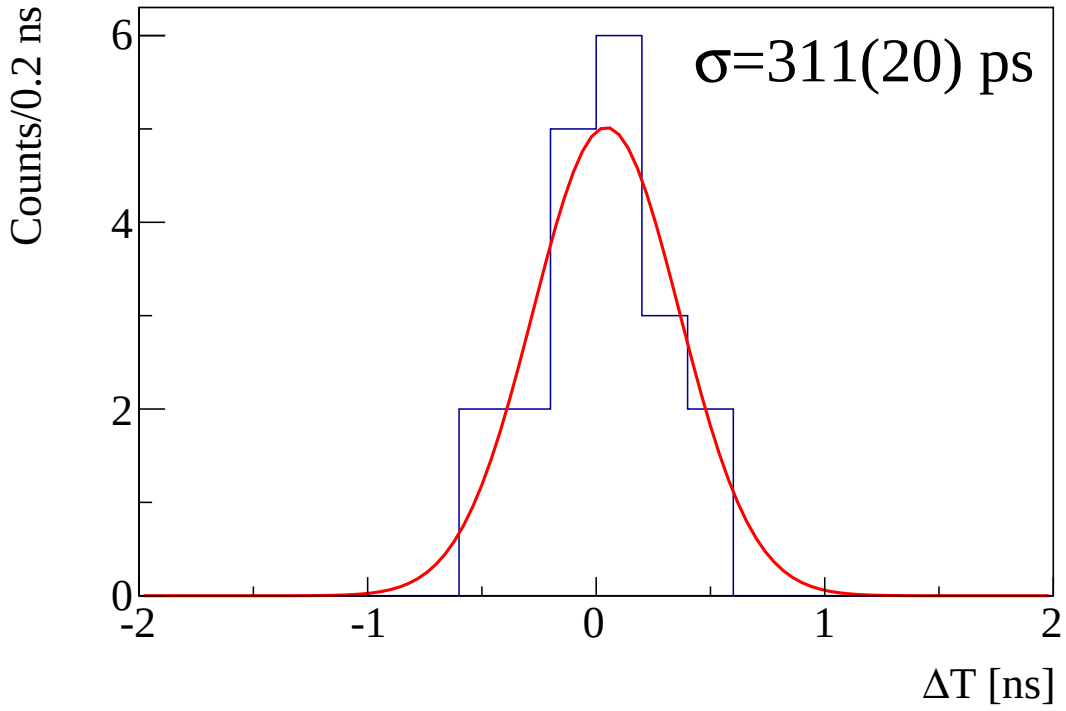

Figure 5.6: The time-difference between a β-detection in the β-plastic detectors from an ^{102}Y decay and the observation of the 160-keV transition from the decay of the 5^- state in ^{102}Zr.

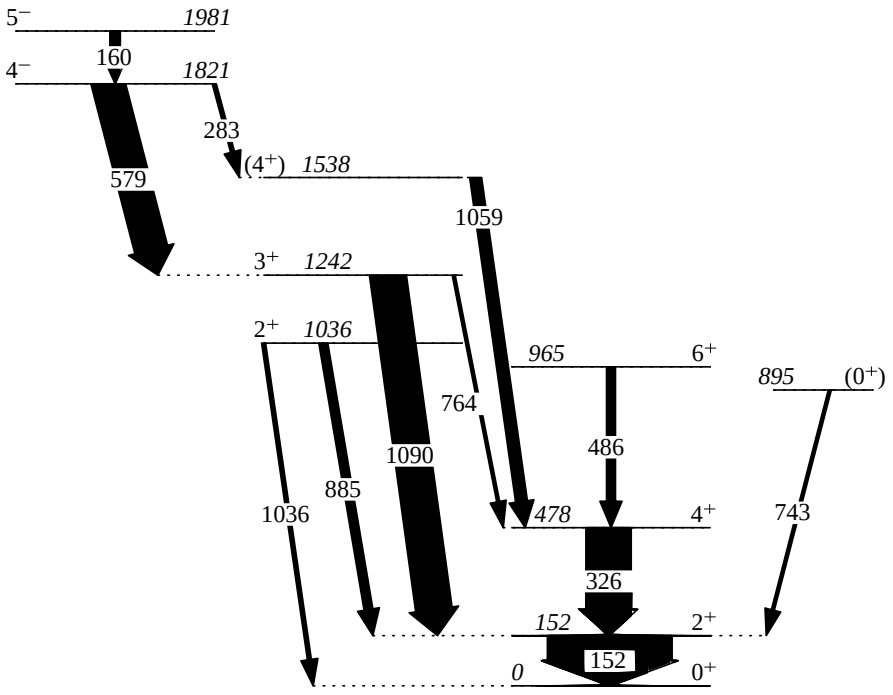

Figure 5.7: Partial level scheme of ^{102}Zr showing levels and transitions relevant to this work. Spins and parities of states are taken from Ref. [13], except for the 1820 keV level, which has tentative parity in Ref. [13], but firmly assigned as positive parity in Ref. [96] through angular correlation measurements. See Sec. 6.1 for further details. The width of each arrow corresponds to the relative γ-ray intensity, as given in Tab. 5.1.

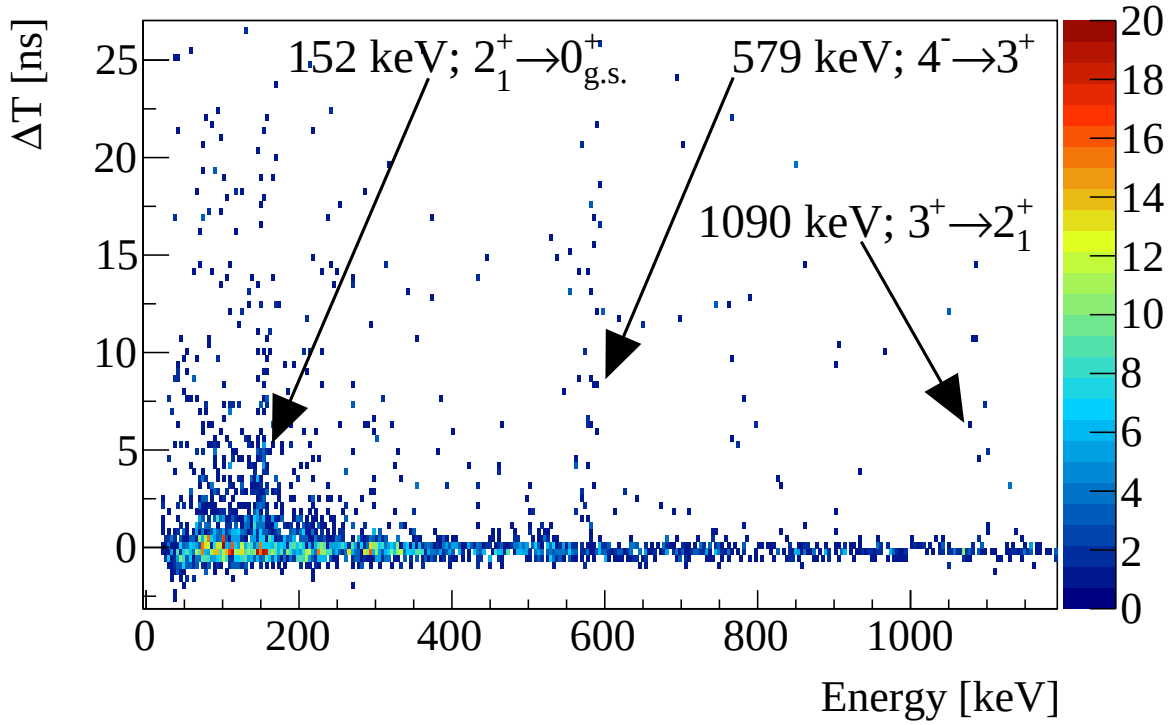

Figure 5.8: The energy-time matrix measured within 1 s of correlated β-decays of ^{102}Y.

5.6.1 Lifetime measurement of the 4^- state

The $5^- \rightarrow 4^-$ transition has been measured to be prompt, see Sec. 5.5, and no states higher than the 5^- state are populated in this experiment, as shown by Fig. 5.10, which depicts the EURICA spectrum gated on 160-keV γ rays also detected by EURICA. As such, the delayed structure of the 579 keV transition originates only from the 4^- state, therefore, the shape of its decay curve is given by Eq. 5.3. A time projection was taken from Fig. 5.8 gated on the energy peak of the 579-keV transition, which is shown clearly in the delayed spectrum of Fig. 5.9. The background was selected only from the higher energy region of the spectrum to avoid the subtraction from the time peak of Compton-scattered events, i.e. those with the same time-profile, but at a lower energy. The resultant time-difference spectrum is shown in Fig. 5.11, where a delayed component is evident. The M.L.M. returned a value of τ=7(2) ns, where the uncertainty was obtained by the method described in Sec. 5.4.2 and depicted in Fig. 5.5.

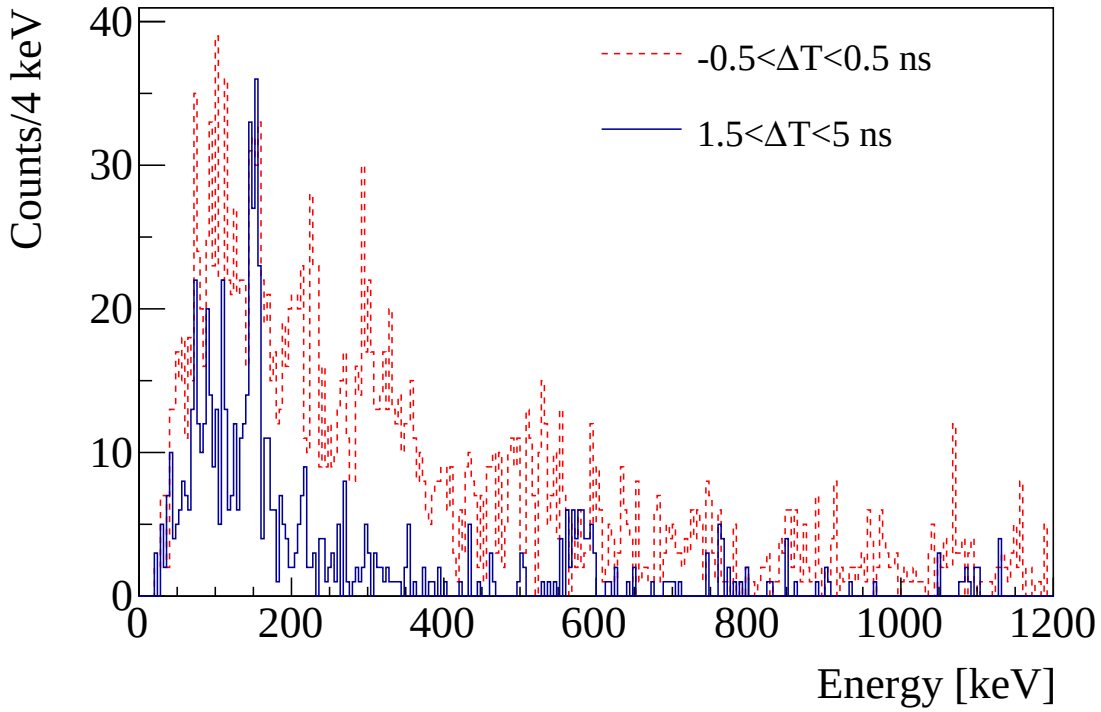

Figure 5.9: Prompt (red dashed line) and delayed (solid blue) energy projections of the energy-time matrix, shown in Fig. 5.8, measured by the $LaBr_3$(Ce) array. The 579-keV transition is clearly observed as a delayed peak, in addition to the 152-keV $2_1^+ \rightarrow 0_{g.s}^+$ transition. The prompt spectrum shows that a multitude of prompt transitions are also present, in particular the 327-keV $4_1^+ \rightarrow 2_1^+$ transition.

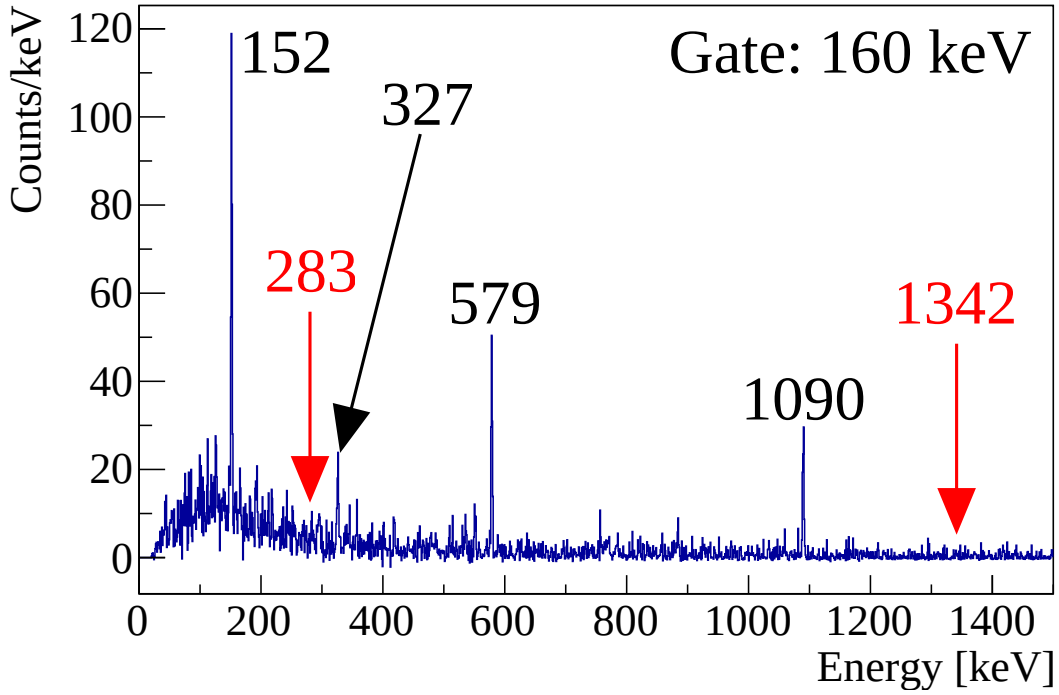

Figure 5.10: A γ-ray energy spectrum measured by EURICA observed in coincidence with 160-keV transitions, also measured in EURICA, which feeds the isomeric 4^- state. The red labels indicate the positions of peaks observed in the works of Ref. [98] and [96], which are absent in the current work. The black labels show the energies of the transition which are observed in this work as well as those of Refs. [98], [96] and [95].

5.6.2 Measurement of the lifetime of the 2_1^+ state

The intensities of the transitions measured in the EURICA singles spectrum, shown in Fig. 5.12, are given in Tab. 5.1. These intensities show that about 40% of the feeding of the 2_1^+ of ^{102}Zr originates from the 4^- state. This presents a problem when measuring the lifetime of the 2_1^+ state just through the β-γ time-difference, since the delayed nature of the 4^- state will retard the population and, therefore, the decay of the 2_1^+ state. This effect is clearly seen in Fig. 5.13, where there is a long-lived "tail" evident from $\Delta T > 10$ ns that is absent from Figs. 5.14c and 5.15c, which show the time distributions of the 2_1^+ ($\tau \approx 2.65$ ns) states of ^{104,106}Zr, respectively. An assumption is made that the only delayed component which feeds the 2_1^+ state originates from the 4^- state, therefore, the Bateman equation, accounting for the side-feeding from prompt

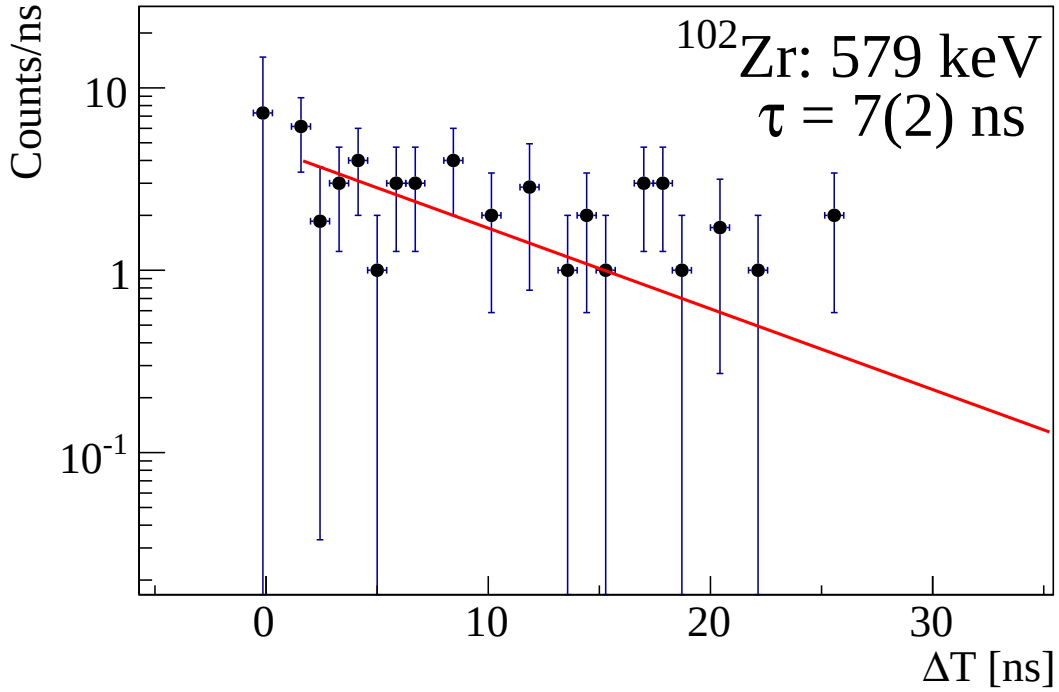

Figure 5.11: The background-subtracted time-difference spectrum of the 579-keV transition derived from the projections of the energy-time matrix shown in Fig. 5.8. The red line is the result of a M.L.M. fit of Eq. 5.3.

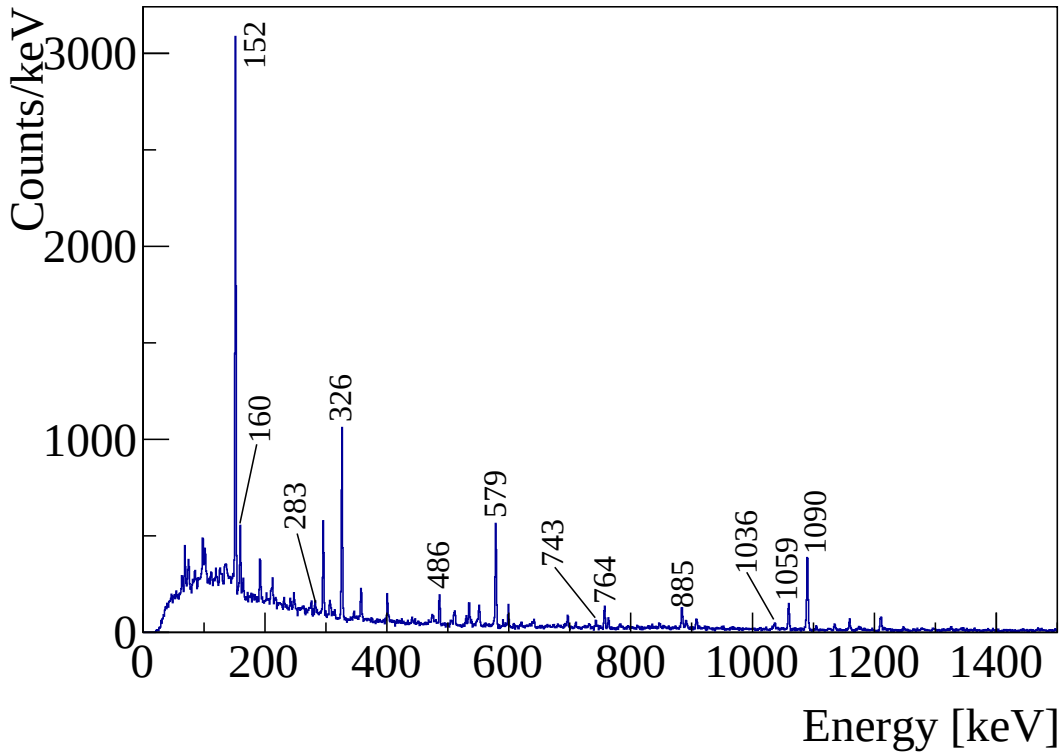

Figure 5.12: γ-ray energy spectrum observed in EURICA measured within 1 s of correlated β-decays of ^{102}Y. The transitions relevant to this work are labelled with their energies.

Table 5.1: Summary of intensities of transitions observed from the de-excitation of ^{102}Zr as populated through the β-decay of ^{102}Y. Intensities are normalised to the 152-keV transition. Presented alongside the present work are previous studies of the decay of ^{102}Y. The production mechanisms were from the neutron-induced fission of ^{235}U at the JOSEF facility [99] and the projectile fission of ^{238}U at GSI [100]. The intensities and energies measured are consistent with each other.

Present work		JOSEF [99]	GSI [100]
E_γ [keV]	I_γ^{rel}	I_γ^{rel}	I_γ^{rel}
151.8(4)	100(8)	100(3)	100(4)
159.7(4)	11(1)	8.0(8)	10(2)
283(2)	5(5)	-	-
326.9(1)	44(3)	44(3)	47(3)
486.5(2)	9(1)	6.7(11)	8(2)
578.8(2)	34(2)	28(3)	35(3)
743(1)	4(1)	3.5(14)	4(1)
764.0(2)	3(1)	-	-
884.5(2)	9(1)	-	-
1059.5(1)	12(1)	14(1)	15(2)
1090.2(2)	38(3)	33(3)	35(3)

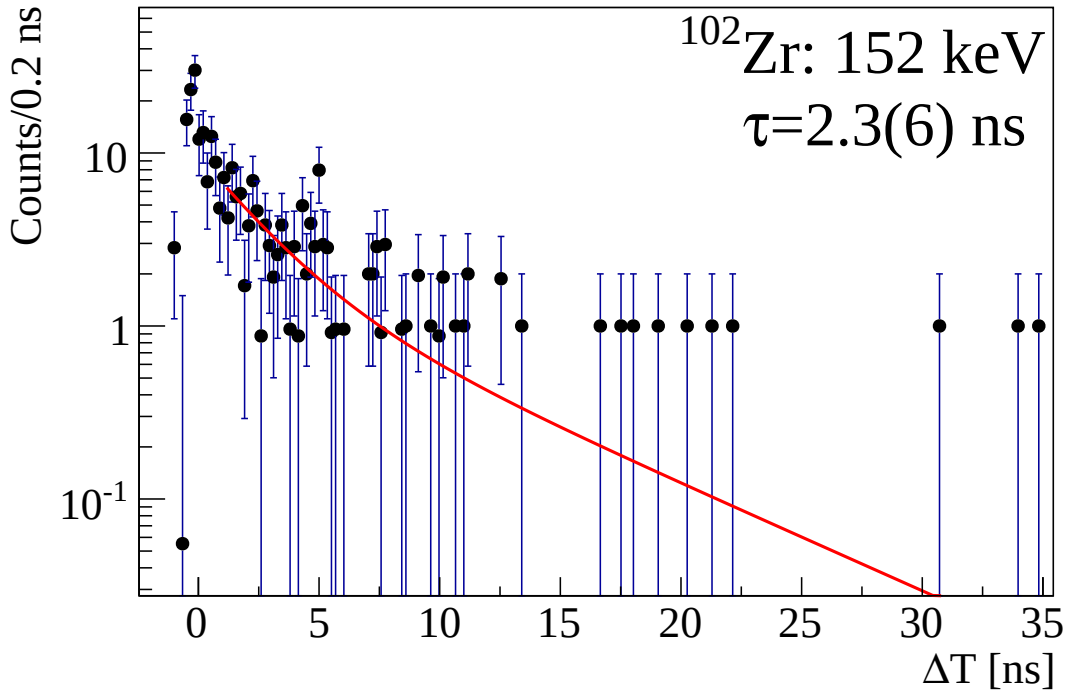

Figure 5.13: The background-subtracted time-difference spectrum of the 152-keV $2_1^+ \rightarrow 0_{g.s}^+$ transition obtained from the projections of the energy-time matrix shown in Fig. 5.8. The red line is the result of a M.L.M. fit of Eq. 5.12.

transitions, of the decay distribution of the 2_1^+ state would take the form [97],

$$E'(t) = \frac{a_0 \tau_{2+}}{\tau_{4-} - \tau_{2+}} \left[\exp\left(\frac{t}{\tau_{4-}}\right) - \exp\left(\frac{t}{\tau_{2+}}\right) \right] + a_1 \exp\left(\frac{t}{\tau_{2+}}\right), \tag{5.12}$$

where τ_{4-} is the lifetime of the 4^- state and is fixed to 7 ns, τ_{2+} is the lifetime of the 2_1^+ state and a_0 and a_1 are constants which relate to the intensity of feeding of the 2_1^+ state from the 4^- state and from other, prompt, transitions, respectively. The result of the M.L.M. fit is shown as the red line in Fig. 5.13, which gives the most probable value of τ_{2+} as 2.3(6) ns, which is within one standard deviation of the literature value of $\tau = 2.6(5)$ ns [101]. The fit values of the parameters a_0 and a_1, are 0.2(6) and 10(2), respectively, the ratio of which is consistent with the transition intensities listed in Tab. 5.1.

5.7 Lifetime measurement of the 2_1^+ state of ^{104}Zr

The case of ^{104}Zr provides an excellent benchmark for the efficacy of the experimental set-up, since its energy-time matrix and delayed energy spectra, Figs. 5.14a and 5.14b, respectively, show no evidence of delayed transitions, other than the $2_1^+ \rightarrow 0_{g.s}^+$ transition. The signal and background of the time-difference spectra of the $2_1^+ \rightarrow 0_{g.s}^+$ transition were selected in the same manner as described in Sec. 5.6, i.e. the 140-keV energy peak was used to select the signal and only a higher energy background was selected. The resultant spectrum is shown in Fig. 5.14c. By virtue of the absence of feeding transitions with significant delayed components, it is possible to extract the lifetime using two approaches. The first fitted a single decay component, Eq. 5.3, to the delayed shoulder of the time-difference distribution between the limits of 2 and 10 ns, as shown by the dotted blue curve of Fig. 5.14, which yielded $\tau = 3.0(4)$ ns. Secondly, the solid red curve shows the result of using the convolution of the detector resolution and an exponential decay as the fit function, given by Eq. 5.7, which gives $\tau = 2.87(20)$. In this case, the values and uncertainties were obtained through the method described in Sec. 5.4 and depicted in Fig. 5.5. The weighted mean value of the results from the two methods gives $\tau = 2.90(23)$, which is in agreement with the value of Ref. [26] of 2.89(43) ns, but with a higher precision. Whilst the delayed components of the feeding transitions are too short to be observed with the experimental set-up, their influence on the measured lifetime should be included as a systematic uncertainty. The intensity corrected peak areas from the EURICA singles spectrum show that the predominant feeding of the 2_1^+ state in ^{104}Zr is from the 4_1^+ state. Although the lifetime of this state is as yet unmeasured, an estimate of it can be made from the systematics of the known values in the region as ∼50 ps [102, 103, 104], which is included as the upper limit to the uncertainty. Therefore, the result obtained in this work is 2.90^{+25}_{-20} ns.

5.8 Lifetime of the 2_1^+ state in ^{106}Zr

As with ^{104}Zr, the energy-time matrix, Fig. 5.15a, and the delayed energy spectrum, Fig. 5.15b, show no delayed components other than that of the $2_1^+ \rightarrow 0_{g.s}^+$ transition. Therefore, the procedure of extracting τ from Fig. 5.15c is carried out in the same way as described in Sec. 5.7. The result of the single decay component fit gives,

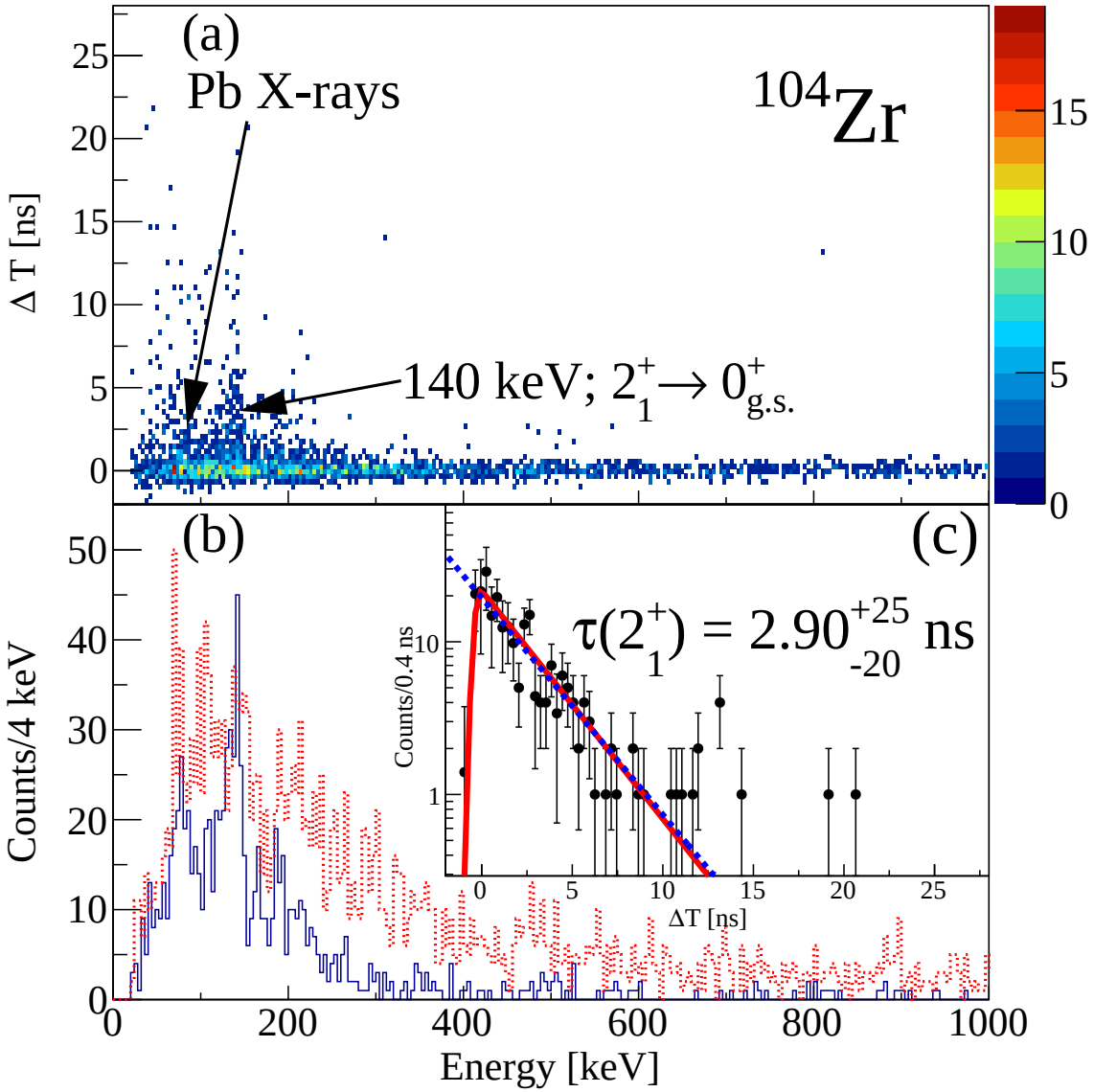

Figure 5.14: (a) Energy-time-difference matrix observed in coincidence with β-electrons detected within 1 s of an ^{104}Y implantation. (b) The γ-ray energy spectrum of the delayed (solid blue) and prompt (dashed red) components of the matrix. (c) Background subtracted time difference spectrum for the $2^+_1 \rightarrow 0^+_{g.s}$ transition. (See text for details of the fits).

$\tau = 2.63(36)$ ns, and the fit of the convolution giving $\tau = 2.59(16)$ ns. The weighted mean is $\tau = 2.60(15)$ ns. The uncertainty is lower than in the case of ^{104}Zr, due to the higher statistics accumulated for this nuclide. However, the same 50 ps upper limit on the uncertainty must be included, yielding a result of $\tau = 2.60^{+20}_{-15}$ ns.

5.9 New isomeric states

New isomeric states have been discovered in ^{113}Nb and ^{115}Mo through the observation of delayed energy structures in the EURICA spectrum with respect to their implantation time.

The construction of the energy-time matrices employs the add-back algorithm to increase statistics and reduce background. In the event of the add-back routine being implemented, it is the time of the first γ-ray interaction which is used as the time for the energy-summed event. The time-difference is then between the time of an ion implantation, provided by the F11 plastic, and the γ-ray time measurement.

5.9.1 The energy and lifetime of an isomeric state in ^{113}Nb

The energy-time matrix in Fig. 5.16a shows a clear long-lived component, with an energy determined by a Gaussian fit to the peak shown in the energy projection of Fig 5.17, to be 135.3(5) keV. The inset of Fig. 5.17 shows the background-subtracted time-difference spectrum of the 135 keV transition, where red line represents a fit of Eq. 5.3, whose limits are outside of the prompt-flash region and yields a result of $\tau = 9(2)$ μs for the state the γ ray depopulates.

5.9.2 The energy and lifetime of an isomeric state in ^{115}Mo

The energy-time matrix of ^{115}Mo, Fig. 5.18, shows a very long-lived distribution, which even extends further than the 110 μs range of the acquisition gate. The energy projection of the matrix shown in Fig. 5.18 shows an additional two peaks of low intensity. The strongest transition's energy is 187.8(5) keV, and the other two have energies of 94(1) keV and 198.5(5) keV. There exist no observable coincidences between the γ rays. The lifetime of the state from which the 187.8 keV transition originates was measured by using the p.d.f. defined in Eq. 5.3 to obtain a value of 50(5) μs.

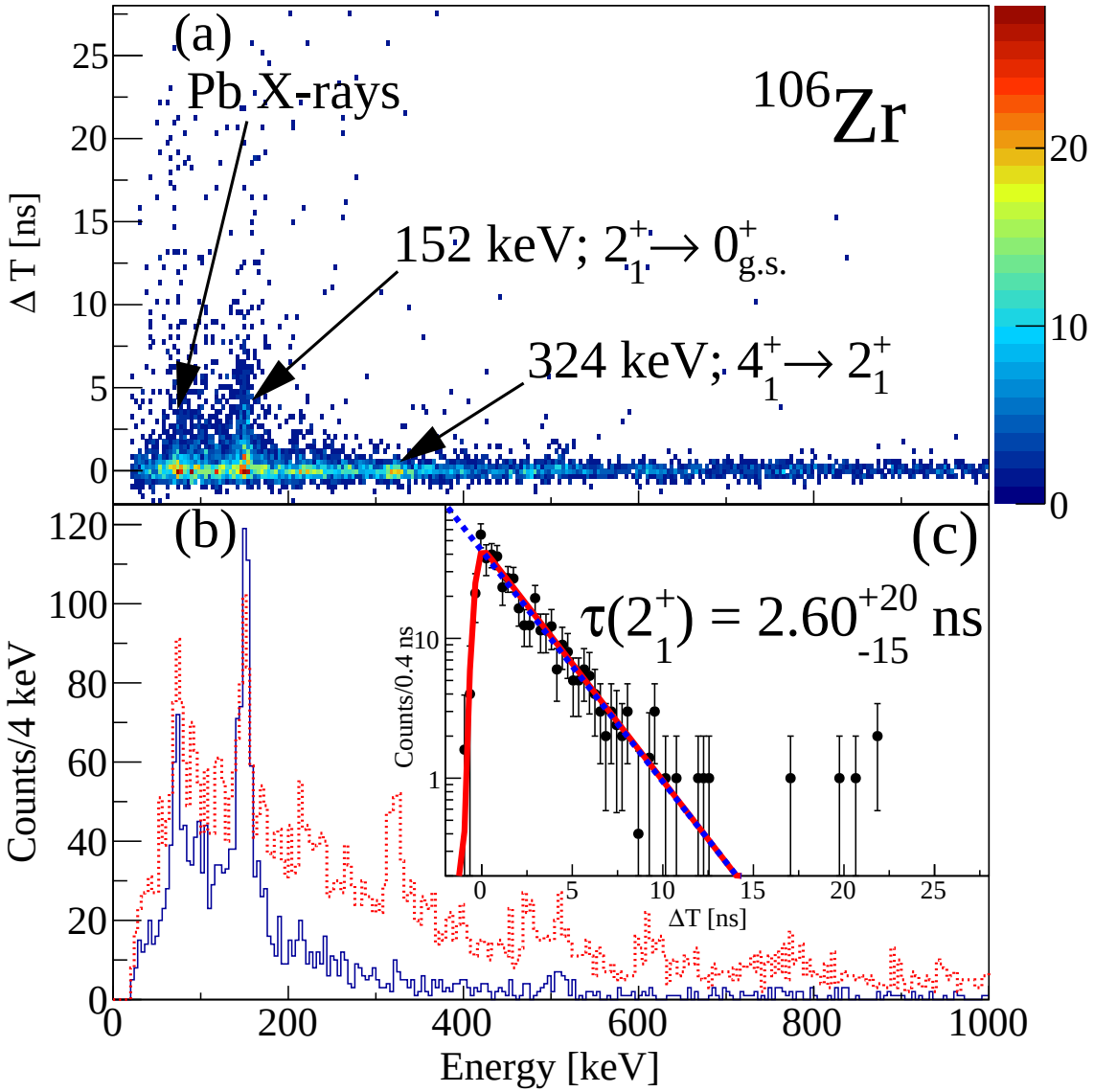

Figure 5.15: (Color online) (a) Energy-time-difference matrix observed in coincidence with β-electrons detected within 0.3 s of an ^{104}Y implantation. (b) The γ-ray energy spectrum of the delayed (solid blue) and prompt (dashed red) components of the matrix. (c) Background subtracted time difference spectrum for the $2^+_1 \rightarrow 0^+_{g.s}$ transition (See text for details of the fits).

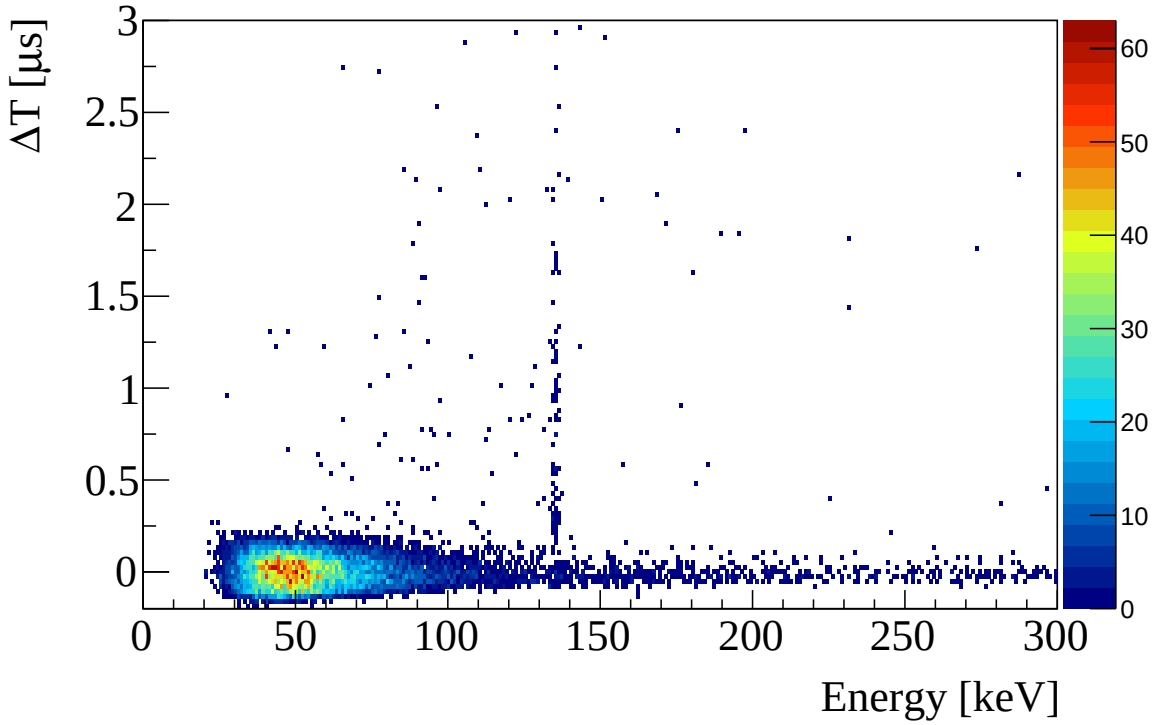

Figure 5.16: The energy-time matrix associated with the implation of ^{113}Nb ions. The isomeric transition at 135 keV is very clear.

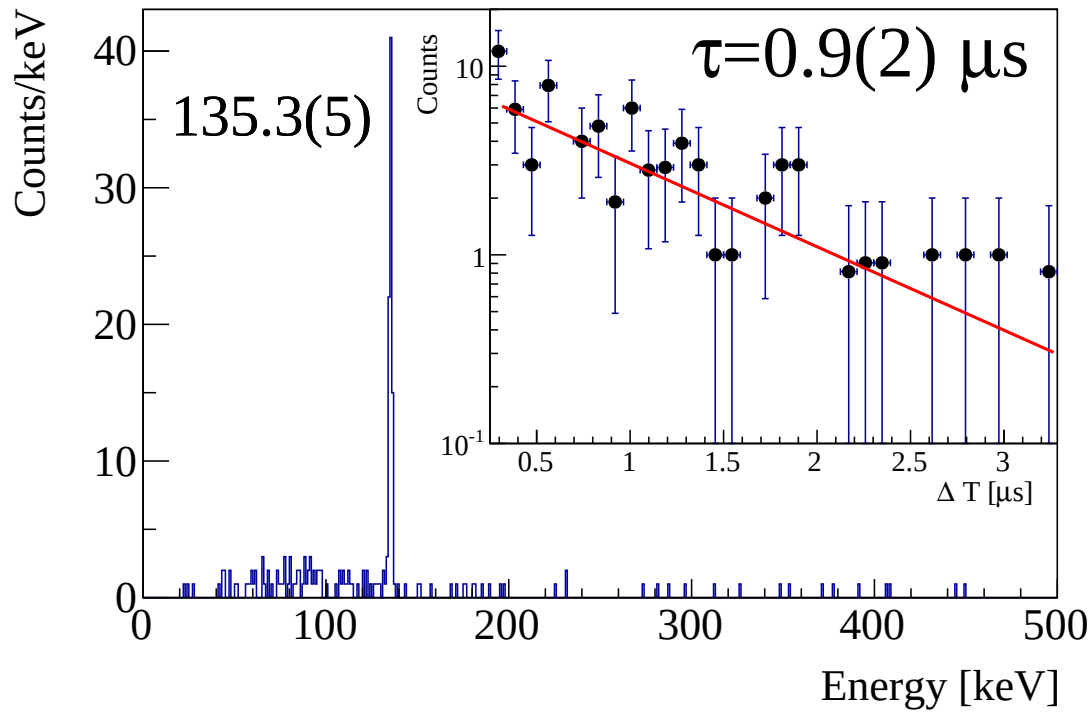

Figure 5.17: The time-projected energy spectrum of Fig. 5.16, between the limits of 0.2 and 3 μs. The inset shows the background-subtracted time-difference spectrum of the 135-keV transition.

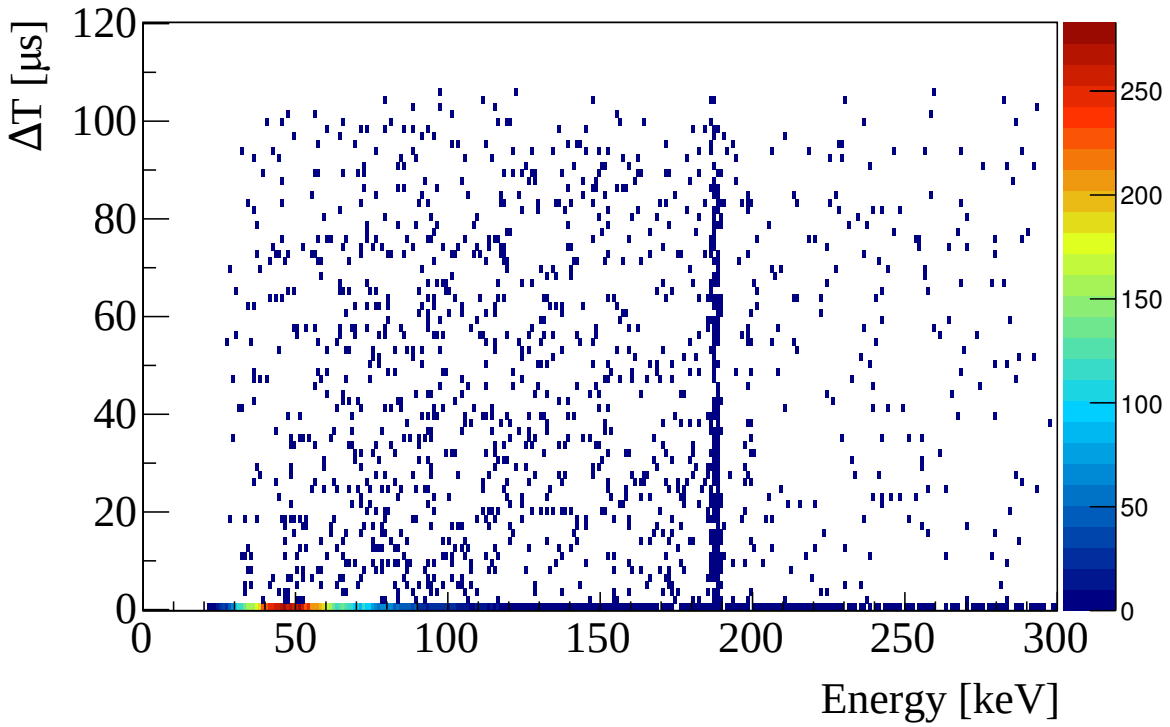

Figure 5.18: The energy-time matrix associated with the implantation of ^{115}Mo. The isomeric transition at 188 keV very clear and very long-lived, so long, in fact, that the decay component goes even beyond the 110 μs range of the acquisition gate.

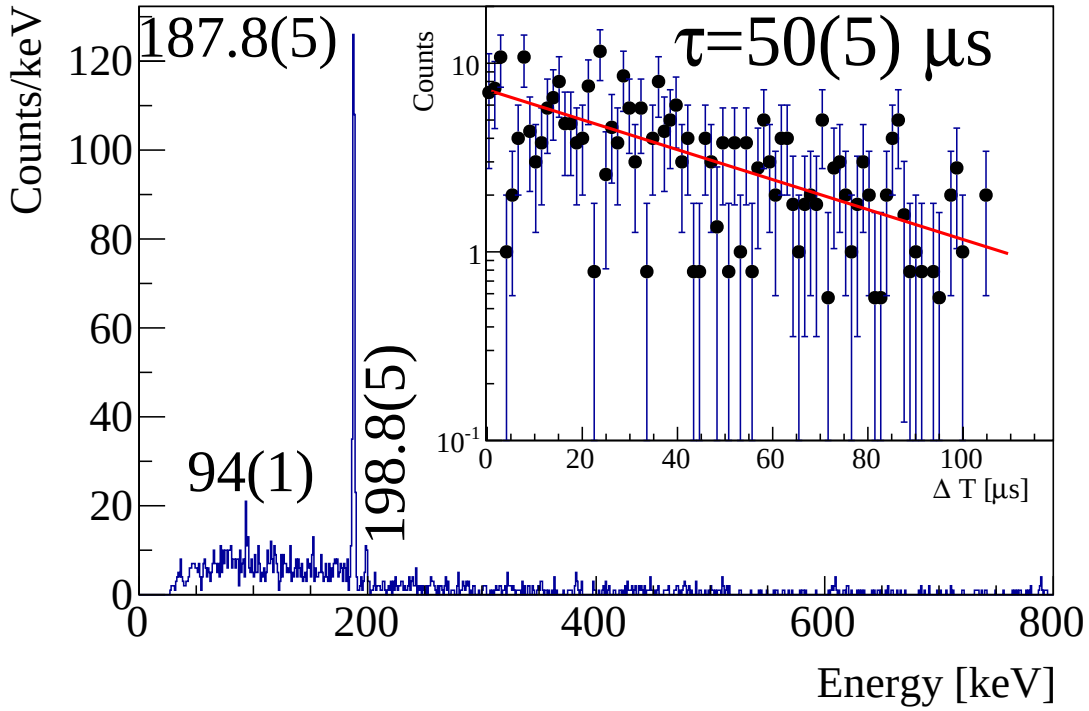

Figure 5.19: The time-projected energy spectrum of Fig. 5.18, between the limits of 0.2 and 110 μs. The inset shows the background-subtracted time-difference spectrum of the 188-keV transition.

Chapter 6

Interpretation of results

Detailed here are the interpretations of the results reported in Chap. 5, specifically the isomerism of the 4^- state in ^{102}Zr, the lifetimes of the 2_1^+ states of ^{104}Zr and ^{106}Zr, and the isomerism present in ^{113}Nb and ^{115}Mo. The isomerism of the 4^- state in ^{102}Zr shall be discussed in terms of a change of configuration between it and the 3^+ state to which it decays. The reduced transition probabilities of the ground-state transitions shall be determined for ^{104}Zr and ^{106}Zr, and from these the ground-state deformations will be derived from a model-dependent relation. Isomerism of the odd-odd ^{113}Nb and even-odd ^{115}Mo shall be discussed in terms of shape stabilisation.

6.1 The lifetime of the 4^- state of ^{102}Zr

The 4^- state is suggested [98] to be a $K^\pi = 4^-$ 2 quasi-neutron state with configuration, $\nu\frac{5}{2}^-[532] \otimes \nu\frac{3}{2}^+[411]$, which decays via a 579-keV transition into a 3^+ state which is a member of the γ-vibrational band [95, 96], see Fig. 5.7. The coefficients of angular correlation measured in Ref. [96] of the $4^- \xrightarrow{579\text{ keV}} 3^+ \xrightarrow{1090\text{ keV}} 2^+$ cascade are consistent with a pure dipole transition for the 579-keV transition, and a quadrupole transition for the 1090-keV. The pure dipole character suggests an $E1$ transition, as opposed to the mixed $M1/E2$ transition, which indicates the change of parity between the 4^- and 3^+ states.

The hindrance factor of a transition is defined as the ratio of the observed γ-ray transition lifetime, τ_γ, to the single-particle, or Weisskopf lifetime estimate, τ_W [105]. If the measured lifetime is much larger than the Weisskopf estimate there is little

overlap between the wavefunctions of the initial and final states. However, should the measured lifetime be much faster than τ_W many nucleons with coherent wavefunctions are involved in the transition.

The result reported in Sec. 5.6 of $\tau = 7(2)$ ns corresponds to the total decay rate of the 4^- state, therefore, the competing decay modes must be accounted for in order to make the comparison with the Weisskopf estimate of the 579-keV transition. The works of Refs. [98] and [96] report 283- and 1343-keV γ-decays competing with the prominent 579-keV transition to depopulate the 4^- state. Whilst Ref. [98] does not quote intensities, the decay scheme presented shows very small and equal intensities for the 283- and 1343-keV transitions. Conversely, Ref. [96] reports a much stronger intensity for the 283-keV transition, see Tab. 6.1. If the correct intensity of the 283-keV transition was that in Ref. [96], its peak should be larger than the 579-keV peak observed in the 160-keV-gated spectrum shown in Fig. 5.10. However, there is no evidence of a peak at 283 keV in the spectrum displayed in Fig. 5.10 suggesting a much lower intensity of this transition than reported in Ref. [96]. The relative intensities of the 283- and 1343-keV transitions relative to the 579-keV transitions obtained from this work are shown along side those from Refs. [98] and [96] in Tab. 6.1. Due to the low intensity and relatively high energy of the 1343-keV transition, it was not observed at all in the EURICA spectrum. However, an upper limit can be imposed on its intensity based on an assumption that only 5 counts would be required for the peak to be observable above background. The intensities, with respect to the 579-keV transition, of the 283- and 1343-keV γ rays are given in Tab. 6.1. It is evident from the values of Tab. 6.1 that the results reported in this work are consistent with those of Ref. [98], a possible explanation of the discrepancy in the work of Ref. [96] could be their inclusion of the 283.5-keV transition in ^{147}Ce, the fission partner of ^{102}Zr, in their energy spectra.

Additional to the γ-decay modes are the internal conversions of the transitions, whereby the energy of the transition is imparted directly to an electron whose wavefunction overlaps with that of the excited state. The probability of the internal conversion is given the coefficient, α, and is calculated by the online BrIcc code [106] and given in the last column of Tab. 6.1. The partial γ-ray lifetime of the $4^- \rightarrow 3^+$

Table 6.1: Summary of intensities of transitions depopulating the 4^- state in ^{102}Zr. Intensities are normalised to the 579-keV transition. The x represents an unknown, but equal value for the intensity, and is assumed to be less than 25% based on the line thickness of the level scheme presented in Ref. [98].

	I_γ [%]			
E_γ [keV]	^{248}Cf(S.F.)[98]	^{252}Cf(S.F.)[96]	This work	α[106]
283	x	76	6(3)	0.005695
579	100	100	100(13)	0.0009151
1343	x	6	<6	0.0003028

(579 keV) transition is then,

$$\tau_\gamma = \tau_{\text{level}}\left(1 + \alpha_{579} + I_\gamma(283)(1+\alpha_{283}) + I_\gamma(1343)(1+\alpha_{1343})\right), \tag{6.1}$$

$$= 7.86(200)\text{ ns}, \tag{6.2}$$

where the last terms of Eq. 6.1 represent the contribution to the measured lifetime from the 283- and 1343-keV transitions, respectively.

The Weisskopf estimate of the lifetime of the transition is given by [107],

$$\tau_W = \left(1.03 \times 10^5 A^{2/3} E_\gamma^3\right)^{-1}, \tag{6.3}$$

where A is the atomic mass of the nuclide, and E_γ is the energy of the γ-ray transition in keV. For $E_\gamma = 579$ keV and $A = 102$,

$$\tau_W = 2.36 \times 10^{-6}\text{ ns}. \tag{6.4}$$

Then the Weisskopf hindrance of the transition is,

$$F_W = \frac{\tau_\gamma}{\tau_W}, \tag{6.5}$$

$$= 3.3(8) \times 10^6. \tag{6.6}$$

The Rusinov rule [108] states that the hindrances, F_W, should, for a transition between

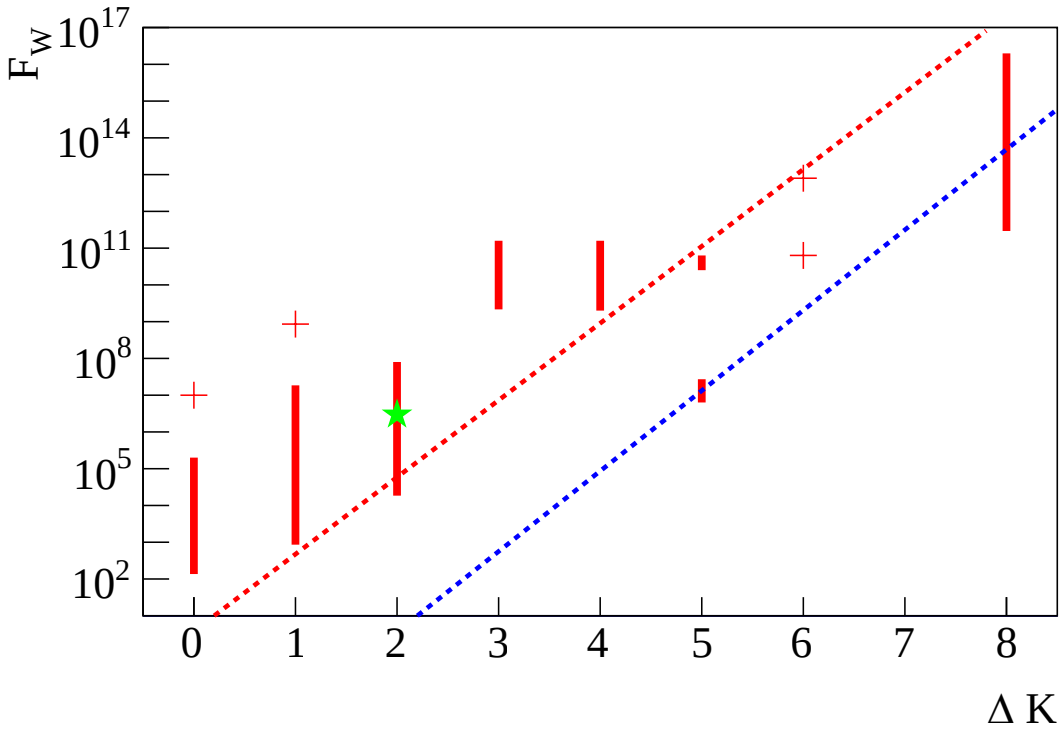

Figure 6.1: Hindrance factors, F_W, of a γ-ray transition of multipolarity $E1$ as a function of the change in the K quantum number of the transition. The red bars and crosses are the ranges and points of the experimentally confirmed hindrances with a change of K. The dashed blue line is the emprical relation of Eq. 6.7. The dashed red line is intended to guide the eye through the data points. The green star is the hindrance of the 579-keV transition in ^{102}Zr. Figure adapted from Ref. [105].

states with good quantum number, K, follow the empirical relation,

$$\log F_W \;=\; 2\,(|\Delta K| - \lambda)\,, \tag{6.7}$$

where ΔK is the change in the K quantum number between the initial and final states, and λ is the multipolarity of the radiation emitted. For an $E1$ transition, Eq. 6.7 is plotted in Fig. 6.1 as the dashed blue line, along with the ranges and points of the measured hindrance factors, red bars and crosses, respectively. As stated in Ref. [105], Rusinov's rule represents well the trend of the hindrance factors as a function of K-forbiddenness, albeit shifted to higher values, as demonstrated by the translation of the dashed blue line in Fig. 6.1 with respect to the data. The collected experimental data's trend is shown by the dashed red line of Fig. 6.1 and the value obtained for the 579-keV transition, depicted by the green star, is consistent with those previously measured

hindered transitions which change the K quantum number by 2. Therefore, the nature of this isomeric state is interpreted as a change in structure from the intrinsic $K^\pi = 4^-$ 2 quasi-neutron state to the collective $K^\pi = 2^+$ state in the γ-vibrational band.

6.2 The shape evolution of zirconium isotopes

In even-even nuclei, the lifetime measurements of the 2_1^+ states, in conjunction with their energy, provides a precise, albeit model-dependent, value of a nuclide's ground-state deformation. To obtain this, the reduced transition probability, $B(E2; 2_1^+ \rightarrow 0_{g.s.}^+)$, values must be computed, which provide access to the intrinsic quadrupole moment, Q_0, of the nucleus, which provides the ground-state quadrupole deformation, β_2, assuming that the first excited state is purely rotational.

The reduced transition probability is related to the lifetime and energy measurements by the following relation [101][1],

$$B(E2; 2_1^+ \rightarrow 0_{g.s.}) = \frac{8.162 \times 10^{10}}{\tau_\gamma E_\gamma^5}, \tag{6.8}$$

where τ_γ is as described by Eq. 6.1 in nanoseconds, and E_γ is the transition energy in keV. The data points of $B(E2; 2_1^+ \rightarrow 0_{g.s.}^+)$ values shown in Fig. 6.3a were obtained following the prescription of Ref. [101], that is, that upper and lower limits of $B(E2; 2_1^+ \rightarrow 0_{g.s.}^+)$ were calculated according to the uncertainties on the values of τ, E_γ and α (for the determination of τ_γ). For the upper limit, $B(E2)^+$, the values

$$E_\gamma^+ = E_\gamma + \sigma_{E\gamma}, \tag{6.9}$$

$$\tau^- = \tau - \sigma_\tau, \tag{6.10}$$

$$\alpha^- = \alpha - \sigma_\alpha \tag{6.11}$$

[1]This is modified from Eq. 1 in Ref. [101] to reflect a *de-excitation* of a 2_1^+ state and so that τ is expressed in nanoseconds.

were used in Eq. 6.8, and for the lower limit, $B(E2)^-$,

$$E_\gamma^- = E_\gamma - \sigma_{E\gamma}, \tag{6.12}$$

$$\tau^+ = \tau + \sigma_\tau, \tag{6.13}$$

$$\alpha^+ = \alpha + \sigma_\alpha, \tag{6.14}$$

were used. The quoted $B(E2)$ value is then given by,

$$B(E2) = \frac{1}{2}\left[B(E2)^+ + B(E2)^-\right], \tag{6.15}$$

and the uncertainty given by,

$$\sigma_{B(E2)} = B(E2) - B(E2)^- \equiv B(E2)^+ - B(E2). \tag{6.16}$$

The authors of Ref. [101] suggest this procedure better represents the range of $B(E2)$ values from a lifetime measurement which has relatively large ($\gtrsim 10\%$) and asymmetric uncertainties. It is, therefore, well suited to the lifetime measurements of the 2_1^+ states presented in Secs. 5.7 and 5.8 which both have an asymmetric error and relative uncertainties of $\sim$7%. This procedure yields values of 0.39(2) $e^2\text{b}^2$ and 0.31(1) $e^2\text{b}^2$ for ^{104}Zr and ^{106}Zr, respectively. These values, along with those for the $96 \leq A \leq 102$ Zr isotopes are given in Tab. 6.2.

We now transform the observational value of the reduced transition probability into values which have a deeper physical meaning. The square of the intrinsic quadrupole moment from the $B(E2)$ is computed by [43],

$$Q_0^2 = \frac{16\pi B(E2)}{5\left|\langle J_i K 20 | J_f K\rangle\right|^2}, \tag{6.17}$$

where the $|\langle J_i K 20|J_f K\rangle|$ is the Clebsch-Gordon coefficient. Under the assumption that the 2_1^+ state is purely rotational and has $K = 0$, the Clebsch-Gordan coefficient is $|\langle 2020|00\rangle|$ and has the value $\sqrt{1/5}$ [109]. Therefore, Eq. 6.17 can be simplified to,

$$Q_0 = \sqrt{16\pi B(E2)}. \tag{6.18}$$

It should be noted that as a consequence of Eqs. 6.17 and 6.18, the sign of Q_0, which

shows whether the nucleus is prolate, or oblate, is indeterminable using this method.

Assuming a quadrupoloid shape (as described in Eq. 2.12) and that the deformation is the same for both states, the intrinsic quadrupole moment is related to deformation by [39],

$$Q_0 = \frac{3}{\sqrt{5\pi}} Z R^2 \beta_2 \left(1 + \frac{2}{7}\sqrt{\frac{5}{\pi}}\beta_2 + \frac{1}{14\pi}\beta_2^2\right), \tag{6.19}$$

where Z is the atomic number of the nucleus, and R is the radius of the nucleus if its same volume were to be spherically distributed, given in fm by $1.2A^{1/3}$, where A is the atomic mass of the nucleus. Equation 6.19 is depicted for ^{106}Zr by the blue line of Fig. 6.2. To determine β_2, Eq. 6.19 was solved numerically for the experimental value of Q_0 obtained from Eq. 6.18 and this is depicted as the solid black line on Fig. 6.2. The uncertainties associated with this value of β_2 were obtained by finding the corresponding values of β_2 for $Q_0 + \sigma_{Q0}$ and $Q_0 - \sigma_{Q0}$, shown as the dashed red lines in Fig. 6.2. The results of these calculations are presented in the last column of Tab. 6.2 and shown in Fig. 6.3b.

The β_2 values extracted for ^{104}Zr and ^{106}Zr are $\beta_2 = 0.39(1)$ and $0.36(1)$, respectively, assuming a purely rigid-rotational model. The observation that the $E(4_1^+)/E(2_1^+)$ ratios, shown in Fig. 6.3c, approach the limiting value of 3.33 for $N > 60$, provides evidence that the rigid-rotor model is a good approximation in which to interpret these nuclei. Moreover, the FRDM discussed in Sec. 2.7 suggest that the higher multipole shapes shall be small for both ^{104}Zr and ^{106}Zr. Therefore, the effects of non-rotational aspects of the 2_1^+ state, and small perturbations to the quadrupole shape should have a small effect on the uncertainty of the β_2 values for ^{104,106}Zr. The new lifetime measurement shows that ^{104}Zr is the most deformed of the neutron-rich Zr isotopes, assuming axial symmetry and rigid-rotational excitation. Whilst the approximation of axial symmetry doesn't hold for the $N < 60$ isotopes, the calculation of their β_2 values still effectively demonstrates the rapid onset of deformation.

Figure 6.3b compares the extracted model-dependent β_2 values with those calculated using the finite-range droplet model (FRDM) [27] (solid line), as well as prolate and oblate solutions of Hartree-Fock-Bogolyubov (HFB) calculations [29] (red and blue dashed lines, respectively). The FRDM predicts strong prolate minima for $N > 56$, whereas the HFB solutions indicate prolate-oblate shape coexistence with small energy differences between the two shapes, e.g. less 0.5 MeV for $N = 56$, as discussed

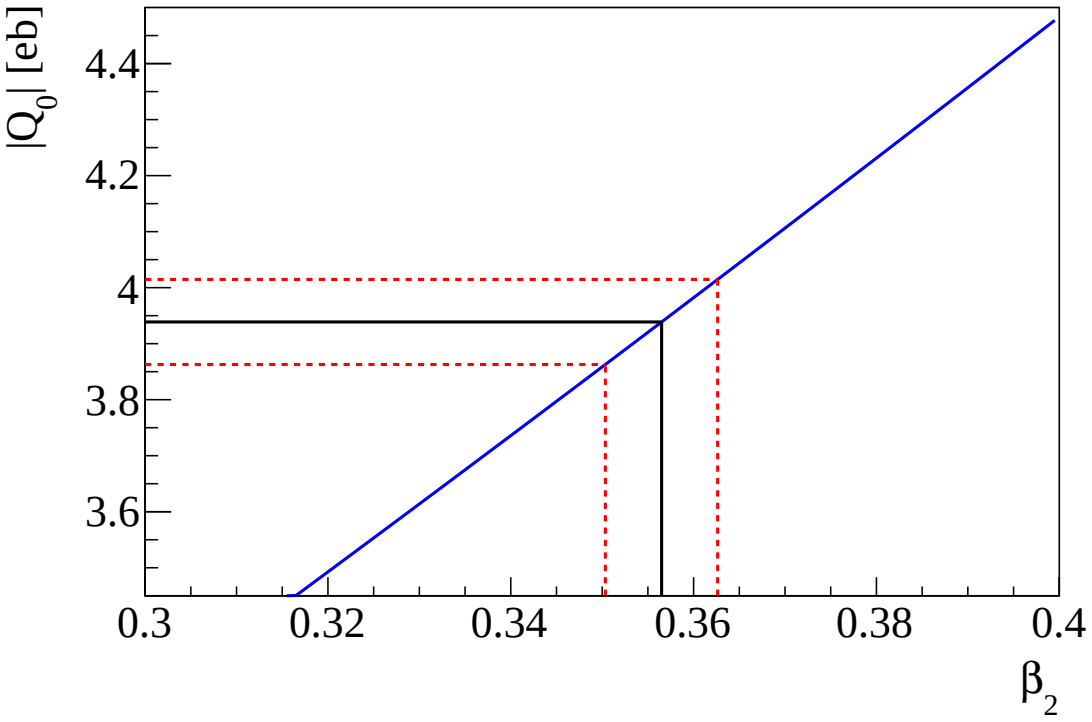

Figure 6.2: The blue line shows the relation between the quadrupole deformation and the intrinsic quadrupole moment, as given by Eq. 6.19, for ^{106}Zr. The solid black line starting from the Q_0 axis represents the experimentally obtained Q_0 value according to Eq. 6.18, and the dashed red lines its associated uncertainties. The solid black and dashed red lines extending towards the β_2 axis are then the corresponding value of β_2 and its associated uncertainties, respectively.

Table 6.2: A summary of the relevant experimental information used to extract the ground-state deformations. The values quoted without citation are those obtained in the current work. The $B(E2)$ values are calculated with Eqs. 6.8, 6.15 and 6.16. The Q_0 values are those derived from the $B(E2)$ value according to Eq. 6.18, and the β_2 values are obtained from Eq. 6.19, assuming a purely rotational model.

A	$E(2_1^+)$ [keV]	$\tau(2_1^+)$ [ns]	$B(E2)$ [e^2b^2]	$\lvert Q_0\rvert$ [eb]	$\lvert\beta_2\rvert$
96	1750.497(15)[13]	5.4(21)$\times10^{-4}$[101]	0.011(4)	0.738(2)	0.0784(2)
98	1222.92(12)[13]	<0.016[110]	>0.002	>0.3	>0.03
100	212.530(9)[13]	0.79(4)[101]	0.22(3)	3.36(4)	0.320(4)
102	151.78(11)[13]	2.6(5)[101]	0.33(4)	4.08(8)	0.376(7)
104	139.3(3)[13]	2.9(4)[26],2.90^{+25}_{-20}	0.39(2)	4.1(1)	0.39(1)
106	152.1(10)[13]	2.60^{+20}_{-15}	0.31(1)	3.94(8)	0.36(1)

in Secs. 2.7 and 2.8. Comparison to the β_2 values extracted from the data strongly supports the conclusion of prolate shapes for the $N > 60$ Zr nuclei, assuming that they

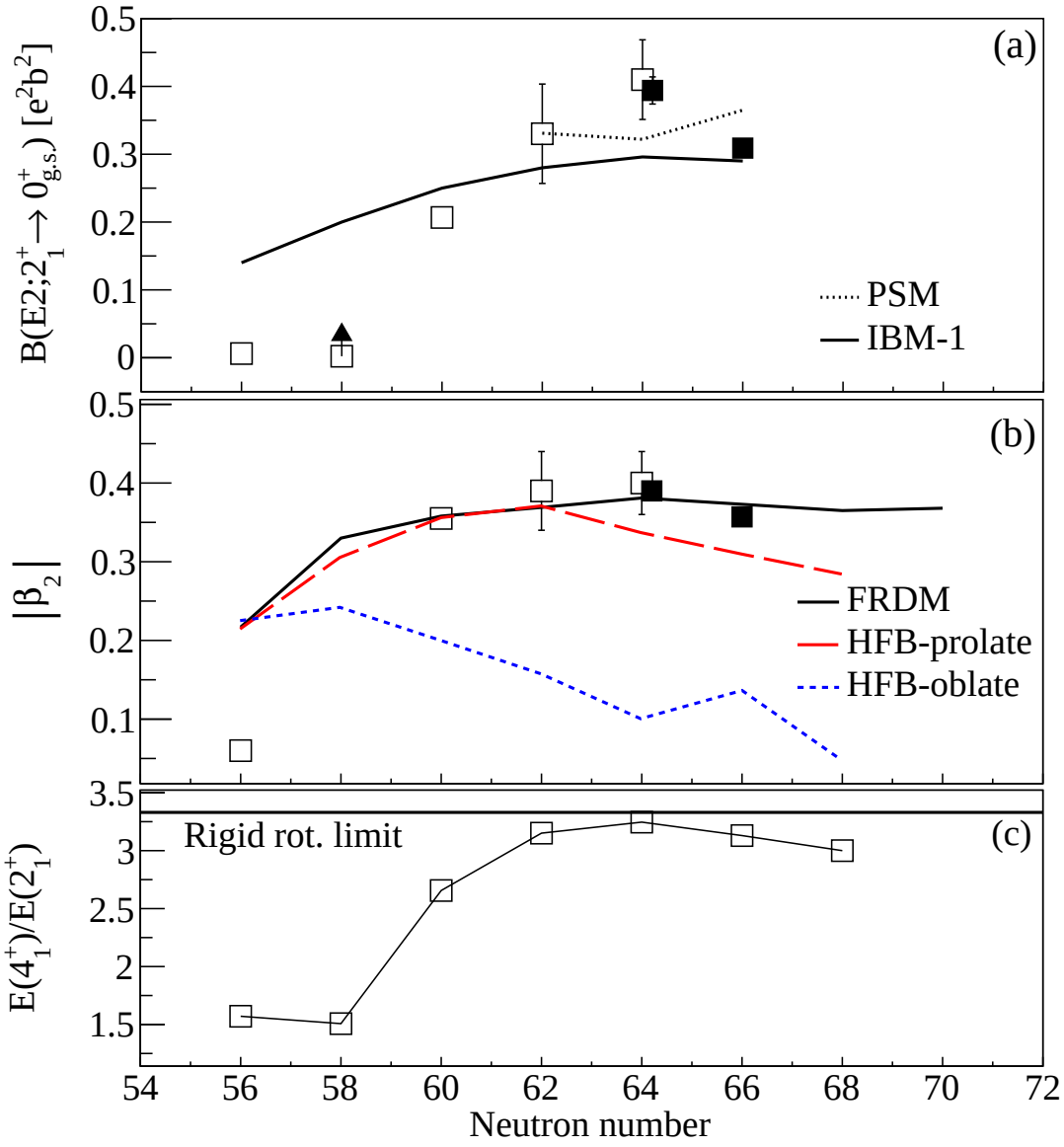

Figure 6.3: (a) Experimental $B(E2; 2_1^+ \rightarrow 0_{g.s.}^+)$ values for even-even $^{96\text{-}106}$Zr isotopes, compared with the results of PSM [63] and IBM-1 [64] calculations. The arrow on the $N = 58$ point reflects the fact the data point is a limit. (b) Experimentally determined β_2 values for $^{96\text{-}106}$Zr, compared with the results of mean-field calculations. (c) The $E(4_1^+)/E(2_1^+)$ ratios for $^{96\text{-}108}$Zr. The open symbols are from Refs. [111, 112, 113, 114, 115, 12] and closed symbols are from the current work.

exhibit purely rotational behaviour.

The direct comparison between experimentally determined $B(E2; 2_1^+ \rightarrow 0_{g.s.}^+)$ values and model predictions provides significant insight into microscopic structure of nuclei. In particular, the projected shell model (PSM) provides the framework in which the single-particle shell model can be applied to deformed nuclei. The PSM calculations depicted in Fig. 6.3a (dotted line) [63] use deformations from Ref. [27] as input pa-

rameters, with the exception of ^{104}Zr for which the β_2 value is artificially reduced. The predicted $B(E2; 2_1^+ \rightarrow 0_{g.s.}^+)$ values are particularly sensitive to the quadrupole-quadrupole interaction [63], which is derived self-consistently with the β_2 parameter, as discussed in Sec. 2.9. Therefore, experimentally derived β_2 values are a valuable constraint to impose on the model.

The solid line in Fig. 6.3a shows the $B(E2; 2_1^+ \rightarrow 0_{g.s.}^+)$ values calculated using the interacting boson model (IBM-1) [64] and the set of global parameters discussed in Sec. 2.10. Whilst the results do show a maximum $B(E2; 2_1^+ \rightarrow 0_{g.s.}^+)$ value at $N = 64$, the maximum calculated value is significantly lower than that observed. This difference could be due to the parameters of the Hamiltonian being obtained through fitting to energy levels and $B(E2)$ values of the triaxially deformed Mo, Pd and Ru nuclei [116, 117, 22, 118] in addition to the well deformed $N \geq 60$ Zr nuclei. Since the energy levels and $B(E2)$ values of triaxial Mo and Ru isotopes are well reproduced [64], the deviation of the calculations to the observations may be attributed to the IBM-1 Hamiltonian not reflecting the axial symmetry of the zirconium nuclei for $N > 60$.

6.3 Proposed nature of newly observed isomeric states

The nature of the isomerism of ^{113}Nb and ^{115}Mo is discussed by first investigating the possible types of transitions de-exciting the isomeric states, based on the hindrances of the γ-ray transitions with respect to the single-particle estimates. The origin of the isomerism is then discussed in terms of the predicted energy differences between competing shapes predicted by macroscopic models, and their comparison to the energy of the transitions involved.

6.3.1 ^{113}Nb

The hindrances of the delayed transitions observed in ^{113}Nb are presented for possible $E1$, $M1$, $E2$ and $M2$ multipolarities in Tab. 6.3. Comparison of the hindrances with the estimates of Ref. [105] suggest that the higher multipole transitions are inconsistent with the lifetime of the decay. The hindrance factor of the $E1$ transition ($5.5(1)\times10^6$) is of the same order as that found for a proposed 114-keV $E1$ transition from an isomeric state discovered in ^{113}Tc (3×10^6) [23]. In the same experiment, an

isomeric state was also discovered in the neighbouring ^{112}Tc, and both ^{112}Tc and ^{113}Tc were interpreted as having an oblate ground-state with a triaxially deformed isomeric configuration. It is then instructive to draw on the results of Ref. [22], which provide evidence that the Mo isotopic chain is transitioning through a γ-soft phase into a region of stable oblate deformation. Since ^{113}Nb has an extra 5 neutrons with respect to ^{110}Mo, it is reasonable to expect that its ground-state is stabilised to an oblate shape. It is predicted from the FRDM that a ground-state deformation transition from prolate to oblate occurs between ^{113}Nb (β_2=0.424) and ^{114}Nb (β_2=-0.224) [27]. The energy difference between the prolate and oblate minima of the neighbouring ^{112}Zr and ^{114}Mo isotopes reported by Ref. [119], are 0.42 and -0.07 MeV, respectively, where a positive number favours a prolate solution. The average energy differences in Zr and Mo is 190 keV, which is similar to the energy of the isomeric transition in ^{113}Nb, 135 keV, suggesting the $E1$ transition is hindered due to a transition from a prolate to oblate shape.

Table 6.3: γ-ray lifetimes and hindrances of the isomeric transition in ^{113}Nb assuming different multipolarities. These are compared to the single-particle estimates, τ_W, to give the hindrance factors, F_W, as in Eq. 6.5.

	$\sigma\lambda$	α[106]	τ_γ [μs]	τ_W [μs]	F_W
E_γ=135.3(5) keV	E1	0.04961	0.95(21)	173×10^{-9}	$5.5(1)\times10^{6}$
	M1	0.09826	1.01(22)	130×10^{-7}	$7.7(2)\times10^{4}$
	E2	0.3865	1.28(28)	0.546	2.3(5)
	M2	0.79	1.77(39)	42.9	0.04(1)

6.3.2 ^{115}Mo

The different intensities of the γ-ray transitions in ^{115}Mo observed in Fig. 5.19 and listed in Tab. 6.4 suggest that they do not form a cascade. The energy of the strong 188-keV transition is twice the value of the weak 94-keV transition, which allows for the possibility that a cascade of two ~94-keV γ rays decays parallel to the 188-keV transition. If the 199-keV transition is also parallel to the strong 188-keV transition, and both proceed to the ground-state, it is possible that the isomeric state has an excitation energy of 199 keV, suggesting that an unobserved and intense 11-keV transition feeds

Table 6.4: Efficiency corrected intensities of γ-ray transitions in ^{115}Mo. Intensities are normalised to the most intense 188-keV transition.

E_γ [keV]	I_γ
94	6(3)
94	6(3)
187.8(5)	100(9)
198.8(5)	8(3)

a 188-keV level. This scenario is depicted in Fig. 6.4.

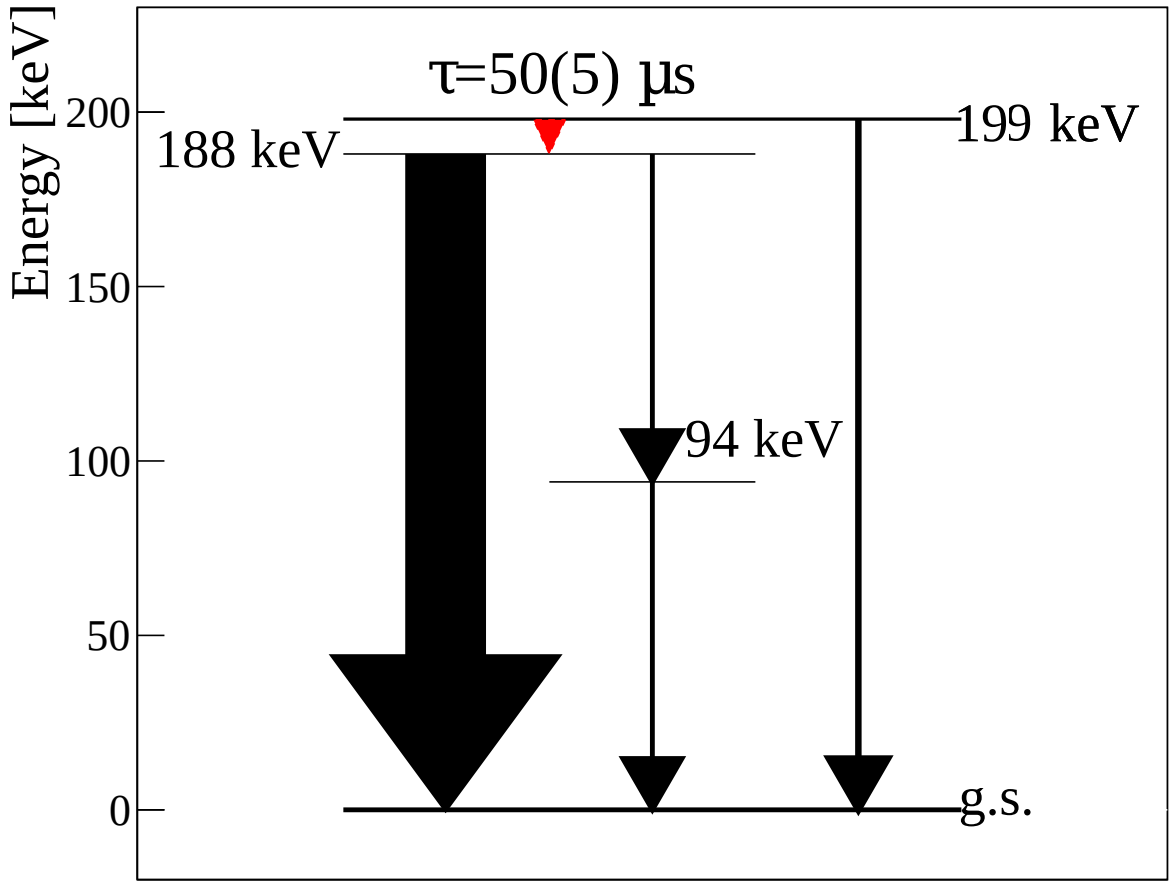

Figure 6.4: Proposed level scheme of ^{115}Mo. The red arrow represents the unobserved 11-keV transition, and the black arrows represent the observed γ-ray transitions. The thickness of the lines of the γ-ray transitions represent their observed intensity. The energy labels refer to the energy.

If it assumed that the 199-keV level is the only isomeric state, then its lifetime is measured in the inset of Fig. 5.19. Therefore, to deduce the possible multipolarities of the 198- and 11-keV transitions, their partial lifetimes should be calculated. Assuming that the 188-keV and 2×94-keV transitions are of $E2$ and $M1$ transition types, based on

energy systematics of the region, respectively, their efficiency- and internal conversion-corrected γ-ray intensities are, 100(7) and 7(2), respectively. All of this intensity should originate from the feeding of the unseen 11-keV transition, which should therefore have an intensity of 107(9), with respect to the 188-keV transition. To determine the multipolarity of the 199-keV transition, its Weisskopf hindrances were calculated for a variety of transition types, these are depicted in Tab. 6.5. Comparison of hindrances to Ref. [105] indicate that the 199-keV transition is most consistent with a multipolarity of $E3$. With the fixed conversion coefficient for the 199-keV transition, hindrance factors of the 11-keV transition can be calculated in a similar fashion to Tab. 6.5. The comparison of the results for the 11-keV transition with Ref. [105] are consistent with both $E1$ and $M1$ transition types, however, based on the arguments of the parities of the levels, here it is tentatively assigned as an $E1$ transition.

Table 6.5: γ-ray lifetimes and hindrances of the 199-keV isomeric transition in ^{115}Mo assuming different multipolarities. These are compared to the single-particle estimates, τ_W, to give the hindrance factors, F_W, as in Eq. 6.5.

	$\sigma\lambda$	α[106]	τ_γ [μs]	τ_W [μs]	F_W
E_γ=198.5(5) keV	E1	0.01750	770(245)	545×10^{-10}	$1.4(4)\times10^{10}$
	M1	0.03934	771(241)	416×10^{-8}	$1.9(6)\times10^{8}$
	E2	0.1027	774(231)	0.079	$9(3)\times10^{3}$
	M2	0.2338	780(213)	6.316	124(34)
	E3	0.5404	796(185)	181×10^{3}	0.004(1)
	M3	1.2800	833(154)	1363×10^{4}	$6(1)\times10^{-5}$
	E4	2.921	915(135)	62×10^{10}	$1.5(2)\times10^{-10}$
	M4	7.901	915(135)	49×10^{12}	$3.9(6)\times10^{-11}$

The FRDM predicts Mo isotopes of $113 < A < 122$ to have an oblate ground-state [27] with ^{115}Mo having $\beta_2 = -0.231$. Based on the proximity of ^{113}Nb and ^{115}Mo in the nuclear chart, ^{115}Mo having one proton and one neutron more than ^{113}Nb, it is expected they would exhibit the same structural phenomena. For ^{116}Mo, the calculated energy difference between the prolate and oblate minima is large, 2.22 MeV, and favours an oblate ground-state [119]. It is possible that the prolate minimum could be lower than predicted by Ref. [119], suggesting that, like ^{113}Nb, the excited state is a prolate shape. However, unlike ^{113}Nb, in addition to the transition which de-excites the isomeric state

directly to the ground-state, a cascade is also populated. The energies of the γ rays in the cascade are consistent with a rotational state which has the same, or similar, intrinsic deformation of that of the ground-state, suggesting that the 10-keV transition decays from a prolate shape and feeds an excited oblate state.

6.4 Concluding remarks

The interpretation of the results presented in this chapter begins with evidence that the observed isomeric 4^- state in ^{102}Zr is due to a change in the K-quantum number of the intrinsic states of the initial and final band. From the lifetime measurements of the 2_1^+ states of ^{104,106}Zr the transition probabilities and ground-state deformations are derived assuming a purely rotational ellipsoid. These show a stabilisation of the prolate shape, despite the predicted shape change at $N = 66$ [29]. The isomeric states observed in ^{113}Nb and ^{115}Mo are compared to isomers of a similar nature [23] in the region, and are postulated to have a similar structure of an oblate ground-state with a isomeric state of a different shape, postulated to prolate based on the energy predictions of shape energy differences [119]. This assertion is backed up by the predicted stabilisation of an oblate ground-state in the $Z > 40$, $N > 64$ isotopes [27, 119].

Chapter 7

Concluding remarks

This thesis reports on the γ-ray spectroscopy of states populated through the β-decay of radioactive isotope (RI) beams, as well as of isomeric states populated in the fission process. The focus of those states populated through β-decay was on the first implementation of a fast-timing configurations of stopped RI beams. This unique experiment provided conclusive evidence that ^{106}Zr is prolate deformed, and the maximum deformation is observed before the neutron mid-shell. Through this novel technique, the 4^- state in ^{102}Zr was found to be isomeric. Additionally, a search for nuclear isomers has yielded two erstwhile unknown isomeric states in ^{113}Nb and ^{115}Mo isotopes.

7.1 Overview

Here is recounted a brief overview of the experiment and the key results.

7.1.1 Experiment

The experiment was conducted at the RIKEN Nishina Center, Wakō-shi, Japan, which houses the Radioactive Isotope Beam Factory (RIBF). The relevant ions from the high-intensity cocktail of RI beams were selected by the first stage of the Big RIKEN Projectile Fragment Separator and identified by a combination of its second stage and an ionisation chamber located at the final focal plane of the ZeroDegree Spectrometer. The selected nuclei were implanted into the Wide-range Active Silicon Strip Stopper Array for β and Ion detection (WAS3ABi). If isomeric states were present, their decay would be measured in the EUROBALL-RIKEN Cluster Array

(EURICA) and cerium-doped lanthanum tri-bromide ($LaBr_3(Ce)$) array directly after the implantation. Candidate β-decay events were correlated off-line with their parents, such that β-delayed γ rays could be detected in the EURICA and $LaBr_3(Ce)$ array. If an electron ejected from β-decay was measured in one of the plastic scintillators located up- and down-stream of WAS3ABi, and a β-delayed γ ray was measured in a $LaBr_3(Ce)$ detector, the time resolution of the two events was sufficient to measure lifetimes of excited states in the nanosecond regime.

7.1.2 Results

The lifetime measurements of the 2_1^+ states in ^{104,106}Zr show that ^{104}Zr is the most deformed of the neutron-rich Zr isotopes. Additionally, the comparison of the magnitude of the extracted deformations, which assume purely rotational nuclei, with the results of FRDM and HFB calculations [27, 29] indicate a persistence of prolate deformation.

Moreover, we have demonstrated that the technique of lifetime measurements following the β-decay of RI beams is a feasible method of extracting spectroscopic information at the contemporary limits of experimentally accessible nuclei. Such techniques can be further exploited at the RIBF, and also at future projects such as Facility for Antiproton and Ion Research (FAIR) [120]. The resolution of the $LaBr_3(Ce)$ detectors allowed for the discovery of an isomeric state in ^{102}Zr populated through the β-decay of ^{102}Y, which is said to be a result of K-isomerism. The discovery of transitions originating from isomeric states in two nuclei, ^{113}Nb and ^{115}Mo, have also been reported, and tentatively interpreted as arising from the shape stabilisation of excited states.

7.2 Outlook

Whilst the knowledge of the lifetimes of the yrast states provides information as to the static ground-state deformation of an atomic nucleus, the lifetimes of the sidebands can provide a greater insight into the role of shape-coexistence. An experiment recently performed at the Argonne National Laboratory [121], where a mixed array of $LaBr_3(Ce)$ and HPGe detectors will give better access to these states by virtue of much improved statistics and selectivity of transitions through multiple gates on the

high-purity germanium spectra.

A full understanding of ^{102}Zr and its immediate region rests on its β-decay parent, ^{102}Y. It is of interest due to it having two isomeric states which decay via β-decay, but are difficult to separate. A novel technique using a Penning trap has been demonstrated to be capable of separating such states [122], and is to be implemented at the Ion Guide Isotope Separator On-Line of the Accelerator Laboratory of the University of Jyväskylä (JYFL) to separate the states of ^{102}Y [123].

Since the production cross-section of ^{108}Y is very low in the abrasion-fission reaction, the measurement of its 2_1^+ state's lifetime is unachievable in the method employed in this work. However, the deployment of the Fast Timing Array array [120] at FAIR, which has a high γ-γ efficiency, could be used to determine the lifetime of this state from the time-difference between the $2_1^+ \rightarrow 0_{g.s}^+$ transition and the states which feed the 2_1^+ state.

Since there is no isomeric state present in ^{110}Zr and productions cross-sections of ^{110}Y negligible, its structure can only be probed by in-beam γ-ray spectroscopy of RI beams. Such an experiment has been performed as a part of the Shell Evolution And Search for Two-plus energies At RIBF (SEASTAR) campaign [124], where states of ^{110}Zr were populated through proton knock-out reaction induced by the liquid hydrogen target of the Magic Numbers Off Stability (MINOS) device and subsequent prompt γ rays detected using the Detector Array for Low Intensity radiation 2 (DALI2).

References

[1] O. Haxel, J. H. D. Jensen, and H. E. Suess, "On the "Magic Numbers" in Nuclear Structure," Phys. Rev. **75**, 1766 (1949).

[2] M. G. Mayer, "On Closed Shells in Nuclei. II," Phys. Rev. **75**, 1969 (1949).

[3] W. Nazarewicz, "Microscopic origin of nuclear deformations," Nucl. Phys. A **574**, 27 (1994).

[4] K. Kaneko, M. Hasegawa, T. Mizusaki, and Y. Sun, "Magicity and occurrence of a band with enhanced $B(E2)$ in neutron-rich nuclei ^{68}Ni and ^{90}Zr," Phys. Rev. C **74**, 024321 (2006).

[5] P. E. Garrett, W. Younes, J. A. Becker, L. A. Bernstein, E. M. Baum, D. P. DiPrete, R. A. Gatenby, E. L. Johnson, C. A. McGrath, S. W. Yates, M. Devlin, N. Fotiades, R. O. Nelson, and B. A. Brown, "Nuclear structure of the closed subshell nucleus ^{90}Zr studied with the $(n, n'\gamma)$ reaction," Phys. Rev. C **68**, 024312 (2003).

[6] A. Chakraborty *et al.*, "Collective structure in ^{94}Zr and subshell effects in shape coexistence," Phys. Rev. Lett. **110**, 022504 (2013).

[7] V. Werner *et al.*, "Evidence for the microscopic formation of mixed-symmetry states from magnetic moment measurements," Phys. Rev. C **78**, 031301 (2008).

[8] S. Rinta-Antila, S. Kopecky, V. S. Kolhinen, J. Hakala, J. Huikari, A. Jokinen, A. Nieminen, J. Äystö, and J. Szerypo, "Direct mass measurements of neutron-rich zirconium isotopes up to ^{104}Zr," Phys. Rev. C **70**, 011301 (2004).

[9] J. E. García-Ramos, K. Heyde, R. Fossion, V. Hellemans, and S. De Baerdemacker, "A theoretical description of energy spectra and two-neutron

separation energies for neutron-rich zirconium isotopes," Eur. Phys. J. A **26**, 221 (2005).

[10] S. Anghel, G. Cata-Danil, and N. V. Zamfir, "Structure features revealed from the two neutron separation energies," Rom. Journ. Phys. **54**, 301 (2009).

[11] E. Cheifetz, R. C. Jared, S. G. Thompson, and J. B. Wilhelmy, "Experimental information concerning deformation of neutron rich nuclei in the $A \sim 100$ region," Phys. Rev. Lett. **25**, 38 (1970).

[12] T. Sumikama *et al.*, "Structural evolution in the neutron-rich nuclei ^{106}Zr and ^{108}Zr," Phys. Rev. Lett. **106**, 202501 (2011).

[13] "ENSDF Database," `http://www.nndc.bnl.gov/ensdf/`, Accessed: 2015-02-01.

[14] S. Michiaki and A. Akito, "Shape transition of nuclei with mass around A = 100," Nucl. Phys. A **515**, 77 (1990).

[15] P. Federman and S. Pittel, "Unified shell-model description of nuclear deformation," Phys. Rev. C **20**, 820 (1979).

[16] W. Urban, J. Pinston, T. Rzaça-Urban, A. Złomaniec, G. Simpson, J. Durell, W. Phillips, A. G. Smith, B. Varley, I. Ahmad, and N. Schulz, "First observation of the $\nu 9/2[404]$ orbital in the A$\sim$100 mass region," Eur. Phys. J. A **16**, 11 (2003).

[17] W. Urban, J. Pinston, J. Genevey, T. Rzaça-Urban, A. Złomaniec, G. S. Simpson, J. Durell, W. Phillips, A. G. Smith, B. Varley, I. Ahmad, and N. Schulz, "The $\nu 9/2[404]$ orbital and the deformation in the A$\sim$100 region," Eur. Phys. J. A **22**, 241 (2004).

[18] W. Nazarewicz, *International Conference on Contemporary Topics in Nuclear Structure Physics* (World Scientific, Singapore, 1988) pp. 467–486a.

[19] A. G. Smith *et al.*, "The influence of $\nu h 11/2$ occupancy on the magnetic moments of collective 2_1^+ states in A$\sim$100 fission fragments," Phys. Lett. B **591**, 55 (2004).

[20] P. Campbell, H. L. Thayer, J. Billowes, P. Dendooven, K. T. Flanagan, D. H. Forest, J. A. R. Griffith, J. Huikari, A. Jokinen, R. Moore, A. Nieminen, G. Tun-

gate, S. Zemlyanoi, and J. Äystö, "Laser spectroscopy of cooled zirconium fission fragments," Phys. Rev. Lett. **89**, 082501 (2002).

[21] Y. Luo *et al.*, "Shape transitions and triaxiality in neutron-rich odd-mass Y and Nb isotopes," Eur. Phys. J. A (Suppl.) **25**, 469 (2005).

[22] H. Watanabe *et al.*, "Development of axial asymmetry in the neutron-rich nucleus ^{110}Mo," Phys. Lett. B **704**, 270 (2011).

[23] A. M. Bruce *et al.*, "Shape coexistence and isomeric states in neutron-rich ^{112}Tc and ^{113}Tc," Phys. Rev. C **82**, 044312 (2010).

[24] P.-A. Söderström *et al.*, "Shape evolution in ^{116,118}Ru: Triaxiality and transition between the O(6) and U(5) dynamical symmetries," Phys. Rev. C **88**, 024301 (2013).

[25] H. Mach, F. Wohn, G. Molnár, K. Sistemich, J. C. Hill, M. Moszyński, R. Gill, W. Krips, and D. Brenner, "Retardation of $B(E2; 0_1^+ \rightarrow 2_1^+)$ rates in $^{90\text{-}96}$Sr and strong subshell closure effects in the A∼100 region," Nucl. Phys. A **523**, 197 (1991).

[26] J. K. Hwang, A. V. Ramayya, J. H. Hamilton, Y. X. Luo, A. V. Daniel, G. M. Ter-Akopian, J. D. Cole, and S. J. Zhu, "Half-life measurements of several states in ^{95,97}Sr,^{97,100,104} Zr,^{106} Mo, and ^{148}Ce," Phys. Rev. C **73**, 044316 (2006).

[27] P. Moller, J. Nix, W. Myers, and W. Swiatecki, "Nuclear Ground-State Masses and Deformations," At. Data Nucl. Data Tables **59**, 185 (1995).

[28] M. Bender, P.-H. Heenen, and P.-G. Reinhard, "Self-consistent mean-field models for nuclear structure," Rev. Mod. Phys. **75**, 121 (2003).

[29] R. Rodríguez-Guzmán, P. Sarriguren, L. Robledo, and S. Perez-Martin, "Charge radii and structural evolution in Sr, Zr, and Mo isotopes," Phys. Lett. B **691**, 202 (2010).

[30] K. Hara and Y. Sun, "Projected Shell Model and High-spin Spectroscopy," Int. J. Mod. Phys. E **04**, 637 (1995).

[31] A. Arima and F. Iachello, "Collective Nuclear States as Representations of a SU(6) Group," Phys. Rev. Lett. **35**, 1069 (1975).

[32] C. F. v. Weizsäcker, "Zur Theorie der Kernmassen," Zeitschrift für Physik **96**, 431 (1935).

[33] H. A. Bethe and R. F. Bacher, "Nuclear Physics A. Stationary States of Nuclei," Rev. Mod. Phys. **8**, 82 (1936).

[34] N. Zeldes, A. Grill, and K. Simievic, Mat. Fys. Skr. Dan. Vid. Selsk. **3** (1967).

[35] A. Wapstra, "The 1971 Atomic Mass Evaluation," in *Atomic Masses and Fundamental Constants 4*, edited by J. Sanders and A. Wapstra (Springer US, 1972) pp. 283–293.

[36] K. S. Krane, *Introductory Nuclear Physics*, 3rd ed. (Wiley and sons, New York, 1988).

[37] R. D. Woods and D. S. Saxon, "Diffuse Surface Optical Model for Nucleon-Nuclei Scattering," Phys. Rev. **95**, 577 (1954).

[38] W. F. Hornyak, in *Nuclear Structure*, edited by W. F. Hornyak (Academic Press, New York, 1975) pp. 233 – 283.

[39] K. E. G. Lobner, M. Vetter, and V. Honig, "Nuclear intrinsic quadrupole moments and deformation parameters," Nucl. Data Tab. **A7**, 495 (1970).

[40] K. Alder, A. Bohr, T. Huus, B. Mottelson, and A. Winther, "Study of Nuclear Structure by Electromagnetic Excitation with Accelerated Ions," Rev. Mod. Phys. **28**, 432 (1956).

[41] K. Heyde, *Basic Ideas and Concepts in Nuclear Physics* (Institute of Physics Publishing, Bristol, 1994).

[42] S. G. Nilsson, K. Dan. Vidensk. Selsk. Mat. Fys. Medd. **29** (1955).

[43] R. F. Casten, *Nuclear structure from a simple perspective* (Oxford University Press, Oxford, 1990).

[44] P. Ring and P.Schuck, *The Nuclear Many-Body Problem* (Springer, Berlin, 2000).

[45] A. Bohr and B. R. Mottelson, *Nuclear Structure, volume 2.* (World Scientific, Singapore, 1998).

[46] G. Scharff-Goldhaber and J. Weneser, "System of Even-Even Nuclei," Phys. Rev. **98**, 212 (1955).

[47] E. Wold, "The centrifugal stretching model and the deviation from the L(L+1) rule for rare-earth nuclei," Nucl. Phys. A **130**, 650 (1969).

[48] W. Ogle, S. Wahlborn, R. Piepenbring, and S. Fredkirsson, "Single-Particle Levels of Nonspherical Nuclei In The Region $150 < A < 190$," Rev. Mod. Phys. **43**, 424 (1971).

[49] R. R. Chasman, I. Ahmad, A. M. Friedman, and J. R. Erskine, "Survey of single-particle states in the mass region $A > 228$," Rev. Mod. Phys. **49**, 833 (1977).

[50] V. Strutinsky, "Shell effects in nuclear masses and deformation energies," Nuclear Physics A **95**, 420 (1967).

[51] H. J. Lipkin, "Collective motion in many-particle systems," Annals of Physics **9**, 272 (1960).

[52] Y. Nogami, "Improved superconductivity approximation for the pairing interaction in nuclei," Phys. Rev. **134**, B313 (1964).

[53] A. Arzhanov, *Gogny-Hartree-Fock-Bogolyubov Nuclear Mass Models with Application to r-Process Stellar Nucleosynthesis*, Ph.D. thesis, AlbaNova University Centre (2013).

[54] J. Dechargé and D. Gogny, "Hartree-Fock-Bogolyubov calculations with the $D1$ effective interaction on spherical nuclei," Phys. Rev. C **21**, 1568 (1980).

[55] J. Berger, M. Girod, and D. Gogny, "Microscopic analysis of collective dynamics in low energy fission," Nucl. Phys. A **428**, 23 (1984).

[56] K. Hara and S. Iwasaki, "On the quantum number projection: (I). General theory," Nucl. Phys. A **332**, 61 (1979).

[57] K. Hara and S. Iwasaki, "On the quantum number projection: (III). Simultaneous J- and N-projection," Nucl. Phys. A **348**, 200 (1980).

[58] J. P. Elliott, "Collective Motion in the Nuclear Shell Model. I. Classification Schemes for States of Mixed Configurations," Proc. R. Soc. A **245**, 128 (1958).

[59] V. Velázquez, J. Hirsch, and Y. Sun, "Self-consistency in the projected shell model," Nucl. Phys. A **643**, 39 (1998).

[60] J. Bardeen, L. N. Cooper, and J. R. Schrieffer, "Theory of Superconductivity," Phys. Rev. **108**, 1175 (1957).

[61] Y. Sun and K. Hara, "Fortran code of the Projected Shell Model: feasible shell model calculations for heavy nuclei," Comput. Phys. Commun. **104**, 245 (1997).

[62] Y. Sun and J. Egido, "Angular-momentum-projected description of the yrast line of dysprosium isotopes," Nucl. Phys. A **580**, 1 (1994).

[63] Y.-X. Liu, Y. Sun, X.-H. Zhou, Y.-H. Zhang, S.-Y. Yu, Y.-C. Yang, and H. Jin, "A systematical study of neutron-rich Zr isotopes by the projected shell model," Nucl. Phys. A **858**, 11 (2011).

[64] M. Böyükata, P. V. Isacker, and İ. Uluer, "Description of nuclei in the A∼100 mass region with the interacting boson model," J. Phys. G **37**, 105102 (2010).

[65] X.-W. Pan, T. Otsuka, J.-Q. Chen, and A. Arima, "A pairing effect in γ-soft nuclei," Phys. Lett. B **287**, 1 (1992).

[66] D. D. Warner and R. F. Casten, "Revised Formulation of the Phenomenological Interacting Boson Approximation," Phys. Rev. Lett. **48**, 1385 (1982).

[67] Y. Higurashi, J. Ohnishi, T. Nakagawa, H. Haba, M. Tamura, T. Aihara, M. Fujimaki, M. Komiyama, A. Uchiyama, and O. Kamigaito, "Production of a highly charged uranium ion beam with RIKEN superconducting electron cyclotron resonance ion source," Rev. Sci. Instrum. **83**, 02 (2012).

[68] H. Okuno, J. Ohnishi, N. Fukunishi, T. Tominaka, K. Ikegami, and A. Goto, "Magnets for the RIKEN superconducting ring cyclotron," Proc. 17th Int. Conf. on Cyclotrons and Their Applications, Tokyo, Japan , 373 (2004).

[69] A. S. Nettleton, *A study of the framentation-fission of ^{238}U on a ^{9}Be target at 81 MeV/u*, Ph.D. thesis, Michigan State University (2011).

[70] T. Kubo, D. Kameda, H. Suzuki, N. Fukuda, H. Takeda, Y. Yanagisawa, M. Ohtake, K. Kusaka, K. Yoshida, N. Inabe, T. Ohnishi, A. Yoshida, K. Tanaka, and Y. Mizoi, "BigRIPS separator and ZeroDegree spectrometer at RIKEN RI Beam Factory," Prog. Theor. Exp. Phys. **2012**, 03C003 (2012).

[71] K.-H. Schmidt, E. Hanelt, H. Geissel, G. Münzenberg, and J. Dufour, "The momentum-loss achromat – A new method for the isotopical separation of relativistic heavy ions," Nucl. Instrum. Methods in Phys. Res., Sect. B **260**, 287 (1987).

[72] G. F. Knoll, *Radiation Detection and Measurement* (John Wiley & Sons, Inc, New York, 2000).

[73] H. Kumagai, T. Ohnishi, N. Fukuda, H. Takeda, D. Kameda, N. Inabe, K. Yoshida, and T. Kubo, "Development of Parallel Plate Avalanche Counter (PPAC) for BigRIPS fragment separator," Nucl. Instrum. Methods Phys. Res., Sect. B **317, Part B**, 717 (2013), XVIth International Conference on ElectroMagnetic Isotope Separators and Techniques Related to their Applications, December 2−7, 2012 at Matsue, Japan.

[74] "Delay-line PPAC," http://ribf.riken.jp/BigRIPSInfo/detector/ppac.html, Accessed: 2014-01-01.

[75] K. Kimura, T. Izumikawa, R. Koyama, T. Ohnishi, T. Ohtsubo, A. Ozawa, W. Shinozaki, T. Suzuki, M. Takahashi, I. Tanihata, T. Yamaguchi, and Y. Yamaguchi, "High-rate particle identification of high-energy heavy ions using a tilted electrode gas ionization chamber," Nucl. Instrum. Methods Phys. Res., Sect A **538**, 608 (2005).

[76] S. Pietri, P. H. Regan, Z. Podolyák, D. Rudolph, M. Górska, A. Jungclaus, and M. Pfützner, "First Results from the Stopped Beam Isomer Rising Campaign at GSI," Acta Phys. Pol. B **38**, 1255 (2007).

[77] J. Eberth, P. V. Brentano, W. Teichert, H. Thomas, A. Werth, R. Lieder, H. Jäger, H. Kämmerling, D. Kutchin, K. Maier, M. Berst, D. Gutknecht, and R. Henck, "Development of a composite Ge detector for EUROBALL," Prog. Part. Nucl. Phys **28**, 495 (1992).

[78] A. M. D. Bacelar, *Isomeric ratios of high-spin states in neutron-deficient N≈126 nuclei produced in projectile fragmentation reactions*, Ph.D. thesis, University of Brighton (2011).

[79] http://radware.phy.ornl.gov/gf3/gf3.html.

[80] T. Sumikama, "Private communication," .

[81] http://ribf.riken.jp/BigRIPSInfo/.

[82] https://www.gsi.de/fileadmin/EE/Module/VULOM/vulom4_einsatz.pdf.

[83] J. Hoffmann, N. Kurz, and M. Richter, "TRIVA, VME Trigger Module," GSI Helmholtzzentrum für Schwerionenforschung GmbH (2007).

[84] Z. Y. Xu, *Beta-decay spectroscopy on neutron-rich nuclei in a range of Z = 26 − 32*, Ph.D. thesis, University of Tokyo (2015).

[85] http://www.xia.com/DGF-4C.html.

[86] https://web-docs.gsi.de/~weick/atima/.

[87] N. Fukuda, T. Kubo, T. Ohnishi, N. Inabe, H. Takeda, D. Kameda, and H. Suzuki, "Identification and separation of radioactive isotope beams by the BigRIPS separator at the RIKEN RI Beam Factory," Nucl. Instrum. Methods B **317**, 323 (2013).

[88] http://www.bt.pa.msu.edu/index_cosy.htm.

[89] S. Nishimura, G. Lorusso, Z. Xu, J. Wu, R. Gernhäuser, H. S. Jung, Y. K. Kwon, Z. Li, K. Steiger, and H. Sakurai, "WAS3ABi: The beta-counting system for the EURICA project," RIKEN Accel. Prog. Rep. **46**, 182 (2013).

[90] P. Doornenbal, personal communication.

[91] D. R. Lide, *Handbook of Chemistry and Physics*, 76th ed. (CRC Press, Florida, 1995).

[92] L. Lyons, *Statistics for nuclear and particle physicists* (Cambridge University Press, Cambridge, 1986).

[93] E. Grushka, "Characterization of exponentially modified gaussian peaks in chromatography," Analytical Chemistry **44**, 1733 (1972).

[94] F. James and M. Roos, "Minuit - a system for function minimization and analysis of the parameter errors and correlations," Comput. Phys. Commun. **10**, 343 (1975).

[95] H. Hua, C. Y. Wu, D. Cline, A. B. Hayes, R. Teng, R. M. Clark, P. Fallon, A. Goergen, A. O. Macchiavelli, and K. Vetter, "Triaxiality and the aligned $h_{\frac{11}{2}}$ neutron orbitals in neutron-rich Zr and Mo isotopes," Phys. Rev. C **69**, 014317 (2004).

[96] K. Li *et al.*, "Identification of new collective bands in neutron-rich ^{102}Zr," Phys. Rev. C **78**, 044317 (2008).

[97] H. Bateman, "The solution of a system of differential equations occuring in the theory of radio-active transformations," Proceedings of the Cambridge Philosophical Society **15**, 423 (1910).

[98] J. L. Durell *et al.*, "Pairing strength in neutron-rich isotopes of Zr," Phys. Rev. C **52**, R2306 (1995).

[99] J. C. Hill, D. D. Schwellenbach, F. K. Wohn, J. A. Winger, R. L. Gill, H. Ohm, and K. Sistemich, "Structure of highly deformed ^{102}Zr populated in decay of low- and high-spin isomers of ^{102}Y," Phys. Rev. C **43**, 2591 (1991).

[100] A. M. Bruce *et al.*, "β decay of ^{102}Y produced in projectile fission of ^{238}U," Journal of Physics: Conference Series **381**, 012053 (2012).

[101] S. Raman, C. J. Nestor, and P. Tikkanen, "Transition probability from the ground to the first-excited 2^+ state of eveneven nuclides," At. Data Nucl. Data Tables **78**, 1 (2001).

[102] A. G. Smith *et al.*, "Lifetimes of yrast rotational states of the fission fragments ^{100}Zr and ^{104}Mo measured using a differential plunger," J. Phys. G **28**, 2307 (2002).

[103] C. Hutter *et al.*, "$B(E2)$ values and the search for the critical point symmetry X(5) in ^{104}Mo and ^{106}Mo," Phys. Rev. C **67**, 054315 (2003).

[104] H. Ohm, M. Liang, G. Molnár, and K. Sistemich, "The collectivity in the yrast band of ^{100}Zr: the half-life of the 4_1^+ state," Z. Phys. A **334**, 519 (1989).

[105] K. Löbner, "Systematics of absolute transition probabilities of K-forbidden gamma-ray transitions," Phys. Lett. B **26**, 369 (1968).

[106] T. Kibédi, T. Burrows, M. Trzhaskovskaya, P. Davidson, and C. N. Jr., "Evaluation of theoretical conversion coefficients using BrIcc," Nucl. Instrum. Methods Phys. Res., Sect. A **589**, 202 (2008).

[107] W. D. Hamilton, *The electromagnetic interaction in nuclear spectroscopy* (North-Holland Publishing Company, Oxford, 1975).

[108] L. I. Rusinov, "Nuclear isomerism," Physics-Uspekhi **4**, 282 (1961).

[109] P. Stevenson, "Analytic angular momentum coupling coefficient calculators," Comput. Phys. Commun. **147**, 853 (2002).

[110] L. Bettermann, J.-M. Régis, T. Materna, J. Jolie, U. Köster, K. Moschner, and D. Radeck, "Lifetime measurement of excited states in the shape-phase-transitional nucleus ^{98}Zr," Phys. Rev. C **82**, 044310 (2010).

[111] D. Abriola and A. Sonzogni, "Nuclear data sheets for A = 96," Nucl. Data Sheets **109**, 2501 (2008).

[112] B. Singh and Z. Hu, "Nuclear data sheets for A = 98," Nucl. Data Sheets **98**, 335 (2003).

[113] B. Singh, "Nuclear data sheets for A = 100," Nucl. Data Sheets **109**, 297 (2008).

[114] D. D. Frenne, "Nuclear data sheets for A = 102," Nucl. Data Sheets **110**, 1745 (2009).

[115] J. Blachot, "Nuclear data sheets for A = 104," Nucl. Data Sheets **108**, 2035 (2007).

[116] A. Guessous *et al.*, "Prompt γ-ray spectroscopy of the ^{104}Mo and ^{108}Mo fission fragments," Phys. Rev. C **53**, 1191 (1996).

[117] A. Guessous, N. Schulz, W. R. Phillips, I. Ahmad, M. Bentaleb, J. L. Durell, M. A. Jones, M. Leddy, E. Lubkiewicz, L. R. Morss, R. Piepenbring, A. G. Smith, W. Urban, and B. J. Varley, "Harmonic two-phonon γ-vibrational state in neutron-rich ^{106}Mo," Phys. Rev. Lett. **75**, 2280 (1995).

[118] S. Lalkovski *et al.*, "Two-quasiparticle and collective excitations in transitional ^{108,110}Pd nuclei," Eur. Phys. J. A **18**, 589 (2003).

[119] J. Skalski, S. Mizutori, and W. Nazarewicz, "Equilibrium shapes and high-spin properties of the neutron-rich $A \approx$100 nuclei," Nucl. Phys. A **617**, 282 (1997).

[120] O. J. Roberts, A. M. Bruce, P. H. Regan, Z. Podolyák, C. M. Townsley, J. F. Smith, K. F. Mulholland, and A. Smith, "A $LaBr_3$: Ce fast-timing array for DESPEC at FAIR," Nucl. Instrum. Methods A **748**, 91 (2014).

[121] S. Lalkovski *et al.*, "Sub-nanosecond lifetime measurement with ^{252}Cf source and a hybrid Gammasphere," ANL Proposal (2015).

[122] C. R. Triguero *et al.*, "Trap-assisted separation of nuclear states for gamma-ray spectroscopy: the example of ^{100}Nb," J. Phys. G **39**, 015101 (2012).

[123] A. M. Bruce, C. R. Nobs, E. Gamba, Z. Podolyák, P. M. Walker, G. Simpson, and J. Kurpeta, "The spin, parity and mass of ^{102,102m}Y," Proposal for Nuclear Physics Experiment at JYFL (2015).

[124] P. Doornenbal and A. Orbetelli, "Shell Evolution and Systematic Search for 2_1^+ Energies," Proposal for Nuclear Physics Experiment at RI Beam Factory (2013).

Appendix A

Publication

Physics Letters B 750 (2015) 448–452

Contents lists available at ScienceDirect

Physics Letters B

www.elsevier.com/locate/physletb

Lifetime measurements of the first 2^+ states in ^{104,106}Zr: Evolution of ground-state deformations

F. Browne [a,b,*], A.M. Bruce [a], T. Sumikama [c,b], I. Nishizuka [c], S. Nishimura [b], P. Doornenbal [b], G. Lorusso [b], P.-A. Söderström [b], H. Watanabe [d,b], R. Daido [e], Z. Patel [f,b], S. Rice [f,b], L. Sinclair [g,b], J. Wu [h,b], Z.Y. Xu [i,j], A. Yagi [e], H. Baba [b], N. Chiga [c,b], R. Carroll [f], F. Didierjean [k], Y. Fang [e], N. Fukuda [b], G. Gey [l,m,b], E. Ideguchi [e], N. Inabe [b], T. Isobe [b], D. Kameda [b], I. Kojouharov [n], N. Kurz [n], T. Kubo [b], S. Lalkovski [o], Z. Li [h], R. Lozeva [k], H. Nishibata [e], A. Odahara [e], Zs. Podolyák [f], P.H. Regan [f,p], O.J. Roberts [a], H. Sakurai [i,b], H. Schaffner [n], G.S. Simpson [l], H. Suzuki [b], H. Takeda [b], M. Tanaka [e], J. Taprogge [q,r,b], V. Werner [s,t], O. Wieland [u]

[a] School of Computing, Engineering and Mathematics, University of Brighton, Brighton, BN2 4GJ, United Kingdom
[b] RIKEN Nishina Center, 2-1 Hirosawa, Wako-shi, Saitama 351-0198, Japan
[c] Department of Physics, Tohoku University, Aoba, Sendai, Miyagi 980-8578, Japan
[d] IRCNPC, School of Physics and Nuclear Energy Engineering, Beihang University, Beijing 100191, China
[e] Department of Physics, Osaka University, Toyonaka, Osaka 560-0043, Japan
[f] Department of Physics, University of Surrey, Guildford GU2 7XH, United Kingdom
[g] Department of Physics, University of York, Heslington, York YO10 5DD, United Kingdom
[h] Department of Physics, Peking University, Beijing 100871, China
[i] Department of Physics, University of Tokyo, Hongo, Bunkyo-ku, Tokyo 113-0033, Japan
[j] Department of Physics, University of Hong Kong, Pokfulam Road, Hong Kong
[k] IPHC, CNRS/IN2P3, Université de Strasbourg, 67037 Strasbourg, France
[l] LPSC, Université Grenoble-Alpes, CNRS/IN2P3, F-38026 Grenoble Cedex, France
[m] ILL, 38042 Grenoble Cedex, France
[n] GSI Helmholtzzentrum für Schwerionenforschung GmbH, 64291 Darmstadt, Germany
[o] Department of Physics, University of Sofia, 1164 Sofia, Bulgaria
[p] National Physical Laboratory, Teddington, Middlesex, TW11 0LW, United Kingdom
[q] Departamento de Física Teórica, Universidad Autónoma de Madrid, E-28049 Madrid, Spain
[r] Instituto de Estructura de la Materia, CSIC, E-28006 Madrid, Spain
[s] A.W. Wright Nuclear Structure Laboratory, Yale University, New Haven, CT 06520, USA
[t] Institut für Kernphysik, Technische Universitäat Darmstadt, 64289 Darmstadt, Germany
[u] INFN Sezione di Milano, I-20133 Milano, Italy

ARTICLE INFO

Article history:
Received 24 July 2015
Received in revised form 9 September 2015
Accepted 16 September 2015
Available online 25 September 2015
Editor: V. Metag

ABSTRACT

The first fast-timing measurements from nuclides produced via the in-flight fission mechanism are reported. The lifetimes of the first 2^+ states in ^{104,106}Zr nuclei have been measured via β-delayed γ-ray timing of stopped radioactive isotope beams. An improved precision for the lifetime of the 2_1^+ state in ^{104}Zr was obtained, $\tau(2_1^+) = 2.90^{+25}_{-20}$ ns, as well as a first measurement of the 2_1^+ state in ^{106}Zr, $\tau(2_1^+) = 2.60^{+20}_{-15}$ ns, with corresponding reduced transition probabilities of $B(\mathrm{E2}; 2_1^+ \rightarrow 0_{g.s.}^+) = 0.39(2)\ e^2\mathrm{b}^2$ and $0.31(1)\ e^2\mathrm{b}^2$, respectively. Comparisons of the extracted ground-state deformations, $\beta_2 = 0.39(1)$ (^{104}Zr) and $\beta_2 = 0.36(1)$ (^{106}Zr) with model calculations indicate a persistence of prolate deformation. The data show that ^{104}Zr is the most deformed of the neutron-rich Zr isotopes measured so far.

* Corresponding author at: School of Computing, Engineering and Mathematics, University of Brighton, Brighton, BN2 4GJ, United Kingdom.
E-mail address: f.browne@brighton.ac.uk (F. Browne).

http://dx.doi.org/10.1016/j.physletb.2015.09.043

The shape of the atomic nucleus is one of its most fundamental properties. When the nuclear shells are filled to the "magic numbers" [1,2], the nucleonic distribution is spherical. In-between these major shell closures, the nuclear shape can stabilise to a non-spherical deformed configuration. The simplest of these is the quadrupole deformation, of which the two varieties are labelled as prolate (rugby ball) and oblate (discus) shapes. The quantification of these shapes in regions of the nuclear chart which display rapid shape changes as a function of nucleon number provides stringent tests to a variety of nuclear models. They also provide essential input for developing contemporary theoretical frameworks [3].

The zirconium isotopes ($Z = 40$) are located centrally with respect to the $1f_{7/2}$ ($Z = 28$) and $1g_{9/2}$ ($Z = 50$) major shell closures, making them an exemplary case study of mid-shell nuclei. The most abundant isotope of zirconium ($N = 50$) exhibits doubly magic behaviour due to the reinforcement of the *pf* proton shell closure at $Z = 40$ by the major $N = 50$ neutron shell closure [4,5]. A region of weak proton–neutron coupling follows [6,7] up to the nearly doubly-magic ^{96}Zr ($N = 56$) [8]. A rapid shape-phase transition (or shape coexistence) occurs across $N = 60$ [9–12], and from thereon a large degree of collectivity and static ground-state quadrupole deformation is manifest towards the middle of the $N = 50$–82 shell [12,13]. The onset of deformation has been ascribed to the proton–neutron interactions of the spin–orbit partner orbitals, $\pi g_{9/2}$ and $\nu g_{7/2}$ [14,15], and is reinforced in $N \geq 60$ nuclei by the increased occupancy of the high-j low-Ω $\nu h_{11/2}$ orbitals [16–19]. Laser spectroscopy measurements have shown this ground-state deformation to be strongly prolate for ^{101}Zr [20]. The axial symmetry of the $N > 60$ Zr isotopes is at odds with its higher-Z neighbours, which exhibit triaxiality [21–24], conversely lower-Z Sr isotopes exhibit a more severe transition to strongly deformed ground-state deformations [25]. The simplicity of their axially symmetric deformation could make the $N > 60$ Zr isotopes a good reference case for the global understanding of this wide mid-shell region. Although the number of active neutrons (or holes) is maximum at the mid-shell ($N = 66$), the observed increase of 2^+_1 energies suggests a decrease in deformation after $N = 64$ [13]. This has been discussed with respect to the possibility of an $N = 70$ sub-shell [26] with important implications for waiting points of the astrophysical *r*-process.

In this Letter, the first application of β-delayed γ-ray (β-γ) fast-timing measurements of radioactive isotope beams produced through the in-flight fission mechanism is used to measure the lifetimes of the 2^+_1 states in ^{104,106}Zr. The reduced transition probabilities, $B(\mathrm{E2}; 2^+_1 \rightarrow 0^+_{g.s.})$, an observable which measures the correlations between ground- and excited-states, are extracted and compared to theoretical values from projected shell model and algebraic model calculations. The quadrupole deformation of the ground-states are extracted from the $B(\mathrm{E2}; 2^+_1 \rightarrow 0^+_{g.s.})$ values and compared to a variety of nuclear mean-field calculations.

The experimental investigation of ^{104,106}Zr was carried out at the Radioactive Isotope Beam Factory (RIBF), operated by the RIKEN Nishina Center (RNC) and the Center for Nuclear Study, University of Tokyo. A $^{238}U^{86+}$ primary beam of average intensity 6.24×10^{10} particles/s was accelerated to an energy of 345 MeV/nucleon. The in-flight abrasion fission of the beam was induced by a 555 mg/cm^2 ^{9}Be production target situated at the entrance of the BigRIPS fragment separator [27]. Fission fragments were selected through the $B\rho$–ΔE–$B\rho$ method and identified using the TOF–$B\rho$–ΔE method [28]. The data were collected using two different settings of the BigRIPS and ZeroDegree spectrometers [27], centred on the β-decay parents of ^{104,106}Zr. A total of 6.2×10^5 ^{106}Y ions were transmitted in a wide-range and very neutron-rich setting, and 3.8×10^5 ^{104}Y ions in a setting with a focus on a less exotic region [29].

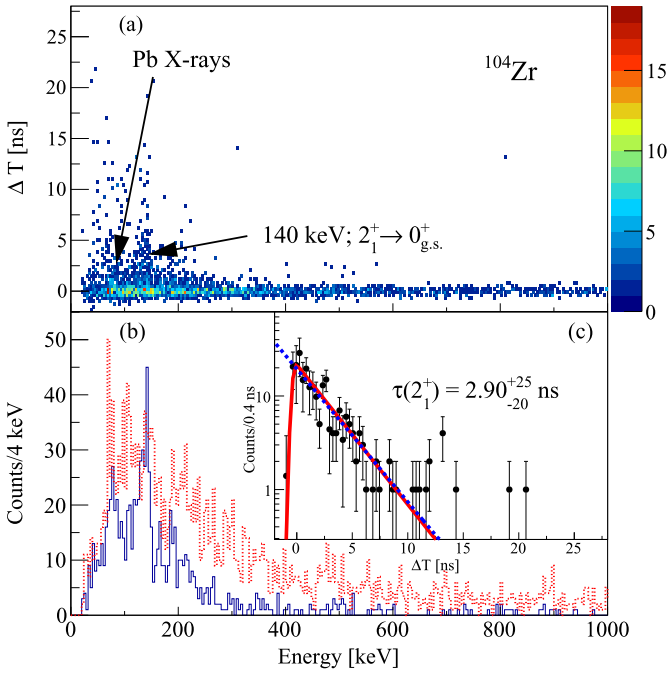

Fig. 1. (Colour online.) (a) Energy–time-difference matrix observed in coincidence with β-electrons detected within 1 s of an ^{104}Y implantation. (b) The γ-ray energy spectrum of the delayed (solid blue) and prompt (dashed red) components of the matrix. (c) Background subtracted time difference spectrum for the $2^+_1 \rightarrow 0^+_{g.s.}$ transition. (See text for details of the fits.)

The secondary beam was implanted into the WAS3ABi silicon array [30], which detected ion implantations and their subsequent β-decay electrons. For this experiment, WAS3ABi comprised 5 layers of double-sided silicon strip detectors placed 0.5 mm apart, each with 60 vertical and 40 horizontal strips. The width and depth of each strip were both 1 mm, giving a total active area of 60×40 mm^2. Candidate β decays had to be detected within the same implantation pixel as the preceding ion, and within approximately five times the β-decay half-life of the parent nuclide. For the purpose of precision timing of electrons for β–γ measurements, BC-148 plastic scintillators (β-plastics) of 2-mm thickness and area 65×45 mm^2 were installed upstream and downstream of WAS3ABi, these were each optically coupled to two photomultiplier tubes (PMT), with the arithmetic mean of the time signals used as the β^- detection time. The absolute efficiency of the β-plastics was ∼50%.

An array of 18 small $LaBr_3$(Ce) crystals was constructed for the measurement of level lifetimes in a low-yield and low-background environment [31]. This array, as well as the EURICA [32] HPGe array, surrounded WAS3ABi for the purpose of measuring isomeric and β-delayed γ rays. The nominal distance between the centre of WAS3ABi and the front of the $LaBr_3$(Ce) detectors was 24 cm and each cylindrical crystal had a diameter of 38.1 mm and a depth of 50.8 mm. At the energies of interest (150–170 keV) the absolute efficiency of the array was measured to be ∼4%, the energy resolution to be 10% and the time resolution FWHM = 825(25) ps. Energy–time matrices were constructed using the γ-ray energy measured in the $LaBr_3$(Ce) array, and the time-difference, ΔT, between the β^- and γ-ray detection. Figs. 1(a) and 2(a) show the matrices for ^{104}Zr and ^{106}Zr, respectively.

Figs. 1(b) and 2(b) show the prompt (red dashed line, $\Delta T < \pm 0.5$ ns) and delayed (solid blue line, $1.5 < \Delta T < 25$ ns) projections of γ-ray energy. Both show lead X-rays which are produced by γ-ray interactions with the passive anti-Compton lead shielding surrounding each $LaBr_3$(Ce) crystal. The delayed spectrum of

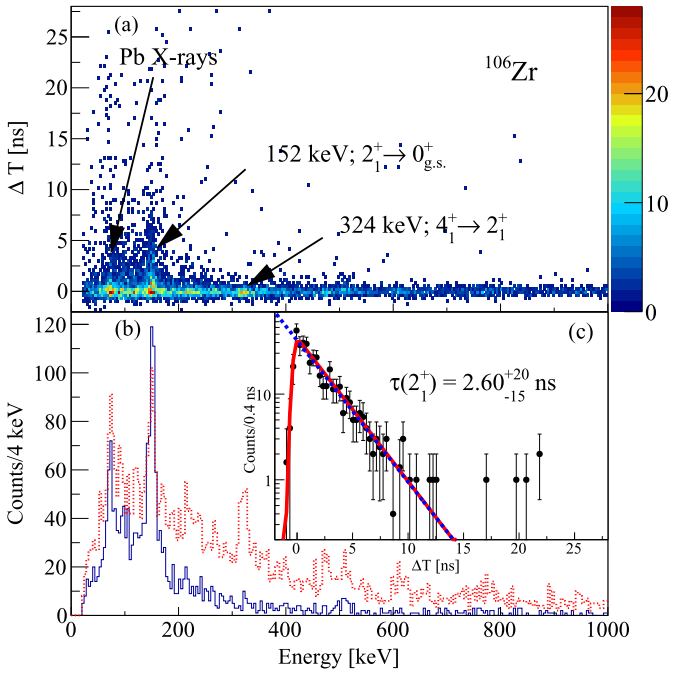

Fig. 2. (Colour online.) (a) Energy–time-difference matrix observed in coincidence with β^- detected within 0.3 s of an ^{106}Y implantation. (b) The γ-ray energy spectrum of the delayed (solid blue) and prompt (dashed red) components of the matrix. (c) Background subtracted time difference spectrum for the $2^+_1 \rightarrow 0^+_{g.s.}$ transition. (See text for details of the fits.)

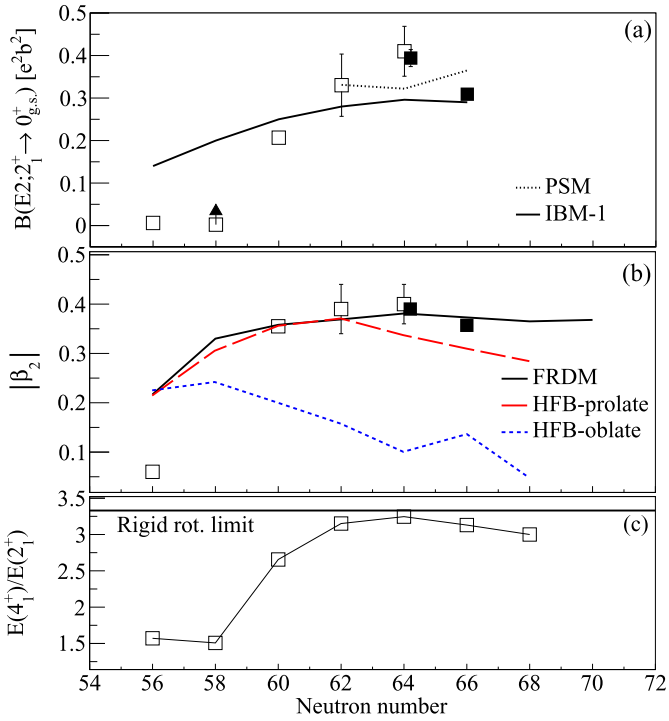

Fig. 3. (Colour online.) (a) Experimental $B(E2; 2^+_1 \rightarrow 0^+_{g.s.})$ values of even–even $^{96-106}$Zr isotopes, compared with the results of PSM [38] and IBM-1 [39] calculations. The arrow on the $N = 58$ point reflects the fact the data point is a limit. (b) Experimentally determined β_2 values for $^{100-106}$Zr, compared with the results of mean-field calculations. (c) The $E(4^+_1)/E(2^+_1)$ ratios for $^{96-108}$Zr. The open symbols are from Refs. [40–44,13] and closed symbols are from the current work.

Fig. 1(b) shows the 140-keV $2^+_1 \rightarrow 0^+_{g.s.}$ transition in ^{104}Zr. The delayed γ-ray energy spectrum of ^{106}Zr, Fig. 2(b) shows the 152 keV $2^+_1 \rightarrow 0^+_{g.s.}$ transition. It is noteworthy that in the prompt (red) spectrum of Fig. 2(b), the 324-keV $4^+_1 \rightarrow 2^+_1$ transition is clearly observed, implying strong feeding of the 2^+_1 state from the 4^+_1 state. Indeed, in both nuclei the efficiency-corrected intensities from the EURICA spectra indicate the feeding of the 2^+_1 levels is ∼50% from the 4^+_1 level and ∼20% each from two other, as yet, unassigned transitions with energies between 600–800 keV. The energy–time matrices of Figs. 1(a) and 2(a) indicate that there exist no measurable delayed structures from these transitions. Therefore, a systematic uncertainty of 50 ps has been included in the upper limit of the lifetime of the 2^+_1 state based on lifetimes of the 4^+_1 state estimated from Refs. [33–35].

Figs. 1(c) and 2(c) show the time-difference spectra for the $2^+_1 \rightarrow 0^+_{g.s.}$ transition of ^{104}Zr and ^{106}Zr, respectively. Lifetimes were extracted using two approaches. The first, fitted a single decay component to the delayed shoulder of the time-difference distribution between the limits of 2 and 10 ns, as shown by the dotted blue curve. Secondly, the solid red curve shows the result of using the convolution of the detector resolution and an exponential decay as the fit function. The resolution of the detector was assumed to be Gaussian shaped, with a width obtained from a fit to the $(5^-) \rightarrow (4^-)$ 159 keV transition in ^{102}Zr [36], which was observed to be prompt. We obtain consistent lifetimes with the two methods of $\tau(2^+_1) = 2.90^{+25}_{-20}$ ns and 2.60^{+20}_{-15} ns for ^{104}Zr and ^{106}Zr, respectively. The former is in agreement with the value in Ref. [37], 2.9(4) ns, but has a higher precision.

The $B(E2; 2^+_1 \rightarrow 0^+_{g.s.})$ values of Fig. 3(a) were obtained following the prescription of Ref. [45], yielding values of 0.39(2) e^2b^2 and 0.31(1) e^2b^2 for ^{104}Zr and ^{106}Zr, respectively. The β_2 values shown in Fig. 3(b) were derived from the $B(E2; 2^+_1 \rightarrow 0^+_{g.s.})$ values shown in Fig. 3(a), assuming a quadrupoloid shape and including terms to 3rd order [46]. For ^{104}Zr and ^{106}Zr, this procedure gives $\beta_2 = 0.39(1)$ and 0.36(1), respectively. The observation that the $E(4^+_1)/E(2^+_1)$ ratios, shown in Fig. 3(c), approach the limiting value of 3.33 for $N > 60$, provides evidence that the rigid-rotor model is a good approximation in which to interpret these nuclei. The new lifetime measurement shows that ^{104}Zr is the most deformed of the neutron-rich Zr isotopes.

Fig. 3(b) shows β_2 values calculated using the finite-range droplet model (FRDM) [47] (solid line), as well as prolate and oblate solutions of Hartree–Fock–Bogolyubov (HFB) calculations employing the Gogny-D1S interaction [48] (red and blue dashed lines, respectively). The FRDM predicts strong prolate minima for $N > 56$, whereas the HFB solutions indicate prolate–oblate shape coexistence with small energy differences between the two shapes, e.g. less 0.2 MeV for $N = 56$. Comparison to the β_2 values extracted from the data strongly supports the conclusion of prolate shapes for the $N > 60$ Zr nuclei.

The direct comparison between experimentally determined $B(E2; 2^+_1 \rightarrow 0^+_{g.s.})$ values and model predictions provides significant insight to microscopic structure. In particular, the projected shell model (PSM) provides the framework in which the single-particle shell model can be applied to deformed nuclei. The PSM calculations depicted in Fig. 3(a) (dotted line) [38] use deformations from Ref. [47] as input parameters, with the exception of ^{104}Zr for which the β_2 value is artificially reduced. The predicted $B(E2; 2^+_1 \rightarrow 0^+_{g.s.})$ values are particularly sensitive to the quadrupole–quadrupole interaction [38], which is derived self-consistently with the β_2 parameter. Therefore, experimentally derived $B(E2; 2^+_1 \rightarrow 0^+_{g.s.})$ values are a valuable constraint to impose on the model.

The solid line in Fig. 3(a) shows the $B(E2; 2^+_1 \rightarrow 0^+_{g.s.})$ values calculated using the interacting boson model (IBM-1) [39] and a set of global parameters. Whilst the results do show a maximum

$B(\mathrm{E2}; 2_1^+ \rightarrow 0_{g.s.}^+)$ value at $N = 64$, the maximum is significantly lower than that observed. This difference could be due to fact that the parameters of the Hamiltonian were obtained through fitting to energy levels and $B(\mathrm{E2})$ values of the triaxially deformed nuclei Mo, Pd and Ru nuclei [49,50,22,51] in addition to the well deformed $N \geq 60$ Zr nuclei. Since the energy levels and $B(\mathrm{E2})$ values of triaxial Mo and Ru isotopes are well reproduced [39], the deviation of the calculations to the observations may be attributed to the IBM-1 Hamiltonian not reflecting the axial symmetry of the zirconium nuclei for $N > 60$.

In summary, we have reported on lifetime measurements of 2_1^+ states in ^{104,106}Zr, which show that ^{104}Zr is the most deformed of the neutron-rich Zr isotopes. In addition, comparison of the magnitude of the extracted deformation with the results of model calculations [47,48] indicate that these nuclei are prolate deformed. Moreover, we have demonstrated that the technique of lifetime measurements following the β-decay of RI beams is a feasible method of extracting spectroscopic information at the contemporary limits of experimentally accessible nuclei. Such techniques can be further exploited at the RIBF, and also at future projects such as FAIR [52,53].

Acknowledgements

We would like to express our gratitude to the RIKEN Nishina Center accelerator department for providing a stable and high intensity ^{238}U primary beam. F.B. is grateful to C.R. Nita for invaluable discussions on fast-timing measurements using $LaBr_3$(Ce) detectors. This work was supported by JSPS KAKENHI Grants Nos. 26800117 and 25247045. UK authors were supported by STFC Grant Nos. ST/J000132/1, ST/J000051/1 and ST/K502431/1. P.H.R. acknowledges support from the UK National Measurement Office (NMO). P.-A.S. was financed by JSPS Grant No. 23 01752 and the RIKEN Foreign Postdoctoral Researcher Program. V.W. was supported by DOE Grant No. DE-FG02-91ER-40609. J.T. was financed by Spanish Ministerio de Ciencia e Innovación under Contracts No. FPA2009-13377-C02 and No. FPA2011-29854-C04. We acknowledge the EUROBALL Owners Committee for the loan of germanium detectors and the PreSpec Collaboration for the readout electronics of the cluster detectors.

References

[1] O. Haxel, J.H.D. Jensen, H.E. Suess, On the "magic numbers" in nuclear structure, Phys. Rev. 75 (1949) 1766.
[2] M.G. Mayer, On closed shells in nuclei. II, Phys. Rev. 75 (1949) 1969.
[3] W. Nazarewicz, Microscopic origin of nuclear deformations, Nucl. Phys. A 574 (1994) 27.
[4] K. Kaneko, M. Hasegawa, T. Mizusaki, Y. Sun, Magicity and occurrence of a band with enhanced $B(E2)$ in neutron-rich nuclei ^{68}Ni and ^{90}Zr, Phys. Rev. C 74 (2006) 024321.
[5] P.E. Garrett, W. Younes, J.A. Becker, L.A. Bernstein, E.M. Baum, D.P. DiPrete, R.A. Gatenby, E.L. Johnson, C.A. McGrath, S.W. Yates, M. Devlin, N. Fotiades, R.O. Nelson, B.A. Brown, Nuclear structure of the closed subshell nucleus ^{90}Zr studied with the $(n, n'\gamma)$ reaction, Phys. Rev. C 68 (2003) 024312.
[6] V. Werner, et al., Evidence for the microscopic formation of mixed-symmetry states from magnetic moment measurements, Phys. Rev. C 78 (2008) 031301.
[7] A. Chakraborty, et al., Collective structure in ^{94}Zr and subshell effects in shape coexistence, Phys. Rev. Lett. 110 (2013) 022504.
[8] I. Boboshin, V. Varlamov, B. Ishkhanov, E. Romanovsky, New double-magic nucleus ^{96}Zr and conditions for existence of new magic nuclei, Phys. At. Nucl. 70 (2007) 1363.
[9] S. Rinta-Antila, S. Kopecky, V.S. Kolhinen, J. Hakala, J. Huikari, A. Jokinen, A. Nieminen, J. Äystö, J. Szerypo, Direct mass measurements of neutron-rich zirconium isotopes up to ^{104}Zr, Phys. Rev. C 70 (2004) 011301.
[10] J.E. García-Ramos, K. Heyde, R. Fossion, V. Hellemans, S. De Baerdemacker, A theoretical description of energy spectra and two-neutron separation energies for neutron-rich zirconium isotopes, Eur. Phys. J. A 26 (2005) 221.
[11] S. Anghel, G. Cata-Danil, N.V. Zamfir, Structure features revealed from the two neutron separation energies, Rom. J. Phys. 54 (2009) 301.
[12] E. Cheifetz, R.C. Jared, S.G. Thompson, J.B. Wilhelmy, Experimental information concerning deformation of neutron rich nuclei in the A ∼ 100 region, Phys. Rev. Lett. 25 (1970) 38.
[13] T. Sumikama, et al., Structural evolution in the neutron-rich nuclei ^{106}Zr and ^{108}Zr, Phys. Rev. Lett. 106 (2011) 202501.
[14] S. Michiaki, A. Akito, Shape transition of nuclei with mass around A = 100, Nucl. Phys. A 515 (1990) 77.
[15] P. Federman, S. Pittel, Unified shell-model description of nuclear deformation, Phys. Rev. C 20 (1979) 820.
[16] W. Urban, J. Pinston, T. Rzaca-Urban, A. Złomaniec, G. Simpson, J. Durell, W. Phillips, A.G. Smith, B. Varley, I. Ahmad, N. Schulz, First observation of the $\nu 9/2[404]$ orbital in the A ∼ 100 mass region, Eur. Phys. J. A 16 (2003) 11.
[17] W. Urban, J. Pinston, J. Genevey, T. Rzaca-Urban, A. Złomaniec, G.S. Simpson, J. Durell, W. Phillips, A.G. Smith, B. Varley, I. Ahmad, N. Schulz, The $\nu 9/2[404]$ orbital and the deformation in the A ∼ 100 region, Eur. Phys. J. A 22 (2004) 241.
[18] W. Nazarewicz, in: International Conference on Contemporary Topics in Nuclear Structure Physics, World Scientific, 1988, pp. 467–486.
[19] A.G. Smith, et al., The influence of $\nu h 11/2$ occupancy on the magnetic moments of collective 2_1^+ states in A ∼ 100 fission fragments, Phys. Lett. B 591 (2004) 55.
[20] P. Campbell, H.L. Thayer, J. Billowes, P. Dendooven, K.T. Flanagan, D.H. Forest, J.A.R. Griffith, J. Huikari, A. Jokinen, R. Moore, A. Nieminen, G. Tungate, S. Zemlyanoi, J. Äystö, Laser spectroscopy of cooled zirconium fission fragments, Phys. Rev. Lett. 89 (2002) 082501.
[21] Y. Luo, et al., Shape transitions and triaxiality in neutron-rich odd-mass Y and Nb isotopes, Eur. Phys. J. A (Suppl.) 25 (2005) 469.
[22] H. Watanabe, et al., Development of axial asymmetry in the neutron-rich nucleus ^{110}Mo, Phys. Lett. B 704 (2011) 270.
[23] A.M. Bruce, et al., Shape coexistence and isomeric states in neutron-rich ^{112}Tc and ^{113}Tc, Phys. Rev. C 82 (2010) 044312.
[24] P.-A. Söderström, et al., Shape evolution in ^{116,118}Ru: triaxiality and transition between the O(6) and U(5) dynamical symmetries, Phys. Rev. C 88 (2013) 024301.
[25] H. Mach, F. Wohn, G. Molnár, K. Sistemich, J.C. Hill, M. Moszyński, R. Gill, W. Krips, D. Brenner, Retardation of $B(E2; 0_1^+ \rightarrow 2_1^+)$ rates in $^{90-96}$Sr and strong subshell closure effects in the A ∼ 100 region, Nucl. Phys. A 523 (1991) 197.
[26] M. Bender, K. Bennaceur, T. Duguet, P.H. Heenen, T. Lesinski, J. Meyer, Tensor part of the Skyrme energy density functional. II. Deformation properties of magic and semi-magic nuclei, Phys. Rev. C 80 (2009) 064302.
[27] T. Kubo, D. Kameda, H. Suzuki, N. Fukuda, H. Takeda, Y. Yanagisawa, M. Ohtake, K. Kusaka, K. Yoshida, N. Inabe, T. Ohnishi, A. Yoshida, K. Tanaka, Y. Mizoi, BigRIPS separator and ZeroDegree spectrometer at RIKEN RI Beam Factory, Prog. Theor. Exp. Phys. 2012 (2012) 03C003.
[28] N. Fukuda, T. Kubo, T. Ohnishi, N. Inabe, H. Takeda, D. Kameda, H. Suzuki, Identification and separation of radioactive isotope beams by the BigRIPS separator at the RIKEN RI Beam Factory, Nucl. Instrum. Methods Phys. Res., Sect. B, Beam Interact. Mater. Atoms 317 (2013) 323.
[29] T. Sumikama, et al., Structure of neutron-rich Zr and Mo isotopes, RIKEN Accel. Prog. Rep. 47 (2014) 9.
[30] S. Nishimura, Beta-gamma spectroscopy at RIBF, Prog. Theor. Exp. Phys. 2012 (2012) 03C006.
[31] Z. Patel, et al., Commissioning of a $LaBr_3$(Ce) array with EURICA at RIBF, RIKEN Accel. Prog. Rep. 47 (2014) 13.
[32] P.-A. Söderström, et al., Installation and commissioning of EURICA – Euroball-RIKEN Cluster Array, Nucl. Instrum. Methods Phys. Res., Sect. B, Beam Interact. Mater. Atoms 317 (2013) 649.
[33] A.G. Smith, et al., Lifetimes of yrast rotational states of the fission fragments ^{100}Zr and ^{104}Mo measured using a differential plunger, J. Phys. G 28 (2002) 2307.
[34] H. Ohm, M. Liang, G. Molnár, K. Sistemich, The collectivity in the yrast band of ^{100}Zr: the half-life of the 4_1^+ state, Z. Phys. A 334 (1989) 519.
[35] C. Hutter, et al., $B(E2)$ values and the search for the critical point symmetry X(5) in ^{104}Mo and ^{106}Mo, Phys. Rev. C 67 (2003) 054315.
[36] H. Hua, C.Y. Wu, D. Cline, A.B. Hayes, R. Teng, R.M. Clark, P. Fallon, A. Goergen, A.O. Macchiavelli, K. Vetter, Triaxiality and the aligned h_{112} neutron orbitals in neutron-rich Zr and Mo isotopes, Phys. Rev. C 69 (2004) 014317.
[37] J.K. Hwang, A.V. Ramayya, J.H. Hamilton, Y.X. Luo, A.V. Daniel, G.M. Ter-Akopian, J.D. Cole, S.J. Zhu, Half-life measurements of several states in ^{95,97}Sr, ^{97,100,104}Zr, ^{106}Mo, and ^{148}Ce, Phys. Rev. C 73 (2006) 044316.
[38] Y.-X. Liu, Y. Sun, X.-H. Zhou, Y.-H. Zhang, S.-Y. Yu, Y.-C. Yang, H. Jin, A systematical study of neutron-rich Zr isotopes by the projected shell model, Nucl. Phys. A 858 (2011) 11.
[39] M. Böyükata, P.V. Isacker, İ. Uluer, Description of nuclei in the A ∼ 100 mass region with the interacting boson model, J. Phys. G 37 (2010) 105102.
[40] D. Abriola, A. Sonzogni, Nuclear data sheets for A = 96, Nucl. Data Sheets 109 (2008) 2501.
[41] B. Singh, Z. Hu, Nuclear data sheets for A = 98, Nucl. Data Sheets 98 (2003) 335.

[42] B. Singh, Nuclear data sheets for A = 100, Nucl. Data Sheets 109 (2008) 297.
[43] D.D. Frenne, Nuclear data sheets for A = 102, Nucl. Data Sheets 110 (2009) 1745.
[44] J. Blachot, Nuclear data sheets for A = 104, Nucl. Data Sheets 108 (2007) 2035.
[45] S. Raman, C.W. Nestor Jr., P. Tikkanen, Transition probability from the ground to the first-excited 2^+ state of even–even nuclides, At. Data Nucl. Data Tables 78 (2001) 1.
[46] K.E.G. Lobner, M. Vetter, V. Honig, Nuclear intrinsic quadrupole moments and deformation parameters, Nucl. Data Tables A 7 (1970) 495.
[47] P. Moller, J. Nix, W. Myers, W. Swiatecki, Nuclear ground-state masses and deformations, At. Data Nucl. Data Tables 59 (1995) 185.
[48] R. Rodríguez-Guzmán, P. Sarriguren, L. Robledo, S. Perez-Martin, Charge radii and structural evolution in Sr, Zr, and Mo isotopes, Phys. Lett. B 691 (2010) 202.
[49] A. Guessous, et al., Prompt γ-ray spectroscopy of the ^{104}Mo and ^{108}Mo fission fragments, Phys. Rev. C 53 (1996) 1191.
[50] A. Guessous, N. Schulz, W.R. Phillips, I. Ahmad, M. Bentaleb, J.L. Durell, M.A. Jones, M. Leddy, E. Lubkiewicz, L.R. Morss, R. Piepenbring, A.G. Smith, W. Urban, B.J. Varley, Harmonic two-phonon γ-vibrational state in neutron-rich ^{106}Mo, Phys. Rev. Lett. 75 (1995) 2280.
[51] S. Lalkovski, et al., Two-quasiparticle and collective excitations in transitional ^{108,110}Pd nuclei, Eur. Phys. J. A 18 (2003) 589.
[52] O.J. Roberts, A.M. Bruce, P.H. Regan, Z. Podolyák, C.M. Townsley, J.F. Smith, K.F. Mulholland, A. Smith, A $LaBr_3$: Ce fast-timing array for DESPEC at FAIR, Nucl. Instrum. Methods Phys. Res., Sect. A, Accel. Spectrom. Detect. Assoc. Equip. 748 (2014) 91.
[53] P. Regan, From RISING to the DESPEC fast-timing project within NUSTAR at FAIR: sub-nanosecond nuclear timing spectroscopy with $LaBr_3$ scintillators, Appl. Radiat. Isot. 70 (2012) 1125.